Peruvian stalagmites as archives of Holocene temperature and rainfall variability

ISBN 978 90 8659 304 0

Peruvian stalagmites as archives of Holocene temperature and rainfall variability [Ph.D. thesis, Vrije Universiteit Amsterdam]

In Dutch: Peruaanse stalagmieten als archieven voor holocene temperatuur- en regenval-variaties [ac. proefschrift, Vrije Universiteit Amsterdam]

Cover photo: Cueva de las Lechuzas

This project was funded by the Netherlands Organisation for Scientific Research (NWO)

VRIJE UNIVERSITEIT

Peruvian stalagmites as archives of Holocene temperature and rainfall variability

ACADEMISCH PROEFSCHRIFT

ter verkrijging van de graad Doctor aan
de Vrije Universiteit Amsterdam,
op gezag van de rector magnificus
prof.dr. L.M. Bouter,
in het openbaar te verdedigen
ten overstaan van de promotiecommissie
van de faculteit der Aard- en Levenswetenschappen
op maandag 11 mei 2009 om 13.45 uur
in de aula van de universiteit,
De Boelelaan 1105

door

Martin Reinier van Breukelen

geboren te 's-Gravenhage

promotor:	prof.dr. D. Kroon
copromotor:	dr. H.B. Vonhof

leescommissie: prof.dr. T.C. Atkinson
prof.dr. H. Hooghiemstra
dr. G.M. Ganssen
dr. D. Genty
dr. S. Verheyden

Contents

Dankwoord

Een proefschrift schrijven doe je zelden alleen. Het proces van denken schrijven en onderzoek doen is zo veelomvattend dat je het niet zonder de hulp van experts maar ook niet zonder de hulp van betrokken 'leken' kan volbrengen.

Grote dank voor zijn bijdrage als expert gaat uit naar Hubert Vonhof, mijn co-promotor. Hij was het die het projectvoorstel schreef en er met al zijn enthousiasme nauw bij betrokken bleef. Hubert, in 2001 kreeg ik de kans om jouw 'collega' te worden als student-assistent in het stabiele-isotopenlab Zo werd ik tijdens mijn studentenperiode in de wereld van stabiele isotopen ingewijd. Het projectvoorstel dat je schreef voor klimaatonderzoek in Peru, wekte mijn interesse en ik ben blij dat ik dit onderzoek heb mogen uitvoeren in al zijn facetten. Het veldwerk in Peru: het exploreren van grotten, en het labwerk waren geweldige gedeelde ervaringen. De histoplasmose die ik helaas opliep bij dit veldwerk, deelden we gelukkig niet. Tijdens deze voor mij onfortuinlijke ervaring heb ik evenwel jouw menselijke kant als erg prettig ervaren. Je assistentie tijdens mijn promotietraject en vooral tijdens de geweldige veldwerken was onmisbaar. Een betere begeleiding voor dit project had ik me niet kunnen wensen.

Ook bedank ik graag Dick Kroon. Dick, als mijn promotor gaf je in het eerste jaar al aan dat jouw bijdrage aan dit proefschrift vooral bij het schrijven zou komen. Geen woord hiervan was gelogen. Snel en grondig werkte je mijn manuscripten door en de trok de boel uit het slop als ik dreigde vast te lopen.

Mijn dank gaat tevens uit naar de leescommissie, bestaande uit prof.dr. T.C. Atkinson, prof.dr. H. Hooghiemstra, G.M. Ganssen, dr. D. Genty en dr. S. Verheyden. Bedankt voor uw commentaar op de eerste versie van dit manuscript.

Mijn speciale dank gaat uit naar Sophie Verheyden en Dominique Genty. Zij stelden hun lab ten Zuiden van Parijs voor een aantal maanden ter beschikking voor het meten van isotopen aan vloeistofinsluitsels. Deze samenwerking resulteerde in een co-auteurschap waarvan het resultaat zichtbaar is in hoofdstuk 5 van dit proefschrift.

De technische steun kwam tijdens mijn promotietraject van Onno Postma. Hij hielp gedurende het project met het bouwen en ontwerpen van de crusher, waarmee uiteindelijk de vloeistofinsluitsels ontsloten konden worden en vervolgens gemeten op hun isotopensamenstelling. Onno, bedankt voor al je onmisbare technische assistentie.

Special thanks go to my English colleagues, Peter Rowe, Alina Marca and Paul Dennis. They are thanked for their scientific contribution and friendship during the period they gave me the opportunity to work in their lab in Norwich. I enjoyed staying there tremendously. Alan Kendall is thanked for his contribution in petrology of the speleothems and fluid inclusions.

De collega's van het isotopenlab ben ik veel dank verschuldigd: Hubert Vonhof, Suzan Warmerdam-Verdegaal, Gareth Davies, Richard Smeets, Coos van Belle, Marin Waaijer, veel dank voor jullie wetenschappelijke en technische bijdragen. Wynanda Koot en Bouk Laçet hebben de stalagmieten tot slijpplaatjes en slaps omgetoverd. De SEM-foto's zijn gemaakt door Saskia Kars.

De collega AIO's en OIO's wil ik bedanken, samen met mijn collega's op de E3-gang, voor de wetenschappelijke discussies, relaxmomenten en borrels.

And thank God there are roommates, for discussion, (lots of) coffee, drinks and lunches. Not to forget that writing is more then a job. Alex Wright and Margot Saher, we will always have: E346.

Tijdens de veldwerken in Peru hebben Quinto Quaresima, Sandro Mariani, Alejandro Lagos Manrique, Elisabetta Ferroni, Lidia Romero-Pittman, Jhon Huaman ons geholpen veilig door de grotten te komen.

Ook wil ik de familie uit Urubamba, Peru, bedanken voor hun gastvrije ontvangsten, als ik plotseling voor hun deur stond. Raúl, Tania y Pedro muchas gracias para toda la ayuda y el tiempo fantástico.

En dan als laatste maar zeker niet als minste: de achterban. Familie en vrienden zijn er om op terug te vallen. Zij zijn de mensen die het mogelijk maakten dat ik dagen achter mijn pc aan dit manuscript zat te werken. Dankzij hen lukte het me tussen alle bedrijven door te verhuizen, te trouwen, te badmintonnen en er zowaar iets van een sociaal leven op na te houden. Graag wil ik hier mijn ouders, Kees en Elly, noemen en danken voor het vertouwen in mij en mijn proefschrift. Pa en Ma, bedankt voor het vertrouwen, alle warme maaltijden en het eeuwige optimisme! Mijn zus en broer, Iris en Frank, mijn paranimfen, dank voor jullie steun en vertrouwen.

Tevens bedank ik mijn schoonfamilie, Anneke, Richard en Stephan, voor al het kluswerk in huis, het meeleven en het zorgen voor Anke.

Pas als laatste genoemd maar als eerste in mijn hoofd: mijn vrouw, Anke. Anke, de laatste jaren heb ik veel uren in de studeerkamer doorgebracht, tijd die afging van onze toch al schaarse tijd samen. Bedankt dat je mijn 'stok achter de deur was' als ik het even niet zag zitten. Bedankt voor alle tijd en vrijheid die je me gegeven hebt om dit te kunnen doen. Toch mooi om te weten dat we de kostbare tijd straks met zijn drieën kunnen delen...

Samenvatting

Opzet van het onderzoek

Grotten bieden informatie in de vorm van speleothemen: kalkformaties die in het stabiele en luchtvochtige klimaat van de grot worden gevormd. De meest bekende speleothemen zijn stalagmieten en stalactieten. Dit klimaatonderzoek richt zich op de informatie van speleothemen en specifiek op de klimaatinformatie zoals die is opgeslagen in stalagmieten.

Veel klimaatreconstructies op land en ook op zee zijn gebaseerd op het meten van subtiele veranderingen in de verhouding tussen de stabiele zuurstofisotopen. Het element zuurstof bestaat uit drie stabiele isotopen (^{16}O, ^{17}O en ^{18}O). Een isotoop heeft een verschillend aantal neutronen maar altijd hetzelfde aantal protonen als een ander isotoop van hetzelfde element. Door fysische processen zullen lichte isotopen (^{16}O, minder neutronen) anders reageren dan de zware isotopen (^{18}O, meer neutronen). Dit resulteert in een verandering in de onderlinge verhouding van de ^{16}O- en ^{18}O-isotopen. De onderlinge verhouding tussen de verschillende isotopen van de elementen zuurstof, koolstof en waterstof levert veel bruikbare informatie op over het klimaat in het verleden, bijvoorbeeld voor het reconstrueren van veranderingen in temperatuur en neerslag. Belangrijke klimaatgegevens kunnen uit (regen)water gehaald worden aan de hand van de verschillende isotopenverhoudingen. Fossiel regenwater is schaars en voornamelijk als ijs in gletsjers en ijskappen beschikbaar. IJskernen vormen een belangrijke basis voor onderzoek naar het klimaat in het Quartair, omdat fossiel water geanalyseerd kan worden. Een nadeel is de geografische verspreiding van ijskernen omdat ze alleen genomen kunnen worden in gebieden met een poolklimaat.

Informatie over de temperatuur wordt tevens vastgelegd in de zuurstofisotopenverhouding van carbonaat (calciet/aragoniet), waar stalagmieten uit bestaan. De verhouding tussen de zuurstofisotopen (^{16}O/^{18}O) is afhankelijk van de temperatuur, hierdoor is er informatie beschikbaar over de temperatuur ten tijde van de carbonaatafzetting. Echter, om de temperatuur in het verleden te kunnen berekenen is het nodig de zuurstofisotopenverhouding van het carbonaat van de stalagmiet en die van het grotwater op het moment van neerslag te kennen. In het carbonaat van speleothemen is een kleine hoeveelheid water ingesloten, zogeheten vloeistofinsluitsels. Wanneer de isotopenverhouding van dit 'fossiele' water gemeten kan worden, is de isotopenverhouding van het oorspronkelijke grotwater bekend en kan, door dit gegeven te combineren met de zuurstofisotopenverhouding van het carbonaat, de temperatuur ten tijde van de carbonaatvorming nauwkeurig gereconstrueerd worden.

In dit onderzoek presenteren we de eerste uit speleothemen afgeleide gegevens over holocene klimaatveranderingen in het Peruaanse Andesgebergte. Ten behoeve van deze klimaatreconstructies hebben we ons gefocust op de analyse van stabiele isotopen en sporenelementen van het carbonaat in speleothemen. Om de variatie in temperatuur en regenval beter te kunnen kwantificeren vanuit deze proxyrecords hebben we een techniek ontwikkeld waarmee we stabiele isotopen kunnen analyseren van fossiel 'druipwater' dat gevangen zit in kleine holtes (vloeistofinsluitingen). De hypothese is dat het combineren van gegevens over stabiele isotopen afkomstig uit vloeistofinsluitingen met die van het bijbehorende carbonaat ons in staat stelt tot een betrouwbare berekening van de temperatuur in vroeger tijden te komen.

Dit proefschrift bestaat uit twee onderdelen. Het eerste deel is technisch georiënteerd (hoofdstuk 2 t/m 5) en omvat de U-Th-dateringstechniek (hoofdstuk 2), een controle-experiment in een grot in Peru (hoofdstuk 3) en twee verschillende technieken om het water aan de speleothemen te onttrekken en de isotopensamenstelling ervan te bepalen (hoofdstuk 4 & 5). Deze technieken zijn toegepast op stalagmieten afkomstig uit drie grotten in Peru. De resultaten hiervan komen aan de orde in de hoofdstukken 6 t/m 9. In hoofdstuk 6 & 7 worden de resultaten geïnterpreteerd van de gegevens uit twee laaglandgrotten uit het Amazonebekken, terwijl in hoofdstuk 8 de allereerste klimaatgegevens gepresenteerd worden die afkomstig zijn van een stalagmiet uit een grot in het hooggebergte van de Andes. In hoofdstuk 9 zijn alle gemeten vloeistofinsluitsels met elkaar vergeleken met een eenvoudig neerslagisotopenfractionatiemodel.

Samenvatting per hoofdstuk

Hoofdstuk 1: Introduction

Algemene informatie over het klimaat van Zuid-Amerika en het ontstaan van stalagmieten.

Hoofdstuk 2: Uranium-series dating method applied on speleothems

De uranium-series dateringstechniek is complex, maar fundamenteel voor op speleothemen gebaseerd klimaatonderzoek, omdat ze een onafhankelijk en betrouwbaar ouderdomskader biedt. Alle in Peru verzamelde stalagmieten werden aan de Vrije Universiteit van Amsterdam (VUA) op basis van het radioactief verval van uranium naar thorium gedateerd. Behalve een ouderdomskader zijn er lageresolutiegegevens van stabiele isotopen vastgelegd. Op basis van de combinatie van dit ouderdomskader en de gegevens van stabiele isotopen is het geschiktste materiaal om het holoceen te onderzoeken geselecteerd. De voor dit onderzoek verzamelde en gedateerde speleothemen worden in dit hoofdstuk gepresenteerd, maar zonder nadere details.

Hoofdstuk 3: Seasonal environmental monitoring results from a cave in Peruvian Amazonia

Van september 2003 tot 2004 is tussen twee veldwerkperiodes door een controle-experiment uitgevoerd in de Cueva de las Lechuzas. De data bestaan uit metingen van de stabiele isotopensamenstelling en de sporenelementenconcentraties aan verzamelde watermonsters en het permanent volgen van de temperatuur en de druppelsnelheid op specifieke locaties in de grot. Dit experiment is opgezet om de situatie in de grot te onderzoeken en de wisselwerking met seizoensinvloeden van buiten. Het laat de complexe en dynamische wisselwerking zien van de hydrologie in de grot met de neerslagveranderingen buiten.

Hoofdstuk 4: A continuous-flow crushing device for on-line δ^2H analysis of fluid inclusion water in speleothems

Een van de hoofdzaken van dit proefschrift is de ontwikkeling van een methode om de stabiele-isotopenverhouding (δ^2H) van vloeistofinsluitingen uit calciet van speleothemen nauwkeurig te kunnen analyseren. Twee onafhankelijke technieken om water aan de insluitingen te onttrekken worden beschreven. Hoofdstuk 4 beschrijft een nieuwe, aan de Vrije Universiteit van Amsterdam ontwikkelde, methode. Deze maakt het mogelijk het ingesloten water aan het calciet te onttrekken en de stabiele-isotopenverhouding nauwkeurig te bepalen. Dit is een belangrijke technische doorbraak voor dit type vloeistofonttrekking en voor het doen van metingen eraan en biedt nieuwe mogelijkheden voor klimaatonderzoek met speleothemen. De methode is gebruikt voor de data die gepresenteerd wordt in de hoofdstukken 6 t/m 9.

Hoofdstuk 5: Water release patterns of heated speleothem calcite and hydrogen isotope composition of fluid inclusions

Dit hoofdstuk beschrijft het proces van het vrijkomen van water, wanneer het speleotheem calciet wordt verhit tot ~900° Celsius. Gebleken is dat water vrijkomt gedurende het kapotgaan van de calcietkristallen en bij het omzetten van calciet tot calciumoxide. Beide stadia van het vrijkomen van water werden afzonderlijk bemeten op hun δ^2H-samenstelling, waarbij een klein verschil in isotopensamenstelling kon worden waargenomen. Het voordeel van deze techniek is dat de wateropbrengst hoger is dan bij de Amsterdamse kraaktechniek. Het nadeel is dat de zuurstofisotopen onbetrouwbaar worden na het omzetten van calciet tot calciumoxide. Het gevolg hiervan is dat alleen gegevens van waterstofisotopen kunnen worden verzameld. Dit werk is uitgevoerd in samenwerking met het 'Laboratoire des Sciences du Climat et l'Environnement' (France) en heeft tot een gezamenlijke publicatie geleid.

Hoofdstuk 6: Fossil dripwater in stalagmites reveals Holocene temperature and rainfall variations in Amazonia

Hier wordt aangetoond dat speleotheem materiaal dat het hele holoceen bestrijkt, inzicht kan geven in temperatuur- en neerslagvariatie in het Amazonegebied tijdens die periode. De berekende temperatuurvariatie gedurende het holoceen is gering, wat suggereert dat de neerslagvariatie de dominante factor is die het klimaat in het Amazonebekken beheerst. Het in fase lopen van de isotopengegevens van vloeistofinsluitingen en het calciet wijst erop dat de neerslagvariatie gestuurd wordt door de energie afkomstig van de zon.

Hoofdstuk 7: High resolution stable isotope and trace element speleothem records of the last ~5000 year, Cueva de las Lechuzas, lowland Peruvian Amazonia

Een stalagmiet uit de Cueva de las Lechuzas is bemeten op zijn isotopenverhouding en op concentraties van sporenelementen. Dit materiaal, dat het late holoceen bestrijkt, laat een regelmatige cyclus zien, zowel in de zuurstof- en de koolstofisotopen van het speleotheem calciet als in de concentraties van de sporenelementen. Het patroon is consistent en klopt voor alle gemeten proxy's en de verklaring wordt gevonden in de druppelsnelheid. Aangezien het regenwater de grondwaterstand beïnvloedt wat doorwerkt in de grot, weerspiegelen deze gegevens de veranderingen in de neerslaghoeveelheden en tonen zo de neerslagvariatie gedurende de laatste vijfduizend jaar.

Hoofdstuk 8: Climate reconstruction of the Andean highlands based on a late Holocene speleothem from Gruta de Huagapo

Dit hoofdstuk vertelt hoe een stalagmiet is onderzocht, die afkomstig is uit de Gruta de Huagapo op 3572 meter boven zeeniveau. Analyses van stabiele isotopen en van sporenelementen tonen variatie in neerslag aan. De gecombineerde analyses van stabiele isotopen van vloeistofinsluitingen en van die van het calciet van de speleothemen laten temperatuursveranderingen gedurende de laatste vijfduizend jaar zien. Temperatuurdalingen hangen samen met drogere omstandigheden, terwijl temperatuurstijging op meer neerslag wijst.

Hoofdstuk 9: Late Holocene rainwater stable isotope fractionation patterns as evidenced in fluid inclusions from stalagmites and snow from ice cores in an altitudinal transect over the Andes mountain chain

Dit hoofdstuk laat zien dat de techniek om de stabiele-isotopenverhouding van fossiel regenwater te meten het mogelijk maakt om een hoogteprofiel van de isotopenverhouding van het regenwater dwars over de Andes heen samen te stellen. Gegevens van speleothemen uit laaglandlocaties zijn vergeleken met die van een hooglandlocatie en tenslotte met die van ijskernen uit Quelccaya en Huascarán in de Andes. Al het materiaal bevat stabiele-isotopengegevens die representatief zijn voor fossiel regenwater. Deze gegevens zijn vergeleken met behulp van een eenvoudig Rayleigh distillatiemodel.

Summary

Thesis outline

Speleothems are carbonate concretes formed in the stable and humid environment of cave systems. The most common speleothems are stalagmites and stalactites. This research focuses on the climate information recorded in speleothems and specifically in stalagmites.

Many land and ocean based climate reconstructions are derived from subtle variations in the stable isotope composition of oxygen. In the natural environment, the element oxygen consists of three stable isotopes namely ^{16}O, ^{17}O and ^{18}O. An isotope has a different amount of neutrons but always the same amount of protons as other isotopes of the same element. Due to various physical and chemical processes, the lighter isotope (^{16}O, fewer neutrons) will react differently from the heavy isotope (^{18}O, more neutrons). This results in changes in the ratio of the ^{16}O and ^{18}O isotopes in the natural environment. Ratios of the different isotopes of the elements oxygen, carbon and hydrogen can all provide useful information about the climate of the past, for example reconstructing past changes in temperature and rainfall patterns. Important climatic information can be extracted from (rain) water using these various isotopic ratios, however fossil rainwater is scarce and mainly available as ice in glaciers and polar ice caps. Climate research based on ice cores form an important basis of our understanding of the Quaternary climate, because this fossil water can be analysed. A disadvantage is that ice cores are geographically limited to the polar climates on Earth.

Temperature information is also recorded in the oxygen isotope composition of carbonate (calcite/aragonite), from which cave stalagmites are composed. The ratio between oxygen isotopes ($^{18}O/^{16}O$) is temperature dependent, and therefore will provide temperature information at time of carbonate deposition. However, for paleotemperature calculations we require both the oxygen isotope ratio of the speleothem carbonate and the oxygen isotope composition of the cave water (i.e. fossil water) at the time of deposition. In the speleothem carbonate, a small amount of cave drip water (fossil water) is still present, so-called fluid inclusions. If the isotope composition of this 'fossil' drip water can be measured, the isotope composition of the original drip water is known and in combination with the oxygen isotope composition of the speleothem carbonate, the temperature at the time of deposition can be calculated.

This research details the first speleothem records of Holocene climate changes from the Peruvian Andes. For these climate reconstructions we focused on stable isotope and trace element analyses of speleothem carbonate. To better quantify variability in temperature and rainfall from these proxy records, we further developed a technique for the stable isotope analysis of fossil 'drip water' trapped in small cavities (fluid inclusions) of the speleothem carbonate. The hypothesis is that the combination of fluid inclusion stable isotope data with associated speleothem carbonate stable isotope data enables the calculation of true paleotemperatures.

The thesis is divided in two parts. The first is technically orientated (chapters 2 - 5) and presents the U-Th dating technique (chapter 2), a monitoring study of a Peruvian cave (chapter 3) and two different techniques to extract and measure the isotope composition of speleothem inclusion water (chapter 4 & 5). These techniques are then applied to stalagmites collected from three caves in Peru. The results are presented in chapters 6 – 9. Chapter 6 & 7 present the climate interpretation of two lowland caves from the Amazon basin, whereas chapter 8 presents the first climate record of an Andean highland stalagmite. Chapter 9 compares the fluid inclusion data collected from low- and highland Peru with a simple distillation model.

Chapter 1: Introduction

General information about the climate of South America and the formation of stalagmites.

Chapter 2: Uranium-series dating method applied on speleothems

The Uranium-series dating technique is complex and fundamental for speleothem-based climate research because it provides an independent, robust age framework. All of the collected Peruvian stalagmites were U/Th age dated at the Vrije Universiteit Amsterdam (VUA) and so we begin by detailing the methods used. Besides an age framework, low resolution stable isotope records were also produced. Based on the combined age framework and stable isotope data, we selected the most suitable material to investigate the Holocene period. The collected and dated speleothems for this pilot study are presented in this chapter, but no further detail is given.

Chapter 3: Seasonal environmental monitoring results from a cave in Peruvian Amazonia

During September 2003 and 2004, between two fieldwork periods a monitoring experiment was carried out in Cueva de las Lechuzas. The monitored data consists of stable isotope and trace element measurements on collected water samples in combination with continuously monitored temperature and drip rates at specific locations within the cave. This experiment was set up to investigate the cave environment and its response to seasonal climate changes and shows the complex and dynamic response cave hydrology to outside precipitation.

Chapter 4: A continuous-flow crushing device for on-line δ^2H analysis of fluid inclusion water in speleothems

A key theme in this thesis is the development of a method to accurately measure the stable isotope ratio (δ^2H) of fluid inclusion water from speleothem calcite. This thesis describes two independent techniques for fluid inclusion extraction in chapters 4 and 5 respectively. Chapter 4 describes a new method developed at the VUA, which makes it possible to extract inclusion water from speleothem calcite and accurately measure its stable isotope composition. This is a major technical achievement for fluid inclusions extraction and measurements and offers new possibilities in speleothem climate research (as is published in chapters 6, 7, 8 and 9).

Chapter 5: Water release patterns of heated speleothem calcite and hydrogen isotope composition of fluid inclusions

Chapter 5 describes the process of water release when speleothem calcite is heated up to ~900°C. Observations show that water is released during the break down of the calcite crystals and during the decomposition of the calcite to lime. The two stages of water release were separately measured in terms of δ^2H composition and a small difference was observed. The advantage of this technique is that the water yield is higher in comparison to the 'crushing' technique. The disadvantage is that oxygen isotopes become unreliable after decomposition of calcite to lime and consequently only hydrogen isotope data can be collected. This work is performed in cooperation with the 'Laboratoire des Sciences du Climat et l'Environnement' (France) with resulted in a co-author paper.

Chapter 6: Fossil dripwater in stalagmites reveals Holocene temperature and rainfall variations in Amazonia

A speleothem record covering the complete Holocene provides an insight in Holocene temperature and rainfall variation in Amazonia. The temperature variations calculated remain small throughout the Holocene, suggesting that rainfall variation is the dominant climatic factor in Amazonia. In phase isotope records of fluid inclusion and speleothem calcite suggest that rainfall variation are solar insolation driven.

Chapter 7: High resolution stable isotope and trace element speleothem record of the last ~5000 year, Cueva de las Lechuzas, lowland Peruvian Amazonia

A stalagmite from Cueva de las Lechuzas is measured for stable isotope composition and trace element concentrations. This record covering the late Holocene, shows a distinct centennial-scale cyclicity, visible in both oxygen and carbon isotopes of the speleothem calcite and also in trace element concentrations. The pattern is consistent and in phase for all measured proxies and is interpreted as being drip rate driven. As the cave hydrological reservoir is fed by water of meteoric origin, the data is sensitive to changes in the amount of rainfall and reflects rainfall variation for the last 5000 years.

Chapter 8: Climate reconstruction of the Andean highland based on a late Holocene speleothem from Gruta de Huagapo

A stalagmite from Gruta de Huagapo located at 3572 meters above sealevel is investigated. Stable isotope and trace element analyses of the speleothem calcite reconstruct variations in precipitation. Combined stable isotope analyses on fluid inclusion water and speleothem calcite reveal temperature changes over the last 5000 year. Cooler temperature coincide with periods of dryer conditions, while warmer temperatures show signs of increased rainfall.

Chapter 9: Late Holocene rainwater stable isotope fractionation patterns as evidenced in fluid inclusions from stalagmites and snow from ice cores in an altitudinal transect over the Andes mountain chain

The possibility to directly measure the stable isotope composition of fossil rain water provides the opportunity to create an altitudinal profile of rainwater isotope composition across the Andean mountain chain. Two lowland speleothem records are compared with a highland speleothem record and ultimately with the Andean Ice cores of Quelccaya and Huascarán. All records consist of stable isotope data, representative for fossil rainwater. These data are compared with a simple Rayleigh distillation model.

1

Introduction

1.1 Introduction

The Amazon Basin contains one of the largest tropical rainforests in the world, sustained by a warm and humid climate. The climate history of the Amazon Basin has been studied intensively over the last decades, with particular focus on Glacial-Interglacial variability, and its effect on biodiversity in Amazonia.

Considerable debate still exists concerning the effect of temperature and rainfall variation on the different proxy records. For example, the interpretation of Andean ice core stable isotope data is poorly resolved. Some workers suggest temperature as the controlling factor on ice core δ^{18}O variation (Thompson et al., 1995), while others advocate variation in δ^{18}O of high Andean atmospheric moisture to be more important (Broecker, 1997; Pierrehumbert, 1999; Ramirez et al., 2003). Still, these ice core isotope records remain of primary importance for Holocene Amazonian climate reconstructions, because only few other stable isotope records are available for this region (e.g. Cruz et al., 2005a; Seltzer et al., 2000).

In fact, quantification of climate proxy data into temperature and rainfall variation is difficult for nearly all proxy systems applied in Amazonian paleo-climate reconstructions (e.g. Cruz et al., 2005a; Hooghiemstra and van der Hammen, 1998). Such proxy calibration problems are further complicated by geographical differentiation of climate in Amazonia. For example, highland records are likely to show a different climate signal than lowland records (Vizy and Cook, 2007).

In view of these problems there is a clear need for more, well-dated isotope archives of climate in Amazonia. Speleothem records are able to provide such archives (Fairchild et al., 2006b). Speleothems (stalagmites) record climate change because the cave environment is sensitive to outside climate change. Furthermore they can be precisely dated back to ~500,000 years, by Uranium-series dating. Many examples exists that demonstrate the sensitivity of speleothem geochemistry to climate variations (e.g. Bar-Matthews et al., 1999; Cruz et al., 2005a; Genty et al., 2003; Wang et al., 2005). Speleothems can span 1000-100000 years of time (Fairchild et al., 2006b) capturing a continuous record of detailed information about the cave's environment. Cave temperature represents the annual mean temperature outside the cave. Infiltration of drip water is buffered by the size of the hydrological reservoir. Studies reveal that infiltration and therefore mixing can take years (Caballero et al., 1996; Yonge et al., 1985). This makes speleothem records particularly useful for climate reconstruction over interannual and longer time scales (Fairchild et al., 2006b).

Karstic terrains with stalagmite bearing cave systems are widespread along the Andean mountain chain, but are poorly studied until now. To date, only a handful of speleothem-based climate studies exists for Amazonia (Auler et al., 2004; Bertaux et al., 2002; Cruz et al., 2005a), none of which come from the Andean mountain chain. With this thesis I provide the first speleothem records of Holocene climate changes from the Peruvian Andes. For these climate reconstructions we focused on stable isotope and trace element analyses of speleothem carbonate. To better quantify variability in temperature and rainfall from these proxy records, we further developed a technique for the stable isotope analysis of fossil 'drip water' trapped in small cavities (fluid inclusions) of the speleothem carbonate. The hypothesis is that the combination of fluid inclusion stable isotope data with associated speleothem carbonate stable isotope data enables the calculation of independent paleotemperatures. Furthermore fluid inclusion isotope analyses provide a direct indication of the isotope composition of paleo-rainwater.

1.2 Climate of Amazonia: the InterTropical Convergence Zone (ITCZ)

The isotope composition of rainfall is directly related to the amount of convective rainfall generated by the ITCZ system. Since the ITCZ-system governs both the amount as well as the seasonal distribution of rainfall, the proper reconstruction of its behaviour through time is of fundamental importance to understand the paleo-climate of Amazonia.

The ITCZ is an atmospheric low pressure band, located close to the equator (figures 1.1, 1.2, 1.3). It generally follows the seasonally migrating band of maximum solar insolation. Maximum atmospheric convection takes place in the ITCZ, producing abundant rainfall that seasonally migrates over Amazonia (Marengo and Nobre, 2001).

The ITCZ as shown in figure 1.3 has a typical U-shaped form over South America. Difference in latent heat distribution between continental and ocean surfaces results in some discrepancies in temperature between continental and ocean surface areas. When the maximum solar radiation is on the continent this surface will heat up much faster than ocean water, causing the ITCZ to bend. This phenomenon is typical for South America (figures 1.2 & 1.3). The U-shape structure is further modified by the high Andean mountain chain, which directly affects atmospheric circulation patterns. Our study area in Peruvian Amazonia is under the direct influence of the ITCZ (figure 1.3). Wet season peaks between December and February, while dry season conditions prevail around June - August.

We collected speleothem material in selected caves in lowland Peruvian Amazonia and higher in the Andes. Sites of collection are described here below.

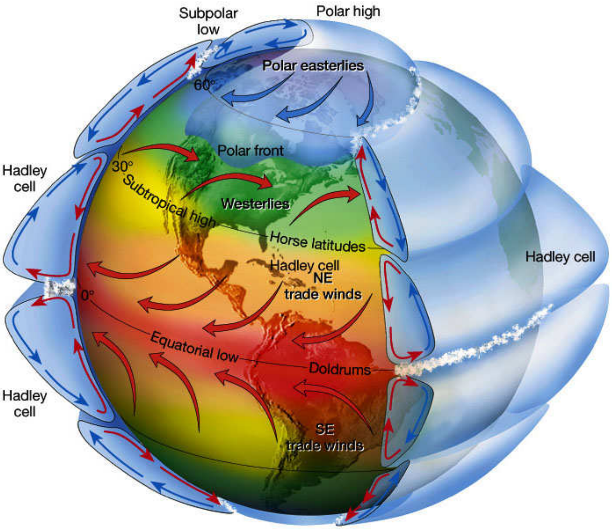

Figure 1.1: Hadley cell configuration over the Earth, with the dominant wind systems. For South America the Low pressure zone is located at the equator, but has an North-South shift during the seasons. The prevailing wind direction in South America is Eastern, transporting water vapor from the Atlantic Ocean over the continent. Figure from http://www.ux1.eiu.edu/∼cfjps/1400/FIG07_006.jpg.

1.3 Description of the sites

During two fieldtrips in Peru, three cave systems were selected out of many caves visited. Modern temperature, humidity were measured and water samples were collected and measured for stable isotope composition.

The three cave systems selected are: 1) Cueva de las Lechuzas; 2) Gruta Huagapo; 3) Cueva del Tigre Perdido (figure 1.3). Cueva de las Lechuzas and Cueva del Tigre Perdido are located in a tropical rainforest (selva alta). In contrast Gruta Huagapo has a mountain climate with less rainfall and scarce vegetation dominated by small plants and bushes.

1.4 Speleothem formation

Speleothems are formed in the exclusive domain of caves as secondary cave deposits. Caves are natural formed underground cavities/spaces (figure 1.4). There are two types of caves: primary and secondary formed ones. Primary formed caves are formed during the deposition of the host rock, while secondary formed caves are formed when the host rock is already deposited. Examples of primary formed caves are lava tubes and cave blisters.

Karstic caves are always secondary formed and form 80% of the world caves. 20% of the earth's continental surfaces is covered by carbonates in which karstic caves can be formed

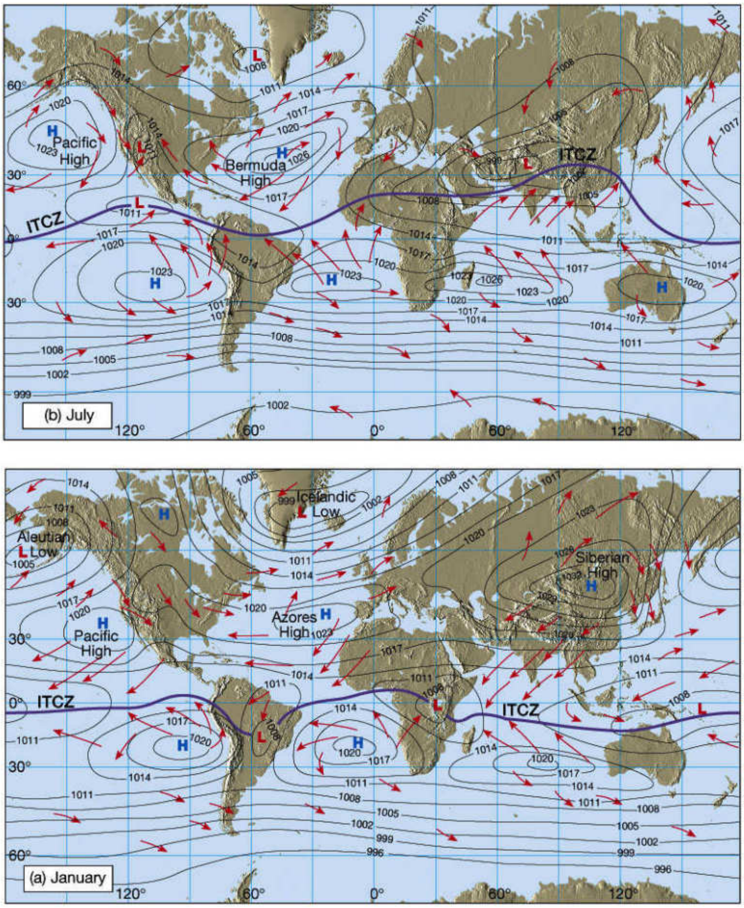

Figure 1.2: The purple line illustrates the ITCZ, following the low pressure zone close to the equator. In July the ITCZ is in South America located just north of the equator, during January the ITCZ is bend southward with a maximum displacement of ∼15°. The U-shape form over South America is caused by the land-sea interaction and the Andean Mountain chain. Figures from http://www.ux1.eiu.edu/∼cfjps/1400/circulation.html.

by dissolution of the carbonate rock (Schwarcz, 1986), resulting in a large geographical coverage of caves and speleothems worldwide. This occurs by slightly acidified water. Water is acidified by the dissolution of CO_2-gas by the following chemical reactions (equation 1.1 to 1.3)

$$CO_2 + H_2O \rightleftharpoons H_2CO_3 \tag{1.1}$$

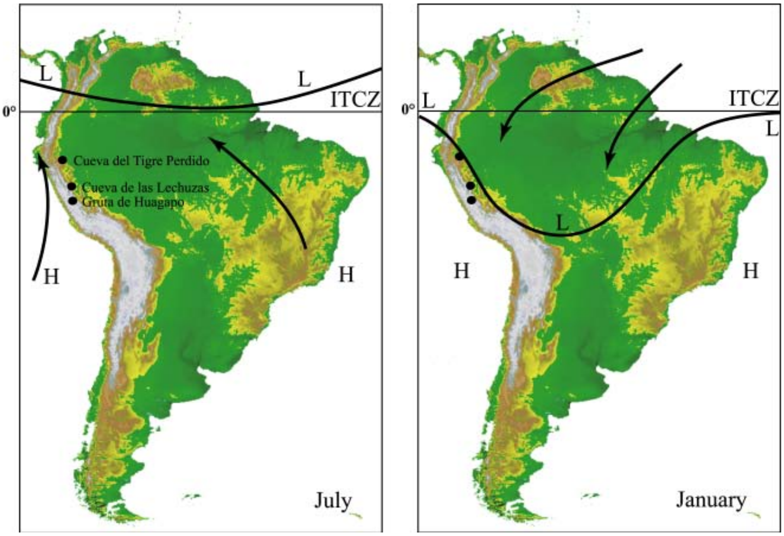

Figure 1.3: This map illustrates South America with the location of the ITCZ (black line) during the seasons and the investigated caves as black dots. The prevailing wind directions are indicated by arrows.

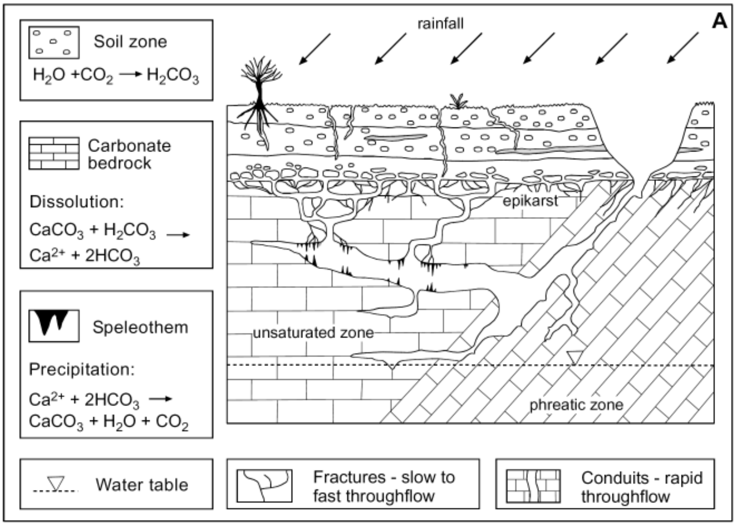

Figure 1.4: Schematic view of infiltration of water in carbonate rock. Dissolution of the carbonate host rock and cave development. Figure from Fairchild et al. (2006a).

$$H_2CO_3 + H_2O \rightleftharpoons H_3O^+ + {HCO_3}^- \tag{1.2}$$

$$ {HCO_3}^- + H_2O \rightleftharpoons H_3O^+ + {CO_3}^{2-} \tag{1.3}$$

The source for CO_2 is the soil above the cave as vegetation brings CO_2-gas by plant roots in the soil due to plant respiration. This acidified water is able to dissolve solid carbonate from the host rock (Hill and Forti, 1997) (equation 1.4). This is a slow process but over tens of thousands or even millions of years large quantities can be chemically dissolved and physically removed resulting in underground cave systems

$$CaCO_3 + {H_2CO_3}^- + H_3O^+ \rightleftharpoons Ca^{2+} + \ + 2\,{HCO_3}^- \tag{1.4}$$

This process can also be reversed by CO_2 degassing from the cave water. When seepage water enters the cave, CO_2 gas is released in the cave atmosphere and carbonate is precipitated from the solution (equation 1.5). This is the fundamental chemical reaction of carbonate deposition and speleothem formation in caves.

$$ {Ca_2}^+ + 2\,{HCO_3}^- \rightleftharpoons CaCO_3(s) + H_2O + CO_2(g) \tag{1.5}$$

Carbonate can be precipitated as calcite and/or aragonite from the solution (figure 1.5). Calcite is the predominant mineral in speleothems, but aragonite can be found and is usually indicative of evaporation processes (Richards and Dorale, 2003).

Precipitation of carbonate due to supersaturation of the cave seepage water occurs by CO_2-degassing and occasionally by evaporation. Cave air is characterized by a high relative humidity typically between 95-100% that minimizes evaporation of drip water. When evaporation occurs it is often close to the cave entrance or where strong air draft is present in the cave (McDermott et al., 2006).

CO_2-degassing from the cave seepage water occurs because of the low CO_2 pressure of the cave atmosphere compared to the seepage water (often 25 to 90 times higher) (Hill and Forti, 1997). Seepage water has an elevated amount of dissolved CO_2 due to the high pCO_2 in the soil above the cave. Soil CO_2 concentrations between 0.1-3.5% (Atkinson, 1977; McDermott et al., 2006) up to 10% in the tropics (Miotke, 1974) and 0.06-0.6% in the cave (McDermott et al., 2006) are reported. Atmospheric CO_2 concentrations are between 0.03%-0.06% (300-600ppm) (Keeling et al., 1976; Keeling et al., 1996).

The deposition of carbonate by CO_2-degassing of the seepage water to the cave's atmosphere results in the formation of speleothems. The word speleothem covers all kind of secondary carbonate depositions in caves, most common are stalagmites, stalactites and flowstones, see for an overview of all secondary cave deposits (Hill and Forti, 1997).

1.5 Petrography

Speleothems, stalagmites and stalactites, can vary in size from small soda-straws to tens of meters high stalagmites. When stalagmites are cut longitudinally or latitudinally, layering

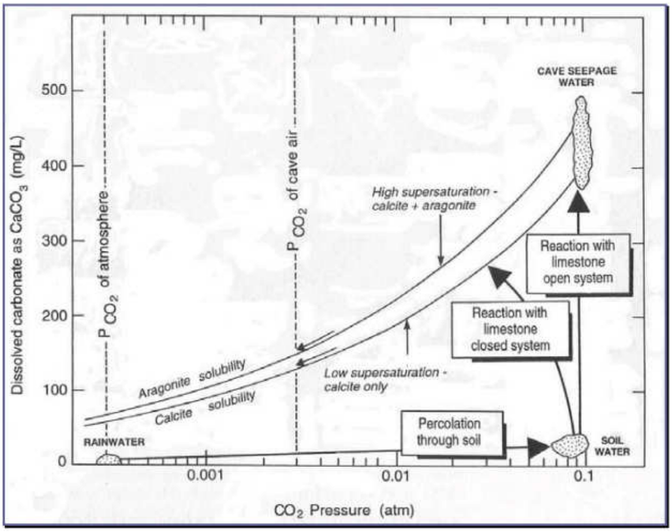

Figure 1.5: Illustrated are the conditions for aragonite and calcite deposition. The deposition conditions are in this figure dependent on the amount of dissolved $CaCO_3$ and the CO_2 pressure. Rainwater (left corner) will take up CO_2 from the soil and shift to the right in the figure. A higher CO_2 concentration in the water acidifies the water. When this acidified water percolates through a limestone host rock it will dissolve $CaCO_3$, resulting in an increased $CaCO_3$ concentration in the water (moving up in the figure). As the CO_2 pressure in the cave is lower then the seepage water, CO_2 degassing occurs resulting in $CaCO_3$ deposition until equilibrium conditions are reached. Figure from White (1988).

is seen (figure 1.6). These growth layers can be formed yearly by deposition of organic material or clay particles but are often random occasions recording changes in the drip water chemistry (Baker et al., 1997a; Baker et al., 2002; Baker et al., 1993; Kendall and Broughton, 1978). A closer look at these banded speleothems reveals that the crystal growth is seldom disturbed. Only relatively thick organic layers or long time growth stops can 'poison' the crystal enough to stop growth and thus new nuclei need to be formed for crystal growth (figure 1.7).

Carbonate is precipitated from a thin fluid layer. This thin layer of $\sim$100 μm (Fairchild et al., 2006a) is evenly distributed over the stalagmite and CO_2-degassing makes carbonate precipitation possible (equation 1.5). Layer by layer the stalagmite is built up although this is not visible in the crystal structure itself, only by layering of organics, clay particles and fluid inclusions.

1.6 Fluid inclusions

Fluid inclusions are microscopic cavities filled with cave drip water. Fluid inclusions often form banding and are elongated parallel to the crystals' growth direction (Kendall and

Figure 1.6: Top of speleothem CLL-3 cut longitudinal, showing clear layering. Photo taken by Saskia Kars (VUA).

Broughton, 1978). During speleothem growth drip water fills up cavities between crystals formed by poisoning of the crystal lattice by organic material and/or by CO_2 gas bubbles.

Fluid inclusion water consist of paleo drip water, which is in turn fed by rainwater, and therefore can serve as a potential proxy for paleo-rainfall isotopes. Stalagmites often show layers of fluid inclusion rich calcite (milky colour) alternating with layers of very dense (transparent) calcite. In general about 0.1 weight percentage of the speleothem consists of water, the total range varies from 0.05 to 5 wt. % (McDermott et al., 2006). Microscopic determination shows that fluid inclusion can vary in size from hundreds of nanometres to centimetre scale (figure 1.8 & 1.9).

Kendall and Broughton (1978) determined five types of inclusion-defined growth layers (figure 1.10).

1. Type 1. Layers are smooth curves; each composed of closely-spaced, parallel to sub-parallel, linear inclusions. Each lineation parallels the optic axis orientation of the host crystal, even when this is oblique to the growth surface. Each crystal thus has

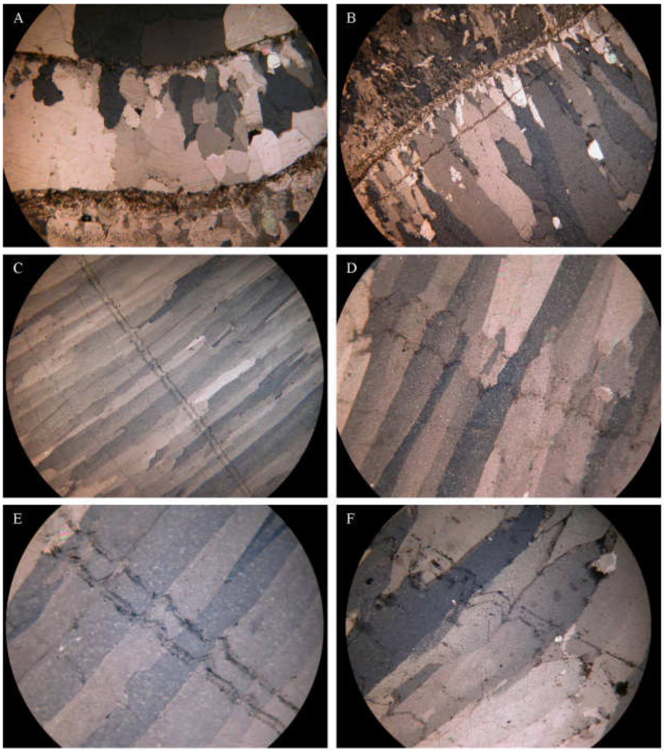

Figure 1.7: Petrographic pictures taken with a light microscope, crossed nickels in. Dark layers are fluid inclusion rich layers. Photo 1.7a and 1.7b show growth termination of the crystals due to contamination of organic material. Pictures 1.7c-f show undisturbed crystal growth while the fluid inclusion layers reveal the original surface of the stalagmite.

its own individual orientation of inclusions and when crystals have a deformed lattice, the linear inclusions are oriented such to faithfully mimic the variation in optic axis orientation.

2. Type 2. Like type 1, but defined by concentrations of inclusion which are not separately resolvable with a light microscope. They impart pseudo-pleochroism to the calcite (brownish colour)

3. Type 3. Are defined by pseudo-pleochroic calcite but instead of being smooth curves they define former position of rhombohedral (rarely scalenohedral) crystal faces (V-shape).

4. Type 4. Like type 3 layers, but are defined by concentrations of linear inclusions.

5. Type 5. Layers are characterised by large quantities of impurities, such that crystal

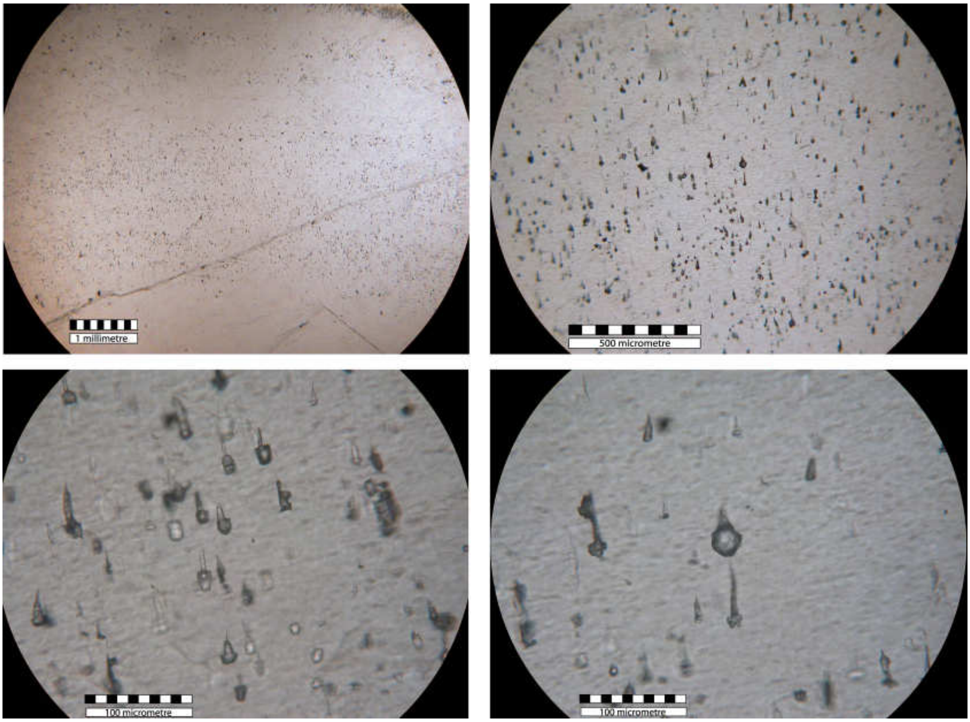

Figure 1.8: Petrographic pictures of fluid inclusion rich calcite. This photo series is taken from stalagmite NC-B.

fabrics are partially to wholly obscured. These layers commonly separate layers with different habits.

6. Type 6. Are essentially inclusion free layers and occur between the other types.

As described by Kendall and Broughton (1978) fluid inclusions are oriented parallel to the C-axes of the crystal. Layers of fluid inclusions also mimic the original growth surface layer. As the stalagmite crystals grow at the very thin water layer this will mimic the original surface (figure 1.10c, d). This can be a smooth surface, but also with a V-shape pattern at the boundaries between crystal and subcrystal boundaries (Kendall and Broughton, 1978).

For fluid inclusion analyses the quality and distribution of fluid inclusions in the speleothem calcite is of importance. Unfortunately it is difficult to assess difference between primary and secondary formed fluid inclusions in the speleothem carbonate based on the petrographic criteria described above. Secondarily formed fluid inclusions (by dissolution) are likely to occur along the C-axes and be of similar shape to primary formed fluid inclusions. Petrographic inspection prior to fluid inclusion isotope analyses still remains useful because high density of fluid inclusions is indicative of interconnection of fluid inclusions, which may lead to undesired exchange or leakage of fluid inclusion water.

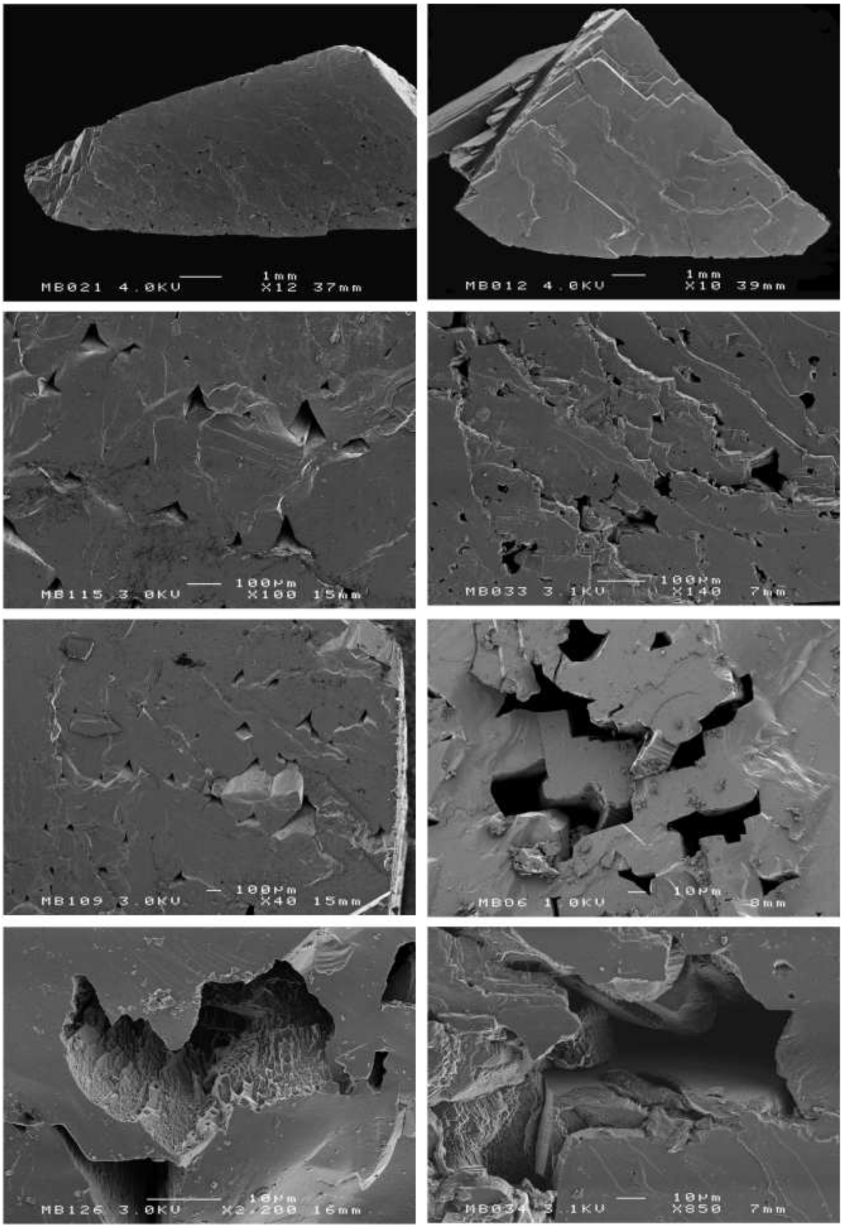

Figure 1.9: SEM pictures of speleothem calcite. The photos are from different stalagmites showing cavities in the calcite, which possibly contained inclusion water.

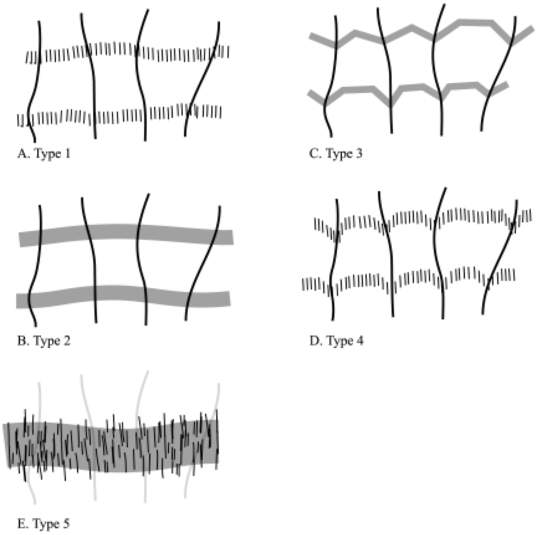

Figure 1.10: Different types of fluid inclusions in speleothem calcite modified after Kendall and Broughton (1978). Figure 1.10a, shows small layers individual fluid inclusions. Figure 1.10b, shows the same layers, but fluid inclusion can not resolved by microscope individually. Layers of fluid inclusion can mimic the original speleothem surface. In figure 1.10c and 1.10d the individual crystal boundaries form the original surface. Figure 1.10e illustrates fluid inclusion rich calcite where no banding can be seen.

1.7 Trace elements

Layering and colouring of a speleothem can be related to trace element concentrations, but is often due to organic material or changes in porosity of the speleothem carbonate (Verheyden, 2005). The relation between trace elements concentrations incorporated in the speleothem carbonate and cave drip water is delicate, and not straightforward to interpret. The trace element signal in speleothem carbonate may give interpretable climate information, but can also record changes in local hydrological circumstances. Many monitoring studies have been performed to unravel the trace element signal (Fairchild et al., 2000; Roberts et al., 1998; Treble et al., 2003; Verheyden, 2005; Verheyden et al., 2000), but it seems that no uniform interpretation is available yet and that trace element concentration can vary at different cave locations. High resolution trace element data showing annual cycles can provide a robust time frame (e.g. Roberts et al., 1998) and suggests that seasonal changes in the cave environment lead to trace element cyclicity in speleothems.

Mg and Sr contents seem to be controlled by dissolution and precipitation processes in the vadose zone. Prior precipitation of calcite from the percolating water along the percolating path will decrease the Sr/Ca and Mg/Ca ratio of the cave seepage water. Strontium and magnesium ions will precipitate prior to calcium from the solution. As dissolution and precipitation in the vadose zone is dependent on the residence time of percolating water, variation in the Sr/Ca and Mg/Ca ratio can be interpreted as changes in the residence time of the percolating water (Fairchild et al., 2000; Huang and Fairchild, 2001; Roberts et al., 1998; Verheyden et al., 2000).

1.8 Stable isotopes

The elements we used for this study are hydrogen, carbon and oxygen. Hydrogen and carbon both have two stable isotopes, ^{1}H, ^{2}H and ^{12}C, ^{13}C, respectively. Oxygen has three stable isotope forms ^{16}O, ^{17}O, ^{18}O. From these three (hydrogen, carbon and oxygen) elements the light isotopes (^{1}H, ^{12}C, ^{16}O) are the most abundant in nature (table 1.1)

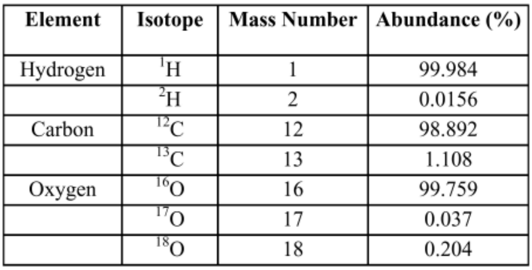

Element	Isotope	Mass Number	Abundance (%)
Hydrogen	^{1}H	1	99.984
	^{2}H	2	0.0156
Carbon	^{12}C	12	98.892
	^{13}C	13	1.108
Oxygen	^{16}O	16	99.759
	^{17}O	17	0.037
	^{18}O	18	0.204

Table 1.1: Natural occurrence of the isotopes hydrogen, carbon and oxygen

Isotope ratios are expressed by equation 1.6.

$$R = \frac{\text{abundance of rare isotope}}{\text{abundance of abundant isotope}} \tag{1.6}$$

However the isotope ratio is generally reported as a deviation of the isotope ratio of a sample relative to that of a standard (equation 1.7 & 1.8)

$$\delta = \frac{\mathrm{R}_{\text{sample}}}{\mathrm{R}_{\text{standard}}} - 1 \tag{1.7}$$

$$\delta^{2}\mathrm{H} = \frac{(^{2}\mathrm{H}/^{1}\mathrm{H})_{\text{sample}}}{(^{2}\mathrm{H}/^{1}\mathrm{H})_{\text{standard}}} - 1 \tag{1.8a}$$

$$\delta^{13}\mathrm{C} = \frac{(^{13}\mathrm{C}/^{12}\mathrm{C})_{\text{sample}}}{(^{13}\mathrm{C}/^{12}\mathrm{C})_{\text{standard}}} - 1 \tag{1.8b}$$

$$\delta^{18}\mathrm{O} = \frac{(^{18}\mathrm{O}/^{16}\mathrm{O})_{\text{sample}}}{(^{18}\mathrm{O}/^{16}\mathrm{O})_{\text{standard}}} - 1 \tag{1.8c}$$

(McKinney et al., 1950)

δ^{18}O, δ^{13}C and δ^{2}H are expressed in per mill (parts per thousand) relative to a standard. Vienna Standard Mean Ocean Water (V-SMOW) is the standard for waters (δ^{18}O and δ^{2}H), while δ^{13}C and δ^{18}O of carbonates are reported relative to Vienna PeeDee Belemnite (V-PDB). The conversion of δ^{18}O between the two standards (V-SMOW – V-PDB) is given by the equations 1.9 & 1.10:

$$\delta^{18}\mathrm{O}_{\mathrm{VSMOW}} = 1.03086 \cdot \delta^{18}\mathrm{O}_{\mathrm{VPDB}} + 30.86 \tag{1.9}$$

$$\delta^{18}\mathrm{O}_{\mathrm{VPDB}} = 0.97006 \cdot \delta^{18}\mathrm{O}_{\mathrm{VSMOW}} - 29.94 \tag{1.10}$$

(Coplen et al., 1983)

1.8.1 Carbon isotopes

The carbon isotope value in speleothem carbonate is a sensitive recorder of climate changes, however δ^{13}C records are difficult to quantify as there are many different carbon reservoirs which all interact with each other. Carbon taken up by the percolating water will reflect the host limestone, atmospheric CO_2, type of surface vegetation and organic components in the soil (Harmon et al., 2004). On top of that, kinetic fractionation and chemical effects occur (Richards and Dorale, 2003). Although separating the different sources of carbon is impossible, all effects are influenced by climate changes like amount of precipitation and temperature. Changes in vegetation and soil are in phase with changes in the climate and these variations are recorded in the δ^{13}C pattern of various speleothems (Baker et al., 1997b; Frappier et al., 2002; Genty et al., 2006; Genty and Massault, 1999). Degassing of CO_2 from the cave drip water will influence the δ^{13}C value of the speleothem calcite. As the fractionation and amount of degassing is related to the drip rate its effect on δ^{13}C of the speleothem carbonate might reflect the surface water balance and the amount of recharge (Banner et al., 2007; Mickler et al., 2006). Although studies reveal that δ^{13}C isotopes may give some indication for climate changes, precise interpretation remains difficult.

1.8.2 Oxygen isotopes

The δ^{18}O value of speleothem carbonate precipitated under isotope equilibrium is controlled by two factors: 1) the oxygen isotope composition of the cave drip water and 2) the temperature at which the precipitation occurs. Thus when the δ^{18}O value of the drip water and the δ^{18}O value of the carbonate at time of precipitation are known, the temperature at the time of precipitation can be reconstructed (equation 1.11). This is the basic principle of paleo-temperature reconstruction based on oxygen isotope archives.

This temperature dependent isotope fractionation was recognised by (Urey, 1947) and converted to a paleo-temperature equation by (Epstein et al., 1951; Epstein et al., 1953). More paleo-temperature equations have been constructed for specific purposes. A compilation study by McDermott et al. (2006) revealed that many of the commonly used paleotemperature equations yield temperatures that are several degrees Celsius lower than actual cave temperatures. Among these paleo-temperature equation the one by Craig (1965) generally gave the most accurate results (figure 1.11). The Craig (1965) equation however is known be based on an empirical derived study of mixed calcite and aragonite mineralogy (Leng and Marshall, 2004) and will therefore deviate from true equilibrium fractionation of water-calcite. Equilibrium fractionation factors published by Grossman and Ku (1986) for aragonite and by Kim and O'Neil (1997) for calcite result in slightly different temperature equation than Craig (1965). As our speleothem have a calcite mineralogy Kim and O'Neil (1997) would be preferred. However we have chosen to use the Craig (1965) equation (1.11as it outperforms most of the other equations, for all temperature reconstructions in this thesis. It is clear that more work is needed to clarify the boundary conditions of equilibrium growth of speleothem calcite.

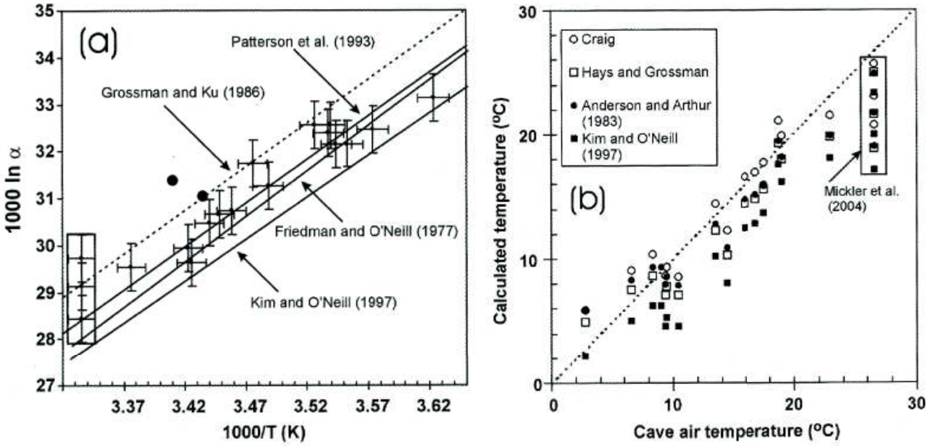

Figure 1.11: (A) Compiled dataset of modern cave calcite (crosses) and aragonite (solid dots) precipitate-dripwater pairs. Error bars represent uncertainty in cave temperature and δ^{18}O dripwater Different carbonate-dripwater fractionation lines are illustrated. (B) Actual cave temperature cross plotted to calculated cave temperatures using recent isotope composition of cave drip water and speleothem calcite. The temperature equation of Craig (1965) gives the best calculated temperatures. Figures from McDermott et al. (2006)

$$\mathrm{T} = 16.9 - 4.2 \cdot (\delta^{18}\mathrm{O}_c - \delta^{18}\mathrm{O}_w) + 0.13 \cdot (\delta^{18}\mathrm{O}_c - \delta^{18}\mathrm{O}_w)^2 \tag{1.11}$$

(Craig, 1965)

Mickler et al. (2006) give an alternative explanation for the δ^{18}O offset in the speleothem carbonate resulting in the over-estimation of the calculated temperatures with the actual cave temperature. CO_2-degassing results in oxygen isotope exchange between DIC and H_2O. This will cause progressive ^{18}O and ^{13}C enrichment in the HCO^{2-} reservoir and ultimately in the deposited calcite. The oxygen isotope enrichment is depending on the CO_2-degassing rate as the slow hydration reaction of CO_2 will equilibrate with the large oxygen reservoir in the drip water (Mickler et al., 2006; Mühlinghaus et al., 2007). CO_2 degassing may explain why almost all stalagmites have calcite oxygen isotope values slightly away from exact equilibrium with water. As CO_2-degassing is influenced by the driprate, it might indirect record changes of rainfall and recharge. For accurate paleotemperature calculation the oxygen isotope composition of both speleothem calcite and drip water need to be known. As the δ^{18}O composition of the fossil drip water is usually unknown and can vary significantly due to local circumstances, past temperature estimates using only δ^{18}O values of the speleothem carbonate are not very accurate. Since the 1970s it has been recognized that speleothems contain small amounts of seepage water trapped in small cavities in the speleothem calcite, so called fluid inclusions (Kendall and Broughton, 1978). If one would be able to analyse the δ^{18}O value of fluid inclusion water, the uncertainty of the above mentioned paleotemperature calculation would be significantly reduced. The development of such an analytical technique has been an important aim of this thesis.

Furthermore, δ^{18}O values of fluid inclusion water provide direct information on the isotope composition of paleo-precipitation as cave seepage water is fed by water with a meteoric origin. Fluid inclusion water thus represents paleo-rainwater which can be used to reconstruct the hydrological cycle of the past. Studies where 'fossil' rainwater can be measured directly are scarce, as rainwater normally does not fossilize. The only other direct measurements are derived from snow in ice cores. Fluid inclusions in speleothems are a new tool providing independent temperature information and direct measurements of fossil rainwater.

It is noteworthy that disequilibrium fractionation has been reported and suggested to be caused by evaporation, supersaturation and rapid deposition of speleothem carbonate (Frisia et al., 2000; Kim and O'Neil, 1997; Mickler et al., 2004). Disequilibrium fractionation can be tested by a so-called 'Hendy'-test. Figure 1.12 shows two Hendy-test performed on stalagmite NC-A and NC-B.

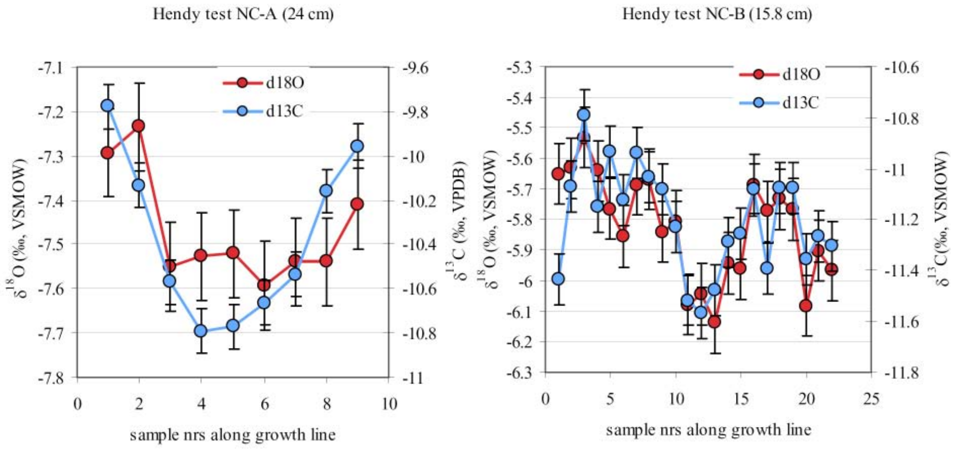

Figure 1.12: Hendy test peformed on a single growth layer of stalagmite NC-A and NC-B.

1.8.3 Hydrogen isotopes

For this thesis hydrogen isotope values were analysed in fluid inclusion water.

The added value of these analyses is that they facilitate the comparison of fluid inclusion water δ^{18}O and δ^{2}H composition to the so-called Global Meteoric Water Line.

In the atmospheric hydrological cycle hydrogen and oxygen isotopes have a fixed relationship, defined by the Global Meteoric Water Line (GMWL) (Dansgaard, 1964). The slope of the GMWL is defined by the Raleigh effect and globally described by equation 1.12.

$$\delta^{2}\mathrm{H} = 8 \cdot \delta^{18}\mathrm{O} + 10 \tag{1.12}$$

(Craig, 1961)

The intercept of the GMWL is controlled by the main source areas for atmospheric moisture. This so called deuterium excess can vary locally and is defined by equation 1.13 rewritten in equation 1.14.

$$\mathrm{d} = \delta^{2}\mathrm{H} - 8 \cdot \delta^{18}\mathrm{O} \tag{1.13}$$

$$\delta^{2}\mathrm{H} = 8 \cdot \delta^{18}\mathrm{O} + \mathrm{d} \tag{1.14}$$

(Dansgaard, 1964)

The fixed relationship of hydrogen and oxygen isotopes in cave seepage and fluid inclusion water is useful to investigate whether secondary effects on the oxygen isotope composition of inclusion water have taken place. If fluid inclusion oxygen isotope composition has moved away from the GMWL by oxygen isotope exchange between inclusion water and the surrounding speleothem carbonate, this results in erroneous paleotemperature calculations. Hydrogen isotopes of fluid inclusion water can not exchange with the host carbonate. Therefore previous studies focused on measuring hydrogen isotopes of fluid inclusion water to avoid erroneous temperature calculations (Harmon et al., 1979; Schwarcz et al., 1976; Yonge, 1982). In this thesis cross plots of hydrogen and oxygen isotope data of fluid inclusion water are used to determine whether they fall on the GMWL as indicator of secondary oxygen isotope exchange (Dennis et al., 2001; Vonhof et al., 2007).

2

Uranium-series dating method applied on speleothems

Abstract

This chapter describes the U-series dating method for speleothems younger than ~ 500 kyr. The method is based on the extreme fractionation of the parent and daughter isotopes due to their different geochemical behaviour in the hydrosphere. The parent isotopes (^{238}U and ^{234}U) are soluble in groundwater where the long-lived daughter ^{230}Th is practically insoluble. As cave drip water contains Uranium, this is always incorporated in speleothem carbonate, whereas Thorium usually is not. The return to secular equilibrium is time dependent and is used to reconstruct at what time carbonate was deposited.

2.1 Introduction

Speleothems as climate archives have become useful because they can be well dated using high-precision Uranium series techniques. This technique resulting in an independent age frame work makes speleothems valuable for paleo-climate research. The lack of direct radiometric dates from ocean and continental records has led some authors to suggest that timings of important climatic events are best estimated from correlation with speleothems' chronologies (e.g., Genty et al., 2003). The Uranium series technique applied on speleothems permits precise chronologies for climate events. For this speleothem based climate study, Uranium series dating is done on a Finnigan MAT262 multi collector Thermal Ionization Mass Spectrometer (TIMS) to obtain precise ages. This chapter gives an historical overview of the discovery of the element Uranium and its radioactive daughters as the technical developments concerning the Uranium series technique available for Earth sciences. This chapter also describes the technique used at the Vrije Universiteit Amsterdam.

2.2 History of element Uranium

The element Uranium was discovered by the German chemist Martin S. Klaproth in 1789. He was the first to extract uraniumoxide from a pitchblende and recognized it as a new element. Uranium itself was first isolated in its metal form ~50 years later in 1841 by Eugene-Melchoir Peligot. The Russian chemist Dimitri Mendeleev argued with his periodical classification that Uranium was the last and heaviest element on Earth. Its radioactive properties were discovered by the French scientist Henri Becquerel in 1896 (Becquerel, 1896a; Becquerel, 1896b).

Entering the 20th century new discoveries were made rapidly. In 1900, Rutherford demonstrated that radioactivity decreased exponentially with time ($dN/dt = -\lambda N$) and introduced the term half-lives (Rutherford, 1900). The understanding that radioactive decay would produce new elements (Rutherford and Soddy, 1902) resulted in the radioactive decay chain concept. In 1903 Marie Curie published the first radioactive decay chain and recognized that radioactivity released heat and Helium. In 1913, Soddy and Fajans independently found that when an α-particle was emitted the original element changed to an element two groups to the left in the periodic table. Each time an element emitted a ß-particle the resulting element was shifted one group to the right (Fajans, 1913; Soddy, 1913). The fundamental work concerning radioactive decay was therefore completed and all the radioactive Uranium daughter elements were discovered with Pb as the final stable product. When the half-lives for most isotopes were known and all the knowledge about radioactive decay was completed the U and Th isotopes became available as a chronostratigraphic tool for earth scientific research.

The developments of the Uranium-series technique for dating mineral deposits less than 500Kyrs old, went synchronous with technical breakthroughs. Due to the small amount of naturally occurring Uranium and Thorium in sediments and rocks, sensitive equipment was needed. The development of alpha and gamma spectrometry in the late 1950s made it possible to start the first precise dating of sediments. The limitation of this technique is that only the decaying atoms are counted, which is only a fraction of the total available U and Th isotopes as half lives are 10^5 years or more. To get statistically meaningful numbers, counting times for Uranium and Thorium took weeks for a single analysis. Developments in mass-spectrometry made it possible to measure the available Uranium and Thorium isotopes, with sufficiently long half-lives, directly. This greatly improved the analytical precision and decreased the required sample size. These techniques improved the resolution of the geochronological framework necessary for geological research. In the late 1980s the first multi-collector thermal ionization mass spectrometry techniques were developed. This greatly advanced analytical capabilities (Chen et al., 1986; Chen and Wasserburg, 1981; Edwards et al., 1987a; Edwards et al., 1987b). MC-TIMS made it possible to measure U, Th, Pa and Ra with high precision and made it able to measure isotope ratios larger than 10^5. Isotope dilution made it possible to measure very precisely the $^{230}Th/^{238}U$ ratio. 0.1%-0.4% precision (2σ) is possible on a multi-collector TIMS (Goldstein and Stirling, 2003). Also the chemistry of the U and Th separation was improved. Actinide specific resins separate U and Th from all other elements easier and better than anion or cation exchange chemistry, solvent extraction, phase separation and/or coprecipiation (Goldstein and Stirling, 2003). Due to all these developments Uranium-series methods provide nowadays by far the most reliable and precise method for dating speleothems younger then 500,000 years.

The first time speleothems were dated using Uranium-series technique was in the beginning of the 1960s using α-counting (e.g., Cherdyntsev et al., 1965; Rosholt and Antal, 1962). The earliest stable isotope records from speleothems for paleoclimate reconstruction were made in the late 1960s and 1970s (Duplessy et al., 1970; Gascoyne, 1983; Harmon et al., 1978; Hendy and Wilson, 1968; Schwarcz et al., 1976; Thompson et al., 1974)

2.3 Theory

The Uranium-series technique is based on the decay chains of three naturally occurring actinide nuclides, namely ^{238}U, ^{235}U, ^{232}Th. These radioactive isotopes have long half lives and decay by alpha and beta emission through intermediate daughters to three stable isotopes of lead (figure 2.1).

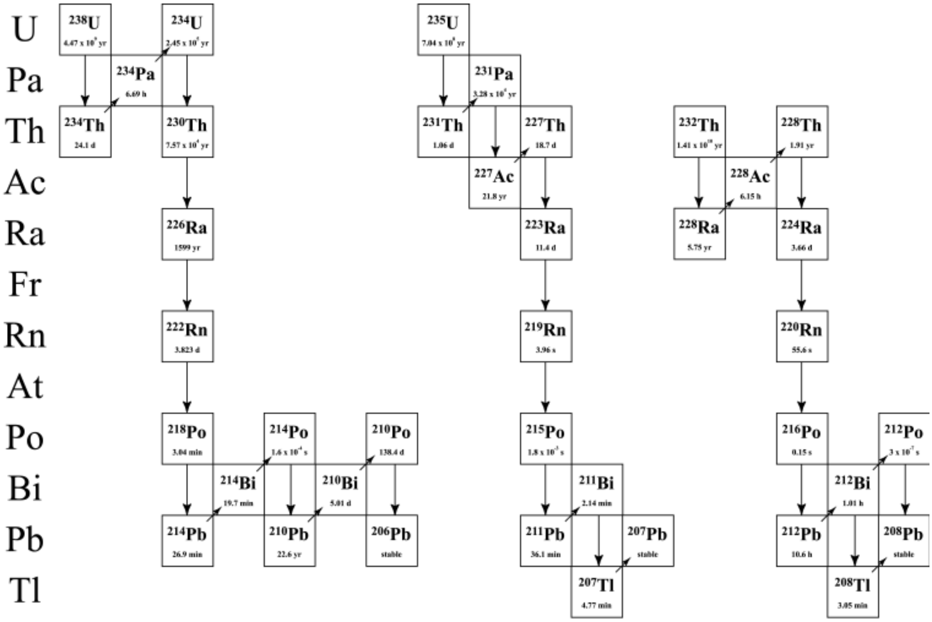

Figure 2.1: The radioactive decay chains of ^{238}U, ^{235}U en ^{232}Th, modified from Bourdon et al., (2003).

^{238}U decays by alpha emission to ^{234}Th, which decays by beta emission to ^{234}Pa, which decays by beta emission to ^{234}U, which decays by alpha emission to ^{230}Th, which decays eventually to ^{206}Pb through a series of intermediate daughters. The half-lives for the selected daughters for Uranium-series dating are given in table 2.1.

As the half-lives for ^{234}Th and ^{234}Pa are very short compared to the ages between 10 to 10^5 years the ^{234}Th and ^{234}Pa are neglected in the mathematical calculation. The nuclides

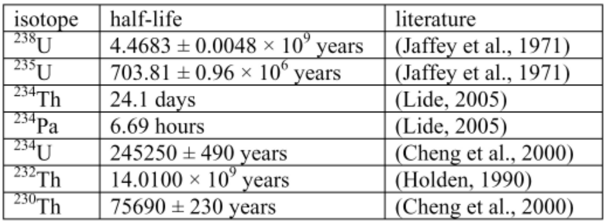

isotope	half-life	literature
^{238}U	4.4683 ± 0.0048 × 10^9 years	(Jaffey et al., 1971)
^{235}U	703.81 ± 0.96 × 10^6 years	(Jaffey et al., 1971)
^{234}Th	24.1 days	(Lide, 2005)
^{234}Pa	6.69 hours	(Lide, 2005)
^{234}U	245250 ± 490 years	(Cheng et al., 2000)
^{232}Th	14.0100 × 10^9 years	(Holden, 1990)
^{230}Th	75690 ± 230 years	(Cheng et al., 2000)

Table 2.1: Half-lives of specific U, Th and Pa isotopes.

used for dating of carbonate systems and specifically corals and speleothems are ^{238}U, ^{234}U and ^{230}Th.

Typical U concentrations of the continental crust range from 0.1 (basalts) to 10 ppm (granites) (van Calsteren and Thomas, 2006; Wedepohl, 1995). Sedimentary rocks have Uranium concentrations of about 2 ppm (van Calsteren and Thomas, 2006). Limestone formations have mean values of about 2 ppm U, but speleothem formation can reach up to 100 ppm U (Spötl et al., 2002; Stirling et al., 2000).

2.4 Secular equilibrium

In the ^{238}U decay chain a secular radioactive equilibrium can be reached. This state is reached when the decay rate of each daughter nuclide in the chain is equal to that of the parent. Activity is defined as the number of atoms times the decay constant (equation 2.1). The activity ratio is given as equation 2.2. When the decay rate of each daughter nuclide is equal to that of the parent, the activity ratio is equal to 1, which is the state of secular equilibrium.

$$\mathrm{A} = \lambda \cdot \mathrm{N} \tag{2.1}$$

$$\mathrm{R}_{\mathrm{activity}} = \frac{\lambda_1 \cdot \mathrm{N}_1}{\lambda_2 \cdot \mathrm{N}_2} \tag{2.2}$$

Secular equilibrium is reached when a system is chemically closed much longer than the longest half-live. In the ^{238}U decay chain a secular equilibrium between ^{234}U/^{238}U is reached after approximately a million years.

Figure 2.2 illustrates the activity of ^{234}U and ^{238}U, showing that the activity ratio does not vary significantly after ~1 million years. To use the ^{238}U decay chain for dating an extreme fractionation between the parent and daughter isotopes due to natural occurring processes is needed to 'reset' the radioactive clock. Two types of mechanisms can be distinguished; 1) difference in geochemical behaviour of the U-series elements 2) α-recoil effects.

U-series elements are naturally fractionated because of their different geochemical behaviour. U has two oxidation states in nature (U^{4+} and U^{6+}). At the Earth's surface

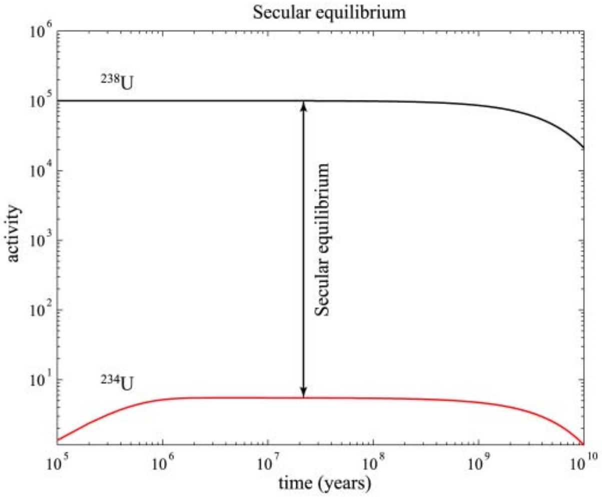

Figure 2.2: Secular equilibrium of ^{234}U and ^{238}U through time. Secular equilibrium is reached after 1 million years and is seen as the parallel activity of ^{238}U and ^{234}U.

the U^{6+} is dominant and forms the soluble $(UO_2)^{2+}$ ion. (Edwards et al., 2003) Th is mainly present in the Th^{4+} state which is insoluble in natural water. Uranium and Thorium are therefore extremely fractionated by the cave hydrology. In cave drip water almost no Thorium is present as its solubility is extremely low and Th is easily adsorbed onto clay particles (Bourdon et al., 2003). Uranium is soluble and will dissolve in the drip water and eventually precipitate in small amounts in speleothem carbonate. Consequently no Thorium is incorporated during speleothem formation, resulting in extreme Th/U fractionation.

The α-recoil effect is a fractionation process which takes place as a result of radioactive decay. When a ^{238}U atom decays to ^{234}U by α-decay kinetic energy is released. The displacement of the ^{234}U nuclide and the α-particle will damage the crystal lattice and this means that the daughter nuclide is more easy mobilized than its parent during the weathering process. Therefore (^{234}U/^{238}U) activity ratios in seawater are ~1.14, a bit out of equilibrium (Chen et al., 1986; Delanghe et al., 2002; Henderson, 2002).

Secular equilibrium will be restored with time, which can be calculated using the equations of radioactive decay and in-growth (Bateman, 1910; figure 2.3).

For the parent nuclide:

$$\frac{dN_1}{dt} = -\lambda_1 N_1 \tag{2.3}$$

N_1 : Number of atoms of first nuclide

λ : decay constant (yr^{-1})

t: time (yr)

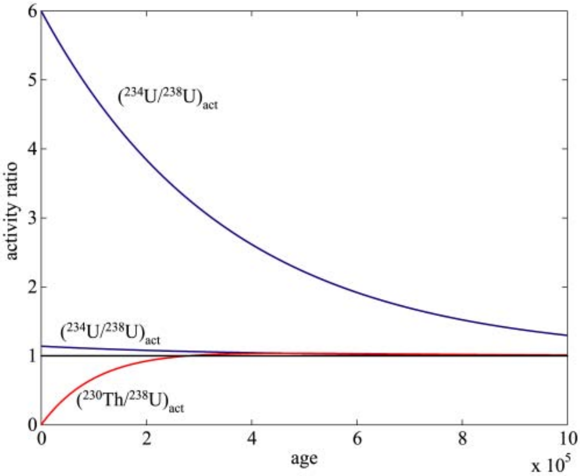

Figure 2.3: The activity ratios of (^{234}U/^{238}U), (^{230}Th/^{238}U) through time under closed-system conditions. Initial activity ratio condition for (^{230}Th/^{238}U) is 0. For (^{234}U/^{238}U) we have taken the initial calculated speleothem (^{234}U/^{238}U) activity ratios, 1.2 and 6. Secular equilibrium for both activity ratios is 1.

$$\lambda = \frac{\ln 2}{t_{1/2}} \tag{2.4}$$

For all the intermediate nuclides of interest:

$$N_i = C_1 e^{-\lambda_1 t} + C_2 e^{-\lambda_2 t} + ... + C_n e^{-\lambda_n t} \tag{2.5a}$$

where

$$C_1 = \frac{\lambda_1 \lambda_2 ... \lambda_{n-1}}{(\lambda_2 - \lambda_1)(\lambda_3 - \lambda_1) ... (\lambda_n - \lambda_1)} N_1^0 \tag{2.5b}$$

$$C_2 = \frac{\lambda_1 \lambda_2 ... \lambda_{n-1}}{(\lambda_1 - \lambda_2)(\lambda_3 - \lambda_2) ... (\lambda_n - \lambda_2)} N_1^0 \tag{2.5c}$$

$$C_n = \frac{\lambda_1 \lambda_2 ... \lambda_{n-1}}{(\lambda_1 - \lambda_n)(\lambda_3 - \lambda_n) ... (\lambda_{n-1} - \lambda_n)} N_1^0 \tag{2.5d}$$

For the first two nuclides in a decay chain we obtain Bateman (1910), by integration of equation 2.3.

$$\mathrm{N}_1 = \mathrm{N}_1^0 e^{-\lambda_1 \mathrm{t}} \tag{2.6}$$

and

$$\mathrm{N}_2 = \frac{\lambda_1}{\lambda_2 - \lambda_1} \mathrm{N}_1^0 (e^{-\lambda_1 \mathrm{t}} - e^{-\lambda_2 \mathrm{t}}) + \mathrm{N}_2^0 e^{-\lambda_2 \mathrm{t}} \tag{2.7}$$

solving the equations 2.3 above.

2.5 Age equation

The ^{230}Th age equation can only be used when the following conditions are assumed (Edwards, 2003):

1) initial (^{230}Th/^{238}U) = 0,

2) radioactive decay is responsible for isotopic changes in Uranium and Thorium,

3) ^{238}U has not decayed appreciably over the timescales of interest (0 to ~500,000 years)

$$\left(\frac{^{230}\mathrm{Th}}{^{238}\mathrm{U}}\right) - 1 = -e^{-\lambda_{230}\mathrm{t}} + \left(\frac{\delta^{234}\mathrm{U}}{1000}\right)\left(\frac{\lambda_{230}}{\lambda_{230} - \lambda_{234}}\right)\left(1 - e^{-(\lambda_{230} - \lambda_{234})\mathrm{t}}\right) \tag{2.8}$$

$$\delta^{234}\mathrm{U} = \left(\frac{(^{234}\mathrm{U}/^{238}\mathrm{U})_{\mathrm{measured}}}{\lambda_{238}/\lambda_{234}} - 1\right) \times 1000 \tag{2.9}$$

$\left(\frac{^{230}\mathrm{Th}}{^{238}\mathrm{U}}\right)$: activity ratio
λ : decay constants
t : age

Equation 2.9 is the present deviation in parts per thousands (per mil) of the (^{234}U/^{238}U) ratio from secular equilibrium. Using isotope dilution/spiking it is possible to calculate the (^{230}Th/^{238}U) and (^{234}U/^{238}U) ratio. As time is the only unknown by then the equation 2.8 can be solved using iteration as age (t) appears twice in the calculation. The relation between δ^{234}U and (^{230}Th/^{238}U) activity ratio and time is illustrated in figure 2.4. After 500 ka a secular equilibrium is reached and Uranium-series can not discriminate between older samples.

As speleothems can have an extreme high δ^{234}U initial value, the age is determined also by the δ^{234}U initial value, which can be significant as illustrated in figure 2.5.

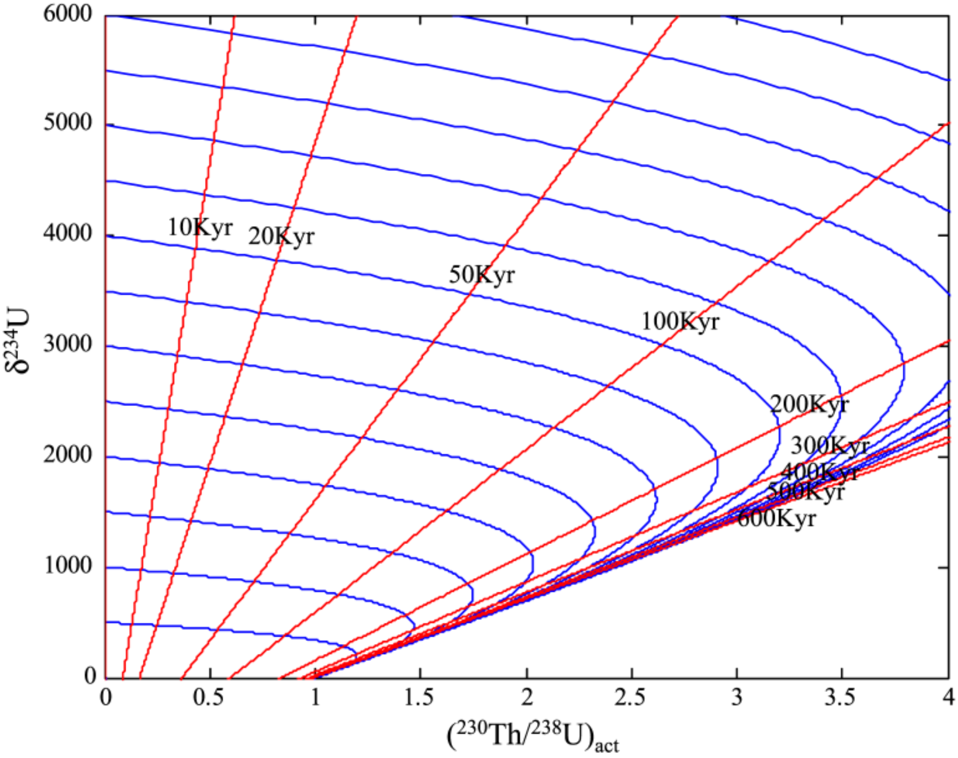

Figure 2.4: Illustrated is the δ^{234}U value versus (^{230}Th/^{238}U) activity ratio through time.

2.6 Correction for detrital contamination

The first assumption for a correct U/Th age calculation is that there is no initial ^{230}Th. These conditions, however, do not always occur in speleothem formation, resulting in an offset of the age, normally an overestimation. In such a case a correction for initial ^{230}Th is necessary. As ^{232}Th has the same chemical properties as ^{230}Th it can be used as an indicator for the amount of initial ^{230}Th contamination. However not always is the (^{232}Th/^{230}Th) activity ratio of the detritus known, often an initial ^{230}Th/^{232}Th atomic ratio of $4.4 \cdot 10^{-6}$ is used (Stirling et al., 1998), assuming a bulk Earth ^{232}Th/^{238}U ratio of 3.8 ± 1.0 (Wedepohl, 1995) and presuming secular equilibrium. When the correction for initial ^{230}Th is large and the ^{230}Th/^{232}Th ratio must be known precisely, isochron methods can be used (Edwards et al., 2003; Ludwig, 2003). To perform an excess ^{230}Th correction an additional term is introduced in equation 2.8 (Cobb et al., 2003)

$$\left(\frac{^{230}\mathrm{Th_{rad}}}{^{238}\mathrm{U}}\right) = \left(\frac{^{230}\mathrm{Th_{meas}}}{^{238}\mathrm{U}}\right) - \left(\frac{^{232}\mathrm{Th}}{^{238}\mathrm{U}}\right) \cdot \left(\frac{^{230}\mathrm{Th_{initial}}}{^{232}\mathrm{Th}}\right) \cdot e^{-\lambda_{230}\mathrm{t}} \tag{2.10}$$

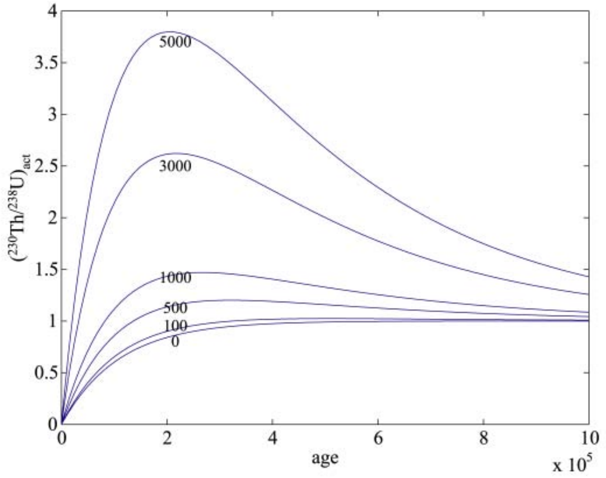

Figure 2.5: The (^{230}Th/^{238}U) activity ratio through time for different initial δ^{234}U values is illustrated. The initial ^{230}Th value is 0. In this study δ^{234}U values close to 5000‰ are measured.

A correction for detrital ^{230}Th can be done, however every correction will always increase the uncertainty in the final age. For this study only samples with a ^{230}Th/^{232}Th activity ratio <100 are corrected for detrital ^{230}Th.

2.7 Chemical separation

Chemical separation to purify the element of interest is important for good measurements on the TIMS as unwanted elements can interfere with the elements of interest. The following chemical procedure is used at the Vrije Univeristeit Amsterdam. Speleothem carbonate samples are cleaned in an ultrasonic bath and dissolved in HNO_3. Any residue is removed by centrifuging. A ^{229}Th/^{233}U mixed spike is added with 229/230 around 1-10. An Fe-carrier is used to co-precipitate U and Th. Ammonia (NH_3) creates a $Fe(OH)_3$ precipitation which co-precipitates U and Th from the solution. The mixture is centrifuged and the supernate is discarded. The residue is rinsed 3 times with MilliQ water.

Purification of U and Th was done using anion exchange columns. An 0.5 ml quartz column with AGIX 200-400 mesh is used to separate U and Th from other elements and each other. Th is further purified with a second column extraction using a 0.17ml quartz column with AGIX 200-400 mesh anion exchange resin. Detailed information about ion-exchange for U and Th chemistry see Lally (1992).

2.8 Thermal Ionization Mass Spectrometry

Thermal Ionization Mass Spectrometry (TIMS) with multi-collector and RPQ/SEM is commercially available for U/Th analyses to the scientific community since the 1990's. The TIMS is a solid source mass spectrometer, which enables the determination of isotope ratios with very high precision. U and Th measurements are performed on a Finnigan MAT262 using a double filament technique. Samples are loaded on the evaporation filament, a second filament is placed opposite the evaporation filament at ∼1mm distance. The evaporation filament is heated up, so the sample evaporates, the ionization filament will bombard the U atoms with electrons to ionize them. The ionized atoms are accelerated in a high voltage field of 10,000 Volt and the ion beam is focused by an electrostatic lens system (Scholz, 2005). A strong magnetic field (∼1 Tesla) will separate isotopes with different masses.

Ion currents higher than 1 mV are measured on the faraday cups, while smaller beams are measured on the Ion Counting Multiplier (ICM) or a second ICM equipped with a Retarding Potential Quadrupole.

U and Th analyses are done separately as they are evaporated at different temperatures ∼1750°C and ∼1800°C respectively.

The Finnigan MAT 262 at the Vrije Universiteit Amsterdam is equipped with 1 RPQ multiplier and 7 movable faradays cups. Samples are normalized for instrumental mass fractionation using the using natural isotope ratio of $^{235}U/^{238}U$ (0.0072527).

Thorium analyses are performed using a jump method on the RPQ.

2.9 Data

To check if the U and Th data is in accordance with a closed system some checks are performed. For speleothems the δ^{234}Uvalue can be between -100‰ up to even 6000‰ (Plagnes et al., 2002) generally -100 to 1000‰ (Richards and Dorale, 2003). In this study the $\delta^{234}U$ values are between 100 to 5000‰. All measured data are plotted in figure 2.6. The $\delta^{234}U$ values are consistent through time as the data points of a single stalagmite are parallel to the ($^{234}U/^{238}U$) activity ratio through time.

The activity ratio ($^{230}Th/^{232}Th$) should be larger than 100. This indicates that there is no significant amount of initial ^{230}Th present in the sample. When the ($^{230}Th/^{232}Th$) activity ratio is below 100 a correction needs to be applied using ^{232}Th as a criterion to correct for the excess non radiogenic ^{230}Th. The correction for initial ^{230}Th is done by using a ratio $^{230}Th/^{232}Th$ of $4.4 \cdot 10^{-6}$. The activity ratio of ($^{230}Th/^{232}Th$) is ∼0.81 assuming a bulk Earth ratio of $^{232}Th/^{238}U$ ratio of 3.8 (Wedepohl, 1995). The correction is applied using formula 2.10.

2.10 Calculation steps

^{238}U and ^{230}Th concentrations of the measured samples can be converted using the half-lives of the different isotopes to the ($^{230}Th/^{238}U$) activity ratio.

The $\delta^{234}U$ values and initial $\delta^{234}U_{\text{activity}}$ ratio are calculated using following equations.

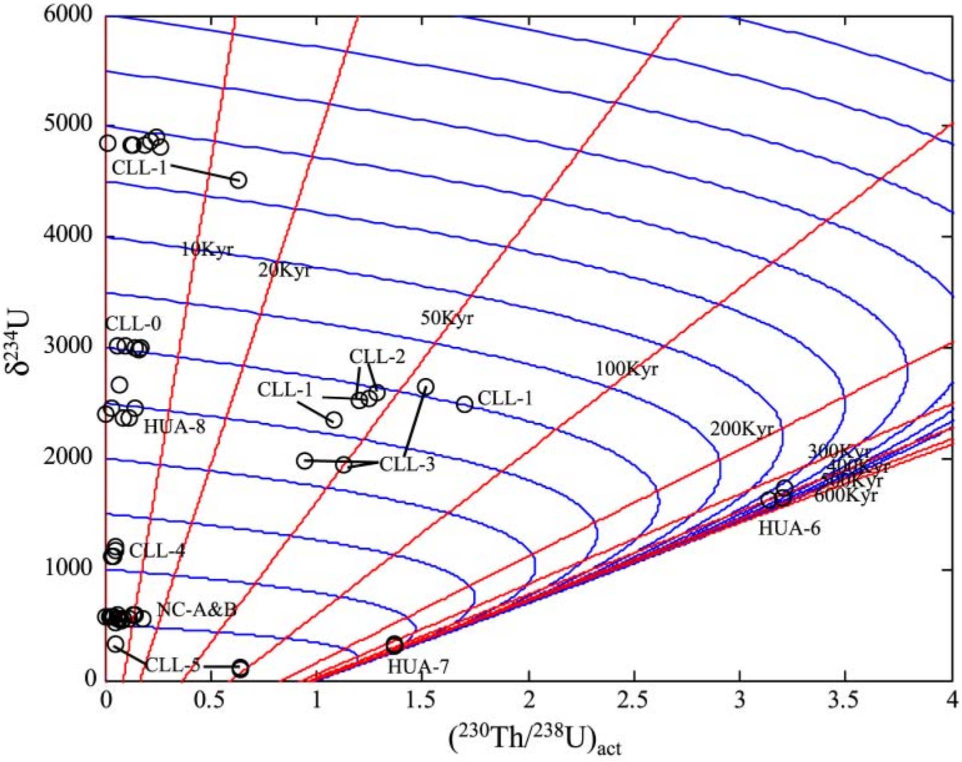

Figure 2.6: Plotted are individual dates of the speleothems. The U/Th age data δ^{234}U vs $(^{230}\mathrm{Th}/^{238}\mathrm{U})_{\mathrm{act}}$ are plotted.

$$\delta^{234}\mathrm{U} = \left(\frac{\left(^{234}\mathrm{U}/^{238}\mathrm{U}\right)_{\mathrm{measured}}}{\lambda_{238}/\lambda_{234}} - 1 \right) \times 1000 \tag{2.11}$$

$$\delta^{234}\mathrm{U}_{\mathrm{initial}} = \delta^{234}\mathrm{U}_{\mathrm{activity}} \cdot e^{\lambda_{234}\mathrm{t}} \tag{2.12}$$

As the $(^{230}\mathrm{Th}/^{238}\mathrm{U})$ activity ratio and the δ^{234}U are known the age equation can be solved by iterating time. The measured samples for this study are listed in Appendix I: Measured data. Whereas the excel macro, modified from Neff (2001), used to calculate the age is shown in Appendix II: Visual Basic Scripts. The speleothems collected in Peru are provided in Appendix III: Speleothems, with a initial δ^{18}O and δ^{13}C record and their U/Th ages.

Measurement uncertainties propagated using a Monte Carlo simulation from Scholz (2005), resulted in slightly smaller age uncertainties than using conventional error propagation as we did.

2.11 Appendix I: Measured data

Constants

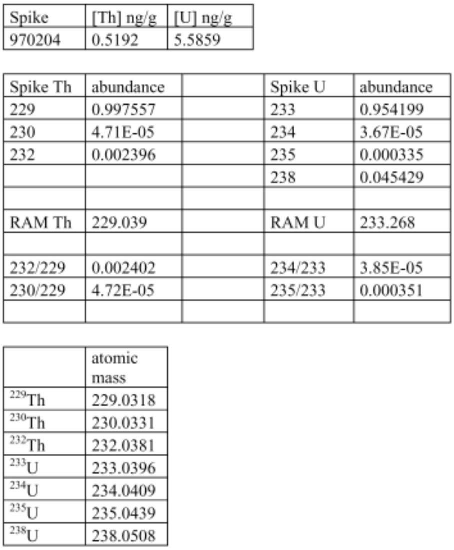

Spike	[Th] ng/g	[U] ng/g
970204	0.5192	5.5859

Spike Th	abundance		Spike U	abundance
229	0.997557		233	0.954199
230	4.71E-05		234	3.67E-05
232	0.002396		235	0.000335
			238	0.045429
RAM Th	229.039		RAM U	233.268
232/229	0.002402		234/233	3.85E-05
230/229	4.72E-05		235/233	0.000351

	atomic mass
^{229}Th	229.0318
^{230}Th	230.0331
^{232}Th	232.0381
^{233}U	233.0396
^{234}U	234.0409
^{235}U	235.0439
^{238}U	238.0508

Table 2.2: Spike concentration for U and Th given as well as the abundancy and the used atomic mass of each isotope.

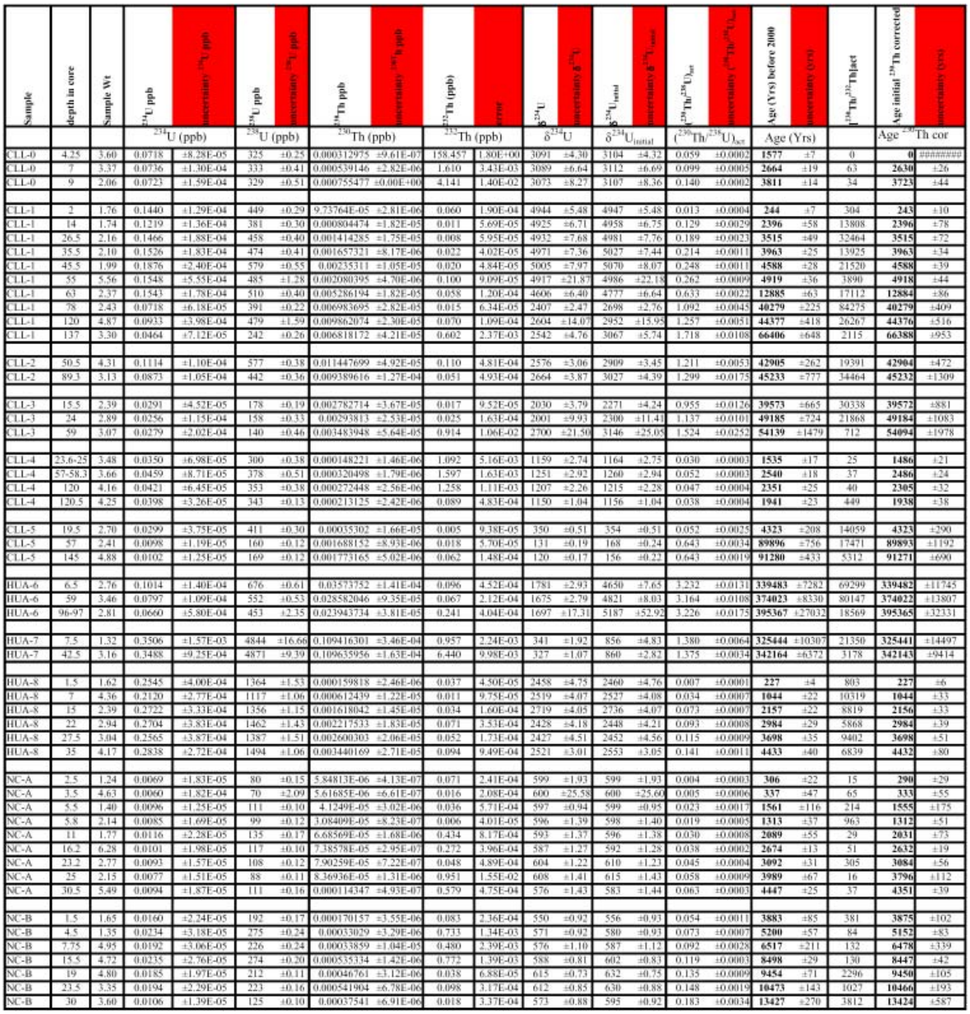

Sample	depth in core	Sample Wt	^{234}U ppb	uncertainty ^{234}U ppb	^{238}U ppb	uncertainty ^{238}U ppb	^{230}Th ppb	uncertainty ^{230}Th ppb	^{232}Th (ppb)	error	δ^{234}U	uncertainty δ^{234}U	$\delta^{234}U_{initial}$	uncertainty $\delta^{234}U_{initial}$	$(^{230}Th/^{238}U)_{act}$	uncertainty $(^{230}Th/^{238}U)_{act}$	Age (Yrs) before 2000	uncertainty (yrs)	$[^{230}Th/^{232}Th]_{act}$	Age initial ^{230}Th corrected	uncertainty (yrs)
			^{234}U (ppb)		^{238}U (ppb)		^{230}Th (ppb)		^{232}Th (ppb)		δ^{234}U		$\delta^{234}U_{initial}$		$(^{230}Th/^{238}U)_{act}$		Age (Yrs)			Age ^{230}Th cor	
CLL-0	4.25	3.60	0.0718	±8.28E-05	325	±0.25	0.000312975	±9.61E-07	158.457	1.80E+00	3091	±4.30	3104	±4.32	0.059	±0.0002	**1577**	±7	0	**0**	########
CLL-0	7	3.37	0.0736	±1.30E-04	333	±0.41	0.000539146	±2.82E-06	1.610	3.43E-03	3089	±6.64	3112	±6.69	0.099	±0.0005	**2664**	±19	63	**2630**	±26
CLL-0	9	2.06	0.0723	±1.59E-04	329	±0.51	0.000755477	±0.00E+00	4.141	1.40E-02	3073	±8.27	3107	±8.36	0.140	±0.0002	**3811**	±14	34	**3723**	±44
CLL-1	2	1.76	0.1440	±1.29E-04	449	±0.29	9.73764E-05	±2.81E-06	0.060	1.90E-04	4944	±5.48	4947	±5.48	0.013	±0.0004	**244**	±7	304	**243**	±10
CLL-1	14	1.74	0.1219	±1.36E-04	381	±0.30	0.000804474	±1.82E-05	0.011	5.69E-05	4925	±6.71	4958	±6.75	0.129	±0.0029	**2396**	±58	13808	**2396**	±78
CLL-1	26.5	2.16	0.1466	±1.88E-04	458	±0.40	0.001414285	±1.75E-05	0.008	5.95E-05	4932	±7.68	4981	±7.76	0.189	±0.0023	**3515**	±49	32464	**3515**	±72
CLL-1	35.5	2.10	0.1526	±1.83E-04	474	±0.41	0.001657321	±8.17E-06	0.022	4.02E-05	4971	±7.36	5027	±7.44	0.214	±0.0011	**3963**	±25	13925	**3963**	±34
CLL-1	45.5	1.99	0.1876	±2.40E-04	579	±0.55	0.00235311	±1.05E-05	0.020	4.84E-05	5005	±7.97	5070	±8.07	0.248	±0.0011	**4588**	±28	21520	**4588**	±39
CLL-1	55	5.56	0.1548	±5.55E-04	485	±1.28	0.002080395	±4.70E-06	0.100	9.09E-05	4917	±21.87	4986	±22.18	0.262	±0.0009	**4919**	±36	3890	**4918**	±44
CLL-1	63	2.37	0.1543	±1.78E-04	510	±0.40	0.005286194	±1.82E-05	0.058	1.20E-04	4606	±6.40	4777	±6.64	0.633	±0.0022	**12885**	±63	17112	**12884**	±86
CLL-1	78	2.43	0.0718	±6.18E-05	391	±0.22	0.006983695	±2.82E-05	0.015	6.34E-05	2407	±2.47	2698	±2.76	1.092	±0.0045	**40279**	±225	84275	**40279**	±409
CLL-1	120	4.87	0.0933	±3.98E-04	479	±1.59	0.009862074	±2.30E-05	0.070	1.09E-04	2604	±14.07	2952	±15.95	1.257	±0.0051	**44377**	±418	26267	**44376**	±516
CLL-1	137	3.30	0.0464	±7.12E-05	242	±0.26	0.006818172	±4.21E-05	0.602	2.37E-03	2542	±4.76	3067	±5.74	1.718	±0.0108	**66406**	±648	2115	**66388**	±953
CLL-2	50.5	4.31	0.1114	±1.10E-04	577	±0.38	0.011447699	±4.92E-05	0.110	4.81E-04	2576	±3.06	2909	±3.45	1.211	±0.0053	**42905**	±262	19391	**42904**	±472
CLL-2	89.3	3.13	0.0873	±1.05E-04	442	±0.36	0.009389616	±1.27E-04	0.051	4.93E-04	2664	±3.87	3027	±4.39	1.299	±0.0175	**45233**	±777	34464	**45232**	±1309
CLL-3	15.5	2.39	0.0291	±4.52E-05	178	±0.19	0.002782714	±3.67E-05	0.017	9.52E-05	2030	±3.79	2271	±4.24	0.955	±0.0126	**39573**	±665	30338	**39572**	±881
CLL-3	24	2.89	0.0256	±1.15E-04	158	±0.33	0.00293813	±2.53E-05	0.025	1.63E-04	2001	±9.93	2300	±11.41	1.137	±0.0101	**49185**	±724	21868	**49184**	±1083
CLL-3	59	3.07	0.0279	±2.02E-04	140	±0.46	0.003483948	±5.64E-05	0.914	1.06E-02	2700	±21.50	3146	±25.05	1.524	±0.0252	**54139**	±1479	712	**54094**	±1978
CLL-4	23.6-25	3.48	0.0350	±6.98E-05	300	±0.38	0.000148221	±1.46E-06	1.092	5.16E-03	1159	±2.74	1164	±2.75	0.030	±0.0003	**1535**	±17	25	**1486**	±21
CLL-4	57-58.3	3.66	0.0459	±8.71E-05	378	±0.51	0.000320498	±1.79E-06	1.597	1.63E-03	1251	±2.92	1260	±2.94	0.052	±0.0003	**2540**	±18	37	**2486**	±24
CLL-4	120	4.16	0.0421	±6.45E-05	353	±0.38	0.000272448	±2.56E-06	1.258	1.11E-03	1207	±2.26	1215	±2.28	0.047	±0.0004	**2351**	±25	40	**2305**	±32
CLL-4	120.5	4.25	0.0398	±3.26E-05	343	±0.13	0.000213125	±2.42E-06	0.089	4.83E-04	1150	±1.04	1156	±1.04	0.038	±0.0004	**1941**	±23	449	**1938**	±38
CLL-5	19.5	2.70	0.0299	±3.75E-05	411	±0.30	0.00035302	±1.66E-05	0.005	9.38E-05	350	±0.51	354	±0.51	0.052	±0.0025	**4323**	±208	14059	**4323**	±290
CLL-5	57	2.41	0.0098	±1.19E-05	160	±0.12	0.001688152	±8.93E-06	0.018	5.70E-05	131	±0.19	168	±0.24	0.643	±0.0034	**89896**	±756	17471	**89893**	±1192
CLL-5	145	4.88	0.0102	±1.25E-05	169	±0.12	0.001773165	±5.02E-06	0.062	1.48E-04	120	±0.17	156	±0.22	0.643	±0.0019	**91280**	±433	5312	**91271**	±690
HUA-6	6.5	2.76	0.1014	±1.40E-04	676	±0.61	0.03573752	±1.41E-04	0.096	4.52E-04	1781	±2.93	4650	±7.65	3.232	±0.0131	**339483**	±7282	69299	**339482**	±11745
HUA-6	59	3.46	0.0797	±1.09E-04	552	±0.53	0.028582046	±9.35E-05	0.067	2.12E-04	1675	±2.79	4821	±8.03	3.164	±0.0108	**374023**	±8330	80147	**374022**	±13807
HUA-6	96-97	2.81	0.0660	±5.80E-04	453	±2.35	0.023943734	±3.81E-05	0.241	4.04E-04	1697	±17.31	5187	±52.92	3.226	±0.0175	**395367**	±27032	18569	**395365**	±32331
HUA-7	7.5	1.32	0.3506	±1.57E-03	4844	±16.66	0.109416301	±3.46E-04	0.957	2.24E-03	341	±1.92	856	±4.83	1.380	±0.0064	**325444**	±10307	21350	**325441**	±14497
HUA-7	42.5	3.16	0.3488	±9.25E-04	4871	±9.39	0.109635956	±1.63E-04	6.440	9.98E-03	327	±1.07	860	±2.82	1.375	±0.0034	**342164**	±6372	3178	**342143**	±9414
HUA-8	1.5	1.62	0.2545	±4.00E-04	1364	±1.53	0.000159818	±2.46E-06	0.037	4.50E-05	2458	±4.75	2460	±4.76	0.007	±0.0001	**227**	±4	803	**227**	±6
HUA-8	7	4.36	0.2120	±2.77E-04	1117	±1.06	0.000612439	±1.22E-05	0.011	9.75E-05	2519	±4.07	2527	±4.08	0.034	±0.0007	**1044**	±22	10319	**1044**	±33
HUA-8	15	2.39	0.2722	±3.33E-04	1356	±1.15	0.001618042	±1.45E-05	0.034	1.60E-04	2719	±4.05	2736	±4.07	0.073	±0.0007	**2157**	±22	8819	**2156**	±33
HUA-8	22	2.94	0.2704	±3.83E-04	1462	±1.43	0.002217533	±1.83E-05	0.071	3.53E-04	2428	±4.18	2448	±4.21	0.093	±0.0008	**2984**	±29	5868	**2984**	±39
HUA-8	27.5	3.04	0.2565	±3.87E-04	1387	±1.51	0.002600303	±2.06E-05	0.052	1.73E-04	2427	±4.51	2452	±4.56	0.115	±0.0009	**3698**	±35	9402	**3698**	±51
HUA-8	35	4.17	0.2838	±2.72E-04	1494	±1.06	0.003440169	±2.71E-05	0.094	9.49E-04	2521	±3.01	2553	±3.05	0.141	±0.0011	**4433**	±40	6839	**4432**	±80
NC-A	2.5	1.24	0.0069	±1.83E-05	80	±0.15	5.84813E-06	±4.13E-07	0.071	2.41E-04	599	±1.93	599	±1.93	0.004	±0.0003	**306**	±22	15	**290**	±29
NC-A	3.5	4.63	0.0060	±1.82E-04	70	±2.09	5.61685E-06	±6.61E-07	0.016	2.08E-04	600	±25.58	600	±25.60	0.005	±0.0006	**337**	±47	65	**333**	±55
NC-A	5.5	1.40	0.0096	±1.25E-05	111	±0.10	4.1249E-05	±3.02E-06	0.036	5.71E-04	597	±0.94	599	±0.95	0.023	±0.0017	**1561**	±116	214	**1555**	±175
NC-A	5.8	2.14	0.0085	±1.69E-05	99	±0.12	3.08409E-05	±8.23E-07	0.006	4.01E-05	596	±1.39	598	±1.40	0.019	±0.0005	**1313**	±37	963	**1312**	±51
NC-A	11	1.77	0.0116	±2.28E-05	135	±0.17	6.68569E-05	±1.68E-06	0.434	8.17E-04	593	±1.37	596	±1.38	0.030	±0.0008	**2089**	±55	29	**2031**	±73
NC-A	16.2	6.28	0.0101	±1.98E-05	117	±0.10	7.38578E-05	±2.95E-07	0.272	3.96E-04	587	±1.27	592	±1.28	0.038	±0.0002	**2674**	±13	51	**2632**	±19
NC-A	23.2	2.77	0.0093	±1.57E-05	108	±0.12	7.90259E-05	±7.22E-07	0.048	4.89E-04	604	±1.22	610	±1.23	0.045	±0.0004	**3092**	±31	305	**3084**	±56
NC-A	25	2.15	0.0077	±1.51E-05	88	±0.11	8.36936E-05	±1.31E-06	0.951	1.55E-02	608	±1.41	615	±1.43	0.058	±0.0009	**3989**	±67	16	**3796**	±112
NC-A	30.5	5.49	0.0094	±1.87E-05	111	±0.16	0.000114347	±4.93E-07	0.579	4.75E-04	576	±1.43	583	±1.44	0.063	±0.0003	**4447**	±25	37	**4351**	±39
NC-B	1.5	1.65	0.0160	±2.24E-05	192	±0.17	0.000170157	±3.55E-06	0.083	2.36E-04	550	±0.92	556	±0.93	0.054	±0.0011	**3883**	±85	381	**3875**	±102
NC-B	4.5	1.35	0.0234	±3.18E-05	275	±0.24	0.00033029	±3.29E-06	0.733	1.34E-03	571	±0.92	580	±0.93	0.073	±0.0007	**5200**	±57	84	**5152**	±83
NC-B	7.75	4.95	0.0192	±3.06E-05	226	±0.24	0.00033859	±1.04E-05	0.480	2.39E-03	576	±1.10	587	±1.12	0.092	±0.0028	**6517**	±211	132	**6478**	±339
NC-B	15.5	4.72	0.0235	±2.76E-05	274	±0.20	0.000535334	±1.42E-06	0.772	1.39E-03	588	±0.81	602	±0.83	0.119	±0.0003	**8498**	±29	130	**8447**	±42
NC-B	19	4.80	0.0185	±1.97E-05	212	±0.11	0.00046761	±3.12E-06	0.038	6.88E-05	615	±0.73	632	±0.75	0.135	±0.0009	**9454**	±71	2296	**9450**	±105
NC-B	23.5	3.35	0.0194	±2.29E-05	223	±0.16	0.000541904	±6.78E-06	0.098	3.17E-04	612	±0.85	630	±0.88	0.148	±0.0019	**10473**	±143	1027	**10466**	±193
NC-B	30	3.60	0.0106	±1.39E-05	125	±0.10	0.00037541	±6.91E-06	0.018	3.37E-04	573	±0.88	595	±0.92	0.183	±0.0034	**13427**	±270	3812	**13424**	±587

Table 2.3: All Uranium and Thorium age dating performed at the Vrije Universiteit Amsterdam for this project

2.12 Appendix II: Visual Basic Scripts

Modified from Neff (2001)

Age calculation

```
Function age(Th230_U238, dU234) As Double
    Dim t As Double

    Dim c As Double
    Const L230Th As Double = 0.0000091577
    Const L234U As Double = 0.0000028263
            For t = 0 To 600000 Step 1
          c = (1 - Exp(-t * L230Th)) + (dU234 * 0.001 * (L230Th / (L230Th - L234U)) * (1 - Exp(-t * (L230Th - L234U))))
             If c >= Th230_U238 Then
              age = t
              GoTo 10
             End If
            Next t
    age = 0
 End Function
```

Maximum age calculation

```
Function agemax(Th230_U238, error_Th230_U238, dU234, error_dU234) As Double
    Dim t As Double
    Dim c As Double
    Const L230Th As Double = 0.0000091577
    Const L234U As Double = 0.0000028263
    Th230_U238 = Th230_U238 + error_Th230_U238
    dU234 = dU234 - error_dU234
            For t = 0 To 600000 Step 1
          c = (1 - Exp(-t * L230Th)) + (dU234 * 0.001 * (L230Th / (L230Th - L234U)) * (1 - Exp(-t * (L230Th - L234U))))
             If c >= Th230_U238 Then
              agemax = t
              GoTo 20
             End If
            Next t
    agemax = 0
20    End Function
```

Minimum age calculation

```
   Function agemin(Th230_U238, error_Th230_U238, dU234, error_dU234) As Double
    Dim t As Double
    Dim c As Double
   Const L230Th As Double = 0.0000091577
    Const L234U As Double = 0.0000028263
    Th230_U238 = Th230_U238 - error_Th230_U238
    dU234 = dU234 + error_dU234
            For t = 0 To 600000 Step 1
         c = (1 - Exp(-t * L230Th)) + (dU234 * 0.001 * (L230Th / (L230Th - L234U)) * (1 - Exp(-t * (L230Th - L234U))))
             If c >= Th230_U238 Then
              agemin = t
              GoTo 30
             End If
            Next t
    agemin = 0
30    End Function
```

2.13 Appendix III: Speleothems

CLL-1

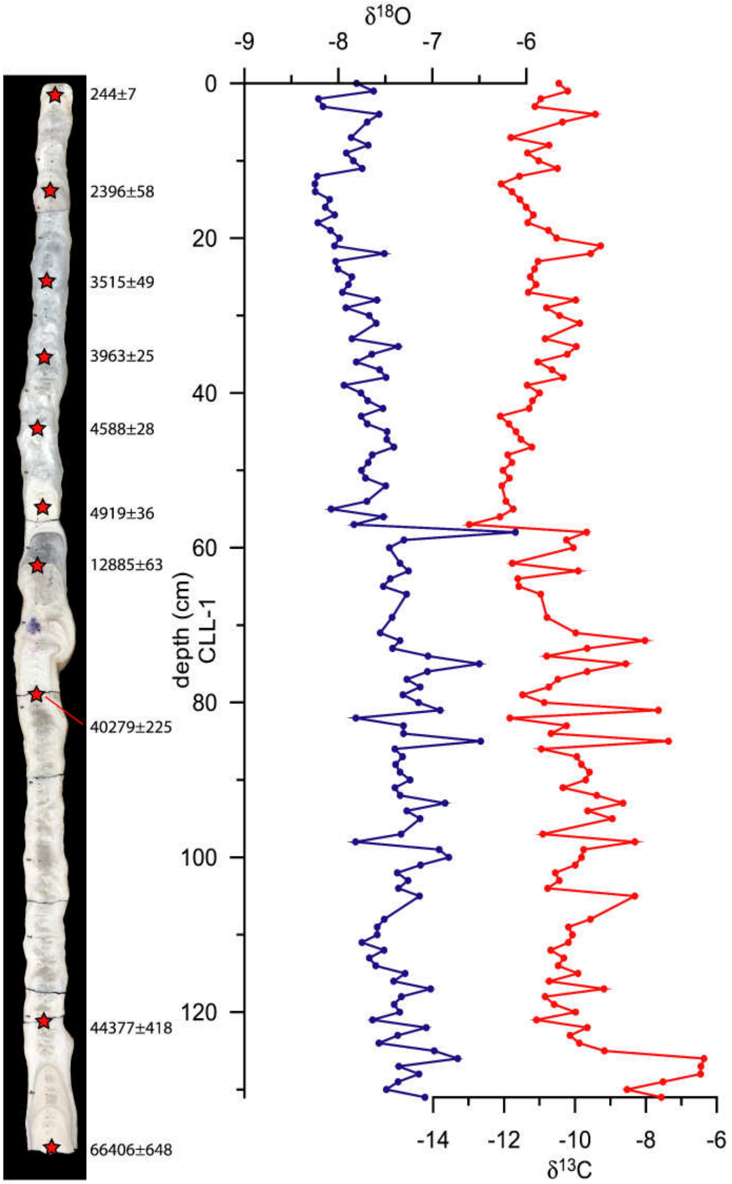

CLL-2

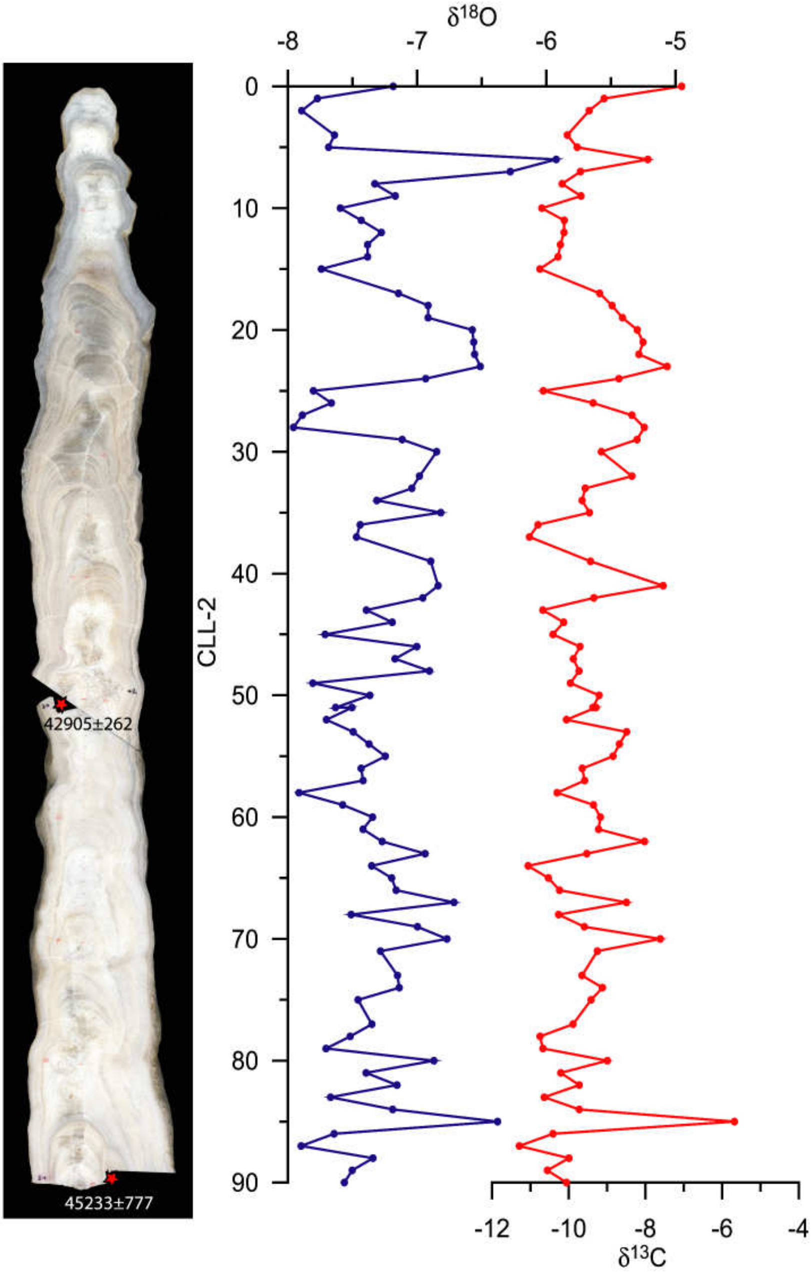
42905±262
45233±777
$\delta^{18}O$
-8
-7
-6
-5
CLL-2
0
10
20
30
40
50
60
70
80
90
-12
-10
-8
-6
-4
$\delta^{13}C$

CLL-3

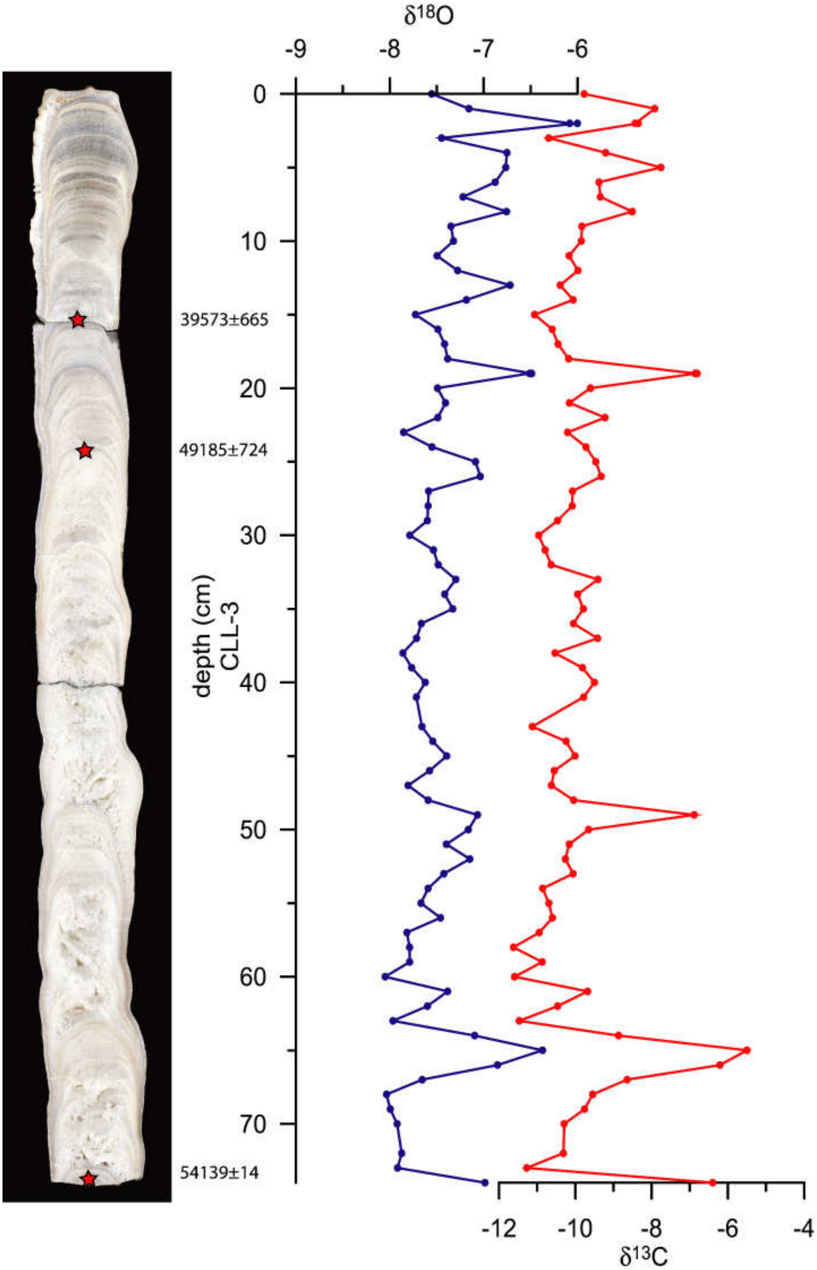
δ18O
-9
-8
-7
-6
0
10
20
30
40
50
60
70
depth (cm)
CLL-3
39573±665
49185±724
54139±14
-12
-10
-8
-6
-4
δ13C

CLL-4

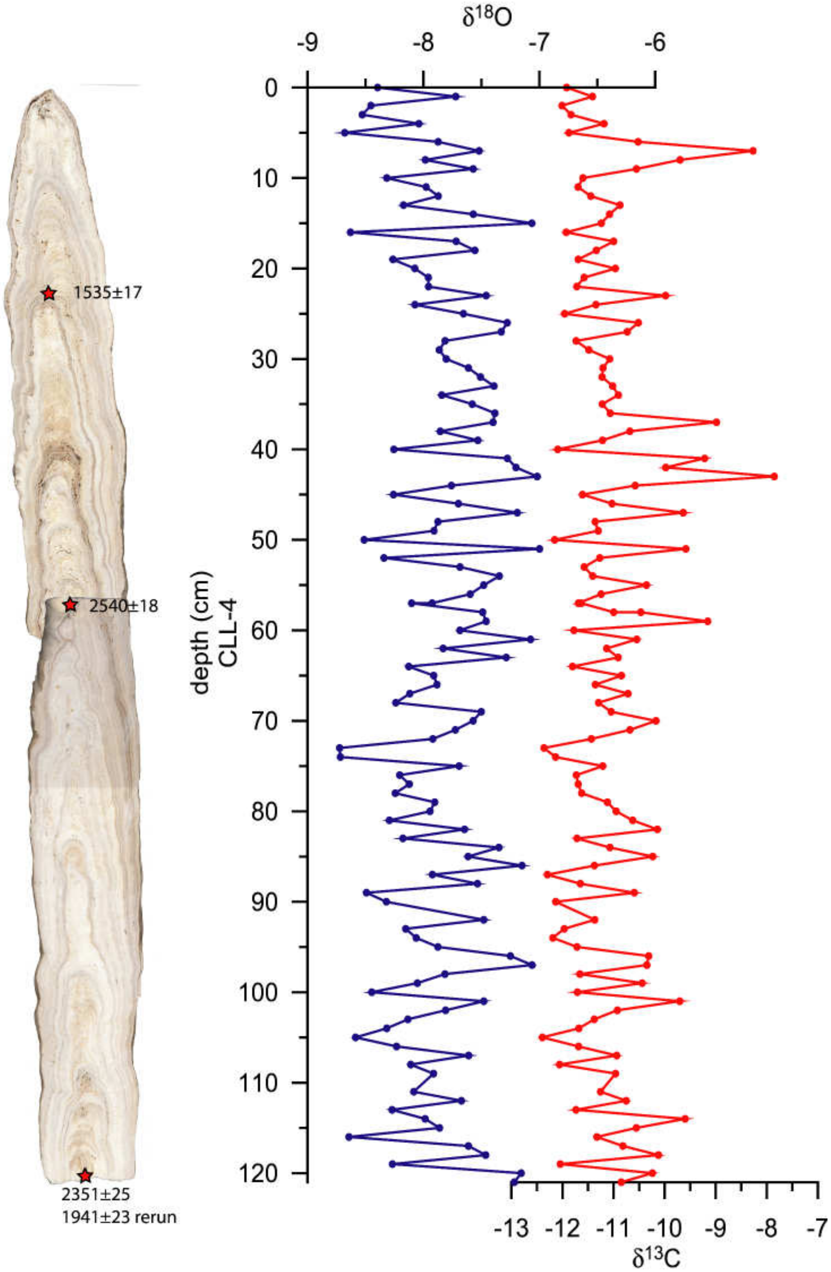
δ18O
-9
-8
-7
-6
0
10
20
30
40
50
60
70
80
90
100
110
120
depth (cm)
CLL-4
-13
-12
-11
-10
-9
-8
-7
δ13C
1535±17
2540±18
2351±25
1941±23 rerun

CLL-5

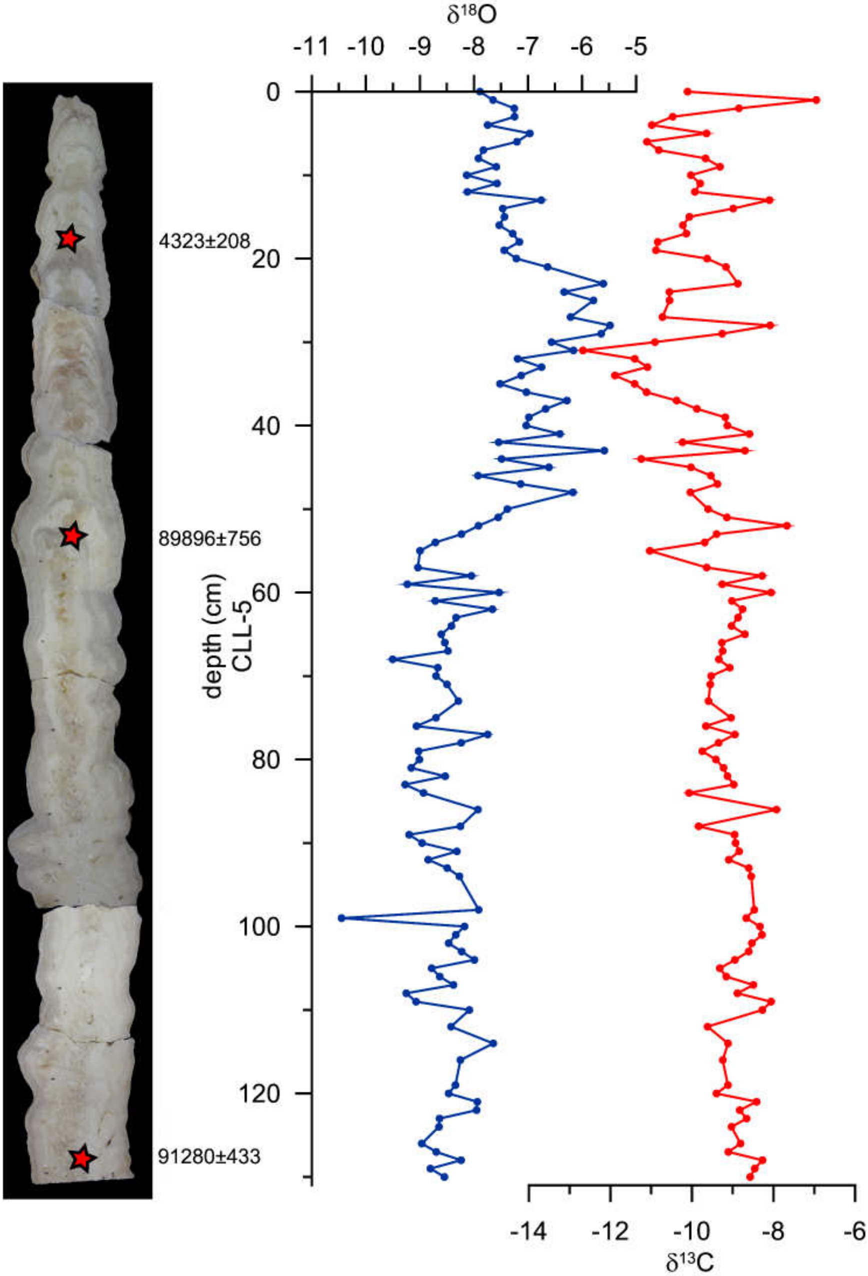
δ18O
-11
-10
-9
-8
-7
-6
-5
0
20
40
60
80
100
120
depth (cm)
CLL-5
4323±208
89896±756
91280±433
-14
-12
-10
-8
-6
δ13C

HUA-6

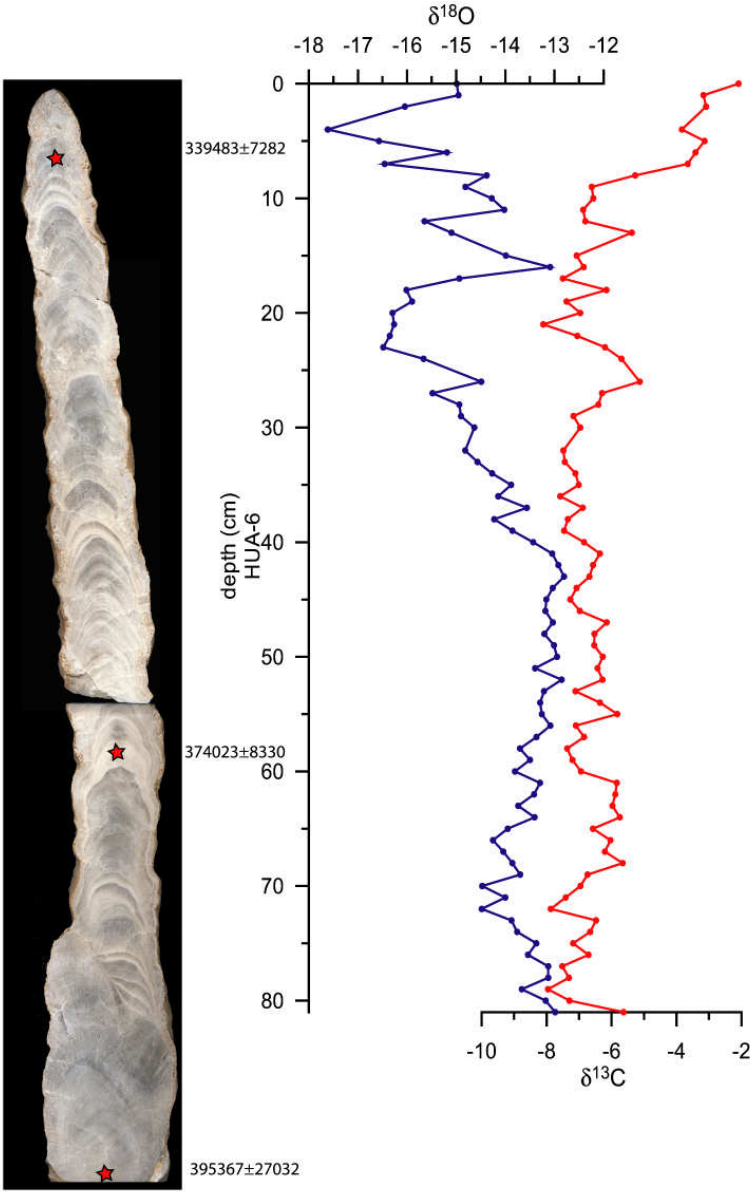
339483±7282
374023±8330
395367±27032
δ18O
-18
-17
-16
-15
-14
-13
-12
depth (cm)
HUA-6
0
10
20
30
40
50
60
70
80
-10
-8
-6
-4
-2
δ13C

HUA-7

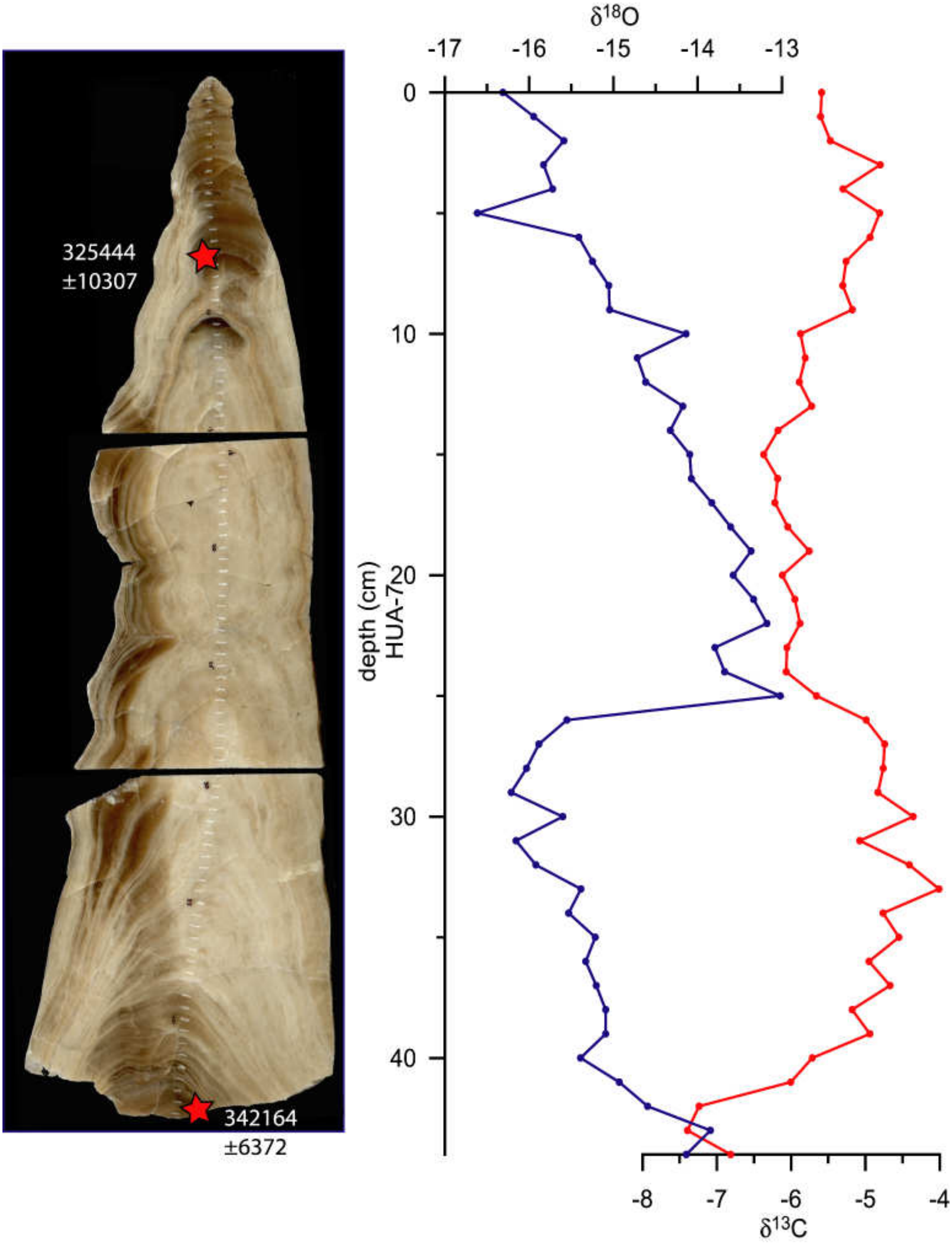
325444
±10307
342164
±6372
δ18O
-17
-16
-15
-14
-13
0
10
20
30
40
depth (cm)
HUA-7
-8
-7
-6
-5
-4
δ13C

HUA-8

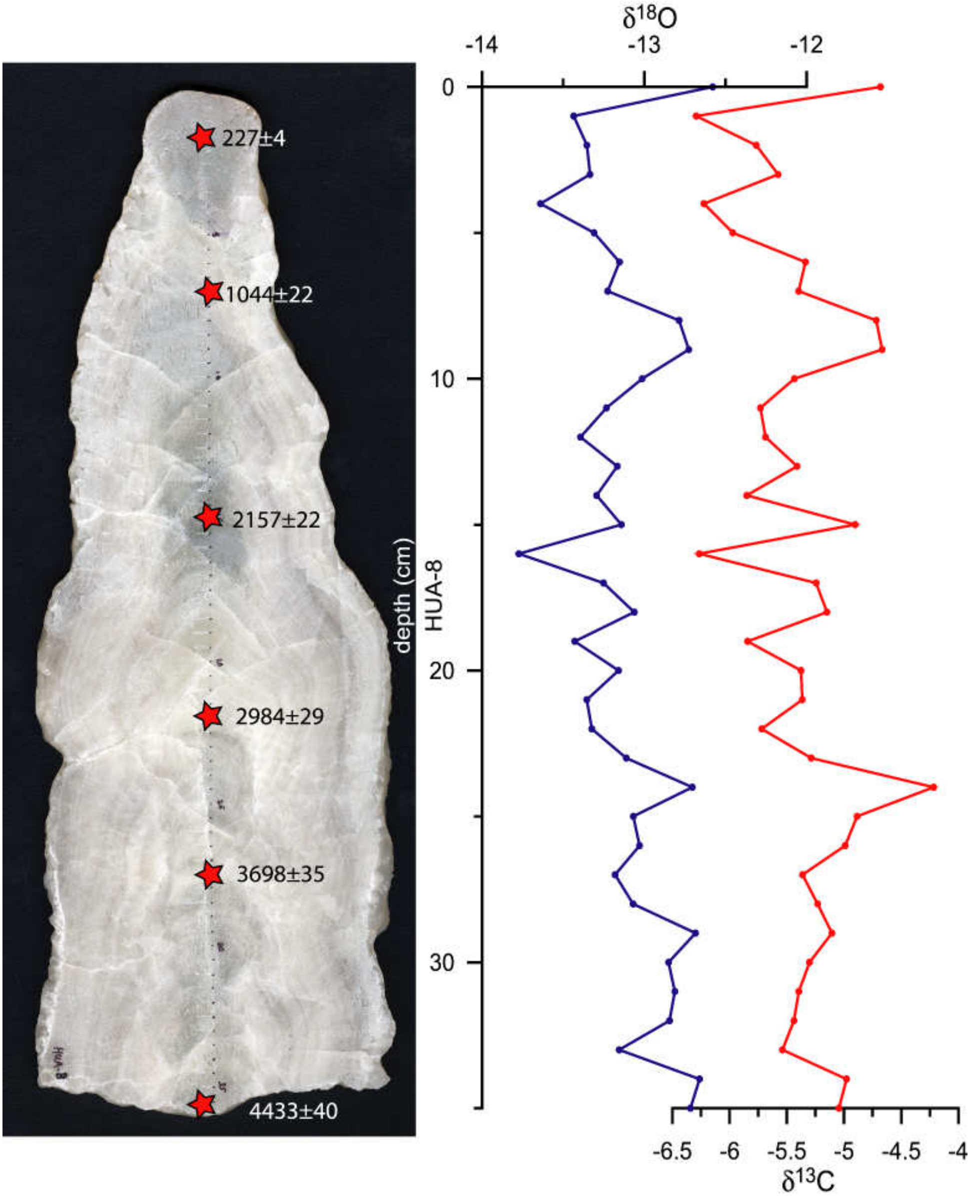
227±4
1044±22
2157±22
2984±29
3698±35
4433±40
HUA-8
δ18O
-14
-13
-12
0
10
20
30
depth (cm)
HUA-8
-6.5
-6
-5.5
-5
-4.5
-4
δ13C

NC-A

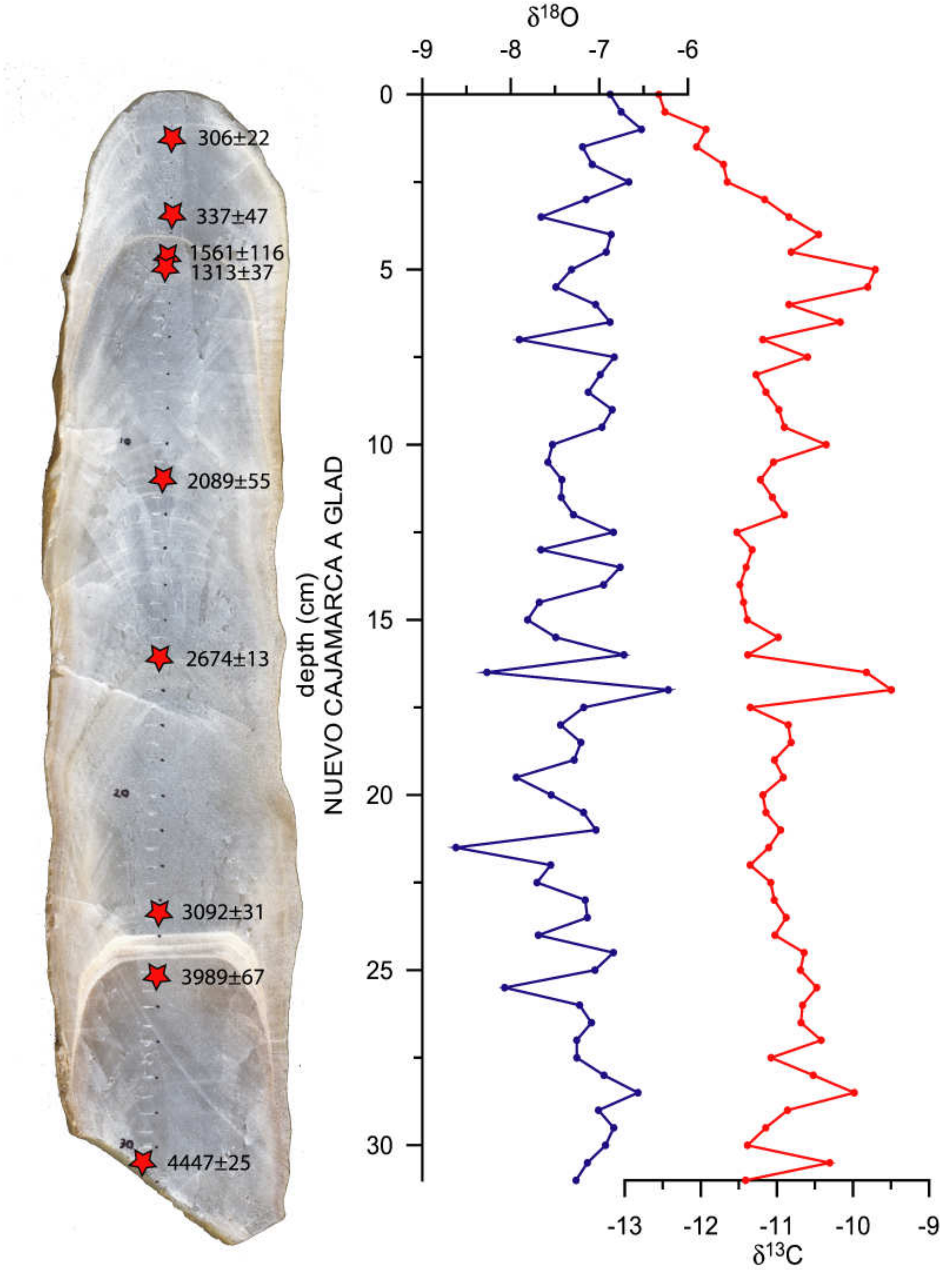
306±22
337±47
1561±116
1313±37
2089±55
2674±13
3092±31
3989±67
4447±25
10
20
30
δ18O
-9
-8
-7
-6
0
5
10
15
20
25
30
depth (cm)
NUEVO CAJAMARCA A GLAD
-13
-12
-11
-10
-9
δ13C

NC-B

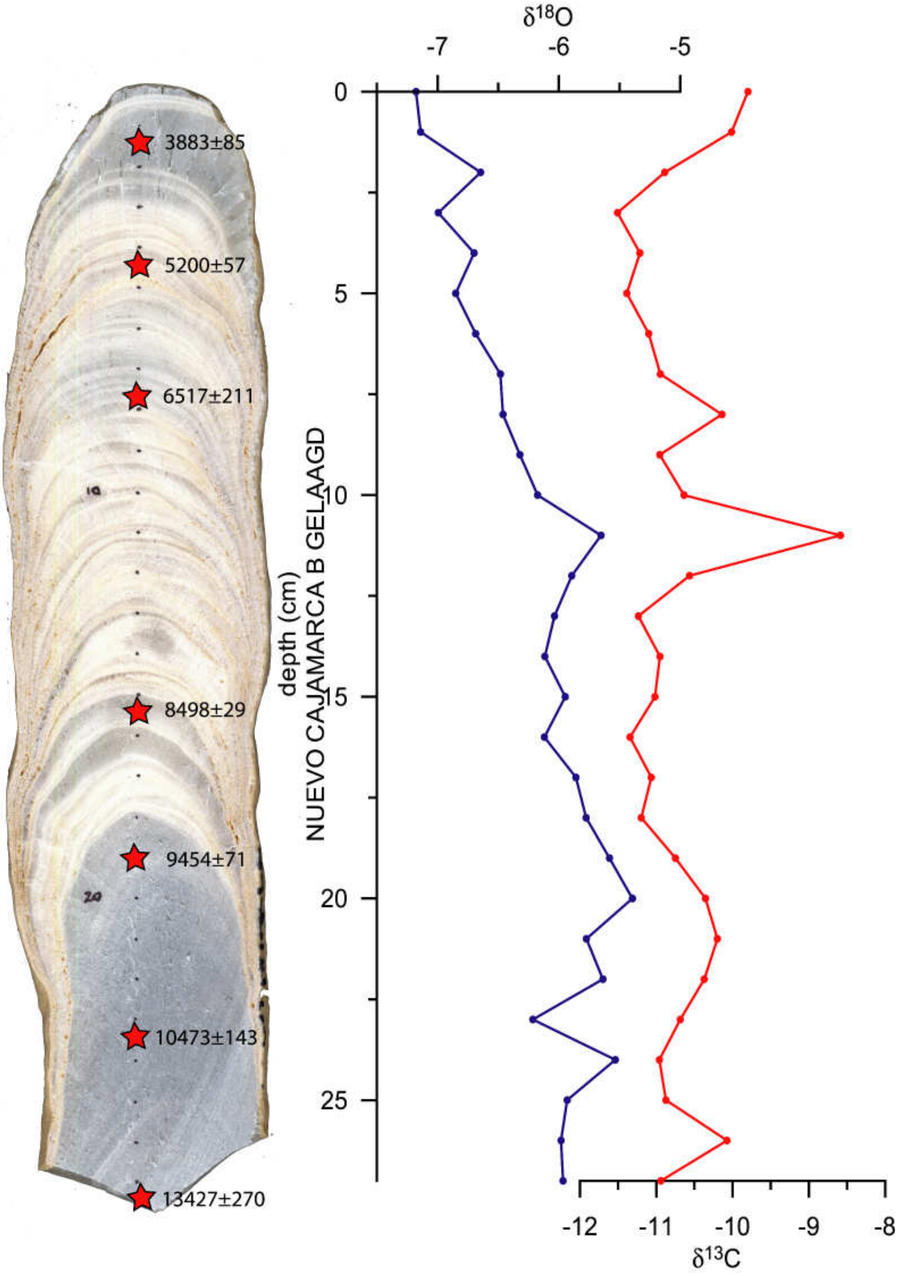
3883±85
5200±57
6517±211
10
8498±29
9454±71
20
10473±143
13427±270
$\delta^{18}O$
-7
-6
-5
0
5
10
15
20
25
depth (cm)
NUEVO CAJAMARCA B GELAAGD
-12
-11
-10
-9
-8
$\delta^{13}C$

3

Seasonal environmental monitoring results from a cave in Peruvian Amazonia

Abstract

Rainfall amounts show strong variation between wet and dry season in the Amazon Basin. A monitoring experiment in a cave in Peruvian Amazonia (Cueva de las Lechuzas) was set up to record to what extent the seasonal precipitation variability influenced the cave hydrology. We monitored temperature, humidity and drip rate, and water samples for isotope and trace element analyses were taken over a one year period.

On one of the monitoring locations we recorded a stable drip rate, providing evidence for a large groundwater reservoir, which buffers seasonal variations in precipitation. At this site, seasonal stable isotope variation of drip water lies in a narrow range. However, at other sites in the cave a clear response of the water supply in the cave with outside precipitation was observed. At these sites, highly variable drip rates show the seasonal isotope composition of the rainfall.

The total set of rain and drip water analysed for this study plots on the Global Meteoric Water Line. Trace element concentrations in drip water are highly variable, and partially support the division into two drip rate regimes.

This chapter is based on: van Breukelen, M.R., Vonhof, H.B., Romero-Pittman, L., Kroon, D., Lagos Marnique, A., Mariani, S. (Submitted) *Hydrological Processes*

3.1 Introduction

Speleothems are increasingly recognized as high resolution, continental proxy recorders for climate change (Bar-Matthews et al., 2000; Cruz et al., 2005a; Genty et al., 2003; Linge et al., 2001; Spötl and Mangini, 2002; Wang et al., 2001). Speleothems dated using the U/Th dating technique provide a precise and independent age framework (Richards and Dorale, 2003). In addition to their precise dates, speleothems have a wide geographical distribution and they can provide long, high resolution records, which make them particularly useful as continental paleoclimatic records (Fairchild et al., 2006b; McDermott, 2004).

Speleothems consist of calcium carbonate precipitated from cave seepage water. Cave seepage water is directly linked with outside precipitation as the cave hydrological reservoir is usually recharged by meteoric water. δ^{18}O values of speleothems therefore record the climate processes that affect rainwater isotopic composition, when deposited under isotopic equilibrium conditions. However the δ^{18}O signal of speleothem carbonate is not straightforward to interpret, because temperature dependent δ^{18}O water-calcite fractionation may counterbalance the δ^{18}O variation of the seepage water (McDermott et al., 2006). To understand the paleoclimatic information recorded in the δ^{18}O of the speleothem carbonate it is necessary to unravel the factors that contribute to the δ^{18}O signal. Cave temperature and δ^{18}O composition of the cave seepage water are the dominant factors controlling the δ^{18}O signal in the speleothem when deposited under isotopic equilibrium conditions. For caves of intermediate depth seasonal temperature variations are likely to be smaller than 1°C (Wigley and Brown, 1976), suggesting that the seasonal δ^{18}O signal in the speleothem is mainly controlled by the isotopic composition of the cave seepage water and/or by seasonally varying isotopic disequilibrium controlled by degassing in response to driprate. On interannual time scales, however, temperature in the caves follows the mean annual surface temperatures.

As cave seepage water is directly fed by meteoric water, which in Amazonia has a significant difference in isotopic composition between the wet and dry season, knowledge of the hydrological recharge conditions and outside rainfall patterns are fundamental to understand the speleothem δ^{18}O record (Ayalon et al., 1998; Cruz et al., 2005b; Gat, 1996). Previous studies provide records of δ^{18}O values of cave seepage water which remain constant throughout the year, with δ^{18}O values close to the mean weighted average of the outside precipitation (Caballero et al., 1996; Yonge et al., 1985; van Beynen and Febbroriello, 2006). The residence time of the percolating water is then long enough for sufficient mixing to prevent seasonal variation in the δ^{18}O seepage water.

Other studies reveal speleothem material providing high resolution (<1 year) records often visually recognized as annual or quasi-annual layering (Baker et al., 1998; Baker et al., 1993; Brook et al., 1999; Frappier et al., 2002; Genty et al., 2001b), indicating direct response to seasonal precipitation outside, which in turn suggests relatively small hydrological reservoirs.

The resolution of the climate signal recorded in speleothem calcite is therefore often directly related to cave aquifer characteristics (Cruz et al., 2005b). For this reason, several monitoring experiments have already been carried out to investigate the relationship between seepage water and outside climate (Baker and Brunsdon, 2003; Baldini et al., 2006; Fairchild et al., 2000; Fernández-Cortés et al., 2007; Genty and Deflandre, 1998; McDonald and Drysdale, 2007; Sondag et al., 2003; van Beynen and Febbroriello, 2006). The present monitoring study in the Cueva de las Lechuzas in Peruvian Amazonia is carried out to investigate the seasonal dynamics of cave hydrology in one of the wettest areas of the world. This region is typified by large seasonal variation in precipitation amounts (figure 3.1) and associated isotopic composition of the rainwater.

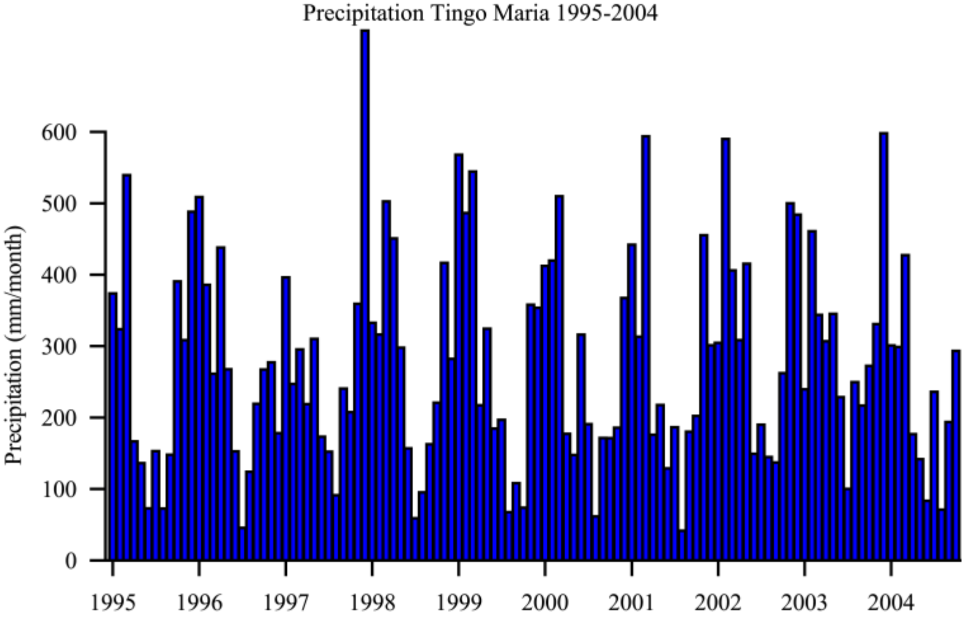

Figure 3.1: Rainfall data from the Tingo Maria meteorological station for 1995-2004. The seasonal dry and wet period are clearly visible in the amount of precipitation.

3.1.1 Cueva de las Lechuzas

Cueva de las Lechuzas is located in the foothills of the Andes close to the town of Tingo Maria at 700 meter altitude (S 09°1'44.4'', W 76°01'37.5''). This cave is in one of the wettest parts of the Amazon basin with up to ~3900mm of annual rainfall (figure 3.1). Karst systems are developed within the Late Triassic limestone of the Grupo Pucará. The cave entrance is located in a very steep cliff face developed by down cutting of the rivers Río Monzón and Río Huallaga. Above the cave, a densely vegetated and gently sloping karst plateau supplies the water recharging the karst system of this cave. The climate is tropical, with a mean annual temperature of 24.7°C.

Cueva de las Lechuzas is located in the National Park 'Tingo Maria', the second oldest National park in Peru. The cave is at least 500 meters long with a vertical displacement of more than 150 meters (figure 3.2). Hall 1 (entrance Hall) of Cueva de las Lechuzas is 25 meters high and open for tourists. Hall 1 is 300m long and the floor is covered with guano from guácharos (*Steatornis caripensis*) and bats. During our exploration of the cave in 2003, several new galleries and several new Halls were discovered, with abundant active speleothem formations. The cave was mapped as far as we explored it. Monitoring equipment was placed in Halls 1, 3 and 5 (figure 3.2).

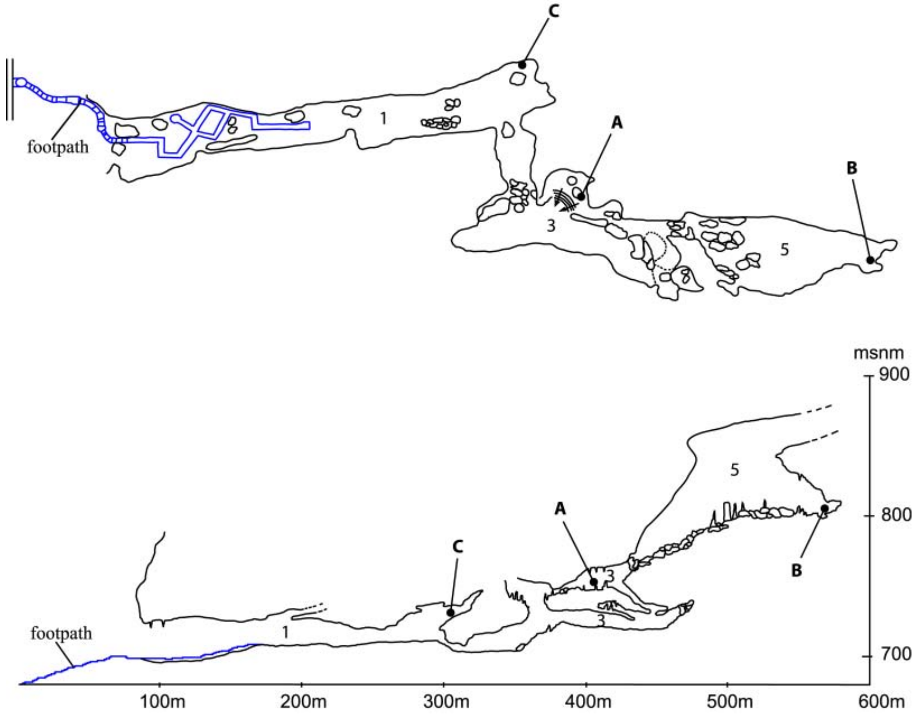

Figure 3.2: Map of Cueva de las Lechuzas. Top view and stretched side view. The wooden touristic footpath is indicated in the figure. Locations A, B and C represent monitoring sites discussed in the text. 1, 2 and 3 are Hall numbers as discussed in the text.

3.1.2 Seasonality and the Inter Tropical Convergence Zone

The climate system in equatorial South America is dominated by the Inter Tropical Convergence Zone (ITCZ). The ITCZ is an atmospheric low pressure zone close to the equator where the north-eastern and south-eastern trade winds converge. In South America the ITCZ has its most northern position during the boreal summer and its most southern position during the austral summer (figure 3.3; Marengo and Nobre, 2001). The ITCZ migrates as it follows the zone of maximum insolation. Due to the distribution of land masses and the tilt of the Earth's axis, solar heat is not evenly distributed, resulting in a stronger north-south displacement of the ITCZ over the seasons on the continent than above sea (Marengo and Nobre, 2001). In South America the ITCZ straddles the Andes mountain chain, which is high enough to affect atmospheric circulation patterns (figure 3.3).

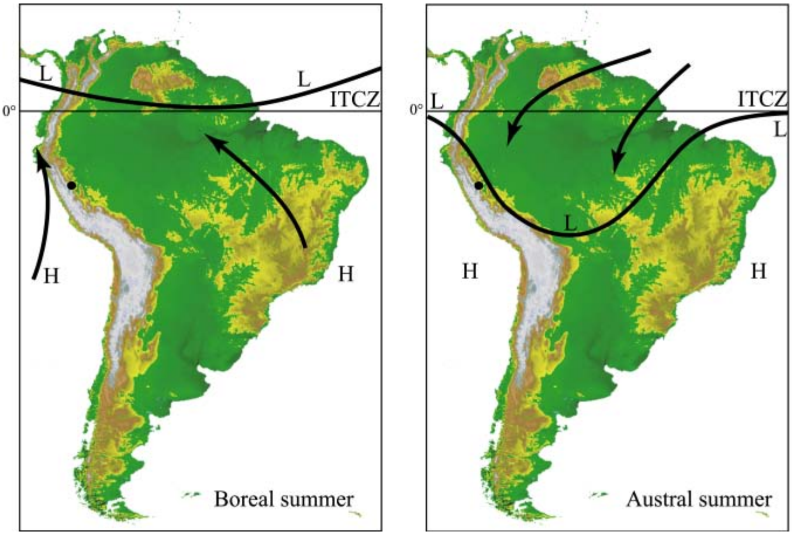

Figure 3.3: Map of South America, showing the generalized location of the Inter Tropical Convergence Zone (ITCZ) during boreal summer (July) and austral summer (January). Cueva de las Lechuzas is indicated with a black dot.

Rainfall patterns in South America are related to the position of the ITCZ. In the centre of the ITCZ, where convection is best developed, maximum amounts of convective precipitation are generated. Therefore seasonal migration of the ITCZ controls precipitation amounts, and causes the wet and dry seasons. During the wettest months in Peru (December, January and February) the amount of rainfall is on average ∼3 times higher than during the driest months (June, July, August).

During austral summer when maximum convection is best developed in its southernmost position, the Amazon basin is one of the wettest places on Earth. As Cueva de las Lechuzas is located close to the foothills of the Andes, additional orographic rainfall occurs, leading to a total annual amount of 3900 mm. The extreme seasonal variation in precipitation amounts in western Amazonia is reflected in a >15‰ seasonal difference in δ^{18}O composition of the precipitation (Grootes et al., 1989; Rozanksi and Araguás-Araguás, 1995; Tardy et al., 2005; Vuille et al., 2003).

3.2 Methods

Temperature and humidity were measured in Hall 5 for one year with a temperature and humidity recorder with 0.3°C resolution for temperature and 0.5% resolution for humidity. A second temperature and humidity recorder installed in Hall 3 malfunctioned and therefore only limited data is available. A temperature logger with 0.1°C resolution was installed in Hall 1 and recorded every hour (figure 3.4). Temperature loggers were intercalibrated in the cave, to assure that observed temperature differences are not analytical artefacts.

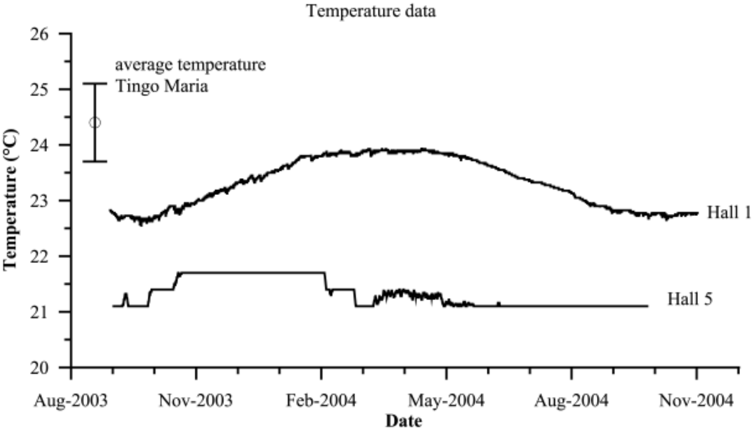

Figure 3.4: Temperature records from Halls 1 and 5. Hall 1, the entrance Hall, shows a clear seasonal variation due to exchange with the atmosphere outside the cave. Deeper in the cave lower temperatures are observed. Seasonal temperature variation in Hall 5 is lower than in Hall 1, and is not in phase with outside seasonal temperature variation.

Stalactite drip rates were measured using an automatic tipping bucket system equipped with a data logger. This tippingbucket system collects ~5.5 ml before it tips. The drip rate was continuously measured at two different locations, Hall 3 and Hall 5, over a period of 12 and 8 months respectively. Precipitation and temperature data from outside the cave is available from a local meteorological station of the Peruvian Government in the town Tingo Maria, 8km south-east of the cave at 664 meter altitude. To verify whether the precipitation data from the Tingo Maria weather station was comparable with rainfall above the cave, we placed a tippingbucket raingauge monitor system in a clearing outside the cave entrance and registered for 1.5 month the amount of rainfall close to the cave. This data set compares well to the data of the meteorological station, which leads us to consider the longer meteorological records of that station representative for the cave area (figure 3.5).

Several drip water samples were taken by park rangers between September 2003 and October 2004 to investigate seasonal variation in seepage water composition. Water samples

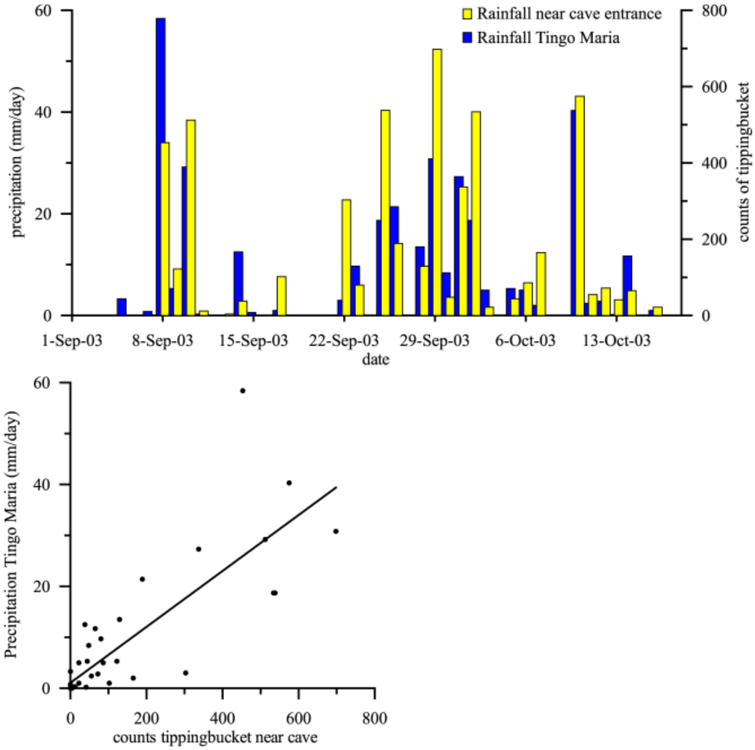

Figure 3.5: The amount of precipitation in the town of Tingo Maria in mm/day and near the cave entrance in registrations of the tippingbucket. Relative good correlation (R^2=0.688) between the two suggests that longer rainwater records from the Tingo Maria weather station are representative for rainfall near the cave.

taken for stable isotope analyses were collected in 30ml glass bottles, two drips of KI solution were added and bottles were sealed without air bubbles. Water samples for trace element measurements were collected in pre-cleaned 100ml low density polyethylene beakers using micropore filters to remove particulate matter. The samples were acidified with ten drops of concentrated suprapure HNO_3.

δ^{18}O and δ^{2}H values of the water samples were measured on a ThermoFinnigan Delta plus XP mass-spectrometer equipped with a TC-EA pyrolysis furnace and reported in ‰ versus V-SMOW. The δ^{13}C values of dissolved inorganic carbon (DIC) of the water samples were measured on a Finnigan Delta plus mass-spectrometer equipped with a Gasbench II and reported in ‰ versus (V-PDB). Long term-reproducibility of in-house water standards lies within 0.10‰ (1σ) for δ^{18}O, 2.0‰ (1σ) for δ^{2}H and 0.15‰ (1σ) for δ^{13}C.

Trace elements measurements (Ca, K, Ba, Mg, Na, Sr) were performed on a Varian Liberty Series II ICP-OES with an analytical error of 0.7-3% (1σ) depending on the solution concentration from ppm to sub-ppb. All analyses were performed at the Vrije Universiteit Amsterdam.

3.3 Results

3.3.1 Seasonal temperature and humidity variation

The temperature recorder in Hall 1 (entrance Hall) showed an average temperature of 23.3°C with a maximum variation of 1.4°C over one year. A weak seasonal cycle was recorded in Hall 1, with a maximum during April, in phase with the outside temperature variation. No day-night temperature variations were detected in Hall 1 by the logger. The temperature recorded in the cave was more than 1°C lower than the temperature of the town Tingo Maria. As Tingo Maria is located more than 50 meters lower as the cave this accounts a part of the temperature difference, but is not sufficient to explain the total offset. Deeper in the cave in Hall 5 the average temperature was 21.3°C with a maximum variation of 0.6°C over the 1-year period. This reduced temperature variation was out of phase compared to that in Hall 1 (figure 3.4). As our logger malfunctioned in Hall 3 we only have limited humidity and temperature data. During our exploration period the temperature in Hall 3 was equal to Hall 5 measured over several days in a row.

The humidity in the cave as recorded by the logger in Hall 5 was close to 100% for the first months. After this period the sensor was completely saturated with water and thus gave 100% humidity for the rest of the monitoring period. Hand measurements made with a sling psychrometer throughout the cave were consistently >96%, and thus confirmed the high values of the electronic loggers. Only close to the cave entrance in Hall 1, sling psychrometer data showed that humidity could drop to ~90%, due to exchange of cave atmosphere with outside air.

3.3.2 Drip rate

The drip rates of several stalactites were monitored to investigate the influence of outside rainfall on cave hydrology. Figure 3.6a and 3.6b show the tipping bucket records of logger A (Hall 3) and logger B (Hall 5) versus the amount of rainfall in Tingo Maria. For logger A, no correlations can be detected between the drip rate and amount of rainfall. The drip rate remains fairly constant over the year, with, what seems to be, a minor decrease in drip rate in the month March, a pattern that appears not to be influenced by seasonal changes in the amount of outside rainfall. Figure 3.6b shows the drip rate of logger B in Hall 5, located deeper in the cave. This drip rate record shows significant variation on short time scales. During wet season, December to May, the drip rate is highest at drip water fluxes of 0.052 ml/min. This seems the maximum drip rate at this location (figure 3.6b). The drip rate is lower during the dry season (June-November) with drip rates lower than 0.015 (ml/min). The rapid oscillations in the drip rate seen in the dry period are likely to be responses of the drip rate to individual rain showers. The maximum drip rate after some of the larger rain showers is reached after ~7 days (arrows in figure 3.6b).

The observations suggest that water transfer from the karst plateau above into Hall 5 is very rapid, implying that an open hydrological connection exists to the surface. The presence in Hall 5 of articulated bones of a wild boar that must have entered the cave alive and pebble sands deposited by subterraneous water flow indeed point towards subterraneous streams that connect Hall 5 to the surface. An open connection to the surface might cause sufficient air draft to explain the relative low cave temperature.

3.3.3 Stable isotopes

Cave drip water samples were collected to investigate the isotopic composition during the dry and wet season. Figure 3.7 shows hydrogen and oxygen isotope values in permil versus V-SMOW of the water samples collected in January 2002 and between September 2003 and October 2004. The range in isotope values of the cave drip water is small compared to the isotopic range of rainwater outside, which is represented by the squares in figure 3.7. The low isotope values are samples of wet season rainwater, while the high value represents a rain shower at the end of the 2003 dry season. The isotope ratio of cave water samples plot in the middle of those extremes, supposedly due to isotopic mixing of water in the cave aquifer. Drip water isotope values outside the cluster represent high drip rates (circled); they are all shifted towards higher isotope values and are probably influenced by dry season rain water as they were sampled in the dry season. All drip water samples give isotope ratios for hydrogen and oxygen that plot on the global meteoric water line.

From August 2003 to September 2004 water sampling took place at the monitoring site near location A in Hall 3. Figure 3.8 shows the isotope values of this site through the seasons. Compared with the large seasonal isotopic variation of the outside precipitation (>13 ‰) the cave seepage water is isotopically almost homogeneous. Total, seasonal isotope variation in the seepage water is close to the analytical error, therefore we interpret these data to show complete buffering of seasonal isotope variation at the monitoring location in Hall 3.

Although Hall 5 was not seasonally monitored for δ^{18}O of the drip water we expect significant seasonal variation in the δ^{18}O of the drip water in phase with the seasonal isotope variation of rainfall outside, based on the irregular drip rate changes through the seasons in Hall 5.

3.3.4 δ^{13}C of Dissolved Inorganic Carbon (DIC)

Although it was not a main target of this experiment, some of the collected drip waters were measured for δ^{13}C of DIC and are shown in figure 3.9.The δ^{13}C value of DIC in cave drip water is influenced by the relative amount of carbon dissolved from the host rock and carbon from overlaying soil. The δ^{13}C value of DIC thus is a mixed signal of soil and host rock δ^{13}C. The range of δ^{13}C values of drip water DIC is about 13‰ from approximately

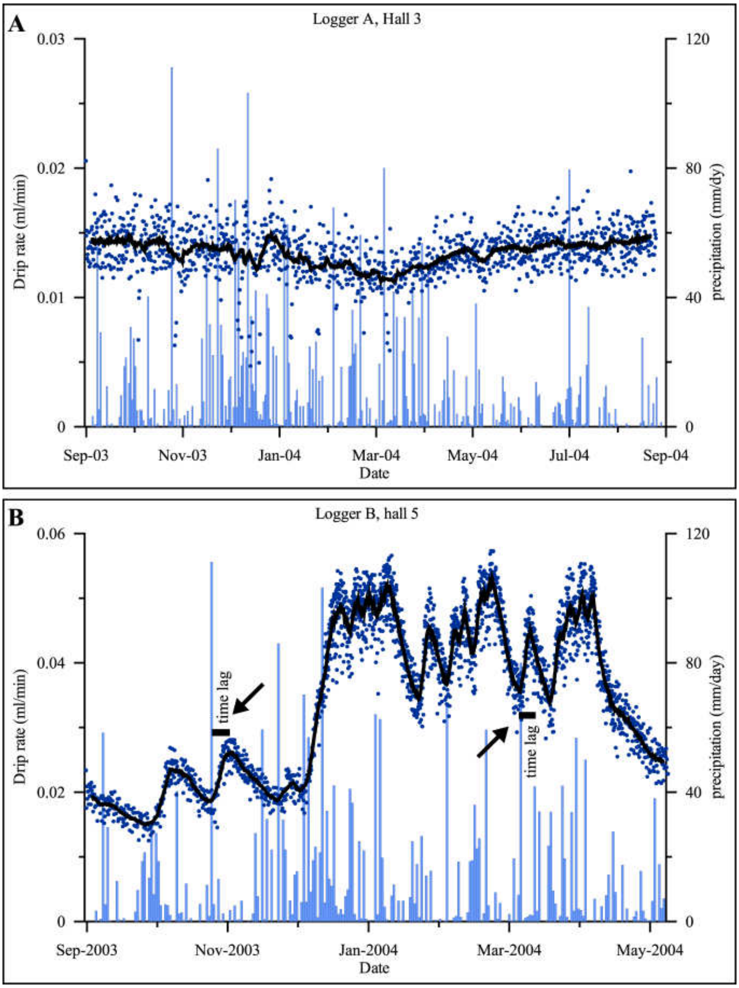

Figure 3.6: A). Logger A, installed in Hall 3 shows in dots the drip rate in mm/min. The bars indicate the daily amount of precipitation in mm recorded at the Tingo Maria weather station during the monitored period (~1-year). The black line is a 31 point running average. There is no correlation between drip rates and rainfall outside the cave. B). Logger B, installed in Hall 5 shows in dots the drip rate in mm/min. The black line is a 31 point running average. The bars indicate the daily amount of precipitation in mm during the monitored period (~8 months). Here, clear correlations exist between drip rates and rainfall outside. Generally, drip rates in wet season run up to a maximum of 0.05 ml/min. Arrows indicate what we interpret to be the response of drip rate to individual rainfall events. Data suggest that maximum drip rates are attained after ~7 days after such events.

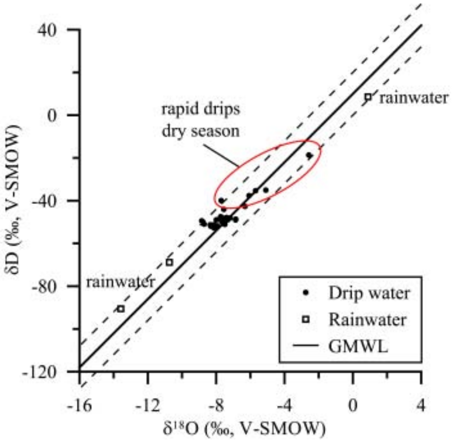

Figure 3.7: δ^{18}O and δD composition of dripwater and rainwater collected in and around Cueva de las Lechuzas (2002-2004). Black line is the GMWL. Encircled are drips from the variable drip rate regime, collected in dry season. The dashed line are representing a deuterium excess of 0 and 20‰.

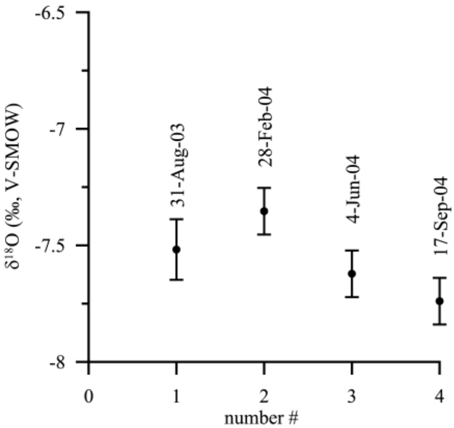

Figure 3.8: Drip water δ^{18}O composition collected at monitoring site A between August 2003 and September 2004. Total isotopic range through the seasons is close to the analytical uncertainty, suggesting efficient buffering of seasonal variation in isotope composition of rainfall recharging the cave aquifer.

-15‰ to -28‰. These low δ^{13}C values of the DIC suggest that most of the carbon comes from the soil as the host rock is a marine limestone with expected δ^{13}C values close to zero. Tropical rainforest vegetation and soils above the cave typically have δ^{13}C values between

-20‰ and -32‰ (e.g., Ehleringer and Cerling, 2002). Figure 3.9 indicates that lower δ^{13}C values of the DIC are associated with lower δ^{18}O values of the drip water. Lower δ^{18}O values are associated with higher precipitation amounts, which generally leads to a decrease of the residence time of percolating water in the aquifer. Higher percolation rates decrease water-rock interaction, which results in an increased contribution of soil carbon to the DIC of drip water.

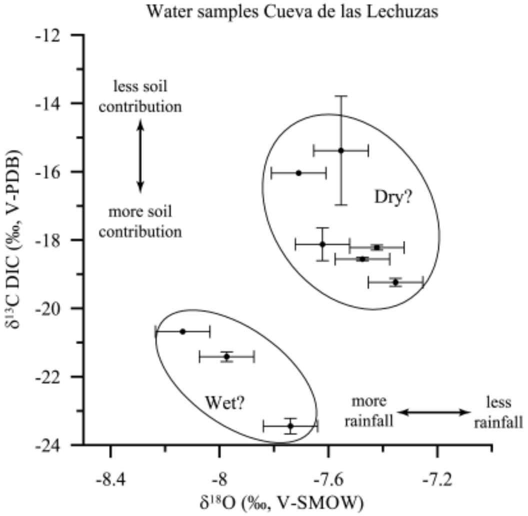

Figure 3.9: δ^{13}C DIC and δ^{18}O values of cave drip water shows two clusters that suggest that higher rainfall amounts (i.e. lower δ^{18}O values) cause lower δ^{13}C values of drip water DIC. For interpretation; see text.

3.3.5 Trace elements

Water samples collected in precleaned low density polyethylene bottles were measured for trace elements. The main cations were measured: Ca, K, Ba, Mg, Na and Sr, all showing a rather wide range of concentrations (table 3.1, figure 3.10). Figure 3.10 illustrates the trace element data classified in groups based on location. Hall 3 is further defined in a variable and stable drip rate regime. The variability of the drip rate is defined by direct observation at time of exploration and sampling of cave seepage water. Some of these drip rates are high due to direct response to rainfall above the cave and slow when rainfall stops. Figure 3.10 illustrates that the calcium concentration is relatively constant compared to the other trace elements which can vary over an order of magnitude. Sr concentrations are also comparable through the cave except for Hall 3, were the variable drips show a relative low Sr concentration. Cave seepage water samples taken from Hall 5 show significantly lower Ba and Mg concentrations than the rest of the cave. The concentration of Mg is lower than 2 ppm in Hall 5 while the rest of the cave has concentrations between 8 and 34 ppm. The amount of Ba in the drip water of Hall 5 was 6.8 ppb or lower. Low Mg and Ba concentrations seems to be related to variable drip rate regimes, as Hall 5 and the variable drips in Hall 3 have low Mg and Ba concentrations and both are expected to have relatively direct connections to the surface. Na and K concentrations are highly variable and difficult to link to a location in the cave or a specific drip rate regime.

sample	Drip rate	Ca (ppm)	K (ppb)	Ba (ppb)	Mg (ppm)	Na (ppb)	Sr (ppb)
Hall 1	variable	51	630	267.6	19.6	610	50
Hall 1	variable	29	604	11.6	14.1	580	59
Hall 1	variable	58	1432	25.3	13.6	550	51
Hall 1	variable	105	4782	28.9	33.5	1102	68
Hall 2	variable	64	2679	12.2	25.7	680	48
Hall 2	variable	62	2878	26.5	25.5	749	49
Hall 3	variable	40	5723	5.5	7.9	1365	14
Hall 3	variable	41	5965	7.0	8.2	1460	16
Hall 3 *	stable	78	4218	567.6	26.5	2192	92
Hall 3 *	stable	34	624	259.2	19.5	792	46
Hall 3 *	stable	56	1590	17.4	21.7	746	32
Hall 3 *	stable	ADL	9341	232.7	33.1	1385	75
Hall 5	variable	50	887	BDL	1.1	529	83
Hall 5	variable	35	373	BDL	0.7	406	76
Hall 5	variable	35	476	BDL	0.7	526	75
Hall 5	variable	53	1452	6.8	1.7	1340	90
Local Tapwater		78	2309	130.8	10.7	10415	642
Rio CLL	river	36	672	15.0	2.4	3201	222
Rio Perdido	river	8	552	0.0	1.6	2665	20
Sulfur lake	---	78	2711	ADL	13.8	ADL	ADL

Table 3.1: Trace element concentrations of cave seepage water collected in and around Cueva de las Lechuzas. Location indicated with a * are water samples taken at drip logger location A. BDL=Below Detection Limit, ADL=Above Detection Limit

3.4 Discussion

3.4.1 Driprate

The two monitoring sites in Cueva de las Lechuzas have similar temperature and humidity conditions. However, the results show that measured drip rate patterns for both locations are different. At location A (Hall 3) the drip rate remains stable over the measured period of 1-year with only minor seasonal cyclicity whereas at location B (Hall 5) deeper in the cave the drip rate pattern is influenced by the rainfall above the cave. This suggests that the two locations are fed by different water reservoirs. The drip rate record of location B (figure 3.6b) shows that there is a nearly direct response of drip rate, which sharply increases after periods of extensive rainfall or even in response to individual tropical showers. Drip water changes following some of the larger rain showers observed, indicate that maximum drip

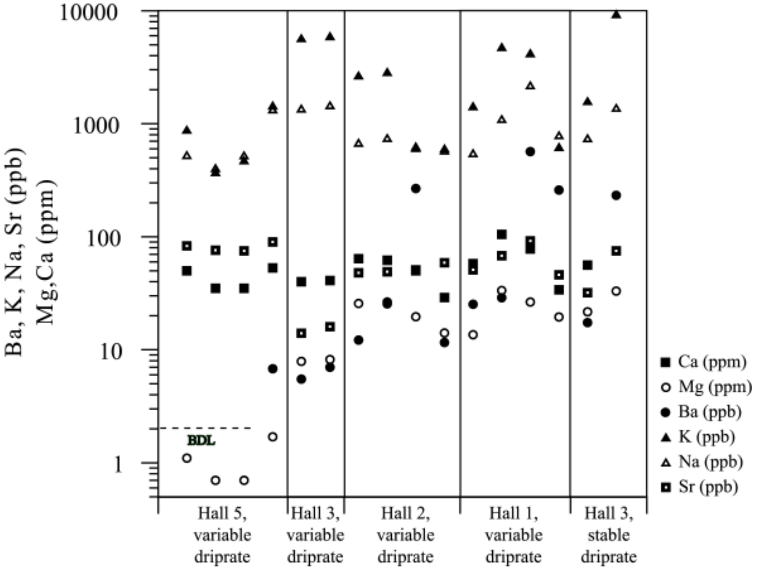

Figure 3.10: Trace element data from different location in the cave, classified on location and drip rate regime. Ca and Mg concentrations are given in ppm, while Ba, K, Na and Sr concentrations are given in ppb. Hall 5 has relative low Ba and Mg concentrations, compared to the rest of the cave drip waters.

rate after a rain shower is reached after ∼7 days (figure 3.6b, arrows). The direct influence of outside precipitation on cave seepage water is also suggested by stable isotope values (figure 3.7) of rapid drips, these tend to shift to the seasonal isotope values of rainwater at the time of collection.

Drip rate patterns are supported by observed internal structures of collected stalagmites. A stalagmite collected from Hall 5 (location B), on which the drip logger was placed shows annual lamination, indicating seasonal variation in seepage water now and in the past. Stalagmites collected from Hall 3 (location A) on the contrary do not show annual lamination (van Breukelen, unpublished data), supporting a constant supply of seepage water as suggested by the logger.

3.4.2 Stable isotopes

Oxygen and hydrogen isotope data from location A (Hall 3) cluster in a narrow range over the seasons, completely buffering the large seasonal range ($> 13‰$) of δ^{18}O in local precipitation (Grootes et al., 1989). This supports the conclusion from the drip rate data that this location is fed by a water reservoir large enough to buffer seasonal variation in δ^{18}O of rainfall and to provide a constant water supply. Although no seasonal isotope drip water record is available for Hall 5 we expect seasonal variation in the δ^{18}O of the drip water to be synchronously with the isotope variation of rainfall as the drip rate data for Hall 5 suggest a relatively direct hydrological connection to the surface.

3.4.3 Trace elements

Trace elements, pH, and stable isotopes (C, O, H) were measured, to see if we could geochemically fingerprint stable versus variable drip rates. The drip rate record and stable isotope data indicate that the two monitored locations A and B tap from different reservoirs. As the trace elements and pH are sampled for a short time interval only, the data set is limited and we only can point out general trends and relationships. The overall pH of the cave seepage water lies in a narrow range between 6.8 and 7.2. The trace element concentration of the drip water is highly variable between different drip locations (figure 3.10; table 3.1). Generally Hall 5 has a distinct water chemistry, with lower Ba and Mg concentrations than the rest of the cave, likely related to the rapid transfer of rain water into this part of the cave. Water samples from Hall 3 (table 3.1) are taken from 2 different drip rate types; 1) Slow and stable drips, and 2) Rapid and variable drips. Stable drips show a significantly higher Mg and Ba concentration than the variable drips, which is indicative for their different percolation pathway and residence time. Rapid and variable drips in Hall 3 chemically resemble drips in Hall 5, more than the stable drips in Hall 3 (figure 3.10).

According to Fairchild et al. (2000) higher Mg/Ca and Sr/Ca ratios are indicative for precipitation of carbonate from seepage water in the epikarst zone, prior to its entrance into the cave. The amount of prior carbonate precipitation increases with longer residence time of the percolating water in the epikarst zone, which results in relative higher Mg and Sr concentrations in cave drip water as Ca concentrations show little variation.

The hydrology of this cave can thus be divided in two general regimes. The rapid variable drips show an almost direct response to rainfall and have low Ba and Mg concentrations, in line with a short residence time of percolating drip water. The stable drips represent the longer residence time regime, with drip rates that buffer variation in rainwater supply above the cave, little seasonal δ^{18}O and δ^{2}H variation, and generally higher Mg and Ba content.

It must be noted that this concerns a generalized subdivision only, which does not necessarily hold on the level of single drips. The rather large ranges of drip water trace element concentrations at hand show that there is significant contribution of factors other than percolation rate on trace element concentrations. This matter needs further study based on additional cave monitoring experiments to be understood in more detail. Hall 5 for example shows extremely low Ba and Mg concentrations, also compared to variable drip rates in other Halls suggesting that variable limestone composition might be present in the cave roof.

3.5 Conclusions

A 1-year monitoring study in the Cueva de las Lechuzas shows two main drip rate regimes to occur in the cave. One regime has slow, stable drip rates throughout the year, completely buffering seasonally varying rainfall above the cave. The second regime, shows distinct seasonal drip rate variation. In this regime, drip rates even respond to individual precipitation events. Stable isotope data of all water samples from the cave straddle the meteoric water line. Most seepage water clusters at a well mixed average, but some drip water samples show isotope ratios shifted along the meteoric water line due to direct influence of seasonal rain water δ^{18}O variation. In general, drips from the seasonally variable drip rate regime have δ^{18}O and δ^{2}H values that can be shifted away from the yearly weighted mean towards the seasonal isotope value of the rain water at time of collection. Drips from the stable drip rate regime consistently show δ^{18}O and δ^{2}H values close to the yearly average value. This regime successfully buffers the seasonal variation of δ^{18}O and δ^{2}H of rainfall recharging the cave aquifer.

Trace element concentrations are highly variable, but tend to have lower Ba and Mg concentrations for drips from the seasonally variable drip rate regime, when compared to drips from the stable drip rate regime. This general difference between the two regimes is consistent with the expected difference in percolation rate between the two regimes: longer residence times of water in the epikarst zone lead to higher Ba and Mg concentrations in drip water.

However, this general subdivision based on trace element concentrations, does not necessarily hold on the level of single drips. There must be significant contribution of factors other than percolation rate on trace element concentrations, like for example the inhomogeneous chemical composition of limestone in the roof of the cave .

The variable drip rate regime is dominant in Hall 5, suggesting that a relatively direct hydrological connection to the surface exists for the entire Hall. Hall 3, on the other hand contains drip clusters in the stable drip rate regime, but also zones in which variable drips were dominant. Thus, the spatial distribution patterns of the two regimes is relatively complex, and simple spatial patterns could not be recognized easily. These observations obviously have implications for future paleoclimate studies based on speleothems records from this cave. Speleothem archives from both regimes are bound to record climatic and environmental parameters at different temporal resolution.

3.6 Acknowledgements

This project is funded by WOTRO-NWO (project nr W76-231). We would like to thank Instituto Geológico Minero y Metalúrgico (INGEMMET) and Instituto Nacional de Recursos Naturales (INRENA) for the given opportunity to explore Cueva de las Lechuzas. A special thanks is for the caving team, Quinto Quaresima and Elisabetta Ferroni. Ing. Maria del Carmen (INGEMMET) is thanked for her logistical help during our stay in Peru. Ing.

Fernando Mejía Vargas (INRENA) and his team collected the cave water samples. Susan Verdegaal and Nel Slimmen are thanked for their help with the analyses of stable isotope ratio and trace element concentrations performed at the Vrije Universiteit Amsterdam.

4

A continuous-flow crushing device for on-line δ^2H analysis of fluid inclusion water in speleothems

Abstract

A method for the isotope analysis of fluid inclusion water in speleothem calcite is presented. The technique is based on a commercially available continuous-flow pyrolysis furnace (ThermoFinnigan TC-EA). The main adaptation made to the standard TC-EA configuration is the addition of a crusher and cold trap unit, which is connected to the carrier gas inlet at the top of the TC-EA reactor tube. A series of tests conducted with this device shows that: (1) standard waters, injected in the crusher, and passed through a cryogenic trapping routine, yield accurate δ^2H values; (2) crushed cubes of speleothem calcite from two Peruvian caves with rather dissimilar seepage water δ^2H values yield fluid inclusion δ^2H values in good accordance with these drip waters. The clear advantage of this continuous-flow technique for fluid inclusion isotope analysis is that it is relatively quick compared with other techniques. Since the conditions of water sample introduction into the TC-EA are identical for δ^2H and δ^{18}O analysis, we expect that only limited adaptations to the extraction procedure are required to provide δ^{18}O analysis of fluid inclusion samples with the same device.

This chapter is based on: Vonhof, H. B., van Breukelen, M. R., Postma, O., Rowe, P. J., Atkinson, T. C. Kroon, D. (2006). A continuous-flow crushing device for on-line δ^2H analysis of fluid inclusion water in speleothems. *Rapid Communications in Mass Spectrometry*, 20(17):2553-2558.

4.1 Introduction

In recent years, high-resolution oxygen and carbon isotope analysis of calcite speleothem (stalagmite) has rapidly gained importance as a tool for climate reconstruction (e.g. Bar-Matthews et al., 1999; Wang et al., 2001). The precise dates that can be obtained on these records using the U-Th technique potentially enable very high chronostratigraphic resolution, particularly when specimens show annual lamination (McDermott et al., 2006).

In addition to investigating the isotopic composition of calcite, various groups have investigated the potential of fluid inclusions to provide direct measurements of the isotope composition of paleo-meteoric water. All previous work relied on crushing and/or thermal decrepitation to release inclusion water for preparation and analysis by dual inlet mass spectrometry. This paper describes the first application of continuous-flow mass spectrometry to this problem, allowing the crushing of samples on-line, and the accurate and rapid measurement of δ^2H in the released water.

Early work on speleothem fluid inclusions yielded promising results for δ^2H analyses (Goede et al., 1986; Harmon et al., 1979; Rozanksi and Dulinski, 1987; Schwarcz et al., 1976). For δ^{18}O analysis, however, it proved very difficult to produce data in accordance with the local seepage water composition, which led to the widely held assumption that fluid inclusion water exchanged oxygen with the surrounding $CaCO_3$ after closure of the fluid inclusion (Schwarcz et al., 1976). For this reason, most subsequent studies focused on the analysis of δ^2H, often converted into an estimated δ^{18}O value based on the δ^2H - δ^{18}O relationship dictated by the Global Meteoric Water Line (GMWL). However, a recent study by Dennis et al.(2001) demonstrated a lack of δ^{18}O exchange effects in a Holocene stalagmite, for which fluid inclusion data (obtained by crushing and heating) plotted on the GMWL and matched cave drip waters.

Previous studies have involved off-line preparation by one of two groups of techniques - crushing at various temperatures, and thermal decrepitation at much higher temperatures with varying degrees of decomposition of the calcite. Many studies adopted thermal decrepitation because of the higher yield of water compared to crushing. However, decrepitation often results in 20-30 permil offset of the δ^2H value below that of the associated seepage water (Goede et al., 1986; Matthews et al., 2000; McGarry et al., 2004; Yonge et al., 1985). Opinions vary on the cause of the offset, which is probably an analytical artefact, (Matthews et al., 2000; McGarry et al., 2004; Verheyden et al., 2005) but might also reflect the presence of an isotopically fractionated pool of water in very tiny inclusions or on crystal boundaries. The practice has developed of compensating for the offset on the assumption that it is constant for a specific location (Goede et al., 1986; Matthews et al., 2000; McGarry et al., 2004). Interestingly, offsets differ between labs, and some decrepitation studies show no offsets at all (Schwarcz and Yonge, 1983; Verheyden et al., 2005).

The original technique of crushing (Harmon et al., 1979; Schwarcz et al., 1976) was re-investigated by Dennis et al. (2001). Their data suggest that earlier problems with the analysis of fluid inclusion δ^2H and δ^{18}O values were caused by incomplete recovery of extracted water. They successfully measured δ^{18}O and found that there was no evidence for post-depositional exchange of oxygen between fluid inclusion water and the surrounding calcite. Their recommended method was to heat the crushing cell and associated vacuum line to 150°C and to minimize possible adsorption surfaces for water in the system. Several subsequent studies (Fleitmann et al., 2003b; Serefiddin et al., 2004) have used this technique successfully. Although these recent studies show that clear progress has been made in improving the analytical methods, fluid inclusion extraction techniques remain rather time consuming, and this has limited the routine application of this technique in speleothem-based paleoclimatological studies until now.

In recent years, advances in continuous-flow mass spectrometry have provided new techniques for the analysis of sub-microliter amounts of water (Eiler and Kitchen, 2001). Particularly promising is the development of on-line pyrolysis techniques that allow for the rapid analysis of δ^2H and δ^{18}O of a single sample (Gehre et al., 2004; Sharp et al., 2001). These techniques are quick, because they do not require high vacuum (which reduces waiting time after sample exchange); nor do they require time-consuming reduction or micro-equilibration procedures.

The present paper describes the first application of this continuous-flow pyrolysis technique to speleothem fluid inclusion analysis. For this purpose, we have constructed a crusher and cold trap unit which operates in a 90 mL/min flow of helium and is connected to the carrier gas inlet at the top of the reactor tube of a standard Finnigan TC-EA pyrolysis furnace (figure 4.1). After cryogenic capture of the water released after crushing, the cold trap can be flash heated to release the water in a short pulse into the TC-EA reactor for analysis. The design of this 'Amsterdam Device', and the results of several fluid inclusion crushing experiments, are described below.

4.2 Design of Device

The Amsterdam Device is constructed around a manual crusher, made of a modified 8BG vacuum valve (figure 4.1(A)). The valve plunger is fitted with a hardened steel piston, which can be lowered into the crushing chamber by turning the valve handle. The steel base plate can quickly be connected and disconnected to the top part of the crusher, for easy sample exchange. A gas-tight connection is achieved by bolting the two parts together, sealed with a 48-mm diameter copper ring.

The crushing chamber has a total volume of $\sim$1.5cm^3 allowing cube-shaped samples of up to $\sim$1 g to be crushed. The crusher is further equipped with a septum port that allows direct injection of sub-microliter amounts of water into the crushing chamber, using a Hamilton 1.2-μl syringe. The crusher is mounted on top of a small (160x140x115mm) oven, which contains a 250W plate heater. A second 250W (rod) heater is inserted in the base plate of the crusher. With both heaters switched on, and an insulating cover placed over the crusher, the whole system can be raised to any desired temperature in the 30-200°C range within 15 min.

Inside the oven (figure 4.1(B)), the crusher is connected to the He carrier flow, and via a

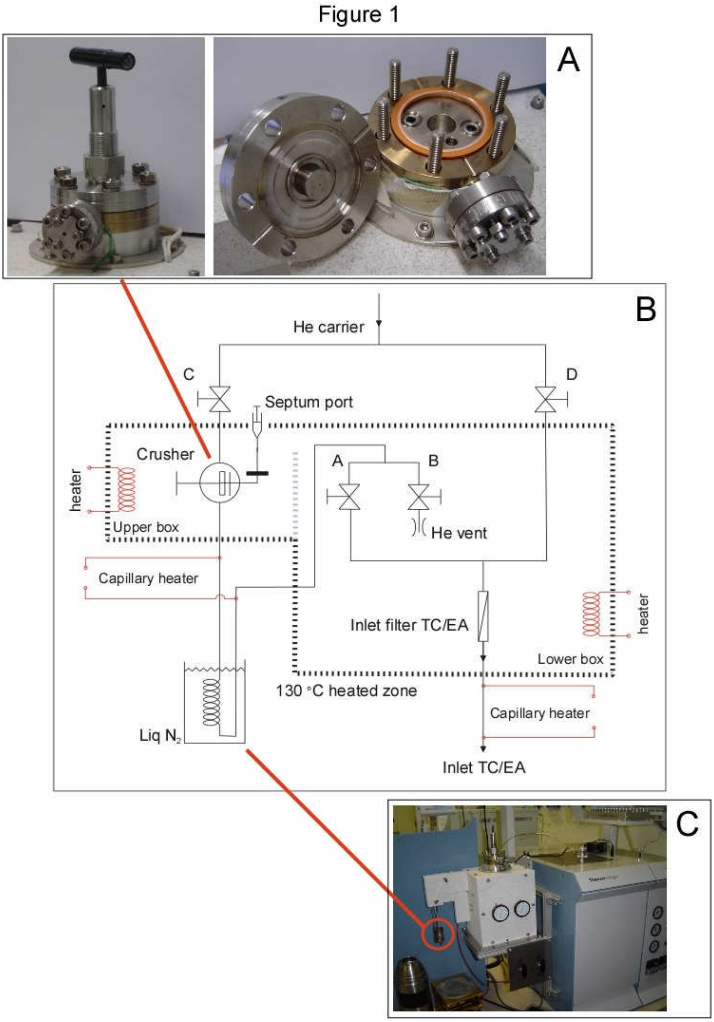

Figure 4.1: (A) Photographs of the crusher mounted on the base plate (left) and opened (right). The right photograph shows the copper sealing ring and the six screws with which the top part of the crusher can be bolted to the base plate. The cylindrical extension in front of the crusher is the septum port for direct injection of water samples into the crusher chamber. (B) Schematic of the Amsterdam Device. The part of the device that can be heated (inside the oven) is enclosed by a rectangular-shaped dotted line. The dotted line drawn around the crusher itself represents the insulating cover that can be placed over the crusher unit on top of the oven. (C) Photograph of the Amsterdam Device as it is connected to the ThermoFinnigan TC-EA. To the left of the device, the cold trap is visible (in the circle). Note that the insulating cover is not shown in this photograph.

cold trap to the TC-EA, with 0.75mm i.d. annealed stainless steel capillary and Swagelock connectors. Two (heat-resistant) Swagelock SS-4BG-VD valves are applied in the oven (valves A and B). For the two valves outside the oven (valves C and D) we used Swagelock SS-42-S4.

4.2.1 Connection to the TC-EA pyrolysis furnace

The Amsterdam Device is connected to the standard inlet of He carrier gas at the top of the TC-EA reactor. Four valves control the He flow through the device, which can be switched in two modes: The default mode is the bypass mode for conventional automatic analyses on the TC-EA system. This mode (with valves A and C closed and D open) leads a 90 mL/min He carrier flow directly to the TC-EA and allows the crusher to be opened and cleaned without any interference with TC-EA functionality. The crusher mode (valves A and C open, valves B and D closed) leads the 90 mL/min He flow through the crushing chamber and cold trap, before entering the TC-EA. This mode is applied for analyses involving crushing or direct injection in the crusher via the septum port. With valves B, C and D open and valve A closed, a reduced (~5 mL/min) flushing flow can be sent through the crusher chamber and cold trap while the system is in bypass mode. This allows for He flushing of the crushing chamber after placement of a new sample, without risk of contamination of the mass spectrometer.

4.2.2 Cold trap and flash heater

A cold trap, made of 1 m of coiled 0.75mm i.d. stainless steel capillary (12 coils of 25mm diameter), is connected to the outlet capillary of the crusher chamber (figure 4.1(C)). The trap is positioned outside the furnace so that it can be immersed in liquid N_2 to trap water carried in the He flow. To rapidly heat up the frozen sample and quantitatively transfer it to the TC-EA, the cold trap and associated capillaries that run from the crusher outlet to the TC-EA inlet are spanned by a capillary heater, which serves to flash-heat the 1/16″ steel capillary to ~200°C by means of a 16A 7.7V electrical current. In this way, the complete length of capillary between the crusher and the TC-EA is kept at >130°C when the samples pass through.

4.3 Results

4.3.1 Isotope measurement procedure

Having set the Amsterdam Device at a temperature of 130°C, we tested for the trapping efficiency of the cold trap and possible fractionation during the cryogenic trapping and release procedure by repeated injection of ~0.25mL amounts of standard water through the septum port of the crusher. On-line monitoring of m/z 2 after injection of a sample while the cold trap was immersed in liquid N_2 showed no detectable increase in background values, suggesting that the cold trap is sufficiently efficient at 90 mL/min carrier flow. Several tests with the flash-heating procedure showed that rapid and quantitative release of sample was best achieved by immersing the deep-frozen cold trap in warm water for 1 s before switching on the capillary heater.

Subsequently, we tested the contribution of background H_2O present in the carrier He (grade 5.0) that accumulates in the cold trap at different freezing times. At a 1-h freezing time (as applied by Dennis et al. 2001) the background builds up to >15% of the sample signal. At an observed δ^2H value of ~-80‰ (Standard Mean Ocean Water, SMOW) of background water, this would significantly influence the isotope composition of fluid inclusion analyses as presented here. At 5 min freezing time, the background contribution is less than 2% of the sample signal, which has a negligible effect on the isotope composition of fluid inclusion samples.

Repeated injection experiments with ~0.25μl of AMSLW 2004 standard water applying 5 min freezing at liquid N_2 temperatures resulted in isotope values within error of the values for the same water run automatically on the TC-EA (table 4.1). This provides support for the negligible background contribution discussed above, and furthermore suggests that no significant fractionation occurs in the Amsterdam Device with a crusher chamber temperature of 130°C, a carrier flow of 90 mL/min, 5 min cryo-trapping under liquid N_2 temperature and subsequent flash-heating of the cold trap to release the sample via the standard carrier flow inlet into the TC-EA. A typical isotope trace of a standard water sample, injected in the crusher, and processed in this manner is given in figure 4.2(a). Figure 4.2(b) shows an isotope trace of a water standard that was directly injected into the TC-EA following the standard automatic run procedure.

4.3.2 Fluid inclusions analysis set-up and results

At this point, a first fluid inclusion crushing experiment was designed with two possible complications in mind, which are: (1) the well-documented memory effect that occurs in the TC-EA and possibly also in the Amsterdam Device, and (2) possible fractionation of fluid inclusion water due to adsorption to the fresh calcite surface of the crushed fluid inclusion sample (Dennis et al., 2001).

The memory effect was minimised by preceding the fluid inclusion measurements by two injections in the crusher of standard water of an isotope composition similar to the fluid inclusion water. After crushing and analysis of the fluid inclusion water, we then injected one more standard water sample into the crushing chamber to see if the presence of freshly crushed calcite in the crushing chamber had an effect on the standard water isotope value. In this scheme each fluid inclusion analysis requires a sequence with three additional standard water analyses. Efficient operation allows for up to eight of these sequences to be run on an average working day.

For the first experiment we cut six (~0.5 g) cubes from a single growth layer of a sub-recent stalagmite-top from the Cueva de las Lechuzas (Peruvian Amazonia; altitude ~750 m),

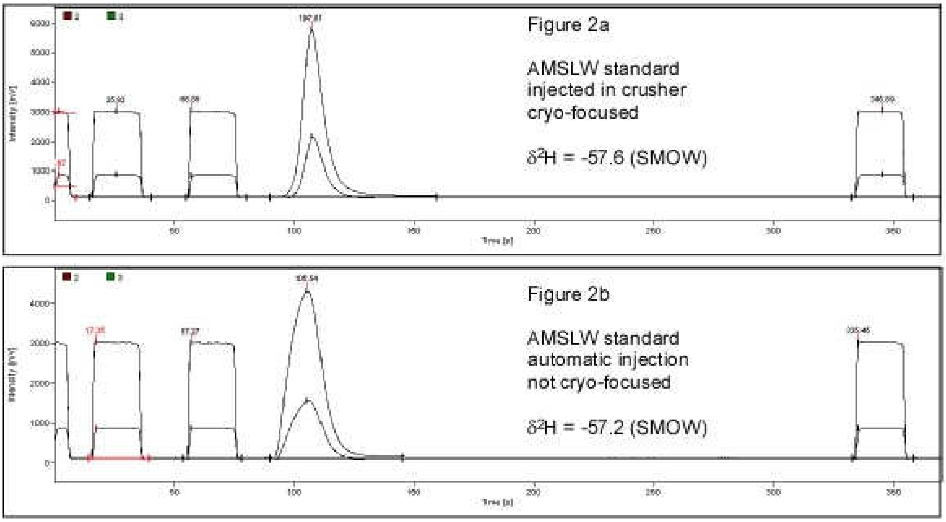

Figure 4.2: (A) The signal intensity trace of m/z 2 and 3 for a 0.25 μl sample of AMSLW standard water injected in the crusher, cryogenically captured and released by flash heating before analysis. (B) The signal intensity trace of m/z 2 and 3 for a 0.25 μl sample of AMSLWstandard water automatically injected into the TC-EA reactor. The relatively narrow sample peak in (a) and the close match of δ^2H values for automatic injections and cryogenically captured samples (table 4.1) indicate quick and quantitative sample transfer when applying the extraction routine described in this paper.

whose isotope composition of modern cave seepage water is known. Samples were analysed as in the previously outlined procedure. The average δ^2H value of -41.6‰ (SMOW) for these fluid inclusion samples (table 4.2) is in good agreement with seepage water values (which average -40.3‰ for that part of the cave), and, at a standard deviation of 1.5‰, replicate fluid inclusion analyses have a reproducibility which is similar to that of the standard water injections. This observation, supported by overlapping values of standard water injections before and after crushing, suggests that no significant adsorption of water on the crushed calcite takes place at a crusher temperature of 130°C.

A second set of fluid inclusion samples was taken from a stalactite of the Cueva Huagapo (Peruvian highlands; altitude ~4000 m), with much more depleted drip water isotope values (δ^2H =-112.0‰ (SMOW)) compared to that of the Cueva de las Lechuzas. For this set of samples we could not cut from a single growth layer, so a larger isotope variation between samples must be expected. The Huagapo samples were analysed as in the previous experiment, enveloped by water sample injections of comparable isotope composition. Isotope values again show good agreement between the seepage water value and the average fluid inclusion composition of this stalagmite (table 4.3), which indicates that the Amsterdam Device produces accurate fluid inclusion isotope values over a relatively wide range of isotope values.

	chron order	δ2H (SMOW)	δ2H (SMOW)
AMSLW2004 automatic	1	−58.0	
AMSLW2004 inj in crusher	2		failed
AMSLW2004 automatic	3	−58.2	
AMSLW2004 inj in crusher	4		−58.5
AMSLW2004 automatic	5	−56.1	
AMSLW2004 inj in crusher	6		−57.4
AMSLW2004 automatic	7	−57.3	
AMSLW2004 inj in crusher	8		−57.4
AMSLW2004 automatic	9	−57.9	
AMSLW2004 inj in crusher	10		−59.9
AMSLW2004 automatic	11	−57.0	
AMSLW2004 inj in crusher	12		−57.3
AMSLW2004 automatic	13	−57.2	
AMSLW2004 inj in crusher	14		−57.6
AMSLW2004 automatic	15	−57.6	
AMSLW2004 inj in crusher	16		−58.7
average		−57.4	−58.1
standard deviation		0.7	1.0

Table 4.1: A series of 16 analyses of AMSLW standard water. The series concerns a rotation of injections in the crusher (with cryogenic capture of the sample to be analysed) and standard automatic injections in the TC-EA reactor. The close match of δ^2H values between the two injection techniques indicates that insignificant fractionation occurs during the cryogenic trapping procedure described in this paper

4.4 Discussion

4.4.1 Isotope fractionation as an analytical artifact

Although over the last decades considerable analytical effort has been put into the isotope analysis of fluid inclusion waters, the technique still is not very widely used in paleoclimate research. This is mainly due to fractionation problems during fluid inclusion extraction and the usually rather time-consuming analytical methods that were required. Fractionation problems appear particularly persistent for thermal decrepitation extraction which commonly fractionates δ^2H more than 20‰ (Matthews et al., 2000; McGarry et al., 2004; Yonge et al., 1985). One plausible cause for this analytical artefact was recently suggested by Verheyden et al., (2005) who observed that non-complete removal of fine CaO from the crusher tubing after decrepitation would hygroscopically capture contaminant atmospheric H_2O during placement of the next sample. Verheyden and co-workers demonstrated that thorough acid cleaning of all tubing between samples largely eliminates isotope fractionation effects for the thermal decrepitation method.

For crushing cell extraction at temperatures <200°C, as described in the present paper, no CaO is produced. A small amount of fine $CaCO_3$ powder that may accumulate in the crushing cell tubing between samples is much less hygroscopic than CaO, and is likely to

		chron. order	δ^2H (SMOW) injected 1th	δ^2H (SMOW) injected 2nd	δ^2H (SMOW) crushed	δ^2H (SMOW) post-crush inj	δ^2H (SMOW) inj comb
	NTW inj in crusher	1	−49.1				
	NTW inj in crusher	2		−47.0			−47.0
0.65	crushed speleothem CLL	3			−43.0		
	NTW inj in crusher	4				−46.7	−46.7
	NTW inj in crusher	5	−51.3				
	NTW inj in crusher	6		−48.4			−48.4
0.72	crushed speleothem CLL	7			−42.1		
	NTW inj in crusher	8				−47.7	−47.7
	NTW inj in crusher	9	−50.7				
	NTW inj in crusher	10		−48.4			−48.4
0.59	crushed speleothem CLL	11			−43.0		
	NTW inj in crusher	12				−46.7	−46.7
	NTW inj in crusher	13	−50.3				
	NTW inj in crusher	14		−48.9			−48.9
0.6	crushed speleothem CLL	15			−40.4		
	NTW inj in crusher	16				−45.1	−45.1
	NTW inj in crusher	17	−49.3				
	NTW inj in crusher	18		−48.0			−48.0
0.76	crushed speleothem CLL	19			−39.3		
	NTW inj in crusher	20				−48.5	−48.5
	NTW inj in crusher	21	−54.4				
	NTW inj in crusher	22		−49.0			−49.0
0.65	crushed speleothem CLL	23			−41.5		
	NTW inj in crusher	24				−46.9	−46.9
	average		−50.9	−48.3	−41.6	−46.9	−47.6
	standard deviation		1.9	0.7	1.5	1.1	1.2

Table 4.2: Replicate δ^2H analyses of NTW standard water (injected and cryogenically focused in the Amsterdam Device) and of fluid inclusions of a series of ∼0.5 g cubes cut from a single stalagmite layer of the Cueva de las Lechuzas cave. The average fluid inclusion δ^2H value of -41.6‰ (SMOW) for this stalagmite is in good agreement with known drip water composition from this part of the cave. The analytical sequence, with two injections of isotopically similar standard water prior to crushing the sample, is set up to minimise memory effects

Sample identity	δ^2H (SMOW)
modern drip water Huagapo	−112.0
Huagapo speleothem 1	−117.5
Huagapo speleothem 2	−110.7
Huagapo speleothem 3	−115.7
Huagapo speleothem 4	−110.3
average speleothem Huagapo	−113.6
standard deviation	3.6

Table 4.3: δ^2H analyses of ∼0.5 g cubes of stalactite carbonate from the Cueva Huagapo. This cave, at an altitude of ∼3800 m, has relatively depleted fluid inclusion δ^2H values which are in good agreement with modern drip waters from the same cave. Note that since calcite cubes could not be cut from a single growth layer, isotope variation between these samples may in part be due to temporal drip water isotope variation

release any adsorbed water when the crusher system is heated above 100°C. Dennis et al. (2001) showed that running at temperatures of about 150°C, and minimising materials such as viton rings that could retain water, seem to be the most important measures to ensure quantitative water sample transfer through a crusher operated under vacuum. The results presented here for the Amsterdam Device suggest that the guidelines recommended by Dennis et al. (2001) to avoid fractionation during crusher-based water extraction are also applicable to continuous-flow systems.

4.4.2 Crushing efficiency

The crusher that we have used for this study typically leaves a poorly sorted crushed residue with a grain size range from <0.1mm up to >1mm sized fragments. This means that not all fluid inclusions are extracted, and that the isotope composition of extracted water will be biased towards that of the larger fluid inclusions. The good match of our fluid inclusion data with local seepage water composition suggests that the larger fluid inclusions provide accurate paleo-drip water isotope values. An unusual case in support of this suggestion was presented by Genty et al. (2002) who conventionally analysed water, extracted with a syringe from macroscopic (mm-sized) voids in stalagmite slabs, and showed the results to be in accordance with estimated paleo-seepage water values. Future experiments with different crushing devices will undoubtedly shed more light on the effect of crushing efficiency in relation to possible isotope fractionation between smaller and larger fluid inclusions.

4.4.3 Applicability to δ^{18}O

Although the present study has been focused on the isotope analysis of hydrogen, the Finnigan TC-EA is able to produce δ^{18}O data from the same type of samples without further technical adaptations (Sharp et al., 2001). Also for the Amsterdam Device itself, no adaptations would be necessary, since the requirements for water sample introduction into the TCEA are identical for δ^{2}H and δ^{18}O analysis. Future work will investigate the proper extraction procedures for fluid inclusion δ^{18}O analysis on this type of continuous-flow system.

4.5 Conclusions

The Amsterdam Device is a relatively low-cost fluid inclusion extraction device that can be connected to a commercially available ThermoFinnigan TC-EA pyrolysis unit for oxygen and hydrogen isotope analyses of fluid inclusion water. To ensure quantitative recovery of released water, we have constructed a full-metal extraction line operated at temperatures >130°C (conforming to the recommendations by Dennis et al. 2001).

Injection experiments show that negligible fractionation occurs for sub-microliter amounts of standard water, which pass through the Amsterdam Device following a cryogenic trapping routine designed for fluid inclusion extraction. Crushing experiments of ~0.5 g speleothem samples from two caves with rather different seepage water isotope composition provide fluid inclusion δ^{2}H values in good accordance with local drip waters. This indicates that the Amsterdam Device produces accurate fluid inclusion isotope values over a relatively wide range of isotope values.

5

Water release patterns of heated speleothem calcite and hydrogen isotope composition of fluid inclusions

Abstract

Speleothem fluid inclusions are a potential paleo-precipitation proxy to reconstruct past rainwater isotopic composition (δ^{18}O, δD). To get a better insight in the extraction of inclusion water from heated speleothem calcite, we monitored the water released from crushed and uncrushed speleothem calcite, heated to 900°C at a rate of 300°C per hour, with a quadrupole mass spectrometer. Crushed calcite released water in three not well individualised peaks between 25 and 360°C, 360 and 650°C and between 650 and 800°C while uncrushed calcite released water in two distinct temperature intervals: between 25 and 550°C and between 550 and 900°C. Water from two speleothems from the Han-sur-Lesse cave was recovered using three different techniques: i) the crushing and heating to 360°C technique, ii) the decrepitation by heating to 550°C and iii) the decomposition by heating to 900°C technique. Measurements of the δD of water recovered by the decomposition of Han-sur-Lesse calcite heated to 900°C did not show a 20 to 30‰ offset as found by previous authors. However a difference of 7‰ was observed between water released before and after decomposition of the calcite. Water recovery from the Han-sur-Lesse samples suggests that a simple heating technique (up to 550°C) without crushing could both (a) recover water

---

This chapter is based on: Verheyden, S., Genty, D., Cattani, O. and van Breukelen, M.R. (2008). Water release patterns of heated speleothem calcite and hydrogen isotope composition of fluid inclusions. *Chemical Geology* , 247(1-2):266-281

with δD representative of that of the drip water and (b) double the water yield as compared to the crushing and heating method.

Our study warns for possible contamination of the recovered inclusion water with hydration water of lime, responsible for the recovery of water with very negative δD values.

5.1 Introduction

Over the last few decades, there has been considerable interest in paleoclimate research using speleothems as a proxy record. The accurate and independent age frame-work, which can be obtained using uranium-series technique, combined with the high-spatial resolution of stable isotope analysis of the calcite makes speleothems particularly useful for paleoclimate studies. Another opportunity provided by the use of speleothems for climate studies is the possibility of measuring 'fossil' seepage water for paleo-rainfall reconstructions as speleothems contain fluid inclusions, that consist of seepage water trapped in inter- and intra-crystalline spaces during the formation of the stalagmite. Inclusions are generally a few microns to a few tens of microns in size (Kendall and Broughton, 1978), although exceptionally some may exceed one centimetre (Genty et al., 2002). In caves of intermediate depth (50 to 150 meters) located in temperate climatic regions, the isotopic composition of the seepage water (δD, δ^{18}O) is a good approximation of the mean annual isotopic composition of local rainwater (Harmon et al., 1979; Harmon, 1979; Yonge et al, 1985; Verheyden, 2001). Consequently, inclusion water trapped within a stalagmite contains important information on the isotopic composition of ancient rainwater, providing that no post-depositional isotopic exchange has occurred (Rozanski and Dulinski, 1987, Genty et al., 2002).

Two methods of water extraction are commonly used: i) crushing of the calcite and subsequent heating to 150°C (Schwarcz et al., 1976; Dennis et al., 1998, 2001; Vonhof et al., 2006) and ii) thermal decrepitation (Yonge 1982, Matthews et al., 2000), better called thermal decomposition or calcination because the speleothem is heated above the decomposition temperature of calcite. The thermal decomposition method of Yonge (1982) and Matthews et al. (2000) has a main advantage compared to the crushing and heating to 150°C method since the water yield obtained with decomposition is often higher than the water yield obtained with crushing of the calcite (Yonge, 1982). However, a major drawback of the decomposition method is that the δD of the recovered inclusion water is approximately 20 to 30‰ depleted compared to the corresponding cave seepage water (Yonge, 1982; Goede et al, 1990; Matthews et al., 2000; McGarry et al., 2004). Since this fractionation is not observed in the macro fluid inclusions directly sampled with a syringe and analysed by Genty et al. (2002) or using the crushing method of Dennis et al. (2001) and Vonhof et al. (2006), the deuterium shift is ascribed to the analytical extraction procedure. Moreover, the offsets differ between labs and the decomposition study of Schwarcz and Yonge (1983) shows no offsets at all. Possible explanations for the deuterium shift include hydride formation (McGarry et al, 2004) or recovery of isotopically differentiated structurally calcite-bound water during the decomposition of the calcite structure (Yonge, 1982, Matthews et al., 2000, McGarry et al, 2004).

In this study, we monitored the release of water from speleothems, during heating of the calcite up to 900°C, by measuring the partial pressures of H_2O released by crushed and uncrushed samples from six speleothems. These monitoring experiments permit us to (1) identify the exact temperature intervals of water release, (2) determine which fraction of released water is recovered with the existing water recovery methodologies and (3) test the necessity of crushing the samples prior to using the decomposition method. Speleothem inclusion water was recovered from a recent (~20-year old) and from a mid Holocene speleothem from the same cave with both existing methodologies (i.e. the crushing and heating method and the thermal decomposition method). The existing crushing and heating to 150°C method (Dennis et al., 1998, 2000) was slightly adapted. The calcite powder was heated up to 360°C, in agreement with the temperature intervals determined by the water release monitoring experiments. The hydrogen isotopic composition of recovered inclusion water was determined with high accuracy (between ±1.5 and ±0.5 ‰) following the method used by Genty et al., 2002. To apply this methodology, between respectively 3 and 9μl inclusion water were needed and therefore, relatively large calcite samples (of ~3 grams) are used. To validate our methodology, the δD values of recovered inclusion water were compared with nowadays cave seepage water δD values. We discuss possible implications of our results for the existing methodologies of water recovery.

5.2 Previous studies

The first experiments using a crushing method on speleothem material, were performed by Thompson (1973), Thompson et al. (1976) Schwarcz et al. (1976) and Harmon et al. (1979). Calcite samples were crushed under vacuum with a hydraulic ram or in metal tubes with a mechanical vice. These authors generally recovered between 0.1 to 1μl water per gram calcite, exceptionally up to 10μl/g (Harmon et al., 1979). Harmon et al. (1979) demonstrated that i) during the extraction of inclusion water no water came from organics or clays since no correlation was observed between the δD of the extracted water and the degree of visible impurities in the calcite samples, and ii) the hydrogen isotopic composition of the inclusion water is probably robust, given the large range and well defined patterns of the δD variations observed over relatively short periods of time (±20,000 years). Generally, post glacial speleothems gave fluid inclusion δD values close to δD values of recent seepage water and local meteoric water. Despite the promising results of these early studies, Yonge (1982) and Goede et al. (1986; 1990) found significant differences between δD values of modern inclusion water, recovered by crushing and heating at 180°C, and that of cave seepage water. Inclusion water showed values up to 30‰ lower than expected from the seepage water. Rozanski and Dulinski (1987) obtained less variable results by heating the crushed calcite up to 450°C for 16 hours. More recently, Dennis et al. (1998, 2001) were able to measure the δD and δ^{18}O isotopic compositions of less than 1μl of inclusion water with a precision of ±3‰ and ±0.4‰, respectively, based on crushing of capillaries containing standard water, together with Iceland spar. These authors and subsequent workers (Fleitmann et al., 2003b) obtained a better correspondence between fluid inclusion δD values and cave water δD values by crushing the samples under vacuum, using an electromagnetically operated piston, and heating the calcite powder up to 150°C during one hour in order to recover all the water adsorbed on the fresh calcite surfaces. Vonhof et al. (2006) innovated the technique with the use of a commercially available continuous-flow pyrolysis furnace (Thermofinnigan TC-EA) connected to a crusher and cold trap unit. Their fluid inclusion δD values were in good agreement with the isotopic composition of drip waters coming from the same cave as the studied speleothems. Continuous flow mass spectrometry for D/H analyses of inclusion water in speleothems was recently also successfully used by Siklosy et al. (2007). Genty et al. (2002) analysed water from macro inclusions by taking 5μl water with a Hamilton syringe through a micro hole in the calcite and directly injecting the water into the uranium furnace reduction line of the mass spectrometer. Despite the high precision obtained (hydrogen isotopic composition better than 0.5‰), this method can be applied only to the few stalagmites that possess such large macroscopic fluid inclusions.

The 'thermal decrepitation method' better called 'decrepitation, followed by decomposition method' (hereafter called decomposition method) was developed for speleothems by Yonge (1982). Samples are heated up to 700-850°C under vacuum, causing decomposition of the calcite to CaO and CO_2 releasing all the water, i.e. inclusion and structural water present in the calcite. Yonge (1982) obtained water yields up to seven times higher than obtained by crushing and heating to 180°C. An increase in water yield with the decomposition method was also observed by Goede et al. (1986) as well as for the decrepitation of quartz (Simon, 2001). The high water yield is the main advantage of this method, especially for speleothems containing small amounts of fluid inclusion water.

Yonge (1982) and Goede et al. (1986) found no systematic difference between the δD of the inclusion water recovered from crushing and that from thermal decomposition, and ascribed this to the large variation in δD values of water recovered with the crushing method. Yonge (1982) observed offsets of 0.7‰ to 59‰ between recovered water from decomposed samples and cave seepage water, but after disregarding suspect samples, the range of offsets was reduced to between 15‰ and 26‰, with a mean value of 22‰. Yonge (1982) investigated the presence of structural water but infrared and neutron diffraction studies failed to reveal the presence of such water. Thus he used 22.1±3.9‰ as a correction factor to calculate the δD composition of cave water from fluid inclusions. However, based on new fluid inclusion δD data, Schwarcz and Yonge (1983) reported uncorrected δD values of inclusion water extracted using either crushing or decomposition methods, which were both consistent with the seepage water. Nevertheless, more recently Matthews et al. (2000) and McGarry et al. (2004) observed variable inclusion water δD values (standard deviations up to 8.7‰) in speleothems of the Soreq cave (Israel), which showed an offset of about -30‰ from cave waters.

An important amount of fluid inclusion studies were done on quartz. Simon (2001) confirmed the presence of two H-reservoirs: (i) H originating from trapped fluid inclusions with a δD close to original hydrothermal fluid and (ii) H originating from structurally bound water depleted in deuterium.

As a consequence, the total water incorporated in quartz has a lower δD value than the original hydrothermal fluid. In addition, his study shows that the δD of thermally extracted water decreased with decreasing grain size fractions due to an increasing contribution of light structural water against heavier inclusion water (lost during grinding). Simon (2001) estimated fractionations to be between 38 and 82‰, depending on the formation temperature of quartz crystals. As in quartz, the contribution of depleted structural water is a possible explanation for the -20‰ to -35‰ δD offset observed in recovered speleothem inclusion water by some authors. However, there is still no consensus on the observed offset between speleothem inclusion water recovered with the decomposition method and corresponding cave seepage water and no explanation has been given for the high variability of this offset.

5.3 Methodology

5.3.1 Samples and operation line

Six speleothems (H1, HP, C, F, L and P, figure 5.1) from five different caves located in Belgium and France were analysed. Samples were chosen to provide a wide range of visible inclusion densities and porosity. Samples C, HP and H1 show alternation of dark compact calcite (DCC) and white porous calcite (WPC), as defined by Genty and Quinif (1996). Since WPC contains many inclusions, a high water yield is expected (Kendall and Broughton 1978; Genty and Quinif, 1996; Genty et al., 2002).

Sample F consists of very translucent dark compact calcite (DCC) and consequently, few inclusions are expected. This is confirmed by binocular inspection (zoom x36), as only few inclusions or pores were visible. Samples L and P are composed of WPC without any layering and are brittle due to their high porosity.

Samples HP and H1 are respectively twenty years old (Verheyden et al., 2006) and of mid Holocene age (Quinif and Bastin, 1986). The age of the other samples was not taken in consideration and is unknown. From each sample, ~1cm^3 chips were sawed for further analysis.

A single operation line (figure 5.2) was used both for monitoring water release as to recover water for δD analyses. The main difference is that monitoring experiments occur under continuous vacuum pumping, while water recovery is done in a closed line, only opened to separate recovered water from CO_2. The operation line (figure 5.2), consists of stainless steel tubes of 2mm internal diameter with a stainless steel cell, a glass trap and a sample recovery tube connected with Ultra-torr (Swagelok) connections and Teflon o-rings with a leaking rate for helium of 4.10^{-9} std cm^3/s. The line (with exception of the cell and traps) is continuously held at a temperature of 120°C using heating wires to avoid adsorption of water on the walls. Vacuum (10^{-6} mbar) is obtained using a turbo pump coupled to a primary rotary vacuum pump. Sample cell and operation line are tested for leaks by diffusing helium

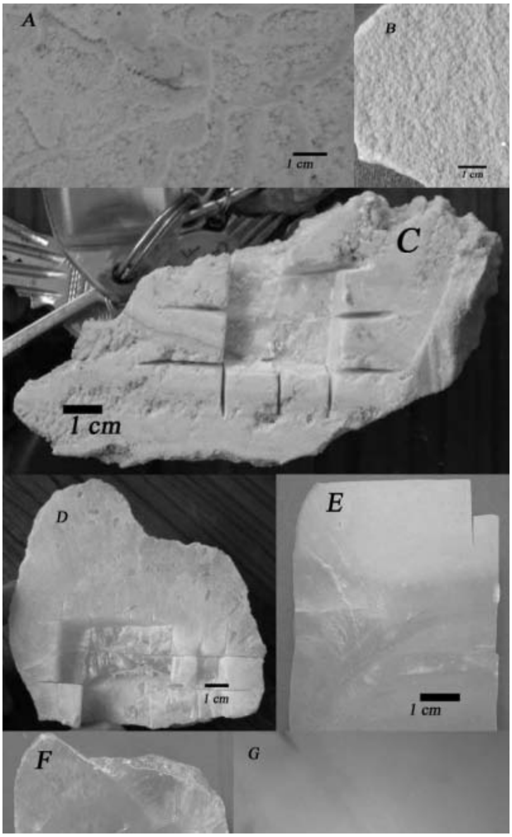

Figure 5.1: The water release of six speleothem calcite samples from Belgian and French caves was monitored. A) L sample from the Lascaux cave in France; B) P sample from the Proumeyssac cave in France; C) H1 sample from the Han-sur-Lesse cave in Belgium, HP sample is of similar macroscopic aspect D) and E) C sample from the Clamouse cave in France and F) and G) F samples from La Faurie cave in France.

around the cell and line. Helium, entering the line through leaks, is directly detected by an online Balzers QMG 064 quadrupole mass spectrometer (QMS). The cold trap and the recovery tube are used only when inclusion water is recovered for δD analyses. To heat the samples, a tubular ceramic oven is placed around the online sample cell. Temperature measurements on the cell showed a difference of maximum 10°C with the temperature of the oven. The online QMS is placed between the sample cell and the vacuum pumps and monitors the partial pressure of H_2O (P_{H_2O}) and of CO_2 (P_{CO_2}) of the gasses passing through the line on their way to the pumps. The water vapour pressure (P_{H_2O}) and the CO_2 vapour pressure (P_{CO_2}) (m/e = 18 and 44 signals) are measured down to 5.10^{-9} mbar, the detection limit of this instrument. The operation line, traps and sample cell were cleaned with 2M HNO_3 acid between two samples to avoid contamination problems that occurred when the line and cell were cleaned only with pressurized clean air (see sections 5.4.3 and 5.5.1)

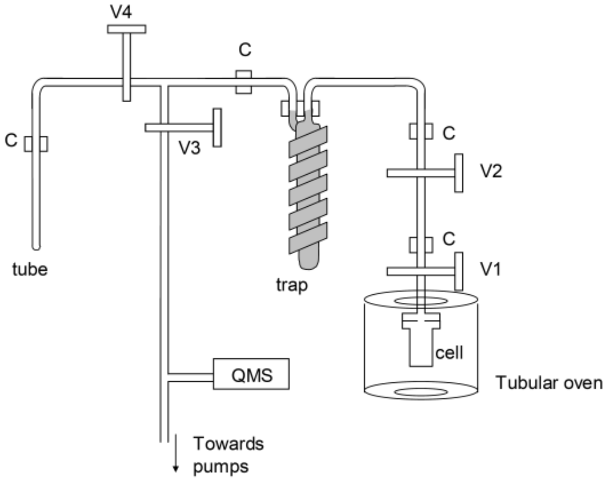

Figure 5.2: The fluid inclusion operation line consists of stainless steel tubes of 2 mm internal diameter with a stainless steel cell, a glass trap and a sample recovery tube. The cell can easily be removed (for the crushing procedure) from the line by closing valve one (V1) and opening the connection (C) above. A tubular oven, placed around the cell heats the sample in the cell. During the heating experiments only V4 is closed. Gasses released from the sample are analysed by a Balzers QMG 064 quadrupole mass spectrometer (QMS) on their way to the pumps. During the water recovery experiments, V3 is closed (after vacuum pumping).The glass cold trap allows the recovery of water that is released from the sample cell. After purifying for P_{CO_2}, the water is transferred (by heating the trap) to the glass tube (dumped in liquid nitrogen) at the end of the line. The glass tube is then sealed, detached from the line and stored for δ^2H analysis.

5.3.2 Crushing

A stainless steel sample cell, diameter of 2 cm, containing a sample chip of between 3 and 6 g and a steel ball of 1.6 cm diameter, was attached to the operation line (figure 5.2). A metal filter of 0.2μm was placed between the sample cell and the line to avoid contamination of the line with $CaCO_3$ or CaO powder. After overnight vacuum pumping at room temperature, the sample cell was closed by valve 1, detached from the line and attached to a modified jig saw. The cell was shaken for 4 minutes, during which the calcite was crushed by the ball, down to grain sizes of between 8 and 500μm, by the movements of the ball. Ideal ball diameter and shaking time (to crush the entire sample) were determined during a series of preliminary tests. Once the sample was crushed, the cell was again attached to the operation line.

5.3.3 Monitoring the water released during heating of the calcite

In the monitoring experiments crushed and uncrushed sample chips were heated to 900°C at a rate of 300°C per hour (thermal decrepitation and finally decomposition of the calcite). Pressure of the released H_2O and CO_2 gas was monitored online under continuous vacuum pumping (V1, V2 and V3 open) to determine the temperature interval and the amount of the released H_2O and CO_2 gasses. The sample cell containing a crushed speleothem sample (see section 5.3.2) was attached to the operation line (V1 closed). When vacuum was obtained in the line, V1 was opened to pump away the high amount of bulk water released from the fluid inclusions during crushing of the calcite to avoid damage to the Quadrupole mass spectrometer. This 'bulk water' is therefore not displayed in the water release curve. When vacuum was obtained, the freshly crushed calcite powder was heated to 900°C at a rate of 300°C/hour. P_{H_2O} and P_{CO_2} of the released gasses were measured by the quadrupole mass spectrometer to monitor the presence of additional water in the crushed calcite and determine in which temperature interval it is released. The monitoring experiment was repeated with uncrushed chips of calcite to test the necessity of crushing the sample when recovering the water by (1) thermal decrepitation when decomposition temperature of calcite is not attained or (2) thermal decrepitation and finally decomposition when decomposition temperature of calcite is exceeded.

5.3.4 Fluid inclusion water recovery and δD measurements

5.3.4.1 Recovery of speleothem water

In contrast to the monitoring experiments, recovery of water occurred in a closed operation line (V1, V2 and V4 open, V3 closed, figure 5.2).

Crushing and heating to 360°C

The total amount of gasses released from 3 to 6 g of crushed calcite heated to 360°C was trapped in a liquid nitrogen cold trap (see figure 5.2). The liquid nitrogen was later replaced by an alcohol slurry at -72°C to remove trapped CO_2 by pumping. After CO_2 removal, the trap was heated to transfer the purified water into the glass recovery tube (in liquid nitrogen). Using this method, between 2 and 4μl of water were collected in the glass recovery tube, which was sealed and stored for subsequent δD analysis as described in section 5.3.4.2.

Thermal decomposition

The gasses released from a 3 to 6 gram calcite chip heated to 900°C were continuously trapped in an alcohol slurry at -72°C. The use of a liquid nitrogen trap caused clogging due to the important amount of CO_2 produced by the decomposition of the calcite at around 700°C. At temperatures between 500°C and 900°C, the line towards the vacuum pump was slightly opened (V3 in figure 5.2) to evacuate the CO_2. At 900°C, the line was closed and the alcohol slurry was removed from the cold trap. Heating the trap with hot air transferred the trapped water to the other side of the the glass recovery tube dumped in liquid nitrogen. Using this method, between 3 and 16μl of water were collected in the glass recovery tube and stored for subsequent δD analysis (see section 5.3.4.2). The inclusion water from the mid-Holocene flowstone H1 (Quinif and Bastin, 1986) and from the 20-year old stalagmite HP (Verheyden et al., 2006), both from the Belgian Han-sur-Lesse cave, was recovered using both extraction methods, i.e. three H1 and one HP samples were crushed, subsequently heated to 360°C and the released water recovered for δD analysis using isotope-ratio mass-spectrometry. Another 13 uncrushed H1 and one HP calcite chips were heated to 900°C and decomposed to CaO to recover all the water enclosed in the calcite, i.e. inclusion water as well as structural water. For both methods ∼1cm^3 of calcite was used, corresponding to ∼3 grams of calcite. In our set-up, it was not possible to recover the water during monitoring or to monitor the water release during water recovery. All δD results of H1 and HP were compared with the annual mean of -51.0 ± 2.8‰ (2σ) VSMOW (n=54) of present-day cave water from the Han-sur-Lesse cave system, sampled approximately once a month between December 1995 and November 1996 (Verheyden, 2001) and every two weeks between July 2003 and February 2004.

For six uncrushed H1 samples, we recovered the water released during two different temperature intervals i.e. between 25 and 550°C (decrepitation) and between 550 and 900°C (decomposition). These temperature intervals were chosen, based on previous monitoring experiments. For both intervals the extracted water was recovered and measured separately.

To characterize observed contamination problems (see section 5.4.1 and 5.4.3), water was recovered from three lime samples (CaO), the product of thermal decomposition of calcite.

5.3.4.2 Deuterium measurements

The glass tubes, containing the recovered speleothem water, were unsealed a few seconds before analysis, after concentrating the water by dumping the tip of the tube in liquid nitrogen. Hydrogen isotopic composition of the recovered inclusion water was measured on a homemade Isotope-Ratio Mass-spectrometer (IRMS) with online uranium reduction (Hageman and Lohez, 1978; Vaughn et al., 1998) constructed and used for ice core water analysis. Prior to sample analysis, a series of reference waters is injected by an automatic Gilson sampler and measured. A Valco rotator with air actuator coupled to the autosampler guarantees the injection into the mass spectrometer of a reproducible quantity of water of 2 μl. Then a series of reference waters are manually injected with a Hamilton syringe into the Valco rotator, keeping the same timing as the automated system. Following the analysis of the reference waters, the recovered fluid inclusion waters, pre-concentrated in the tip of the sample tube with liquid nitrogen, were manually injected and measured. If enough water was available (typically 12 μl) inclusion water was measured up to three times. A second series of reference waters was then measured to correct for possible machine drift. After each injection, water was vaporized at 100°C in a 1.6 l volume and reduced on uranium sheets heated at 600°C. The analytical error on the deuterium measurement depends on the number of replicate measurements and is typically 0.5‰ (n=3), 0.8‰ (n=2) or 1.5‰ (n=1).

Long-term reproducibility of the entire extraction and measurement procedure was determined based on 30 working standards of 15 μl tap water sealed under vacuum in glass tubes, which were extracted using the same method as for crushed calcite samples (aside from the temperature). Briefly, the tubes were crushed in the sample cell, without presence of calcite, using a steel ball and heated to 120°C under vacuum. The water yield was better than 95% for each working standard. δD of recovered standard water against itself was -0.4±2.1‰ (n=30).

5.4 Results

5.4.1 Monitoring experiments

During a first series of monitoring experiments, a sharp water release peak was observed for most samples at around 400°C. Several tests (figure 5.3 revealed that both the operation line (the part close to the oven) and the sample cell released water at 400°C, when they were not cleaned with acid and exposed to atmosphere between two experiments. Finally, this peak was ascribed to the release of adsorbed water on CaO forming $Ca(OH)_2$, coming from the decomposition of previous samples (see also section 5.4.3). For following samples, the operation line and sample cell were cleaned with 2M HNO_3 acid in between each sample and a metal filter of 0.2μm (instead of 10μm) porosity was used just above the sample cell to keep the powder in the extraction cell.

The powder of crushed speleothem samples (figure 5.4) all roughly displayed similar water release patterns. Besides the water released directly during crushing which was not monitored, the calcite powder released water within three temperature intervals: 25-360°C, 360-650°C and 650-800°C. However, the peaks are not well separated and the two latter peaks show considerable overlap. Water release of uncrushed H, C and F sample chips (figure 5.5) showed some discrepancies but occurred within two distinct temperature intervals: between 100 and 550°C and between 550 and 800°C, resulting in two clear, well separated peaks. The water release pattern of the uncrushed L and P samples resembles the water release pattern of crushed calcite. For crushed as well as for uncrushed calcite, CO_2 gas was released only during the last water release peak between 650 and 800°C. Besides roughly similar release patterns for different samples (with exception of uncrushed L and P samples), some discrepancies are observed concerning temperature at which water release starts. For crushed calcite, H1 samples start to release water already at 50 to 100°C while C and F samples do this at 180 to 200°C. For uncrushed samples, water is released at ~100°C for H1 and HP samples (except for one H1 subsample, which released water at 180°C), at ~150°C for L and P, at ~180°C for C and at ~300°C for F samples.

The amount of water released by different speleothem samples, crushed as well as uncrushed (given by the area under the curves in figures 5.4 & 5.5) was not reproducible and

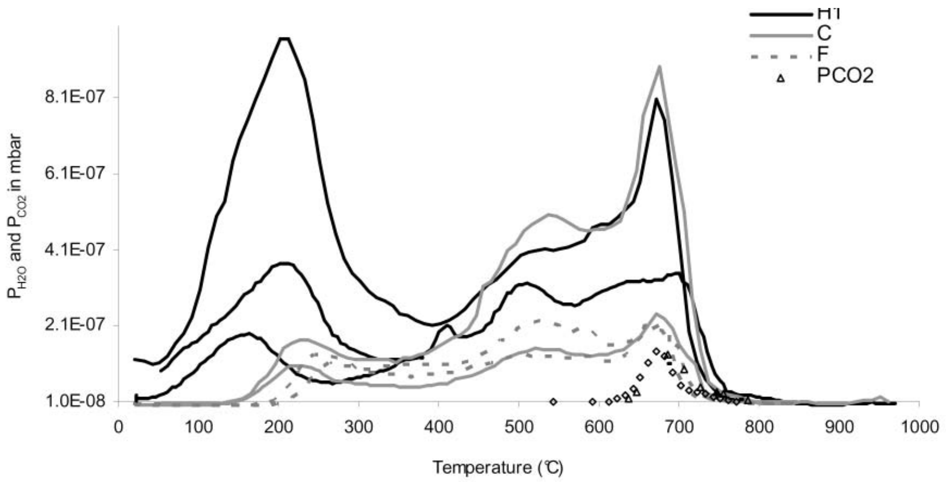

Figure 5.3: Monitoring of water released by heating empty sample cells to 900°C. The water released from dirty cells (i.e. containing traces of CaO from previous decomposed samples) opened to atmosphere before the experiment, is given in grey. The pressure of the 'out of scale' line goes up to $2.2.10^{-5}$ mbar. The water released from lime around 400°C after exposure to the atmosphere for several hours has a δD value of approximately -130‰ vsmow. Water vapour pressures from 'clean cells' (black lines) include 1) one new, never used cell, 2) three dirty cells but which were not exposed to the atmosphere, one of them was filled with N_2 before opening to the atmosphere and 3) two empty cells, cleaned with HNO_3 acid before the experiment to remove all traces of CaO or $CaCO_3$. The pressure of released water does not exceed $6.8.10^{-8}$ mbar.

varied between and within speleothems. There seems to be some relationship with more porous samples (particularly L and P samples) releasing more water but this correlation was not further investigated and lies beyond the scope of these experiments. Variations were smaller between samples from the same speleothem but still significant. Since the signal of the QMS was not calibrated to measure the absolute amount of water or CO_2-gas, only relative comparisons are possible. For the same reason, values for P_{H_2O} and P_{CO_2} are not comparable (figures 5.4 & 5.5). It is interesting to note that as soon as temperature stops increasing, the water vapour pressure abruptly decreases. Moreover, a sample heated to a certain temperature and cooled down to room temperature must be heated above the previous temperature before releasing water again.

5.4.2 Recovery of inclusion water from H1 and H2 samples: water yield and deuterium isotopic composition.

The mean amount of water recovered from the H1 and HP samples (table 5.1, figure 5.6) varied from 1.0 μl water per gram calcite for the crushing method, to 3.2 μl/g for the

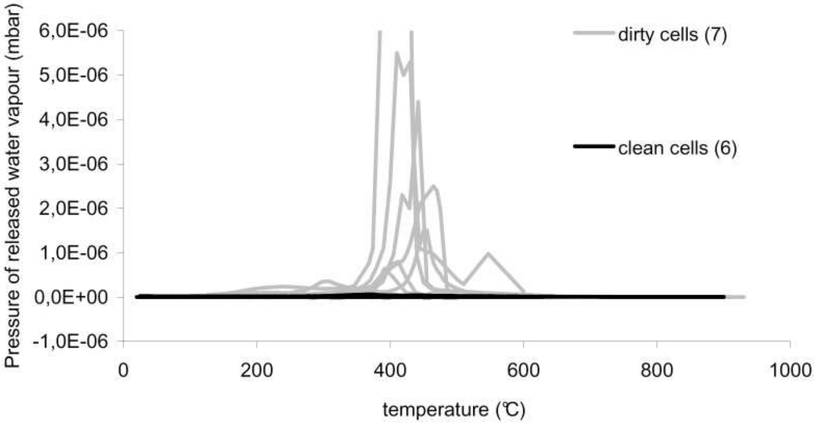

Figure 5.4: Water (lines) and CO_2 (open symbols) vapour pressures of gasses released from a 1 gram crushed calcite powder during heating to 900°C. Measurements of P_{H_2O} are taken every 10°C. Since the QMS was not calibrated to measure absolute quantities, P_{H_2O} and P_{CO_2} are not comparable. Different lines concern sub-samples from the same speleothem. Water vapour pressure measured for an empty cell was $1 \cdot 10^{-8}$ mbar. The water released from the fluid inclusions during crushing of the calcite is not included in the graph since it was pumped away prior to start of the monitoring to avoid damage to the quadrupole mass spectrometer.

thermal decomposition method. Since monitoring experiments revealed important water release up to 360°C for crushed samples, we adapted the existing crushing and heating to 150°C methodology (Dennis et al., 1998; 2001) by increasing the recovery temperature up to 360°C to recover as much water as possible. The water yield from the crushing and heating to 360°C method is similar for all the H1 and HP samples and is of the same order as that observed by other authors (typically 1 to 2 μl/g) (Yonge, 1982, Dennis et al., 2001).

Decomposition of calcite chips produced variable yields during partial recovery between 25 and 550°C (0.98 to 3.24 μl/g) (n=6), while yields during partial recovery between 550 and 900°C are remarkably stable (1.27 to 1.53 μl/g, n=5).

The mean δD value of inclusion water for H1 and HP samples (table 5.1, figure 5.7) recovered with the crushing and heating (360°C) method was -50.1 ±0.9 (1σ)‰ (n=3), which corresponds to present-day cave seepage water values of -51.0 ±1.4 (1σ)‰. The mean δD value of inclusion water recovered with the decomposition method (25-900°C) was -49.4 ±3.5 (1σ)‰ (n=13). This is in good agreement with the observed cave seepage water values. Of the 13 samples, only one lies outside the 2 sigma range (2σ between 1.6 and 3.0‰) of the cave seepage water (table 5.1). We did not observe the 20 to 30 ‰ offset observed by previous authors using the thermal decomposition method (Yonge, 1982; Matthews et al., 2000 and McGarry et al., 2004). However, a difference in δD exists for the two partial water recoveries with lower values (δD = -54.5 ±4.1 (1σ)‰) for water released between 550

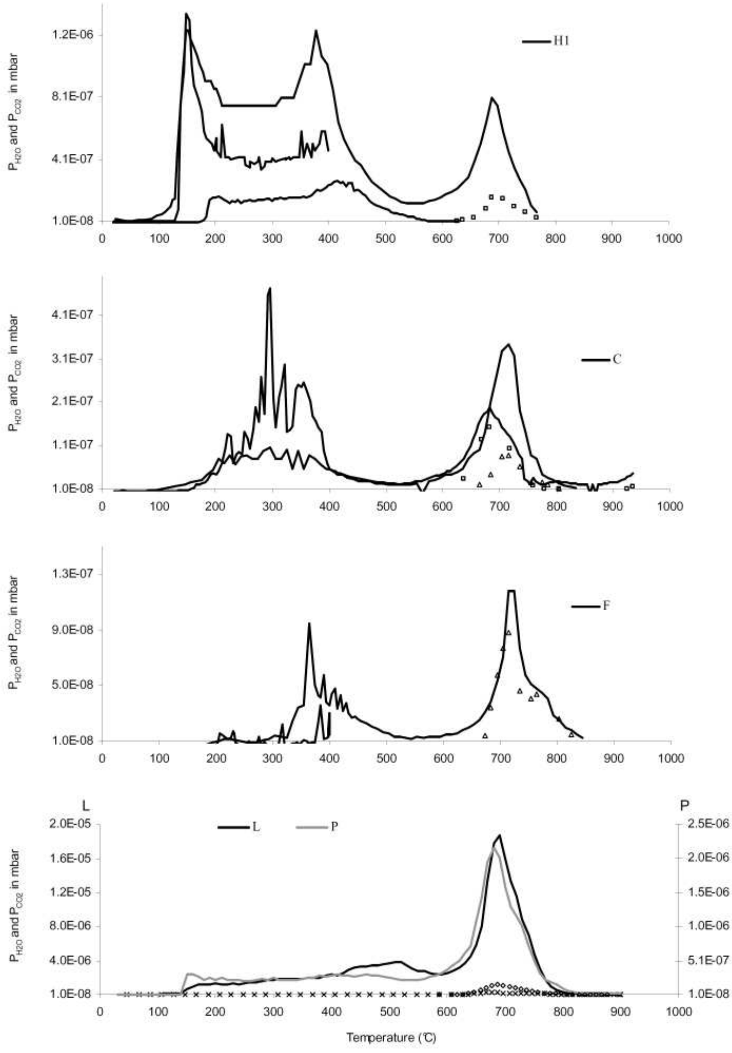

Figure 5.5: Water (lines) and CO_2 (open symbols) vapour pressure of the gasses released from a 1 gram uncrushed calcite chip during heating to 900°C. Measurements of P_{H_2O} are taken every 10°C. Since the QMS was not calibrated to measure absolute quantities, P_{H_2O} and P_{CO_2} are not comparable. Different lines concern sub-samples from the same speleothem. Water vapour pressure measured for an empty cell was $1 \cdot 10^{-8}$ mbar. Note the different scales in water vapour pressures for different speleothems.

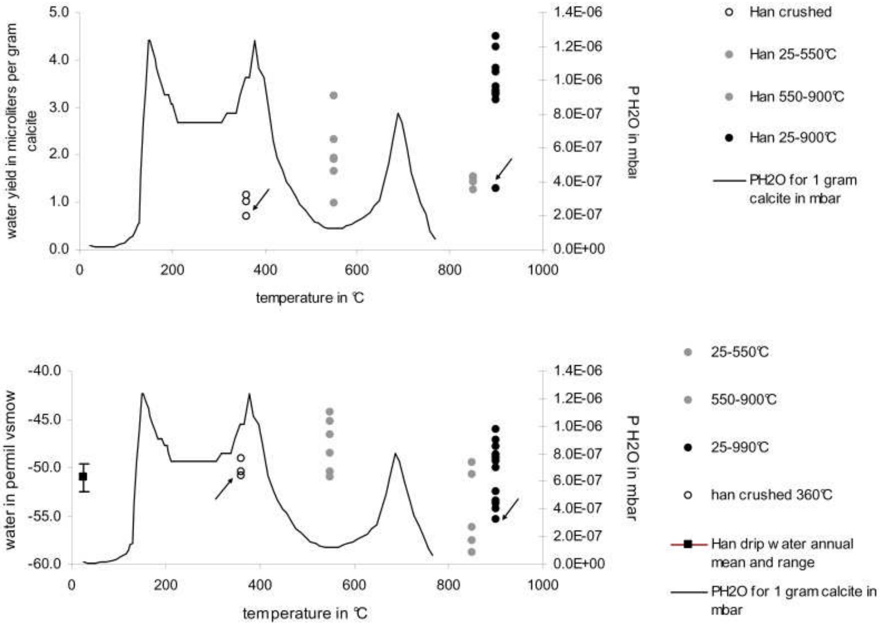

Figure 5.6: A. Water yield for both extraction methodologies.Water yields for the partial recoveries (grey circles) between 25 and 550°C (at 550°C) and between 550 and 900°C (at 850°C) are also given. The arrows indicate the data for the twenty-year old HP calcite. The release of water as measured during the monitoring experiments is given in mbar by the black line. B. δD of recovered water with both methodologies and for the partial recoveries between 25 and 550°C and between 550 and 900°C are compared to the present-day mean seepage water δD (plotted at 25°C). The arrows indicate the data for the twenty-year old HP calcite. The release of water as measured during the monitoring experiments is given in mbar by the black line.

and 900°C compared to water released between 25 and 550°C (δD = -47.7±2.7 (1σ)‰). A maximum difference of 11.8‰ is observed for two partial recoveries from the same sample (figure 5.8).

5.4.3 Recovery of water adsorbed on decomposed calcite (lime)

To investigate the isotopic composition of water released at 400°C as observed in the first monitoring experiments (see section 5.4.1), water was recovered from three previously decomposed calcite samples, which were exposed to the atmosphere for a few hours and heated subsequently to 500°C. The samples released between 40 and 50μl water per gram initial $CaCO_3$, an important amount compared to the ~15 μl inclusion water generally recovered from this amount of calcite. The δD values of the recovered water from the three decomposed calcite (lime) chips are -134.5‰, -128.2‰ and -130.2‰ ±0.5 (1σ)‰.

Han-sur-Lesse Holocene calcite	Crushed and heated (360°C)	Uncrushed heated 25-550°C	Uncrushed heated 550-900°C	Uncrushed heated 25-900°C
δD (‰)	-50.1±0.9	-47.7±2.7	-54.5±4.1	-49.4±3.5
Range (‰)	1.8	6.6	9.2	9.4
Number of samples	3	6	5	13
Mean yield ± 1s (µl/g)	1.0±0.2	2.0±0.8	1.4±0.1	3.2±1.0

Table 5.1: Mean δD in ‰ vsmow and water yield in μl normalised to 1 g of calcite, of recovered inclusion water for the Holocene Han-sur-Lesse calcite (Han-pl1 and Han-stm-P). The mean annual δD of present-day cave seepage water is .51.0 ±2.8‰ (2σ) vsmow (n=54).

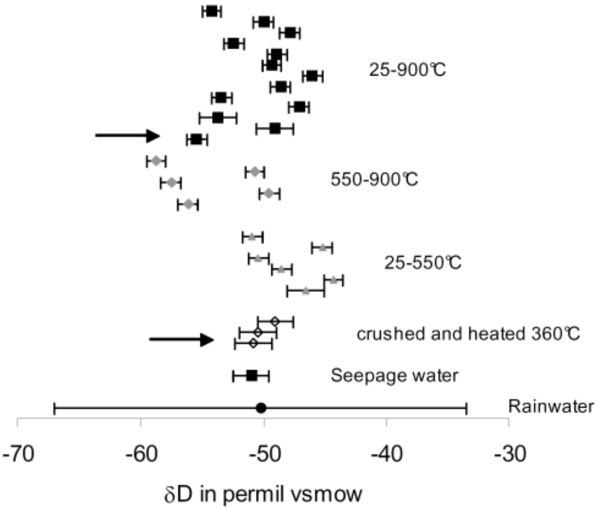

Figure 5.7: Comparison between the 1) δD of Belgian rainwater (Liege, 1966.1970, IAEA GNIP database, mean over 5 years and entire range), 2) the δD of the Han-sur-Lesse system seepage water (2 σ), 3) the δD of inclusion water from the H1 and the modern (twenty-year old) HP (arrows) samples recovered by crushing and heating to 360°C at a rate of 300°C/h, 4) the δD of inclusion water from the H1 samples recovered from a calcite chip heated to 550°C, 5) the δD of inclusion water from the H1 samples released by a chip of calcite between 550 and 900°C and 6) the δD of inclusion water from the H1 and the HP (arrows) samples released by a chip of calcite heated from 25 to 900°C. Error bars are 1 sigma, they represent the analytical uncertainty.

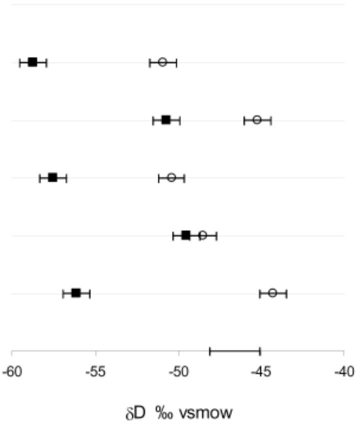

Figure 5.8: The water recovered between 550°C and 900°C (squares) from H1 samples is systematically more depleted in deuterium than the water recovered between 25 and 550°C (circles) for the same sample (on the same grey line). The mean difference between both waters is 6.8‰ .

5.5 Discussion

5.5.1 Methodological artefact

The initial heating experiments (figure 5.3) clearly indicated that water other than speleothem inclusion water is recovered around 400°C when the sample cell and extraction line are cleaned only with pressurized clean air. Therefore, we suggest that residual hydrophilic lime (CaO) formed during decomposition of the speleothem calcite (Zsako and Hints, 1998; Shi et al., 2002) in the sample cell and deposited in the operation line, may be a possible cause for the presence of contaminant water. When the line and cell are exposed to atmosphere during loading of successive samples, residual CaO from the previous decomposed sample, hydrates with atmospheric water vapour to give $Ca(OH)_2$. The release of water at approximately 400°C is in agreement with the dehydration temperature range of $Ca(OH)_2$ at 1atm (420 to 660°C), which depends on its purity and its calcination temperature (Zsako and Hints, 1998; Shi et al., 2002). To further avoid contamination with hydration water of lime powder in the system, we cleaned the sample cell and the line with 2M HNO_3 in between the experiments and we used a metal filter of 0.2μm (instead of 10μm) porosity just above the sample cell to keep the powder as much as possible in the extraction cell. Since the hydration water of lime has very negative values (similar to atmospheric water vapour in the laboratory), contamination with this hydration water may induce negative δD values for the recovered inclusion water. The release of only 1μl of lime hydration water with a δD of around -130‰, during the recovery of 5μl of fluid inclusion water with a δD of -50‰, will result in a measured isotopic composition of -63‰. Contamination is already possible with small amounts of CaO, since lime produced from the same amount of speleothem calcite can release easily 10-50 times more water per gram as is extracted from the speleothem calcite.

5.5.2 Water released from heated speleothem calcite

Water release from crushed calcite (figure 5.4) occurred in three peaks. During the third peak, between 600°C and 750°C, water is released together with CO_2, indicating that decomposition of calcite occurs, i.e. the transformation of $CaCO_3$ to CaO through the reaction $CaCO_3 \rightarrow CaO + CO_2$ (Imhof, 1997 and references therein) with the release of structurally calcite-bound water. Therefore, the release of most of the structural water is expected above ~600°C, the decomposition temperature for crushed calcite as indicated by the monitoring experiments. From our results it is not possible to confirm whether or not additional inclusion water is released during decomposition of calcite. Some nano-inclusions that are too small to exceed the tensile strength of the host mineral, and thus to decrepitate below 600°C may release their water during decomposition of the calcite. Below 600°C crushed calcite released water in two not well separated peaks. The first peak at ~160°C is due to the release of inclusion water re-adsorbed on fresh grain surfaces during crushing (Dennis et al. 2001). However, some water may be released also from inclusions smaller than the grains due to ongoing decrepitation. The second peak at ~550°C could be due to further decrepitation of grains with release of inclusion water. The presence of a large range of grain sizes may be at the base of the poor separation of the different water release peaks and working with a uniform grain size fraction as typically performed for decrepitation of quartz could permit a better control on the water release. However, this technique would decrease the water yield, while a poor water yield is already an important problem in speleothem inclusion recovery studies.

Water released from uncrushed calcite chips displays a different behaviour than water from crushed calcite with two distinct peaks of water release, which are well separated (with exception of the L and P samples). Water release for most H1 and for HP samples begins at ~100°C with a rapid increase of water vapour pressure in the operation line (figure 5.5). Since, after overnight pumping at room temperature, no water is released under 100°C as is the case for a sample heated directly after being placed in the extraction cell (without overnight pumping), the sample seems to have released the majority of the adsorbed atmospheric water vapour. However, based on the work of Gammage and Gregg (1972), Dennis et al (2001) suggested that adsorbed water is released up to 150°C. Nevertheless, this temperature was designed for water adsorbed on freshly crushed calcite. In this study, if adsorbed water was still present on our uncrushed samples and was released between 100 and 150°C, no distinction could be made between this adsorbed water and inclusion water, since rapid increase of water vapour pressure to values comparable to these at temperatures higher than 150°C indicated that release of inclusion water (decrepitation) already began. In the 25-550°C temperature interval water release appears irregular (figure 5.5), in agreement with release along existing cracks or cleavage planes successively opened by the expansion of the inclusion water during heating (decrepitation). A previously heated calcite sample does not release water until the previously attained temperature is exceeded and new cracks are opened, which indicates that the inclusions are not interconnected. The second, well separated peak of water release occurs with the decomposition of the host calcite as indicated by the simultaneous release of CO_2. For the decomposition of uncrushed calcite, as for crushed calcite, we cannot exclude release of water from nano-inclusions, together with structural water. Especially for the L and P samples, the amount of released water is too important to be only structural water. In the case of crushed calcite, these nano-inclusions may release their water at lower temperature, which could explain the second water release peak at ~550°C in case of crushed calcite. The water release patterns of uncrushed L and P samples (figure 5.5) more resembles water release of crushed calcite, which may be related to their high porosity but this should be further investigated.

Separation of water release peaks from uncrushed samples, below and above decomposition temperature is especially important in the context of the recovery of inclusion water since both peaks can be recovered without contamination from the other peak. This suggests that to recover water from the larger fluid inclusions, it is sufficient to heat a sample chip to 550°C, which would be more practical than the currently used thermal decomposition method. If during decomposition of calcite structurally bound water with a distinct δD is released the recovery of both water release peaks will result in isotopic contamination of the inclusion water.

The amount of released water for crushed as well as for uncrushed calcite was not reproducible, neither between speleothems, nor between subsamples from the same speleothem. This variability most likely reflects variations in inclusion densities between speleothems but also within speleothems as previously suggested by the study of Dennis et al. (1998). The temperature at which calcite starts to release water varies between speleothems but also between samples within the same speleothem. Decrepitation of uncrushed H1 samples starts already at 100°C. Early decrepitation can consequently explain why crushed H1 samples begin to release water at temperatures lower than 150°C, which is the expected temperature for the release of water adsorbed on grains (Gammage and Gregg, 1972). One possible explanation for differences in water release temperatures is the difference in internal crystallographic structure (cleavage density and orientation, crystal size, inclusion density, size and distribution) between samples. More monitoring experiments are necessary to evaluate the influence of the internal structure of calcite on the temperature at which water is first released, as well as on the shape of water release peaks.

5.5.3 Water yield and δD of recovered inclusion water from the Han-sur-Lesse samples

Higher water yields (two to four-fold) were obtained with decomposition of the H1 and HP calcite sample chips heated to 900°C as well as with decrepitation of H1 calcite sample chips heated to 550°C compared to the crushing and heating to 360°C method (table 5.1, figure 5.6). The water yield for uncrushed H1 chips heated between 550 and 900°C was much less variable than for those heated between 25 and 550°C. The lower variability in water yield at higher temperatures (550-900°C) supports the idea of the release of 'structurally determined' water with no or minor contribution of additional inclusion water for the H1 samples, although we cannot exclude contribution of water from nano-inclusions as explained in 5.5.2

Water recovered from the 20-year old HP sample with the crushing and heating to 360°C method had δD values identical to present-day seepage water (figure 5.7). The reliability of the δD values from inclusion water recovered with the crushing and heating to 150°C technique was already demonstrated by Dennis et al. (2001). The isotopic composition of water recovered by crushing and heating from the mid-Holocene H1 samples displayed comparable δD values suggesting that mid-Holocene rainwater had a hydrogen isotopic composition similar to that of today. Precise dating of the sample is necessary to use it as a useful proxy for paleo rainwater δD. The variability between samples and the deviation of present day cave seepage water is in agreement with the natural variability in annual mean rainwater and cave seepage δD.

The δD value of water recovered from H1 and HP uncrushed chips with the thermal decomposition method (25-900°C) was close to the δD value of present-day seepage water. A maximum 4.6‰ more depleted δD is observed for the 20-year old HP inclusion water compared to present-day cave seepage water (figure 5.7). No negative offset of -20 to -30‰ as observed in previous studies was obtained for decomposed samples. One of the reasons invoked by previous authors to explain the -20 to -30‰ offset is a possible difference in δD value between water released from fluid inclusions and structurally bound water. Simon (2001) made the same observation for crushed quartz. Based on the δD values of water recovered from different grain sizes, he constructed a linear mixing model using two end members: the δD of inclusion water and the δD of structurally bound water. However, the bimodal water release, observed during the heating of uncrushed as well as crushed speleothem calcite, suggests that a simple mixing model of inclusion/structural water with two δD end members as used by Simon (2001) for quartz may be inappropriate for calcite. Our measurements on H1 suggest that unlike quartz, the structurally bound water shows only a small hydrogen fractionation with the inclusion water. The water released between 550 and 900°C (δD between -49.5 and -58.7‰) is on average 6.8‰ depleted compared to the water released between 25-550°C (δD between -44.3 and -50.9‰) (table 5.1, figures 5.7 & 5.8). As suggested above, water from H1 samples, released between 550 and 900°C, should be composed of solely or nearly solely structural water. If this is the case, the observed fractionation of 6.8‰ should be close to the fractionation between calcite-bound water and inclusion water. In the case of H1 samples, fractionation is certainly not big enough to induce an offset in δD of -20 to -30‰. However, it explains the higher variability for the δD values of water recovered by decrepitation (0-900°C) compared to the δD values for water recovered in the 25-550°C temperature interval, since the δD value depends on the isotopic composition and the amount of water released by both 'water reservoirs'. The δD values obtained for the water recovered between 25 and 550°C (the first water peak) are in good agreement with present-day seepage water (within 2σ or 2.1‰, long-term reproducibility based on water standard replicates). This variation can also be explained by the natural δD variability of the cave water during the growth of the sample. For the 20-year old HP sample (figure 5.7), the lower δD of -55.4‰ of the total recovered water (recovered between 25 and 900°C) may be due to a contribution of depleted calcite-bound decomposition water. However, total recovered water corresponds within the long term reproducibility (2σ=2.1‰) and within the variability of cave water (2σ=2.8‰) to present-day Han-sur-Lesse seepage water (table 5.1).

5.5.4 Implications for the existing fluid inclusion extraction techniques

The monitoring experiments show that inclusion water is released from crushed calcite above 150°C. This water is probably not or only partially recovered with the currently used crushing techniques (Yonge, 1982, Dennis et al., 2001), explaining the relatively poor water yield of this method. However, this partial recovery does not seem to fractionate since Dennis et al. (2001) recovered fluid inclusion water representative of seepage water. Further tests on crushed calcite with partial water recoveries between 25 and 550°C are necessary to study the evolution of the δD values of recovered water and optimize the recovery temperature. In our study, crushing and heating to 360°C of H1 and HP samples gave δD results very close (within 1.5‰, 1σ error) to present-day seepage water. A major drawback of this method is the poor water yield. The decomposition methodology is from this point of view ideal, since the water yield for H1 and HP samples (3.2 μl/g) is three times that of our crushing and heating to 360°C method but in this case, structurally bound water with lower δD values (at least 7‰ for H1 and HP samples) than the initial seepage water is also recovered. δD measurements of Han-sur-Lesse samples suggest that water recovered from uncrushed calcite between 25 and 550°C is representative of the initial seepage water, since no depleted structurally bound water is recovered. The water yield is still twice that of the crushing and heating method and no crushing infrastructure is needed, which also makes it an attractive alternative technique to the crushing and heating method.

An important barrier to study small scale variations in δD of inclusion water is still the poor long-term reproducibility ($1\ \sigma$ = 1.1‰, based on replicate standard waters) of the extraction technique used. Our opinion is that further optimization of the operation line coupled with a certain automation of different operations can improve the reproducibility.

5.6 Conclusions

Monitoring of water release patterns during decrepitation and decomposition of crushed calcite heated to 900°C at a rate of 300°C/hour shows that water is released in three not well separated peaks. Water was released between 25 and 360°C, 360 and 650°C and between 650 and 800°C. The water release peaks include inclusion water re-adsorbed on fresh surfaces during crushing (first release peak), additional water from inclusions smaller than the grain size (all three peaks) and structurally bound water (last peak) but our experiments do not permit to conclude about the type of water that is released. Uncrushed calcite, heated to 900°C at a rate of 300°C/hour shows that water is released in two distinct temperature intervals, between 25 and 550°C (decrepitation) and between 550 and 900°C (decomposition of the calcite), suggesting release of water from two different locations, i.e. fluid inclusions, and structurally bound water. However, release of inclusion water from nano-inclusions during decomposition of calcite between 550 and 900°C may not be excluded.

Heating of calcite and monitoring of released water showed that in the currently used crushing and heating to 150°C water recovery method, part of the inclusion water is not recovered explaining the poor water yield of this method. Recovery and δD measurement of water enclosed in Han-sur-Lesse speleothem calcite suggests that heating to 550°C of an uncrushed calcite sample chip (without decomposition of the calcite), is a reliable and convenient technique to recover fluid inclusions from speleothems. For six H1 samples, twice more water was recovered with our decrepitation to 550°C method than with our crushing and heating to 360°C technique, no crushing infrastructure is needed, the inclusion water is totally (or nearly totally) recovered and there is no contamination with depleted calcite-bound water, since the release of structurally bound water occurs in a distinct temperature interval and can therefore easily be avoided.

Total water recovered with our decomposition method from uncrushed chips of Han-sur-Lesse speleothems displayed δD values close to those of present-day cave seepage water. In contrast to previous authors, no δD offset of -20 to -30‰ was observed. However, the δD value of the water released by Han-sur-Lesse samples during calcite decomposition (550-900°C) was ∼7‰ depleted compared to the δD value of water released before decomposition (25-550°C), i.e. decrepitation. Since the amount of water released during decomposition of Han-sur-Lesse calcite was more reproducible than the amount released before decomposition, the study suggests the release of a 'structurally determined' amount of water with only slightly lower δD values between 550 and 900°C in these speleothems. δD measurements on a wider range of speleothem samples are however needed to generalise the observed differences in δD of water recovered in different temperature intervals.

Contamination of the recovered inclusion water occurred due to the simultaneous recovery of isotopically depleted water (δD of -130‰), bound to lime powder (hydration water of lime) present in the extraction cell and line. The hydration water is released when temperature in the sample cell reaches 400°C. This contamination results in too negative δD values of recovered inclusion water.

5.7 Acknowledgements.

We thank Jean-Michel Geneste (CNP, Périgueux, France), Gérard Delorme (Les Eyzies, Dordogne, France), Proumeyssac and Aven Armand cave managers and Yves Quinif (Faculté Polytechnique de Mons, Belgium) for providing us with the samples used in this study. We are thankful to Daniele Pinti (Univ of Paris XI), Myriam Barr-Matthews (Geological Survey, Israel), and Shioban McGarry (University of Bristol, UK) for their advices and help.

6

Fossil dripwater in stalagmites reveals Holocene temperature and rainfall variations in Amazonia

Abstract

Most proxy records used for reconstruction of Holocene climate of Amazonia are unable to quantitatively distinguish between the effect of temperature and rainfall amounts.

We present a new isotope technique applied to a $\sim$13500 yr old stalagmite archive from Peruvian Amazonia. By analysing the coupled isotope composition of fossil dripwater trapped in stalagmite fluid inclusions, and that of the calcite hosting the fluid inclusions, we were able to calculate independent paleotemperatures and rainfall amounts.

This stalagmite record shows that Holocene climate variation was controlled by orbitally-forced Southward migration of the Inter Tropical Convergence Zone. While temperature remained constant, isotope variation of rainwater, reflected in fluid inclusion water δ^{18}O composition, suggests a $\sim$15-30% increase in convective rainfall through the Holocene.

A comparison of the low-land Peruvian fluid inclusion record with the high Andean Huascaran ice core record shows a constant $\sim$12‰ offset of δ^{18}O curves for the Holocene, suggesting that Andean vertical temperature gradients (lapse rates) did not vary much over the last 9000 years. During the Younger Dryas interval, however, the offset of δ^{18}O values was much higher than in the Holocene. This may be attributed to a relative drop in air

---

This chapter is based on: van Breukelen, M.R., Vonhof, H.B., Hellstrom, J.C., Wester, W.C.G., Kroon, D. (2008). Fossil dripwater in stalagmites reveals Holocene temperature and rainfall variations in Amazonia. *Earth and Planetary Science Letters*, 275(1-2):54-60

temperatures in the highlands (higher lapse rate), caused by long distance teleconnections to climate perturbations in the North Atlantic.

In a wider perspective, fluid inclusion isotope analysis drastically improves paleotemperature reconstructions based on speleothem calcite δ^{18}O data, because it provides the δ^{18}O value of drip water through time, which is usually the most important unknown in paleotemperature equations.

6.1 Introduction

The climate history of the Amazon Basin has been studied intensively over the last decades, with particular focus on Glacial-Interglacial variability, and its effect on biodiversity in Amazonia (Hooghiemstra and van der Hammen, 1998). Of crucial importance for our understanding of the relation between climate and biodiversity is our ability to quantitatively determine temperature and rainfall variation in space and time. However, nearly all currently applied climate proxy records in Amazonia are affected by temperature as well as rainfall amounts (Hooghiemstra and van der Hammen, 1998; Thompson et al., 2000). This is particularly limiting for the interpretation of high-resolution stable isotope climate records, like ice cores (Ramirez et al., 2003; Thompson et al., 1995; Thompson et al., 2000), lacustrine calcite (Seltzer et al., 2002) and speleothems (Cruz et al., 2005a). While these isotope records are highly valuable for our understanding of high resolution Holocene climate variation, quantification of the variation of temperature relative to rainfall amounts remains problematic.

Here, we present new speleothem-based isotope records from Peruvian Amazonia, which allow quantification of the effect of temperature and rainfall amounts on isotope signals in Amazonia. Of pivotal importance in the present study is the application of a technique to analyze the stable isotope composition of fossil dripwater trapped as fluid inclusions in speleothem calcite (Vonhof et al., 2007; Vonhof et al., 2006).

Speleothems (stalagmites) commonly contain microscopic water-filled cavities. These so-called fluid inclusions are filled with cave drip water from the time of formation of the relevant speleothem growth increment (Harmon et al., 1979; Schwarcz et al., 1976). It has been established that cave drip water, and thus fluid inclusion water, is isotopically identical to local rainwater (for δ^{2}H and δ^{18}O; Caballero et al., 1996; McDermott et al., 2006). In arid regions cave drip water may deviate from rainwater due to evaporation. However, this is not likely to be the case in the humid tropical climate of our study area.

Speleothem calcite hosting the fluid inclusions can be dated at high precision by Uranium-series chronology (McDermott et al., 2006; Richards and Dorale, 2003). Stable isotope records from speleothem calcite are commonly used as paleoclimate proxy (Bar-Matthews et al., 1999; Cruz et al., 2005a; Fleitmann et al., 2003a; Genty et al., 2003; Wang et al., 2005; Wang et al., 2001; Yuan et al., 2004). It is a powerful tool, because a wide variety of climate phenomena like El Niño events (Frappier et al., 2002), the Little Ice Age (Holmgren et al., 1999), the Younger Dryas (Bar-Matthews et al., 1999; Genty et al., 2006; Vacco et al., 2005;

Yuan et al., 2004) and Dansgaard Oeschger events (Genty et al., 2003; Wang et al., 2001) are recognised in these isotope records. Oxygen isotope records of carbonates are commonly used as a direct paleotemperature proxy, because at known δ^{18}O values of formation water and calcite that forms from it, the temperature of calcite formation can be calculated (Craig, 1965; Epstein et al., 1953; Kim and O'Neil, 1997). This proxy system is based on the known temperature dependency of oxygen isotope fractionation between calcite and the water in which the calcite precipitates. The most important limitation for the application of this proxy to calculate paleotemperatures concerns the uncertainty on the assumed δ^{18}O value of past formation water. For marine records, this is not too much of a problem because past δ^{18}O variation in the oceans is limited, and relatively well understood (Shackleton and Opdyke, 1973). However, for continental records like speleothems, climate change affects drip water isotope composition in a less predictable way. Therefore, quantification of the contribution of temperature to speleothem δ^{18}O records is impossible based on the δ^{18}O value of the speleothem calcite alone (Fairchild et al., 2006b; Harmon et al., 1978; Hendy and Wilson, 1968; Schwarcz and Yonge, 1983).

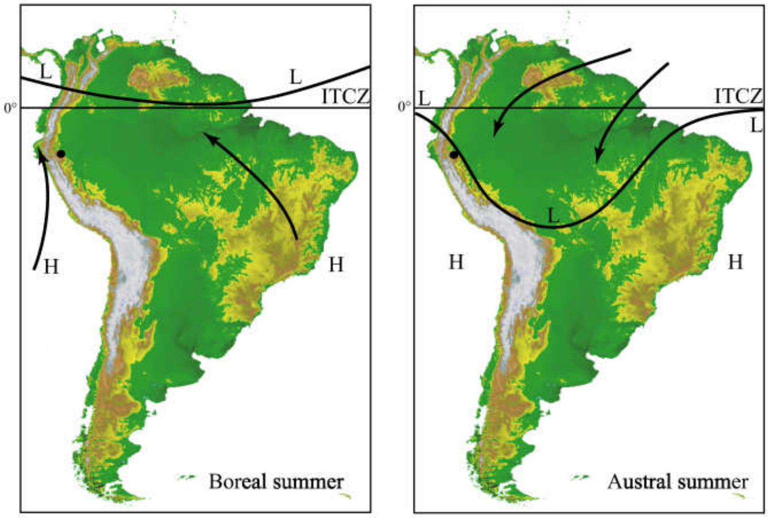

Figure 6.1: Map of South America showing the generalized position of the Inter Tropical Convergence Zone (ITCZ; black line) during Boreal summer (July) and Austral summer (January). The black dot marks the position of Cueva del Tigre Perdido, which lies under the ITCZ in Austral summer. Arrows indicate the prevailing wind direction, during the season. H and L indicate the position of high- and low pressure areas.

The ability to analyse stalagmite fluid inclusion δ^{18}O values eliminates the uncertainty associated with reconstruction of drip water δ^{18}O values back in time, and thus allows for the reconstruction of independent speleothem growth temperatures based on paired fluid inclusion and host $CaCO_3$ δ^{18}O values. Since drip water isotope composition is believed to reflect that of rainfall recharging the cave aquifer, fluid inclusion isotope values in stalagmites furthermore provide temporal records of rainfall isotope variation which can be related to changing rainfall patterns through time (McDermott et al., 2006; Vonhof et al., 2006).

6.2 Results

We analysed δ^{18}O values of fluid inclusions and host calcite of speleothems collected in the Cueva del Tigre Perdido near the town of Nueva Cajamarca in the Peruvian district San Martín (figure 6.1). This cave lies in a densely vegetated area in the foothills of the Andes, at ∼1000 meter above sealevel. The composite record consists of two stalagmites, with an age model based on 15 TIMS U-series ages from the lab of VU University Amsterdam, and 5 additional MC-ICP-MS ages from the lab of Melbourne University (figure 6.2). A high-resolution δ^{18}O record of speleothem calcite shows a long cycle through the Holocene (figure 6.3), with an amplitude of ∼2‰.

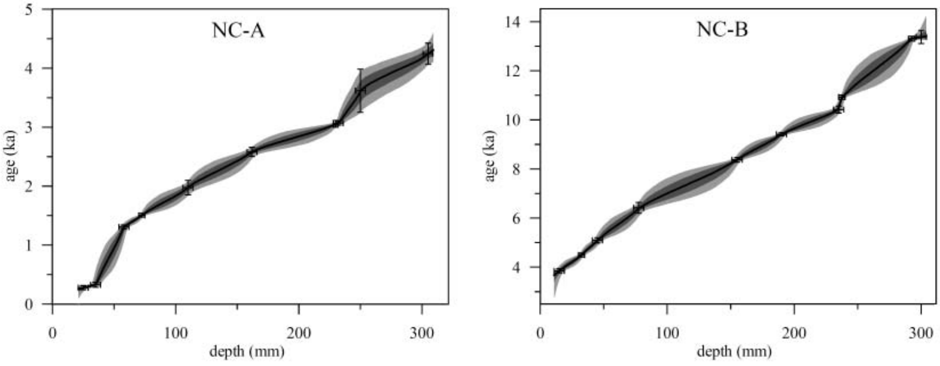

Figure 6.2: Age model of stalagmites NC-A and NC-B. Shown are all TIMS and ICP-MS uranium series ages from labs in Amsterdam and Melbourne combined. 1 and 2 sigma errors are indicated in different shades. Procedure for U and Th isotope analysis at the VU University Amsterdam is given in the additional materials. Procedure for U and Th isotope analysis at the University of Melbourne is described in detail in Hellstrom (2003). The age correction is according to equation 1 of Hellstrom (2006), for an initial [230/232] of 1.5 ± 1.5. The age-depth modelling techniques used are as described in the supplementary materials of Drysdale et al. (2005).

Petrographic analysis of both speleothems studied, reveals the presence of abundant fluid inclusions in speleothem calcite (figure 6.4). Speleothem mineralogy and fluid inclusions are interpreted to be primary, which leads us to conclude that fluid inclusion isotope composition is undisturbed since the time of formation.

A total of 18 cubes of speleothem calcite, weighing ∼0.3 gram each, were cut from a central slab of the stalagmites, crushed, and the liberated inclusion water analyzed for δ^{2}H and

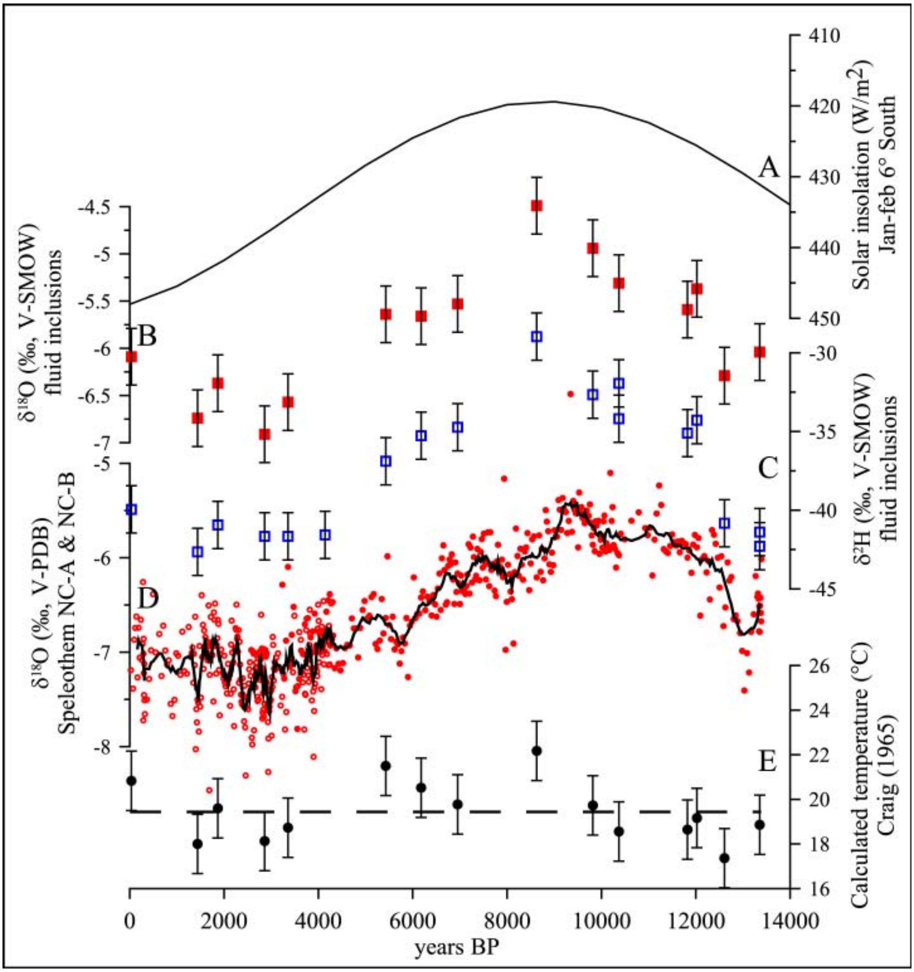

Figure 6.3: Plot of the February solar insolation curve at 6 degrees South (Laskar et al., 2004) (panel A) compared with isotope data obtained from the Cueva del Tigre Perdido record. Shown are δ^{18}O values (panel B) and δ^{2}H values (panel C) of fluid inclusion water. Dating error is smaller then the size of the symbol used. Panel D shows δ^{18}O values of speleothem calcite. Long term trends in all isotope records are in phase with the solar insolation curve. Paleotemperatures, shown in panel E, are calculated based on δ^{18}O data from panel B and D, using the paleotemperature equation by Craig (1965). Horizontal dashed line in panel E represents the average temperature calculated. Error bars on fluid inclusion isotope data and on calculated temperatures are based on 1SD reproducibility of standard waters routinely analyzed within fluid inclusion isotope runs (Vonhof et al., 2007). In panel D, solid (open) dots represent data from the NC-B (NC-A) stalagmite. The black solid curve represents an 11-point running average through the data.

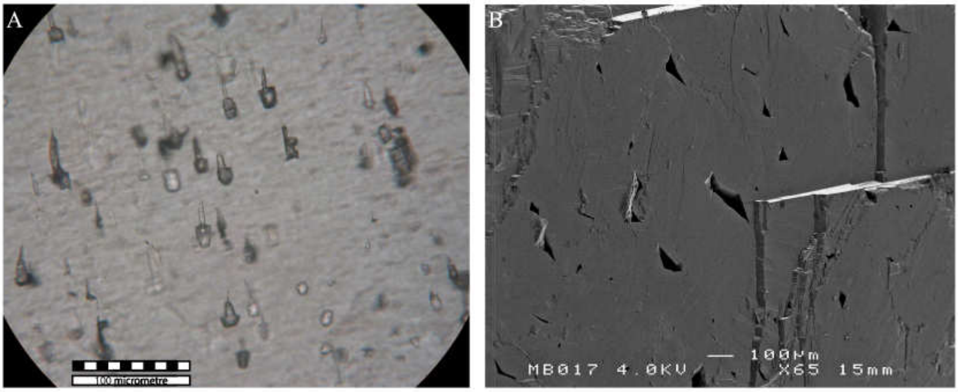

Figure 6.4: Petrographic images of typical fluid inclusions found in the stalagmites studied. Figure 6.4a provides an example of fluid inclusions patterns in thin sections of NC-B stalagmite. Figure 6.4b is a Scanning Electron Microscope (SEM) image of a freshly broken calcite surface from NC-B, showing dense calcite with relatively large fluid inclusions. Distribution and geometry of fluid inclusions suggest that they are not interconnected and have not been diagenetically modified since their formation.

δ^{18}O, applying the technique described by Vonhof et al. (2006, 2007).

Results show ∼15‰ variation in δ^{2}H values and ∼2‰ in δ^{18}O values. δ^{2}H values of the youngest part of the stalagmite record plot at approximately -42‰ (SMOW) which is in reasonably good agreement with the -46‰ value analysed for some local rainshowers and from the river that runs through the cave. δ^{18}O and δ^{2}H values combined plot on the Global Meteoric Water Line (GMWL; figure 6.5). Since modern rainwater isotope data for Amazonia generally plot on the GMWL (Gat and Matsui, 1991), this observation provides further support for the excellent preservation of the original isotope composition of fluid inclusion water in these speleothems, since post-depositional changes in the fluid inclusion water isotope composition would have driven the water away from the GMWL. Three cubes, however, gave isotope values that plotted away from the GMWL. These were samples with a low water yield (<0.1 μl), resulting in erroneous δ^{18}O values, as was confirmed by yield tests with an in-house water standard. Duplication of two of these analyses with larger cubes of calcite, suggests that the δ^{2}H values of these low-yield samples are accurate, but the δ^{18}O values are not. For the following discussion of the data, only the δ^{18}O values of these three low-yield samples were discarded.

6.3 Discussion

Results are plotted stratigraphically in figure 6.3. The δ^{2}H and δ^{18}O values of fluid inclusion water appear to vary in phase with speleothem calcite δ^{18}O values and with orbitally-forced

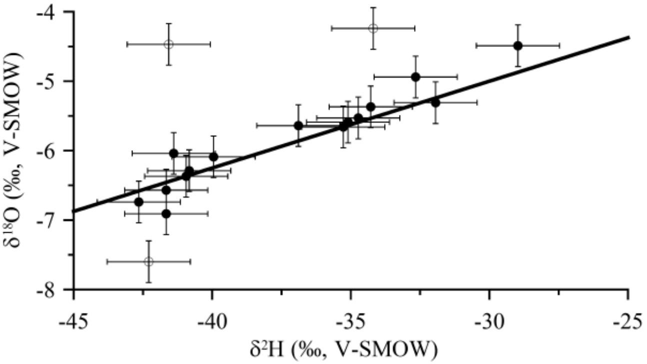

Figure 6.5: δ^{18}O and δ^2H values of all analysed fluid inclusion samples. The black line represents the Global Meteoric Water Line (GMWL) Most fluid inclusion values plot on the GMWL, except for three obvious outliers (open dots). These three samples had the lowest water yields of the dataset at <0.1 microliter per crush. Standard water injection experiments confirmed that δ^{18}O values are no longer reproducible at such low water yields, leading us to reject the δ^{18}O values of these three low-yield samples. Subsequent duplicate analysis of two of these three samples confirmed that δ^2H values of the low-yield samples were still reliable.

wet season (February) insolation (figure 6.3). After an isotope maximum at ~9000 years BP, coincident with the Holocene insolation minimum, a trend towards lower isotope values runs parallel with slowly increasing insolation energy.

Such a Holocene isotope pattern is not unique in Amazonia. Similar isotope trends were reported for the Andean Ice cores (Thompson et al., 2006; Thompson et al., 2000) and Lake Junin on the Peruvian Altiplano (Seltzer et al., 2002) (figure 6.6). Although small differences exist, the general Holocene trend for all these records appears to be insolation-forced.

Although the patterns are similar, the interpretation of these records in terms of Holocene temperature and rainfall variation is still debated. Some interpret the Holocene isotope pattern to be mainly temperature controlled (Thompson et al., 1995; Thompson et al., 2000), while others advocate rainfall as the controlling parameter (Broecker, 1997; Henderson et al., 1999; Ramirez et al., 2003; Seltzer et al., 2002; Vimeux et al., 2005).

Insolation forcing of Holocene Amazonian climate may have affected temperature as well as rainfall amounts, because increased insolation energy can raise surface temperatures, or convert to latent heat and enhance convective rainfall (Thompson et al., 2000; Vuille et al., 2003).

In our study area in Northern Peru, insolation controls the dynamics of the Inter Tropical Convergence Zone (ITCZ; figure 6.1). This results in characteristic seasonal rainfall patterns as the ITCZ band of maximum convection migrates over the continent, tracking the latitudinal displacement of maximum insolation (Marengo and Nobre, 2001). An orbitally-forced southward displacement of the complete ITCZ system through the Holocene resulted in a gradual increase in convective rainfall in our study area, as opposed to a decrease of rainfall over northern South America (Haug et al., 2001; Seltzer et al., 2000). Intensification of convective rainfall typically decreases δ^{18}O values of rain water (Garreaud et al., 2003; Vuille et al., 2003). Southward displacement of the ITCZ system in the Holocene and the associated increase of total insolation in our study area may also have had an effect on surface temperatures, if one assumes that part of the increase in insolation energy was not converted to latent heat (Rozanksi and Araguás-Araguás, 1995).

The Tigre Perdido stalagmite record offers new insights in the relative changes of temperature and convective rainfall through the Holocene, because this record provides independent paleotemperatures and rainfall isotope composition. Paleotemperatures are calculated by using coupled calcite δ^{18}O and fluid inclusion δ^{18}O values as input parameters in a paleotemperature equation. Most commonly used for inorganically precipitated calcite is the equation by Kim and O'Neil (1997). Resulting paleotemperatures for the Tigre Perdido record show little variation, as to be expected for this area in the Holocene. However, at ~17 degrees Celsius, calculated temperatures are much lower than the modern cave temperature which lies at ~22 degrees Celsius. This apparent mismatch is a well known phenomenon for speleothem based paleotemperature reconstructions. Mickler et al. (2004) show that modern speleothem calcite from Barbados precipitates in oxygen isotope disequilibrium, and suggest that this is due to kinetic fractionation. Such fractionation will lead to calculated paleotemperatures that can be several degrees Celsius too low. A recent compilation of available cave monitoring data, McDermott et al. (2006) demonstrates that this effect occurs in other caves as well. This compilation further shows that among the different paleotemperature equations available, the Kim and O'Neil (1997) equation leads to temperatures that are several degrees Celsius too low. More accurate temperatures appear to be calculated by the equation of Craig (1965). Application of the Craig (1965) equation to the Tigre Perdido record results in a Holocene paleotemperature of ~ 20 degrees Celsius (figure 6.3), indeed much closer to modern cave temperatures of ~22 degrees Celsius than the 17 degrees Celsius calculated from the Kim and O'Neil (1997) equation. The total observed variation around the mean value does not exceed the analytical uncertainty on the input parameters, which are largely controlled by the analytical uncertainty of the fluid inclusion isotope analyses (reproducibility (1σ) is <1.5‰ for δ^{2}H, and <0.3‰ for δ^{18}O (Vonhof et al., 2007; Vonhof et al., 2006)).

At stable Holocene temperatures, the observed 2‰ δ^{18}O variation in speleothem calcite and fluid inclusion water apparently reflects rainwater isotope variation related to increasing convective rainfall through the Holocene. Estimates of the relation between δ^{18}O and rainfall amount for the Amazon Basin, based on modern IAEA precipitation data, show that the majority of lowland IAEA stations cluster between -0.4 and -0.8‰ /100 mm (Vuille et al., 2003). For the Tigre Perdido record this would relate to a 250 to 500 mm rainfall increase from 9000 yr BP towards the present day value of ~1500 mm/yr. This must probably be taken as a maximum estimate because Cueva del Tigre Perdido is located at ~1000m ASL, already in the foothills of the Andes, and the slope of the δ^{18}O – rainfall amount relation for highland IAEA stations is significantly steeper than for the lowlands (Vuille et al., 2003).

Tigre Perdido isotope data thus confirm that insolation-forced changes in rainfall, and not temperature, are the dominant parameter affecting the climate of lowland Amazonia, as was already suggested by several previous studies (Cruz et al., 2005a; Ramirez et al., 2003; Seltzer et al., 2002).

To further investigate the transfer of atmospheric moisture from the Amazonian lowlands to the Altiplano, we compare the Tigre Perdido record with the Holocene interval of the Huascaran Ice core record (figure 6.6). There is a striking similarity in the shape of the Holocene δ^{18}O curves of both records, with a nearly constant ∼12‰ offset between Huascaran and Tigre Perdido water δ^{18}O values, in good agreement with the expected orographic fractionation effect for rainfall between the two sites (Grootes et al., 1989; Rozanksi and Araguás-Araguás, 1995; Thompson et al., 2000). This suggests that the Huascaran Ice Core record accumulated from essentially the same moisture that first produced the rainfall trapped in the fluid inclusion record of Tigre Perdido. No isotope fractionation other than the orographic effect is required to match the general Holocene isotope curves between the two sites which implies little variation of the vertical atmospheric temperature gradient (lapse rate) between the two sites through the Holocene.

This situation is different for the Younger Dryas interval (figure 6.6). Here, the Ice core record shows a deep minimum in δ^{18}O values which are ∼6‰ lower than those of the early Holocene (∼9000 yrs BP) and ∼4‰ lower than late Holocene values. The Tigre Perdido δ^{18}O record shows a much smaller Younger Dryas excursion which is ∼2‰ lower than the early Holocene maximum, and comparable to modern values. The extra ∼4‰ decrease of δ^{18}O values for snowfall at Huascaran compared to that of rainfall at Cueva del Tigre Perdido can be interpreted in two ways: The first option is an increased lapse rate, by which the altiplano was ∼2-3 degrees cooler in the Younger Dryas relative to the lowlands. The second option is that atmospheric circulation changes in the Younger Dryas interval drove up the mean condensation level of precipitation over the altiplano, resulting in isotopically colder snow while the lapse rate remained unchanged (Thompson et al., 2000).

The isotope signature of the Younger Dryas interval in the Tigre Perdido stalagmite suggests increased convective rainfall compared to the early Holocene interval of the same record. Isotope values are similar to modern values, suggesting rainfall amounts of ∼1500 mm/yr, while the insolation was distinctly lower. Since the Younger Dryas interval typically is a higher latitude phenomenon, long distance teleconnections are required that translate high latitude cooling to the tropics. Modelling as well as proxy record studies suggest that increased meridional (North to South) sea surface temperature gradients in the Pacific and Atlantic Oceans cause convective rainfall to migrate southwards (Garreaud et al., 2003; Haug et al., 2001), leading to dryer conditions in the northern tropics (Haug et al., 2001) and wetter conditions in the southern tropics (Baker et al., 2001b), where our stalagmite record is located. The seesaw pattern between the northern and southern tropical records is particularly clear in the comparison of the (southern tropics) Tigre Perdido Cajamarca δ^{18}O record with the (northern tropics) Cariaco basin Ti and Fe record (Haug et al.,

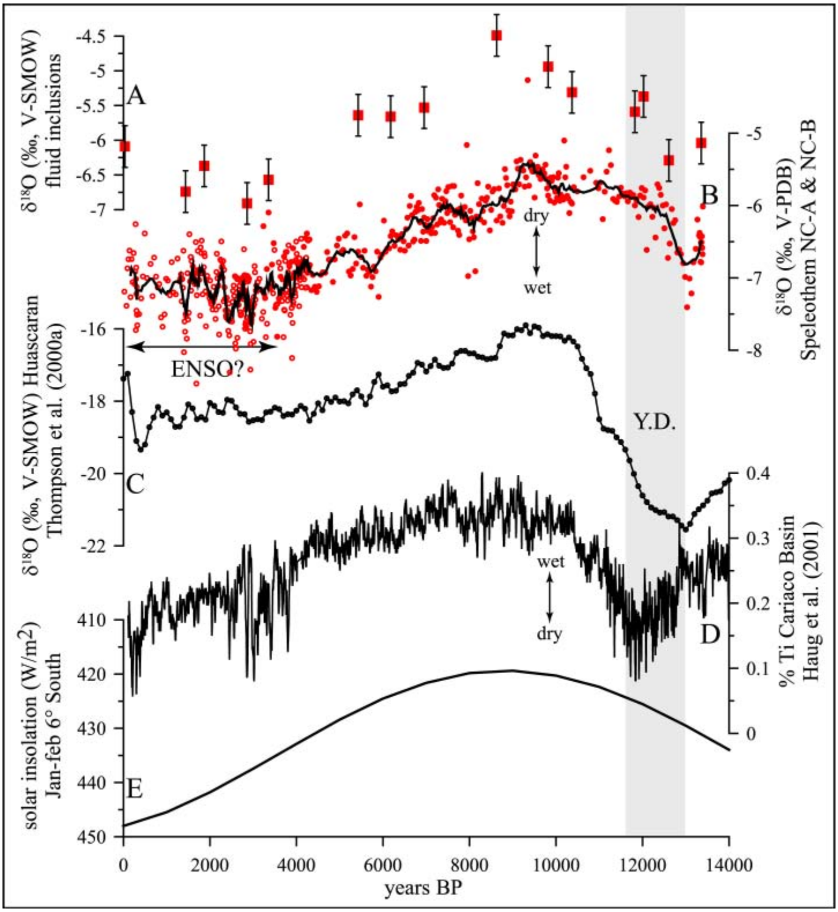

Figure 6.6: Comparison of the Cueva del Tigre Perdido δ^{18}O fluid inclusion (panel A) and δ^{18}O calcite (panel B) records with the Huascaran δ^{18}O ice core record (panel C) (Thompson et al., 2000) and with the Cariaco Basin Ti% record (panel D) (Haug et al., 2001). All records show Holocene trends in phase with the solar insolation curve (panel E). Rapid climate oscillation occurs in all three records during the Younger Dryas (YD) interval (grey zone). The much stronger response in the Huascaran δ^{18}O record, compared to the Cueva del Tigre Perdido δ^{18}O record, suggests a stronger impact of YD climate change in the highlands. A comparison of the Cueva del Tigre Perdido isotope record with the Cariaco Basin Ti% record, reveals that wet YD conditions in Amazonia, coincided with Dry conditions over Northern Venezuela. This seasaw pattern suggests that climate change over Amazonia in the YD interval was primarily controlled by a general Southward movement of the ITCZ. A more detailed comparison of Cueva del Tigre Perdido calcite δ^{18}O with the Cariaco Basin Ti% record shows another similarity between the two records, in that the amplitude of high-resolution variation drastically increases in the last 4000 years. Haug et al. (2001) attributed this to increased ENSO activity from ∼4000 years BP onwards.

2001; figure 6.6). Both records primarily record rainfall amounts on the South American continent over the last ~13500 years. Although thousands of kilometres apart the shape of both curves is remarkably similar, correlating dry phases in Venezuela, with wet phases in Peru (figure 6.6). The consistency of these records underlines the regional significance of the Tigre Perdido record, and again pinpoints ITCZ migration as the main control on tropical South American rainfall patterns. We tentatively suggest that even the higher-frequency variation, interpreted to be ENSO related in the interval after 3800 yrs BP in the Cariaco record (Haug et al., 2001), can be identified in the Tigre Perdido record as well (figure 6.6).

6.4 Conclusions

The present study shows how stalagmite fluid inclusion isotope analyses provide information on the isotope composition of paleorainfall in a datable context.

In Amazonia the δ^{18}O composition of rainwater is affected by temperature and rainfall amounts, which complicates the quantitative interpretation of fluid inclusion isotope data. However, by combination of δ^{18}O values of fluid inclusion water and its surrounding calcite, independent paleotemperatures can be calculated based on the known temperature dependency of δ^{18}O fractionation between speleothem calcite and formation water. By application of this technique to the Cueva del Tigre Perdido stalagmite record, we can distinguish between the effects of temperature and rainfall δ^{18}O values on the isotope patterns in stalagmite calcite.

Holocene climate variation, as recorded in the stalagmite, appears to be controlled by orbitally forced Southward migration of the ITCZ, causing increasing convective rainfall in our study area. While temperature remains stable, isotope variation of rainwater reflected in fluid inclusion water δ^{18}O composition suggests a ~15-30% increase in convective rainfall through the Holocene.

The isotope pattern observed in stalagmite fluid inclusions matches isotope patterns in the high Andean Huascaran Ice Core record. This similarity suggests that Andean lapse rates did not vary much through the Holocene (Vizy and Cook, 2007). Since temperatures calculated for the Cueva del Tigre Perdido stalagmite were stable, it follows that not temperature but ITCZ dynamics controlled the long trend in Holocene δ^{18}O values for Huascaran. This coupling between the two records does not exist for the Younger Dryas interval. Here, the higher amplitude δ^{18}O excursion in the Huascaran record compared to the Cueva del Tigre Perdido record, may suggests a temporarily increased lapse rate or a change in atmospheric circulation over the altiplano, forced by increased meridional sea surface temperature gradients due to cooling of higher latitudes. This same effect would account for a southward shift of the ITCZ, that caused increased rainfall in the southern tropics, and decreased rainfall in the northern tropics during the Younger Dryas.

In a wider perspective, fluid inclusion isotope analysis drastically improves paleotemperature reconstructions based on speleothem calcite δ^{18}O data, because it provides the δ^{18}O value of cave drip water through time, which is usually the most important unknown in paleotemperature equations. Results for the Cueva del Tigre Perdido show that some of the commonly used equations underestimate the actual temperatures in the cave more than others. Our poor understanding of the differences in accuracy between equations underlines the importance of further investigation into isotopic equilibrium during growth of speleothems.

In any case, the technique presented here allows for reconstruction of past rainfall δ^{18}O variation in climate zones where ice cores are scarce or absent. This is highly significant for our understanding of past climate variation, particularly in view of recent developments of isotope modules in climate models (Vuille et al., 2003).

6.5 Acknowledgements

We thank Quinto Quaresima and Jhon Huaman for speleological assistance and INGEMMET and INRENA for logistical support in Peru. We are indebted to Gareth Davies for U/Th dating in Amsterdam. Saskia Kars and Onno Postma gave invaluable technical assistance. This project was financially supported by NWO-WOTRO and the British Council.

7

High resolution stable isotope and trace element speleothem records of the last ~5000 year, Cueva de las Lechuzas, lowland Peruvian Amazonia

Abstract

Stable isotope ratios (δ^{13}C, δ^{18}O) and trace element concentration of Mg, Sr and Ba in a late Holocene speleothem CLL-1 from the Cueva de las Lechuzas in Peruvian Amazonia show a distinct centennial-scale cyclicity for the last ~5000 years.

Cave seepage water feeding the stalagmite consists of water from a meteoric origin. Variability in the measured climate proxies time-series was directly caused by changes in climate outside the cave. Oxygen isotope data of this tropical speleothem calcite reflects variations in the amount of convective rainfall. Low δ^{18}O values are interpreted as increased amounts of rainfall in our study area.

Mg and Sr concentration variation is in phase with stable isotope cyclicity and interpreted as changes in prior calcite precipitation due to variation in the percolation time of the seepage water (Fairchild et al., 2000). High amount of rainfall (i.e. low δ^{18}O values) will reduce the percolation time of seepage water from the surface to the cave interior. This results in reduced Mg and Sr concentration in speleothem calcite because higher percolation rates lead to decreased calcite precipitation along the percolation pathway.

The observed frequency of the cycles is remarkably regular, and in the range of centennial solar cycles. Variation of the insolation energy on itself is limited, but may be amplified

in Amazonia through the sensitive response of the InterTropical Convergence Zone (ITCZ) to changing equatorial Sea Surface Temperatures (SST's). In that case stalagmite CLL-1 from Peruvian Amazonia directly records the intensity of the ITCZ in it's isotope and trace element chemistry.

7.1 Introduction

The Amazon Basin is defined as the drainage area of the Amazon River. This area with an estimated surface of about 2.7 million square kilometres is covered by the world's largest tropical forest. Its existence depends on large quantities of rainfall transported by the Amazonian hydrological cycle, largely controlled by the distribution of solar heat. Knowledge of the behaviour of the hydrological cycle in the past and associated rainfall pattern, are crucial to understand the development of this area.

Stable isotope data provide valuable information to reconstruct paleo-rainfall patterns (Cruz et al., 2006; Vuille et al., 2003). In South America high resolution stable isotope records are available from the Andean Highlands, such as ice cores (Thompson et al., 1998; Thompson et al., 1986; Thompson et al., 1995; Thompson et al., 2000) and sediment cores (Baker et al., 2001a; Baker et al., 2001b; Seltzer et al., 2002). Lowland paleo-climate data are available as pollen records (Hooghiemstra and van der Hammen, 1998) and offshore sediments (Maslin and Burns, 2000), but only few lowland high resolution stable isotope records are available (Cruz et al., 2005a). Speleothems collected in lowland Amazonia can provide this missing data and fill this gap in lowland Peruvian Amazonia stable isotope records.

Speleothems are secondary calcite deposits formed in caves and are widely used as paleoclimate records. Their wide geographical distribution and long time ranges, coupled with the ability to accurately date them back to ~500,000 years by measuring U-series disequilibrium make them particularly useful. Several chemical proxies can be measured to reconstruct paleo-environmental changes. Most commonly used are stable isotope composition (Bar-Matthews et al., 1999; Cruz et al., 2005a; Hendy, 1971) and trace element concentrations (Hellstrom and McCulloch, 2000; Johnson et al., 2006; Roberts et al., 1998; Treble et al., 2003; Verheyden et al., 2000). Traditionally, the focus is more on stable isotope composition, although the interest in trace element composition as paleo-environmental recorder is growing, especially for high resolution annual cycles. These annual cycles aid in the reconstruction of an alternative age framework (Roberts et al., 1998). Paleo-temperature reconstructions using Mg/Ca ratio were suggested, based on the temperature dependent magnesium calcite-water distribution coefficient (Gascoyne, 1983), similar as seawater growing calcite skeletal organisms (Elderfield and Ganssen, 2000). Unfortunately the magnesium concentrations are often highly variable in cave seepage water, making reliable temperature reconstructions based on Mg/Ca ratio impossible (Fairchild et al., 2006b).

Experimental and cave monitoring studies suggest a relationship between the trace element concentration in seepage water and rainfall outside (Treble et al., 2003). It has become clear that hydrological pathways into the cave are particularly important for the trace element signal recorded in the speleothem calcite (Fairchild et al., 2000; Verheyden et al., 2000). Fairchild et al (2000) published a detailed study on the trace element composition of seepage water, giving explanations for typical observed in-phase Sr and Mg concentrations but also antiphase Sr and Mg concentrations. Both observations were explained by precipitation mechanisms occurring along the flow path of the seepage water, namely prior calcite precipitation and incongruent dolomite dissolution.

Here we present high resolution stable isotope and trace element records of a speleothem from Cueva de las Lechuzas, a cave located in lowland western Amazonia. The record exhibits high resolution variability in stable isotopes and trace elements. The control of climate on speleothem trace element variation will be discussed in detail.

7.1.1 Hydrology

As the cave hydrology plays a vital roll in the transfer of the trace element signal to the speleothem calcite, a monitoring study was carried out between 2003-2004 in Cueva de las Lechuzas. This cave, located in the western Amazon basin, showed variable hydrological conditions for different Halls within the same cave (see chapter 2). The drip rate of stalagmite CLL-1 was monitored for a 1-year period, providing no evidence for seasonal variation of the drip rate. This was supported by the stable isotope composition of the drip water, which did not show detectable seasonal variation. Thus climate signals incorporated in the stalagmite calcite would only record variation on interannual time-scales, which makes this stalagmite particularly suitable for a long-term climate study.

7.1.2 Cueva de las Lechuzas

Cueva de las Lechuzas (figure 7.1) is a cave located in a karstic plateau in the high Peruvian rainforest close to the town Tingo Maria at 700 m.a.s.l. (S 09°19'44.4", W 76°01'37.5"). This area is one of the wettest parts of the Amazon basin with up to 3900mm annual rainfall. The Late Triassic Limestone of the Grupo Pucará of Norian age, dipping 45° to 50° southeast, forms the host rock of the cave. Above the cave, dense tropical rainforest vegetation occupies the karst plateau. The climate is tropical with a mean annual temperature of 24.7°C and humidity around 77%.

Cueva de las Lechuzas is a touristic cave and managed by the national governmental organization Instituto Nacional de Recursos Naturales (INRENA; figure 7.1). A wooden pathway and staircases have been built to access the cave. The entrance hall is ~25 meters high and gives shelter to a large colony of guácharos (*Steatornis caripensis)*, a protected cave bird. The floor is covered with a thick layer of bird and bat guano. The entrance hall gives access to a second and third hall, which form the lower level of the cave. In this area bats are still present but guácharos are not. Halls 4 and 5 (figure 7.1) were discovered and mapped during our investigation of the cave system in 2003. The exploration of the cave was not

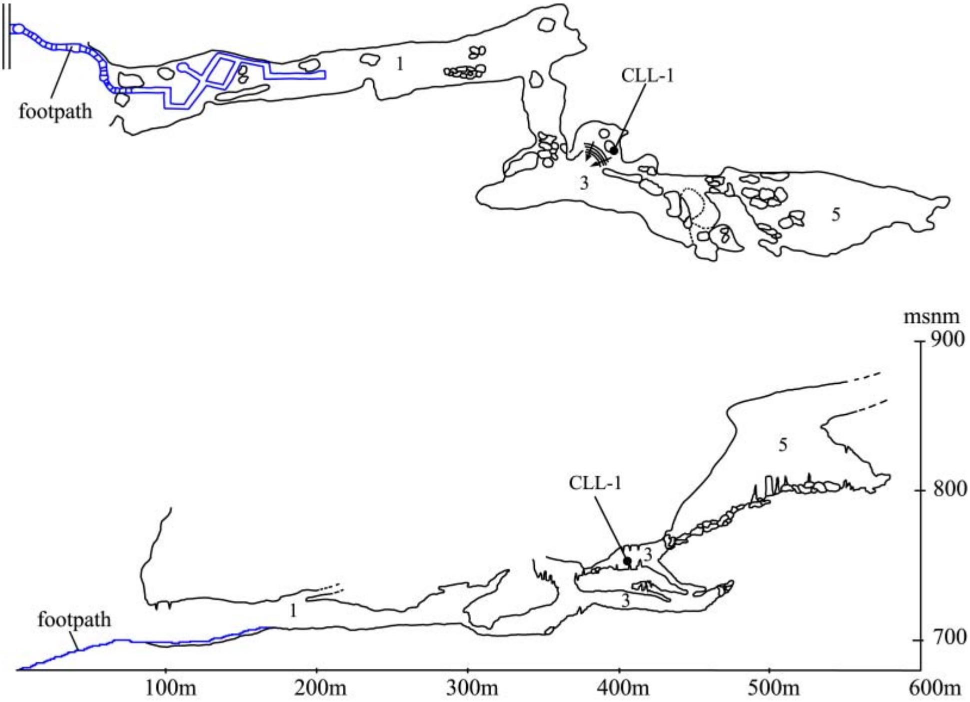

Figure 7.1: Map of Cueva de las Lechuzas with the location of stalagmite CLL-1 indicated. The wooden tourist staircase is indicated in the figure.

completed as the cave continues at the roof of Hall 5. Stalagmite CLL-1 is collected from hall 3, its location is indicated in figure 7.1.

7.2 Material and Methods

7.2.1 Stalagmite CLL-1

Specimen CLL-1 is a ~140cm long 'broomstick' type stalagmite with a diameter of ~7cm. The stalagmite was cut longitudinally into two equal halves. A slice of about 0.5cm thick was cut from each halve. One slice was used to drill small samples for stable isotope and trace element analyses. The other slice was used to cut pieces of carbonate for Uranium-series dating and fluid inclusion isotope analysis.

Large thin sections (5 x 10 cm) were made at the geological technical laboratory at the Vrije Universiteit Amsterdam for petrographic study covering the top 58cm (last ~5,000 years) of the stalagmite. At different depth intervals, Scanning Electron Microscope (SEM) photos were made to visualize the different porosities and carbonate structures in more detail.

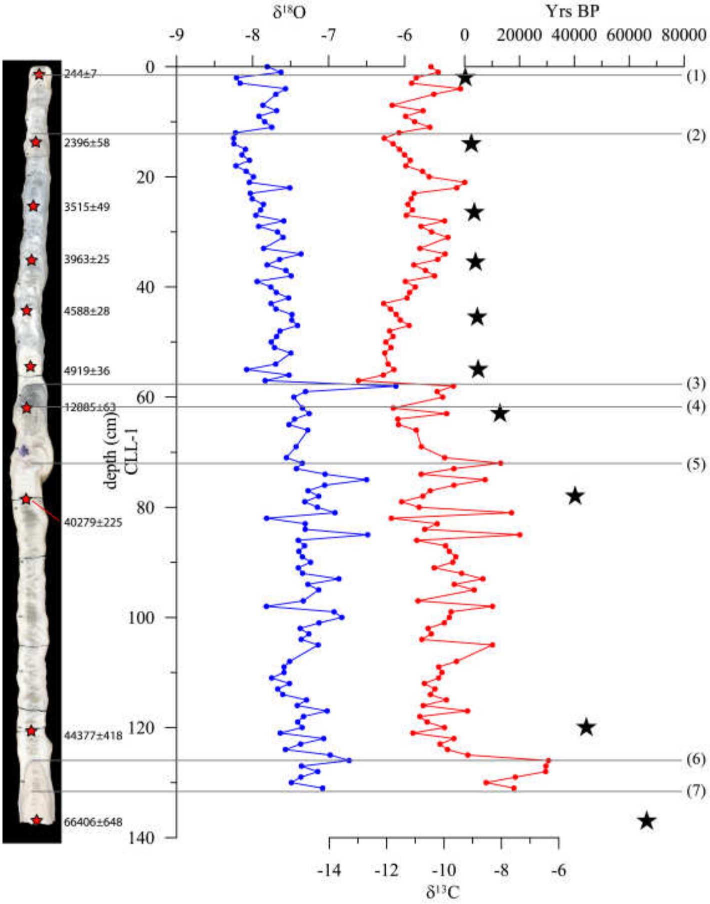

Figure 7.2: Stalagmite CLL-1 with measured U/Th ages indicated. The δ^{18}O and δ^{13}C values are measured at 1cm spatial scale resolution. δ^{18}O and δ^{13}C are measured relative to V-PDB. The starsrepresent the U/Th ages versus depth. The numbered grey lines indicate the visible hiatuses.

7.2.2 Uranium series dating

A total of 11 samples were selected for Uranium-series age dating (table 7.1, figure 7.2). Speleothem CLL-1 has multiple visible hiatuses illustrated in figure 7.2. which are confirmed using U/Th age dating. The top 58cm was formed in the Holocene, at relatively uniform growth rates and covering the last ∼5000 years. As this study focuses on the Holocene, six Uranium-series isotope analyses were performed on the top 58 cm to make a reliable age framework for the last ~5000 year. Speleothems can be dated by the ^{238}U-^{234}U-^{230}Th disequilibrium technique. The ^{238}U-^{234}U-^{230}Th disequilibrium technique on speleothems relies on the fact that speleothems have low Th/U ratios (^{232}Th/^{238}U values of $\sim 8 \cdot 10^{-4}$ to $1 \cdot 10^{-5}$) which is incorporated from the cave seepage water (Dorale et al., 2004; Richards and Dorale, 2003). The extreme fractionation occurs as Th is insoluble in water while U is well soluble. Cave seepage water will therefore mainly contain Uranium. Two of the long-lived daughters of the decay chain from ^{238}U to ^{210}Pb are ^{234}U and ^{230}Th. Through time ^{234}U and ^{230}Th will be formed by the decay of ^{238}U to reach a secular equilibrium state. For Uranium-series age dating speleothem material must have been a closed system since the calcium carbonate was deposited, so that the ^{238}U-^{234}U-^{230}Th ratio is not modified by non-radioactive processes. The ^{230}Th/^{232}Th activity ratio is used to check ^{230}Th contamination at time of deposition. As the activity ratio for ^{230}Th/^{232}Th is well above 100, the amount of non radiogenic ^{230}Th is negligible and no correction for excess thorium is performed (Goede and Vogel, 1991). The equation of Bateman (1910); modified by Edwards et al. (1987b)

$$\left(\frac{^{230}Th}{^{238}U}\right) - 1 = -e^{-\lambda_{230} t} + \left(\frac{\delta^{234}U}{1000}\right)\left(\frac{\lambda_{230}}{\lambda_{230} - \lambda_{234}}\right)\left(1 - e^{-(\lambda_{230} - \lambda_{234})t}\right) \tag{7.1}$$

$$\delta^{234}U = \left(\frac{\left(^{234}U/^{238}U\right)_{measured}}{\lambda_{238}/\lambda_{234}} - 1\right) \times 1000 \tag{7.2}$$

is used to calculate the ages from ^{230}Th, ^{234}U and ^{238}U activities. The λs are decay constants and t is time. The decay constants are: $\lambda_{238} = 1.55125 \cdot 10^{-10}$ yr (Jaffey et al., 1971); $\lambda_{234} = 2.8263 \cdot 10^{-6}$ yr (Cheng et al., 2000); $\lambda_{230} = 9.1577 \cdot 10^{-6}$ yr (Cheng et al., 2000).

The U/Th age dating was performed at the Vrije Universiteit Amsterdam on a Finnigan MAT 262 Thermal Ionization Mass Spectrometer (TIMS). Samples of 2 to 5.5 grams of material were cut from the stalagmite and cleaned in a ultrasonic bath. The samples were dissolved in HNO_3 acid and spiked with a mixed spike containing ^{233}U and ^{229}Th. An Fe-carrier was used to co-precipitate U and Th. Re-dissolved in HNO_3 acid the samples were purified using 1 and 2 column extraction with an anion exchange resin (AGIX 200-400 mesh) for U and Th respectively. The purified U and Th fractions were loaded on a zone-refined rhenium filament for TIMS analyses.

7.2.3 Stable isotopes

Carbonate samples for stable isotope and trace element analyses were drilled at 1 millimetre spatial resolution using a hand held drill tool. δ^{18}O and δ^{13}C values of the carbonate samples were measured on a Finnigan MAT 252 mass-spectrometer, equipped with a Kiel device and on a Finnigan Delta plus mass-spectrometer equipped with a gasbench II. Both instruments are located at the stable isotope laboratory at the Vrije Universiteit Amsterdam. GICS

Sample	depth in core	Sample Wt	^{234}U ppb	uncertainty ^{234}U ppb	^{238}U ppb	uncertainty ^{238}U ppb	^{230}Th ppb	uncertainty ^{230}Th ppb	d^{234}U	uncertainty d^{234}U	d^{234}U$_{initial}$	uncertainty d^{234}U$_{initial}$	(^{230}Th/^{238}U)$_{act}$	uncertainty (^{230}Th/^{238}U)$_{act}$	Age (Yrs) before 2000	uncertainty (yrs)	[^{230}Th/^{232}Th]act	Age initial ^{230}Th corrected	uncertainty (yrs)
			^{234}U (ppb)		^{238}U (ppb)		^{230}Th (ppb)		δ^{234}U		δ^{234}U$_{initial}$		(^{230}Th/^{238}U)$_{act}$		Age (Yrs)			Age ^{230}Th cor	
CLL-1	2	1.76	0.1440	±1.29E-04	449	±0.29	9.7376E-05	±2.81E-06	4944	±5.48	4947	±5.48	0.013	±0.0004	**244**	±7	304	**243**	±10
CLL-1	14	1.74	0.1219	±1.36E-04	381	±0.30	0.00080447	±1.82E-05	4925	±6.71	4958	±6.75	0.129	±0.0029	**2396**	±58	13808	**2396**	±78
CLL-1	26.5	2.16	0.1466	±1.88E-04	458	±0.40	0.00141429	±1.75E-05	4932	±7.68	4981	±7.76	0.189	±0.0023	**3515**	±49	32464	**3515**	±72
CLL-1	35.5	2.10	0.1526	±1.83E-04	474	±0.41	0.00165732	±8.17E-06	4971	±7.36	5027	±7.44	0.214	±0.0011	**3963**	±25	13925	**3963**	±34
CLL-1	45.5	1.99	0.1876	±2.40E-04	579	±0.55	0.00235311	±1.05E-05	5005	±7.97	5070	±8.07	0.248	±0.0011	**4588**	±28	21520	**4588**	±39
CLL-1 (3)	55	5.56	0.1548	±5.55E-04	485	±1.28	0.00208039	±4.70E-06	4917	±21.87	4986	±22.18	0.262	±0.0009	**4919**	±36	3890	**4918**	±44
CLL-1	63	2.37	0.1543	±1.78E-04	510	±0.40	0.00528619	±1.82E-05	4606	±6.40	4777	±6.64	0.633	±0.0022	**12885**	±63	17112	**12884**	±86
CLL-1	78	2.43	0.0718	±6.18E-05	391	±0.22	0.0069837	±2.82E-05	2407	±2.47	2698	±2.76	1.092	±0.0045	**40279**	±225	84275	**40279**	±409
CLL-1 (2)	120	4.87	0.0933	±3.98E-04	479	±1.59	0.00986207	±2.30E-05	2604	±14.07	2952	±15.95	1.257	±0.0051	**44377**	±418	26267	**44376**	±516
CLL-1 (1) bottom	137	3.30	0.0464	±7.12E-05	242	±0.26	0.00681817	±4.21E-05	2542	±4.76	3067	±5.74	1.718	±0.0108	**66406**	±648	2115	**66388**	±953

Table 7.1: The U/Th concentration and ages for stalagmite CLL-1 of Cueva de las Lechuzas. The U/Th measurements are performed on a TIMS at the VUA.

in-house carbonate standard is routinely monitored during sample runs. GICS long-term reproducibility lies within 0.07‰ for δ^{18}O and 0.04‰ for δ^{13}C for the Finnigan MAT 252 and within 0.10‰ for δ^{18}O and 0.10‰ for δ^{13}C on the Finnigan Delta plus mass-spectrometer. The amount of carbonate powder needed for a single measurement is ~20 µg for the MAT252 and ~50 µg for the Delta plus. δ^{18}O measurements of speleothem carbonate are reported in ‰ relative to Vienna PeeDee Belemnite (V-PDB).

7.2.4 Trace elements

Trace elements analyses were performed on a Varian Liberty Series II ICP-OES with a precision of about 0.7-3% depending on the solution concentration ranging from ppm to sub-ppb. The precision is based on the 1σ reproducibility of repeated analyses of 2 control solutions of a standard sample at ppm and sub-ppb level in each run.

7.2.5 Fluid inclusions

Speleothems usually contain small quantities up to 1.0 wt % (McDermott et al., 2006) of so called fluid inclusion water. Eight speleothem samples are measured for fluid inclusion δ^2H and δ^{18}O using a modified continuous flow Thermo TC/EA coupled to a Delta plus XP mass-spectrometer (table 7.2). An online crushing cell and cold trap are attached to the system to crush the sample and collect the water online to focus it for isotope measurements according to the method of Vonhof et al. (2006) (chapter 4). The standard deviation of these measurements are within 2‰ for Hydrogen. Reliable fluid inclusion oxygen isotope data were not obtained for this speleothem, due to technical complications in the mass jump routine required for the generation of fluid inclusion δ^{18}O data. Further technical specifications for this technique can be found in Vonhof et al. (2006) (chapter 4).

7.3 Results

7.3.1 Age model

The ages obtained by Uranium-series dating are shown in table 7.1. Figure 7.2 presents the Uranium-series age versus depth. The bottom of stalagmite CLL-1 is dated back to almost 66.5 Kyr BP, but the speleothem did not grow continuously throughout the whole period. Visible hiatuses are indicated by grey lines in figure 7.2. Two larger hiatuses are seen at 131.5 and 126cm depth, together spanning approximately 20 Kyr year. The hiatus at 126cm depth is also observed in the δ^{13}C values as a rapid shift towards isotopically light carbon. From 126cm (~44 Kyr) depth to 72cm (~40 Kyr) depth a continuous growth period is observed with no visible hiatuses. Between the measured ages at 120 and 78cm depth the speleothem spans ~4000 years in time, growing at an average growth rate of ~80μm/yr. Two other hiatuses are observed at 62 and 58 cm depth spanning together almost ~7 Kyr. The hiatus at 58 cm depth is also observed as a shift to a lighter carbon isotope value. This remarkable shift toward lighter δ^{13}C values marks the transition of δ^{13}C values of the upper Pleistocene and the δ^{13}C values of the Holocene. As this study focuses on the Holocene, we did not perform more Uranium-series analyses to improve the age frame work for the older time period. The top 58 cm covers the last ~5000 years of the Holocene based on 6 Uranium-series ages (table 7.1, figure 7.3). The Holocene section has a detailed age framework but two visible hiatuses are observed: one at 13.2cm depth, the second at 2 cm depth.

Unfortunately the visible hiatus at 13.2 cm depth is not well constrained, with an Uranium series age at 14 cm depth (2396 yrs BP) and an Uranium age at 2 cm depth (244 yrs BP), below the top hiatus (figure 7.3). In summary, stalagmite CLL-1 shows a relatively constant growth rate from 58 until 14 cm depth. For the top 14 cm the growth rate reduces significantly.

We therefore suggest two possible age models: 1) the observed hiatus at 13.2 cm depth is not significant and the growth rate decreased above that level or 2) a significant hiatus is present at 13.2 cm depth and the growth rate in the top 13 cm remained comparable to that in the section below 14cm (figure 7.4). Extra U-series analyses would be required to determine the likelihood of these two possible age models.

The youngest Uranium series age was measured 2 cm below the top and dated at 244 yr BP, just below a potential hiatus layer. This is likely to be a minor hiatus, as the top was actively growing when the speleothem was sampled, and at an average Late Holocene growth rate of ~80 μm/year the top 2 cm would be deposited in ~250 years, which seems to agree best with age model 2.

7.3.2 Petrography

Visual inspection of CLL-1 shows that one can petrographically distinguish between the core and the outer rim of the stalagmite. The core consists of very porous calcite, dominated

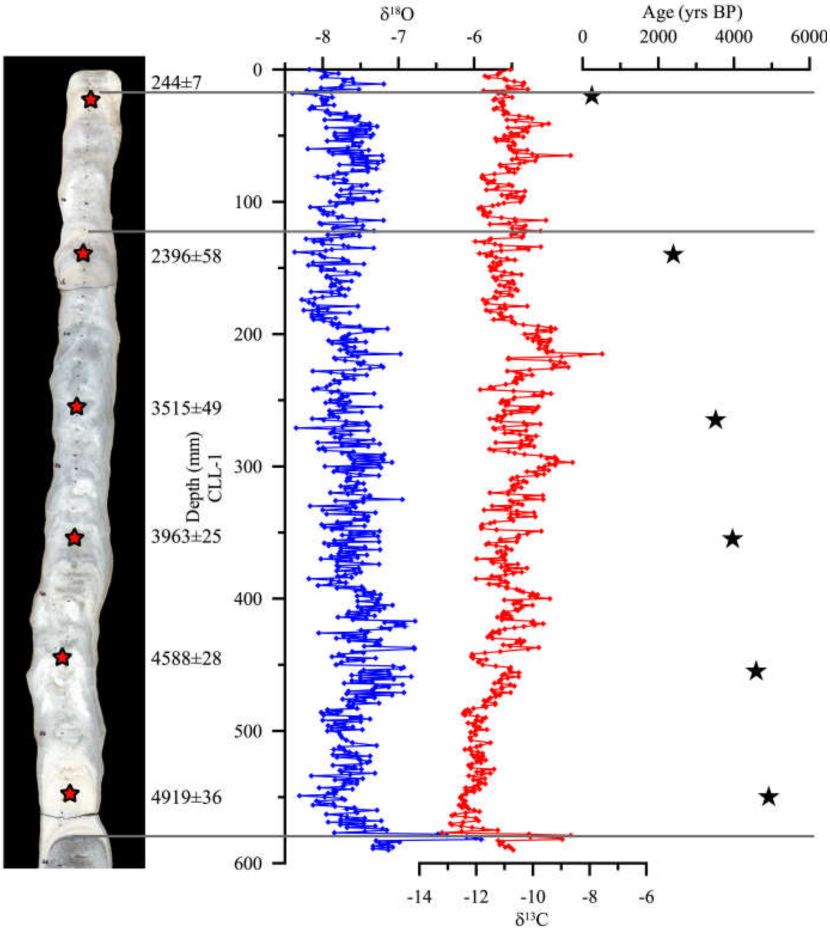

Figure 7.3: The top 58 cm of stalagmite CLL-1, covering the last ∼5000 year. The δ^{18}O and δ^{13}C are measured at 1 mm spatial resolution record and cross plotted versus depth. The stars represent the U/Th ages versus depth.

by columnar and aggregate calcite crystals alternated with dense columnar and palisade calcite crystals. The outer rim always exists of columnar to palisade calcite. The transition to different calcite crystals in the core occurs simultaneously with changes in the shape of the paleo-surface of the top of the stalagmite. During deposition of the stalagmite a drip water pool formed on top of the stalagmite. Drip water falling in this pool and flowing over the edge, formed a thin fluid layer where dense calcite is deposited. However in the pool itself the crystals grew in every direction as they are not limited in space, in contrast to thin fluid layer. Therefore in the supersaturated pool on the top of the stalagmite, crystals

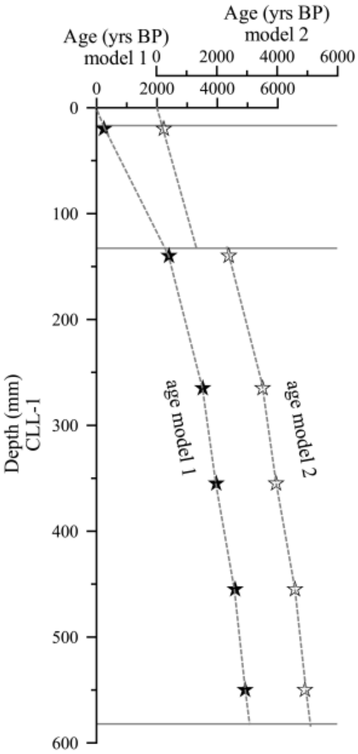

Figure 7.4: Two age models based on 6 Uranium-series ages of the top 58 cm of stalagmite CLL1. Age model 1 is based on a continuous growing stalagmite, while age model 2 is based on a hiatus at ∼12cm depth. The grey lines indicate the visible hiatuses

do not grow perpendicular to the growth axes of the stalagmite, but in random directions. This type of growth observed in CLL-1 results in very porous calcite with large cavities up to 1 cm in diameter (figure 7.5).

Such an open calcite growth structure, potentially provides problems for the reliability of fluid inclusion measurements, as fluid inclusions in such a structure may be interconnected. Exchange between different fluid inclusions and even with external cave water may easily occur. During fluid inclusions isotope analysis we found remarkably low water yields for some of the porous calcite, suggesting that interconnected inclusions could loose their water in the hot crusher prior to analysis.

SEM pictures confirm the results obtained from the thin sections (figure 7.6). Columnar calcite crystals are unidirectional orientated and closely packed with small cavities. A SEM picture of a porous layer is shown in figure 7.6a, 7.6c and 7.6d. The crystals are orientated in different directions, often growing towards each other. The well-developed crystal surfaces

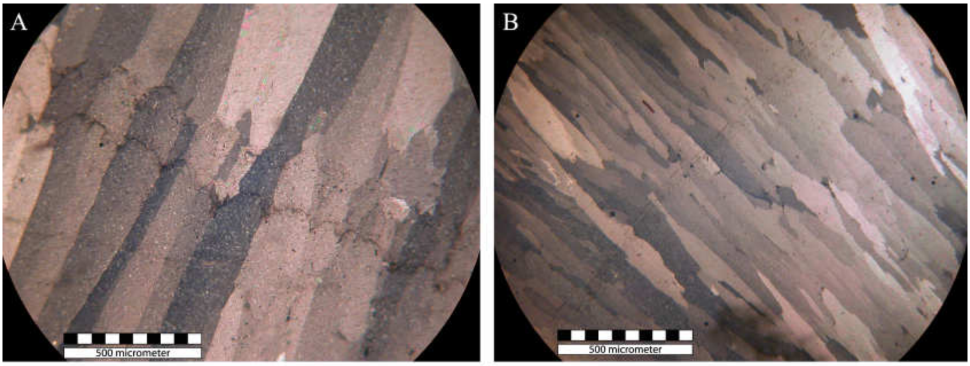

Palisade calcite

Columnar calcite

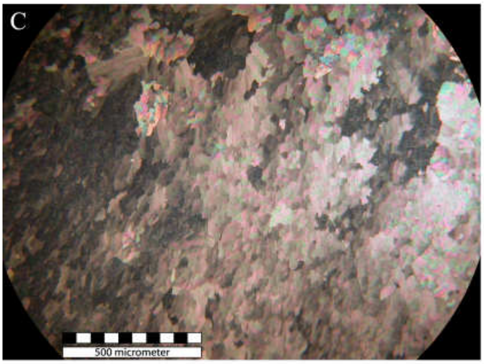

Equant/granular calcite

Figure 7.5: Photographs of thinsections of CLL-1, showing the different type of Calcite crystals. Pictures are taken with crossed nickels. A=palisade calcite; B=columnar calcite; C=granular calcite

indicate that these crystals grew in a open space. As the crystals are well developed and ending in an open space it is clear that these formed large cavities.

Figure 7.6b illustrates how cavities between individual crystals are filled up. Figure 7.6b is a picture taken, perpendicular on the growth direction of the calcite crystals. This piece of calcite is broken on a cavity, the crystals end in the cavity in the centre of the picture. Towards the right edge the calcite is broken, showing the dense structure. It illustrates how the cavities are closed in while the calcite crystals grow further.

7.3.3 Fluid inclusions

All fluid inclusion isotope analyses for δ^2H and δ^{18}O are shown in table 7.2. Due to low water yield of the porous calcite we had to discard four δ^2H analyses. Using δ^2H values for inclusion water combined with the oxygen isotope data of speleothem calcite, it is possible

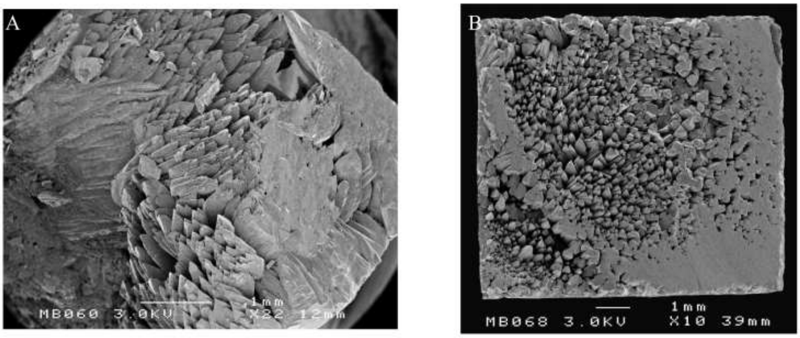

CLL-1 5cm depth

CLL-1 29cm depth

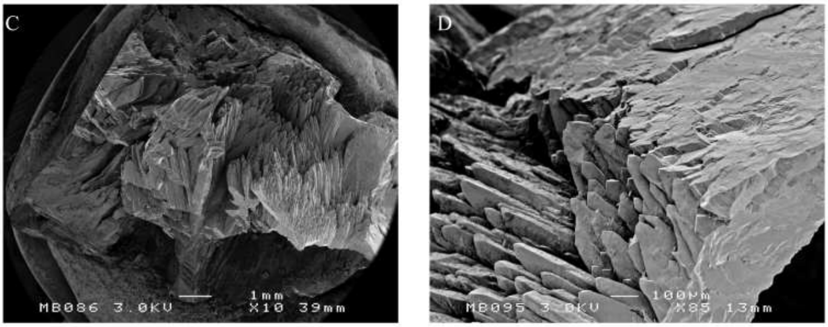

CLL-1 45cm depth

CLL-1 45cm depth

Figure 7.6: SEM pictures of CLL-1 showing the different types of calcite. A-D show a typical open calcite structure representative for CLL-1

to calculate independent cave temperatures. As paleo-temperature calculation is based on the temperature dependent oxygen isotope fractionation, δ^2H values are converted to δ^{18}O values assuming that the cave seepage water is of meteoric origin and plot on the Global Meteoric Water Line (GMWL). Measured cave drip water samples of Cueva de las Lechuzas consistently plot on the GMWL, leading us to believe that this is a safe assumption for this cave system.

Using the calculated δ^{18}O values of the fluid inclusions combined with the δ^{18}O measurements of the speleothem calcite cave temperatures of around 20°C are calculated by the equation of Craig (1965). This is approximately 1-2 degrees lower than the actual cave temperature. This discepancy suggests either that the fluid inclusion measurements are biased towards lighter values, or that there is a disequilibrium with the cave drip water. Figure 7.7 shows that hydrogen isotope values of inclusion water and drip water are similar suggesting that the inclusion water measurements can be trusted.

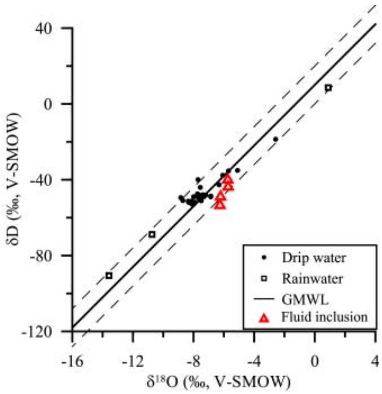

Figure 7.7: Drip and rainwater isotope composition collected at Cueva de las Lechuzas. The triangles represent the isotope composition of the fluid inclusion water of CLL-1. The fluid inclusion water is slightly deviated from the drip water. The dashed lines have the same slope as the GMWL but a deuterium excess of 0 and 20‰, respectively.

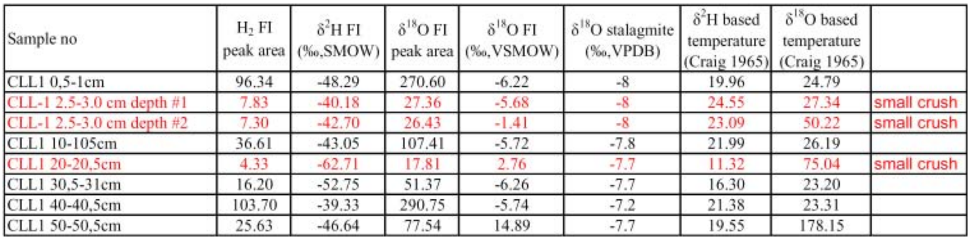

Sample no	H_2 FI peak area	δ^2H FI (‰,SMOW)	δ^{18}O FI peak area	δ^{18}O FI (‰,VSMOW)	δ^{18}O stalagmite (‰,VPDB)	δ^2H based temperature (Craig 1965)	δ^{18}O based temperature (Craig 1965)	
CLL1 0,5-1cm	96.34	-48.29	270.60	-6.22	-8	19.96	24.79	
CLL-1 2.5-3.0 cm depth #1	7.83	-40.18	27.36	-5.68	-8	24.55	27.34	small crush
CLL-1 2.5-3.0 cm depth #2	7.30	-42.70	26.43	-1.41	-8	23.09	50.22	small crush
CLL1 10-105cm	36.61	-43.05	107.41	-5.72	-7.8	21.99	26.19	
CLL1 20-20,5cm	4.33	-62.71	17.81	2.76	-7.7	11.32	75.04	small crush
CLL1 30,5-31cm	16.20	-52.75	51.37	-6.26	-7.7	16.30	23.20	
CLL1 40-40,5cm	103.70	-39.33	290.75	-5.74	-7.2	21.38	23.31	
CLL1 50-50,5cm	25.63	-46.64	77.54	14.89	-7.7	19.55	178.15	

Table 7.2: δ^2H and δ^{18}O values of fluid inclusion measurements on stalagmite CLL-1. Calculated temperatures using the equation of Craig 1965 are given for the δ^2H and δ^{18}O values. Mean calculated temperatures for δ^2H are close to actual cave temperature of 22.4°C. Values of the 'small crushes' are discarded for δ^2H and δ^{18}O due to low water yield of the measured samples.

7.3.4 Stable isotopes and trace element data

Oxygen isotope values measured at 1cm resolution throughout stalagmite CLL-1 show a maximum variation of 1.5 ‰ while δ^{13}C values show over 6 ‰ variation (figure 7.2). The hiatus at 126cm depth is marked by a sudden shift to low δ^{18}O and δ^{13}C values of the speleothem carbonate. The hiatus of ~7 Kyr at 58 cm depth (~12.8 Kyr) has a similar shift to isotopically light oxygen and carbon. As this study focuses on the Holocene period the top 58cm (last ~5000 yr) were measured at millimetre resolution to construct detailed stable isotope records (figure 7.3).

Trace element concentrations of Mg, Sr and Ba are presented in figure 7.8 along with stable isotope data. The stable isotope records (δ^{13}C and δ^{18}O) as well as the trace element records

(Ba, Mg, Sr), show distinct cyclicity. All parameters analysed show in-phase variations. Correlation plots of the different trace elements and stable isotopes are illustrated in figure 7.9. To assess the frequency of observed cyclicity we must consider the two different age models constructed for this record.

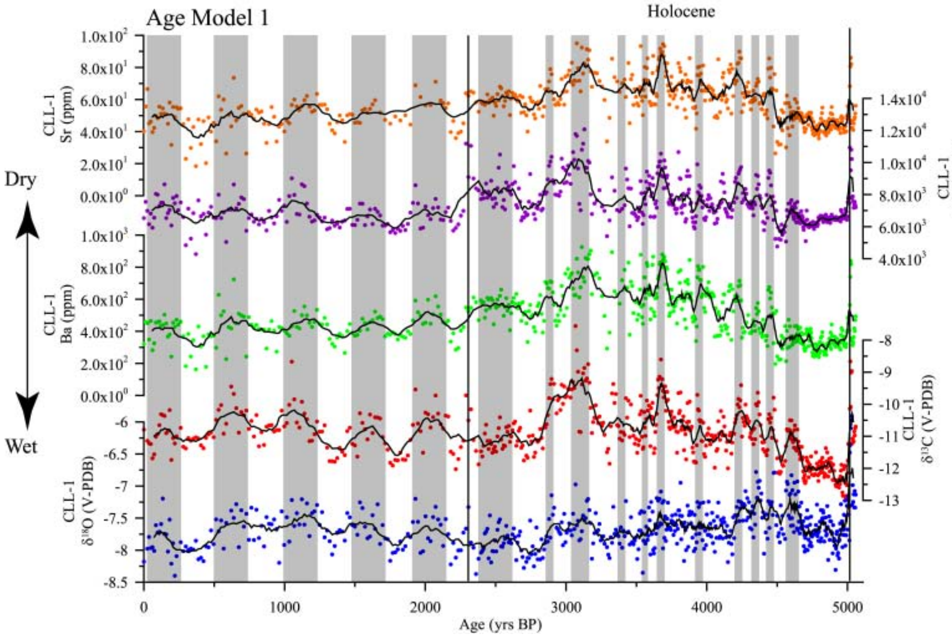

Figure 7.8: Stable isotope(δ^{13}C, δ^{18}O) and trace element (Ba, Mg, Sr) records of CLL-1 versus age. The continuous growth model (age model 1) is used for the age framework. Black line is an 11-point running average. The possible hiatus is indicated at ∼2300 years BP.

7.3.5 Age Model 1 (no hiatus)

Age Model 1 is based on a linear interpolation between the individual Uranium-series ages of CLL-1. No long trends are observed in the stable isotope and trace element records for the last 5000 years of the Holocene, however all records have maxima at 3.2 and 3.6 Kyr, respectively (figure 7.8). The 5000 year record shows many small oscillations with ∼100 to ∼250 years duration in the older part of the record. During the last ∼2200 years five rather regular oscillations are observed, which have an approximate frequency of 550 years in age model 1. All the cycles are consistently seen in the trace elements (Ba, Mg, Sr) as well as in the stable isotope records (δ^{18}O, δ^{13}C).

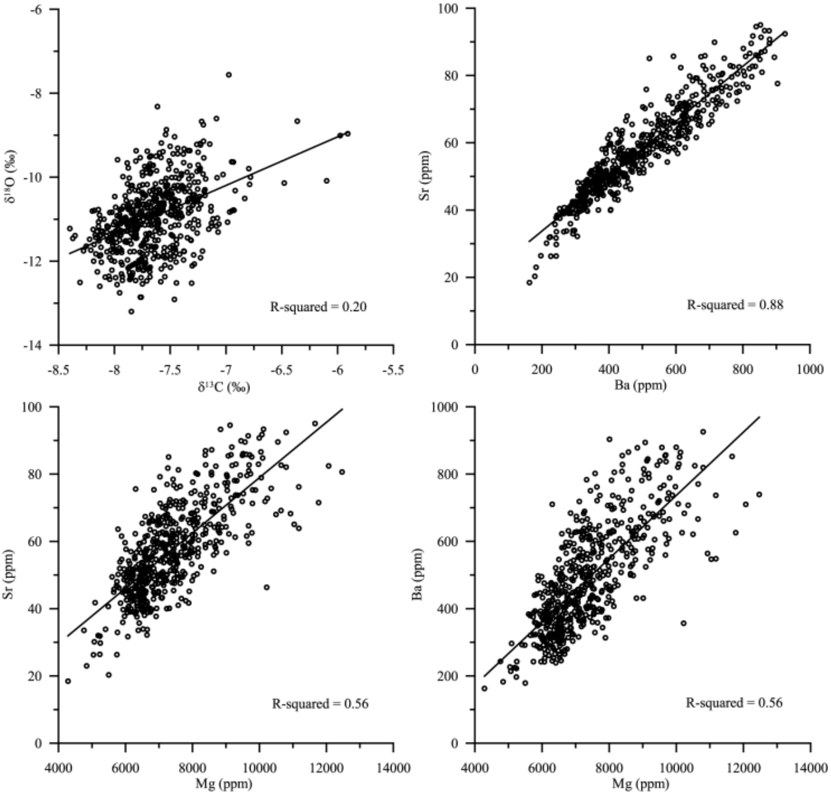

Figure 7.9: Cross plotted are the stable isotopes δ^{13}C and δ^{18}O and the trace elements Sr, Mg and Ba. The correlation is indicated in the figure by the R-square.

7.3.6 Age Model 2 (1000 yr hiatus at 13.2cm)

Age model 2 uses the same Uranium series ages, but assumes a growth rate above the hiatus at 13.2 cm, which is comparable to that below that hiatus. The difference between the two age models is illustrated in figure 7.4.

Figure 7.10 shows the stable isotope and trace element records based on age model 2. The main difference between the two records is the frequency of the last five cycles. Using age model 2, one cycle spans ~250 years, which agrees well with the frequency of the cycles observed in the older part of the stalagmite.

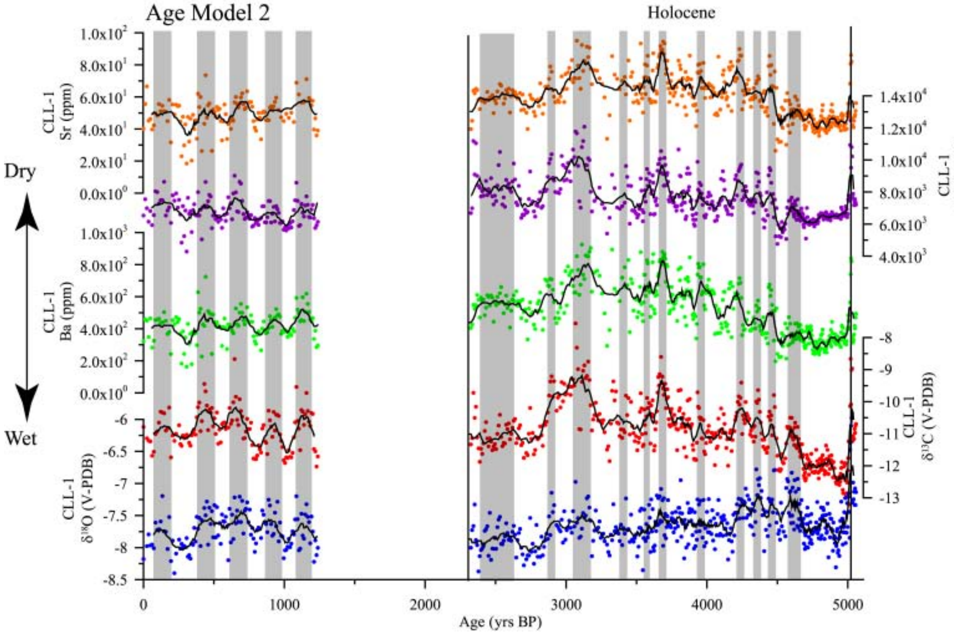

Figure 7.10: Stable isotope(δ^{13}C, δ^{18}O) and trace element (Ba, Mg, Sr) records of CLL-1 versus age. The discontinuous growth model (age model 2) is used for the age framework, the hiatus is clearly seen in the record. The black line is an 11 point running average.

7.4 Discussion

The Cueva de las Lechuzas stalagmite record shows a distinct centennial scale cyclicity, visible in both carbon and oxygen isotope variation. The same pattern is also consistently observed in the concentrations of Magnesium, Strontium and Barium.

Clear correlation between stable isotope and trace element data in speleothems has been observed on different time-scales by previous authors (Hellstrom and McCulloch, 2000; Roberts et al., 1998; Treble et al., 2003; Verheyden et al., 2000). Particularly Verheyden et al. (2000) presented a similar case to the one described in the present chapter. Verheyden and co-workers reported on a Belgian Holocene speleothem record which showed in phase variation in δ^{13}C, δ^{18}O, Mg/Ca and Sr/Ca ratios. This was interpreted to relate to variation in residence time of percolating seepage water and associated variation in prior calcite precipitation along the flow path.

7.4.1 Stable isotopes and trace element concentrations

The δ^{18}O value of speleothem calcite is influenced by two parameters, namely 1) temperature and 2) the isotope composition of the cave seepage water. As tropical Holocene temperatures are expected to be stable in the Late Holocene (chapter 6), the oxygen isotope composition of the cave seepage water is the most dominant factor influencing the δ^{18}O value of speleothem calcite. Thus, δ^{18}O values of cave seepage water are directly representative for δ^{18}O composition of rainfall above the cave. The isotope composition of rainfall in western Amazonia is closely related to the amount of convective precipitation. Rainwater has relatively low δ^{18}O values during high amount of convective precipitation and relatively high δ^{18}O values during low amount of convective precipitation. δ^{18}O values of drip water in a monitoring experiment show no seasonal variation in the isotope composition of the drip water feeding this particular stalagmite (chapter 3). Therefore only interannual variations in cave seepage water δ^{18}O, and therewith in rainfall amounts, are recorded in the speleothem calcite.

Thus, distinct centennial scale cyclicity observed in the stalagmite δ^{18}O record are interpreted to reflect cyclicity in rainfall amounts through the Holocene. Apparently this cyclicity also influences the trace elemental composition of speleothem calcite. Proposed mechanisms are that increased rainfall will influence the cave hydrology by 1) reducing the residence time of the percolating water and 2) reducing the air-filled fraction of pore spaces in the rock above the cave, both resulting in decreased prior calcite precipitation along the flow path. Precipitated calcite along the flow path, will have a Mg/Ca and Sr/Ca ratio lower than the seepage water (relatively more Calcium is deposited during calcite formation than trace elements substitutes), resulting in increased Mg/Ca and Sr/Ca ratios in the percolating water. Therefore relatively low Mg, Sr and Ba concentrations are incorporated in speleothem calcite in wet periods (Fairchild et al., 2000). The in-phase relationship between the oxygen isotope ratio and the trace elements Mg and Sr thus consistently point towards cyclicity in rainfall amounts as the controlling parameter for speleothem chemistry. Low δ^{18}O values and Mg and Sr concentrations occur during periods of high rainfall amounts. High values reflect relatively dry conditions.

In tropical and monsoonal climates, the amount effect is the dominant process that affects the δ^{18}O value of precipitation (Rozanski et al., 1993). This increase in precipitation amount might also cause a decrease in the δ^{13}C value of speleothem calcite by increasing soil moisture content and soil respiration rates (Lachniet et al., 2004) or by reducing water-rock interactions, thereby reducing the amount of ^{13}C-enriched carbon derived from the host limestone (Paulsen et al., 2003; Mickler et al., 2006), resulting in a positive correlation between the δ^{18}O and δ^{13}C values of speleothem calcite (e.g., Li et al., 2000; Burns et al., 2002) δ^{13}C values of speleothem carbonate represent a mixed signal of the carbon taken up by the soil and carbon dissolved from the host rock plus the effects of degassing. Changes in soil acidity and CO_2 concentrations in the soil driven by changes in the vegetation activity will influence the composition of soil water and eventually the seepage water. The δ^{13}C speleothem record is likely to be sensitive to hydrological effects associated with changes in seepage water flow rates (Baker et al., 1997b; Genty et al., 2001a; Genty and Massault, 1999; Hellstrom and McCulloch, 2000; Mickler et al., 2006). As the δ^{13}C record mimics the other proxy records this suggests that δ^{13}C is indeed influenced by the residence time of the percolating water. Mickler et al. (2006) shows that a positive correlation between δ^{13}C and δ^{18}O of the speleothem calcite can occur due to non-equilibrium isotope effects. These effect are mainly controlled by the rate of CO_2-degassing and calcite precipitation. As CO_2-degassing is closely related to the driprate it records changes in the seepage flow rates.

7.4.2 Climate interpretation

Following the above mentioned interpretation of stable isotope and trace element data, the relatively low δ^{18}O and δ^{13}C values and trace element concentrations of the Cueva de las Lechuzas record indicate increased rainfall.

Rainfall amounts in our study area are primarily controlled by the InterTropical Convergence Zone (ITCZ), the seasonally migrating zone of maximum convective precipitation in the tropics. The maximum amount of rainfall is found in the centre of the ITCZ where convection is best developed. The latitudinal position of the ITCZ is primarily forced by the distribution of solar energy. This is why the ITCZ roughly follows the latitude of maximum insolation energy (also known as the caloric equator) on seasonal time-scales. On interannual time-scales, the position and activity of the ITCZ is modulated by changes in meridional sea surface temperature gradients. Cooling in higher latitudes generally results in a more Southward displacement of the seasonal ITCZ cycle (e.g. Broccoli et al., 2006). The stalagmite record shows relatively regular variation on centennial time-scales, suggesting centennial-scale cyclicity in the dynamics of the ITCZ system. Solar insolation cyclicity seems to be the most likely mechanism to cause cyclic rainfall variation in Amazonia at centennial time-scales.

Solar cycles occur in different frequencies: particularly the 11-year sunspots (Schwabe cycle) and the 80-90 year Gleissberg cycles (Gleissberg, 1958) are visible in the instrumental record. Furthermore, a 200-year 'de Vries' cycle and a 500 year cycle are recorded in Δ^{14}C records of tree rings (Stuiver and Braziunas, 1993) in ice cores (Finkel and Nishiizumi, 1997) and in sediment cores from Great Bahama Bank (Roth and Reijmer, 2005). Furthermore, Nyberg et al. (2001) observed cycles in Sea Surface Temperatures (SST) and Sea Surface Salinity (SSS) in the Caribbean Sea which they relate to solar activity cycles.

Solar energy seems the be the most plausible mechanism to cause this cyclic changes in rainfall variation. Changes in solar energy can influence the climate at this study area in various ways. On itself, solar energy increase through these cycles can increase convective precipitation by intensification of the ITCZ system in Amazonia. As the fluctuations in the δ^{18}O record of CLL-1 are relatively small ($\sim$0.5‰) this might be possible. Another possibility is to move the ITCZ system over our study area. Therefore, teleconnections and amplification mechanisms are required to explain the observed cyclic rainfall variation in our stalagmite record. The most likely teleconnections are changes in the meridional tropical

SST gradients which have been shown to correlate strongly with the isotope composition of precipitation in Amazonia (Melice and Roucou, 1998). This correlation is believed to be caused by the sensitive reaction of Hadley cell activity, and therewith of the ITCZ, to changes in tropical SST gradients (Zhou and Lau, 2001). Provided that solar cyclicity influences SST's, this would be the most plausible mechanism by which solar insolation changes can be transferred to rainfall amounts in Amazonia (Broccoli et al., 2006; Lohmann et al., 2004).

To determine which solar cycle frequency would best fit the observed variation in the CLL-1 record we next made closer comparisons between the two age models considered. The two age models only differ for the last ∼2200 years, where a probable hiatus is visible at 13.2 cm in the speleothem.

In model 1 we assumed the age range of the hiatus to be zero (i.e. no hiatus) which results in a record for the last 2200 years that is stretched relative to age model 2 where we assumed an age range of the hiatus of ∼1000 years (so that growth rate before and after the hiatus are the same).

Independent of which age model is used, a clear cyclicity is observed in all five proxies. Five cycles are observed in the top 13 centimetres. Using age-model 1 these five cycles span ∼2200 years, resulting in a frequency of ∼550 years. Using age model 2, five cycles span ∼1250 years, which relates to ∼250 years for each cycle. The earlier part of the record shows cycles with a duration between 100 and 250 years (similar in both age models). From the point of view of consistency, one might therefore conclude that age model 2 is in better agreement with the observed variation, and that this record most likely shows dominant 200 year 'de Vries' cycles in solar activity. However, the only satisfactory way to solve this uncertainty is the (future) U-Th analysis of more samples from this stalagmite record.

7.5 Conclusions

Stalagmite CLL-1 presents an unique paleo-climate record, as five independent proxies show the same consistent pattern, indicative of cyclically varying drip rates on centennial time-scales. Relatively low δ^{18}O values are related to increased rainfall. Changes in solar activity apparently change the location of the caloric equator resulting in significant shifts in the position of the ITCZ system. Increased amount of convective rainfall above the cave will not only lower the δ^{18}O values of the carbonate but also decrease the Sr, Ba and Mg concentrations of the cave seepage water due to changes in the cave hydrology.

Increased rainfall will decrease the residence time of the percolating water, and thus the amount of prior precipitated calcite resulting in a relative decrease in Sr/Ca and Mg/Ca ratios (Fairchild et al., 2000).

Although the age model is not completed yet, the two possible scenarios are presented. The frequency of centennial scale cyclicity seen during 5000-2250 years BP is identical for both scenarios. The most regular cyclicity is observed in the period between 2250-0 BP and present in all measured proxies, at a frequency of ∼500 years in age model 1 and

~250 years in age model 2. Centennial scale cycles most probably relate to changes in solar activity (Stuiver and Braziunas, 1993) and are observed in many different climate records such as GISP ice cores (Grootes and Stuiver, 1997), SST in the Caribbean sea (Nyberg et al., 2001) and in sediments from the Great Bahama Bank (Roth and Reijmer, 2005). The possible age hiatus is responsible for the large difference in length of the last five cycles varying between 200 to 500 years. Age model uncertainties currently do not allow a precise determination of solar cycle frequency in the top part of this record.

Solar insolation variation in Amazonia through these cycles is very limited, and probably requires an amplification mechanism to explain the geochemical variation in this speleothem. The observed sensitivity of ITCZ controlled Amazonian rainfall variation to Atlantic sea surface temperature gradients may well be the amplifier that transfers subtle solar insolation changes to Amazonia.

7.6 Acknowledgement

I would like to thank the speleo-crew, Sandro Mariani, Quinto Quarisima, Elisabetta Ferroni and Alejandro Manrique Lagos. Saskia Kars is thanked for the beautiful SEM-pictures. Alan Kendall and Peter Rowe are thanked for the petrographic discussion at UEA. Susan Verdegaal and Nel Slimmen are thanked for their help with the analyses of stable isotope ratio and trace element concentrations at the Vrije Universiteit Amsterdam. This project is funded by WOTRO-NWO (project nr W76-231).

8

Climate reconstruction of the Andean highlands based on a late Holocene speleothem from Gruta de Huagapo

Abstract

Stable isotope ($\delta^{18}O$, $\delta^{13}C$) data combined with trace element data (Mg, Sr, Ba) from the speleothem calcite and fluid inclusion isotope data ($\delta^{2}H$, $\delta^{18}O$) of a single speleothem from the Peruvian Andes give insight into local climate variations during the last ~4500 years.

Stable isotope data ($\delta^{13}C$, $\delta^{18}O$) of the speleothem carbonate shows in-phase variation with the Mg elemental concentration. Sr and Ba concentration records also show an in-phase pattern but the records differ from the $\delta^{18}O$, $\delta^{13}C$ and Mg records. Variation in the $\delta^{18}O$ values of the speleothem calcite are mainly dominated by isotope composition of the seepage water as reconstructed temperatures are relatively constant. Therefore the $\delta^{18}O$ record of speleothem calcite mainly reflects changes in the amount of rainfall in our study area. We interpret low $\delta^{18}O$ values as increased amounts of rainfall in our study area. We explain these wet periods by increased amount of convective precipitation as a result of increased activity of the InterTropical Convergence Zone (ITCZ) system, either by a southward displacement of the ITCZ over the cave site and/or increased intensity of atmospheric convection.

Calculated paleotemperatures using $\delta^{18}O$ of the speleothem calcite combined with stable isotope values ($\delta^{18}O$, $\delta^{2}H$) of inclusion water show that cave temperatures were relatively stable, between 14-16°C for the last ~4500 years. The observed frequency of the climate cycles in the speleothem calcite are in the range of centennial solar cycles. Although variation

in solar insolation on itself is limited, amplification in the Amazon Basin and sensitive response at high altitude might record the response of the ITCZ to changes in the equatorial sea surface temperatures.

8.1 Introduction

Several speleothem studies have focussed on climate reconstructions in tropical Amazonia (Auler et al., 2004; Cruz et al., 2005a; Cruz et al., 2005b) (this thesis, chapter 6 and 7). However hitherto no speleothem material was collected at high altitude in the Andes of the Peruvian highland. The Andean mountain chain has a high snowline which favours speleothem formation at high altitudes. Temperatures are not below freezing point, and thus speleothem formation and cave formation are possible. Indeed the Andes mountains host caves up to almost 5000 meters altitude. We collected a speleothem at 3572 meters altitude from Gruta de Huagapo to investigate climate processes from the Peruvian highlands.

We measured δ^{18}O and δ^{13}C profiles of speleothem calcite as well as Mg, Ba and Sr concentrations and δ^{18}O and δ^{2}H values of fluid inclusion water. The combination of these proxies results in quantitative reconstructions of temperature and rainfall variation in the high Andes for the last $\sim$4500 years.

Here, we report our results from the high Andes cave as an end member on a transect from lowland Amazonia to the Andean highlands. The results are used in chapter 9 in a data-model comparison to investigate the fit of stable isotope fluid inclusion data and modelled stable isotope values of rainwater.

8.1.1 Gruta de Huagapo

Gruta de Huagapo is an active karst system located at 3572 meter above mean sealevel at the eastern side of the Andes (S 11°16'6.17", W 75°47'13.84", figure 8.1) developed in Triassic limestone. The existing vegetation consists of small bushes and grasses. Current cave temperature is close to 12°C. The relative humidity is 98% as measured with a sling psychrometer. This is based on three short visits to the cave in 2000, 2003 and 2004.

8.2 Materials and Methods

8.2.1 Stalagmite HUA-8

Stalagmite HUA-8 is collected from Gruta de Huagapo at approximately 500 meter from the cave entrance (figure 8.2), during our 2003 field campaign. The stalagmite HUA-8 is a 36 cm long speleothem (figure 8.3). Two slices of about 0.5cm thick were cut along its long axis. One slice was drilled every millimetre with a hand held drill to collect carbonate samples for stable isotope and trace element analyses. The second slice was used to cut material for U-series dating and fluid inclusion isotope analyses. One of the remaining

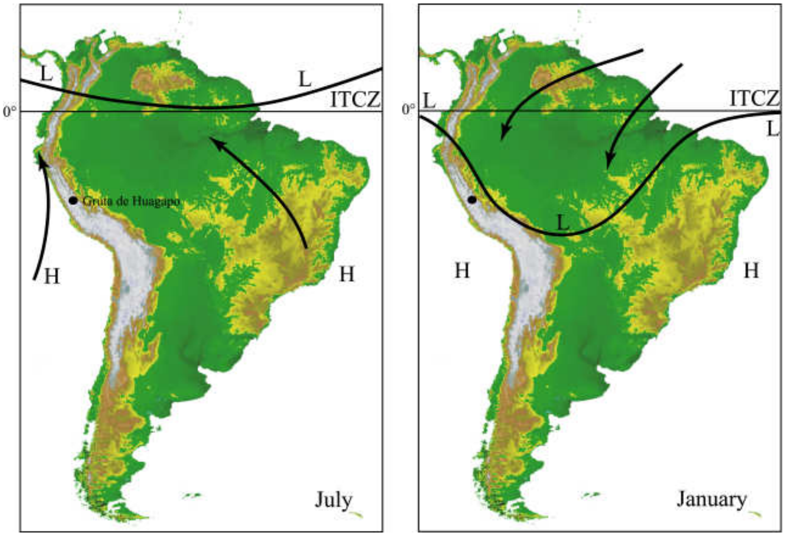

Figure 8.1: Map of South America with location of Gruta de Huagapo indicated as solid black dot. The ITCZ low pressure zone is illustrated as a black line. The seasonal movement of the ITCZ is shown by July and January situation. The arrows are indicative for the prevailing wind direction.

parts of the speleothem was used to make four petrographic thin sections covering the whole vertical extent of the stalagmite.

8.2.2 Petrography

HUA-8 is a dense stalagmite with layering showing its original irregular surface. Four large thin sections (10 x 5 cm) were made to cover the complete stalagmite for petrographic analyses. Petrographic analyses show large crystals with different shapes, often elongated but also areas with uni-dimensional crystals with irregular boundaries occur (figure 8.3; Kendall and Broughton, 1978). HUA-8 is rich in fluid inclusions of various sizes from nano-inclusions to ∼100µm (figure 8.3). Individual crystals are not growing parallel but can grow in different angles, as seen from the orientation of the fluid inclusions (figure 8.4; Kendall and Broughton, 1978). Potential non-deposition surfaces or hiatuses were not observed petrographically. Thus our visual inspection suggests continuous growth of the speleothem, which is in good agreement with the U-series age model (see 8.2.3).

8.2.3 U-series age dating

U-series dating was performed at the Vrije Universiteit Amsterdam on a Finnigan MAT 262 Thermal Ionization Mass Spectrometer (TIMS). We measured six TIMS uranium series

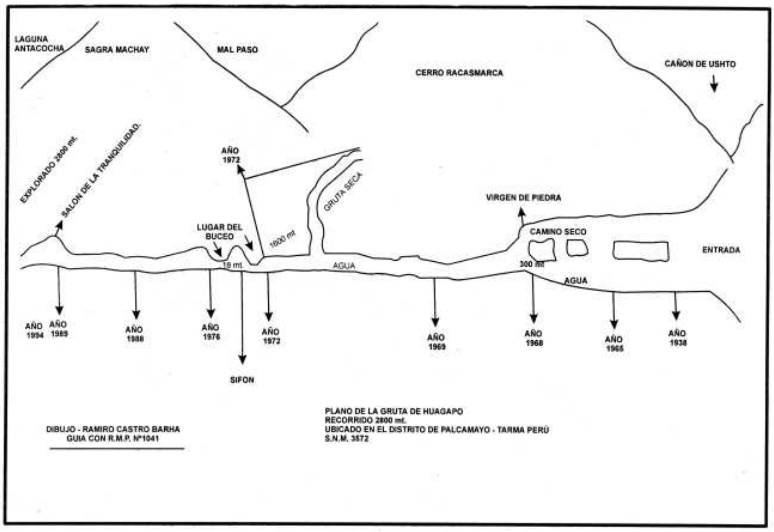

Figure 8.2: Map of Gruta de Huagapo. Stalagmite HUA-8 is collected at the beginning of the 'Gruta Seca'. It is called 'Gruta Seca' as it is the only part of the cave where the river is not running through.

dates for this speleothem (table 8.1). No contamination of excess ^{230}Th was detected as the ^{232}Th/^{230}Th activity ratio was usually more than a 1000 and ^{232}Th less then 0.1 ppb (table 8.1). See also Chapter 2 for a general description of the methods. Interpolation of the measured ages show a nearly linear age-depth correlation (figure 8.5). The growth model used is based on linear interpolation between the individual dates (figure 8.5).

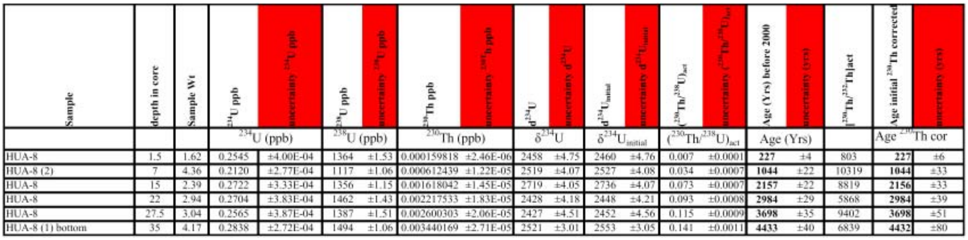

Sample	depth in core	Sample Wt	^{234}U ppb	uncertainty ^{234}U ppb	^{238}U ppb	uncertainty ^{238}U ppb	^{230}Th ppb	uncertainty ^{230}Th ppb	d^{234}U	uncertainty d^{234}U	d^{234}U$_{initial}$	uncertainty d^{234}U$_{initial}$	(^{230}Th/^{238}U)$_{act}$	uncertainty (^{230}Th/^{238}U)$_{act}$	Age (Yrs) before 2000	uncertainty (yrs)	[^{230}Th/^{232}Th]act	Age initial ^{230}Th corrected	uncertainty (yrs)
			^{234}U (ppb)		^{238}U (ppb)		^{230}Th (ppb)		δ^{234}U		δ^{234}U$_{initial}$		(^{230}Th/^{238}U)$_{act}$		Age (Yrs)			Age ^{230}Th cor	
HUA-8	1.5	1.62	0.2545	±4.00E-04	1364	±1.53	0.000159818	±2.46E-06	2458	±4.75	2460	±4.76	0.007	±0.0001	**227**	±4	803	**227**	±6
HUA-8 (2)	7	4.36	0.2120	±2.77E-04	1117	±1.06	0.000612439	±1.22E-05	2519	±4.07	2527	±4.08	0.034	±0.0007	**1044**	±22	10319	**1044**	±33
HUA-8	15	2.39	0.2722	±3.33E-04	1356	±1.15	0.001618042	±1.45E-05	2719	±4.05	2736	±4.07	0.073	±0.0007	**2157**	±22	8819	**2156**	±33
HUA-8	22	2.94	0.2704	±3.83E-04	1462	±1.43	0.002217533	±1.83E-05	2428	±4.18	2448	±4.21	0.093	±0.0008	**2984**	±29	5868	**2984**	±39
HUA-8	27.5	3.04	0.2565	±3.87E-04	1387	±1.51	0.002600303	±2.06E-05	2427	±4.51	2452	±4.56	0.115	±0.0009	**3698**	±35	9402	**3698**	±51
HUA-8 (1) bottom	35	4.17	0.2838	±2.72E-04	1494	±1.06	0.003440169	±2.71E-05	2521	±3.01	2553	±3.05	0.141	±0.0011	**4433**	±40	6839	**4432**	±80

Table 8.1: ^{234}U, ^{238}U, ^{230}Th concentrations and calculated ages of stalagmite HUA-8 from Gruta de Huagapo.

8.2.4 Stable isotopes

The δ^{18}O and δ^{13}C values of carbonate samples were measured on a Finnigan MAT

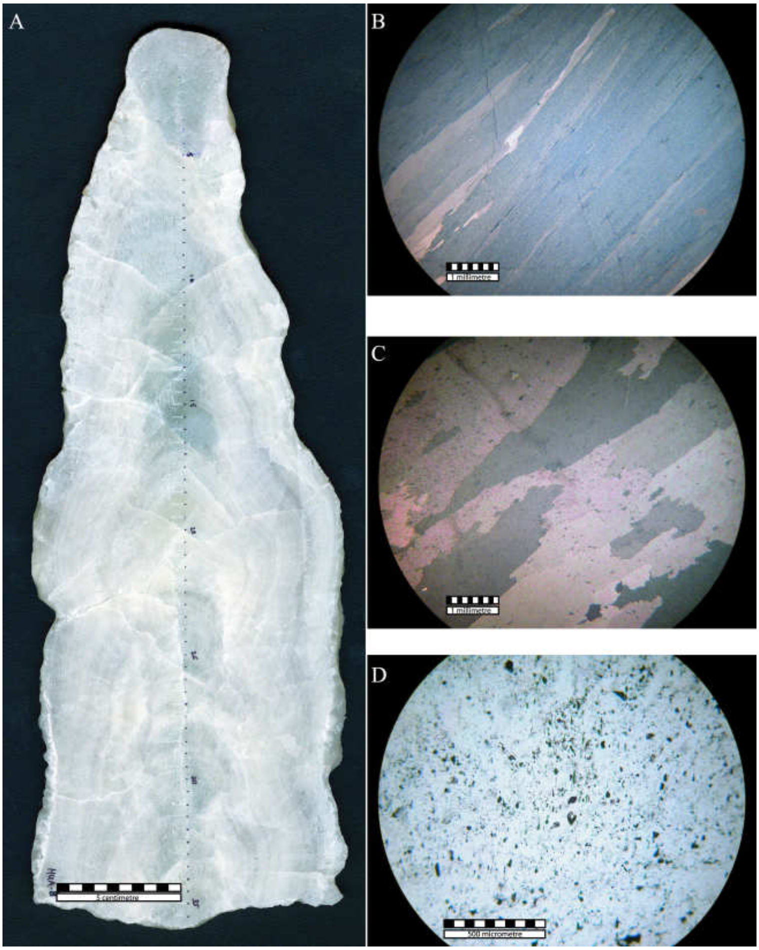

Figure 8.3: A) The center core of stalagmite HUA-8 shows the original shape of the stalagmite in the past. B) Columnar fabrics of calcite crystals. C) Irregular shaped crystals. D) Typical fluid inclusions of speleothem HUA-8.

252 mass-spectrometer, equipped with a Kiel device and on a Finnigan Delta plus mass-spectrometer equipped with a Gasbench, both located at the Vrije Universiteit Amsterdam. GICS in-house carbonate standard was routinely monitored during sample runs. GICS long-term reproducibility lies within 0.07‰ for δ^{18}O and 0.04‰ for δ^{13}C for the Finnigan MAT 252 and within 0.10‰ for δ^{18}O and 0.10‰ for δ^{13}C on the Finnigan Delta plus mass-spectrometer. The amount of carbonate powder needed for a single measurement is ~20 µg for the MAT252 and ~50 µg for the Delta plus. δ^{18}O and δ^{13}C measurements of speleothem carbonate are reported in ‰ relative to the Vienna PeeDee Belemnite (V-PDB) standard.

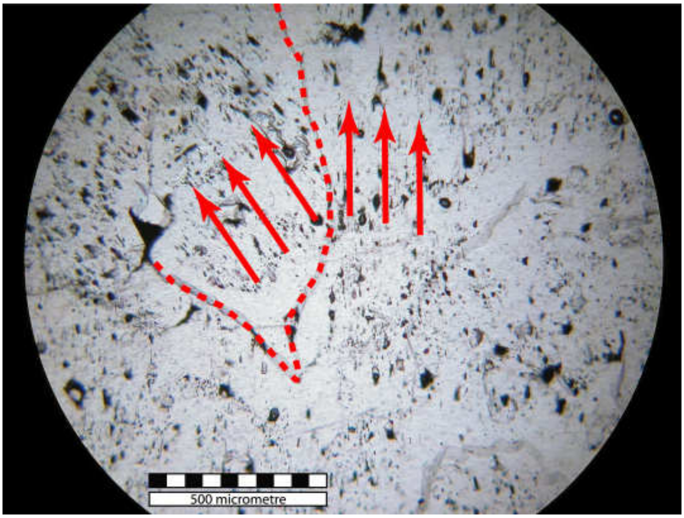

Figure 8.4: Fluid inclusions of HUA-8 perpendicular on the growth direction of the calcite crystal. Illustrated are the different growth directions of the individual crystals.

8.2.5 Trace elements

Trace elements analyses were performed on a Varian Liberty Series II ICP-OES with a precision of about 0.7-3% depending on the solution concentration ranging from ppm to sub-ppb. The precision is based on the 1σ reproducibility of repeated analyses of two control solutions of a standard sample at ppm and sub-ppb level in each run.

8.2.6 Fluid inclusions

Speleothems can contain small quantities up to 1.0 wt % of so called fluid inclusion water (McDermott et al., 2006). Fluid inclusion water δ^2H and δ^{18}O values were determined using a modified continuous flow Thermo TC/EA coupled to a Delta plus XP mass-spectrometer as developed by Vonhof et al. (2006, 2007). An online crushing cell and cold trap are attached to the system to crush the sample and collect the water online and cryofocus it for isotope measurements. The reproducibility and standard deviation on these measurements are 1.5‰ (1σ) for Hydrogen and 0.5‰ (1σ) for Oxygen (Vonhof et al., 2007; Vonhof et al., 2006). Technical specifications can be found in Vonhof et al. 2006, chapter 4. About 0.5 grams of speleothem carbonate is needed to obtain $\sim$ 0.2 µL of fluid inclusion water for stalagmite HUA-8. Stable isotope measurements of hydrogen and oxygen of fluid inclusion water are reported in ‰ relative to the Vienna Standard Mean Ocean Water (V-SMOW).

Fluid inclusion isotope analyses were performed at different time intervals at the VUA, the first series was measured for δ^2H only as combined δ^2H and δ^{18}O analyses were technically

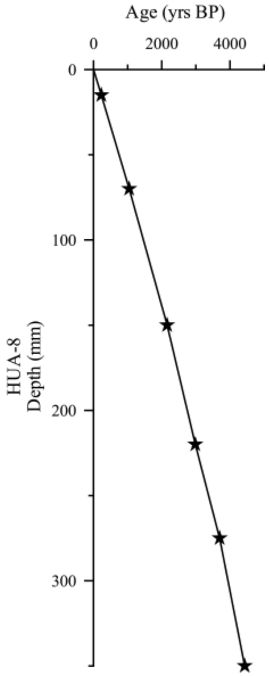

Figure 8.5: Age model of stalagmite HUA-8. The stars illustrate the uranium series ages. The solid line directly connects the age-depth relationship as indicated by the uranium series ages and the origin. It is clear the age-depth relationship matches close to a linear age model and that the stalagmite grew continuously for the last ∼4500 years. For general purposes of this climate reconstruction we use the age model as indicated by the solid line.

not possible at that stage, therefore only δ^2H results are available for this series. The second series was measured when technical modifications were adapted and simultaneous δ^2H and δ^{18}O values were obtained crushing one single sample. As for the first series only δ^2H values were measured, more δ^2H data is available than δ^{18}O data for the fluid inclusion measurements.

8.2.7 Paleotemperatures

Paleotemperature equations are based on the temperature-dependent calcite-water oxygen isotope fractionation. For speleothem calcite this occurs during deposition of calcite when CO_2 outgases from cave seepage water. As fluid inclusion water represents cave seepage water at the time of speleothem formation, the δ^{18}O values of inclusion water, combined with the δ^{18}O values of the surrounding speleothem calcite, provide the input parameters required for isotope-based paleotemperature calculations

Paleotemperatures of Gruta de Huagapo are based on the paleotemperature equation by Craig (1965), as a recent data compilation performed by McDermott et al. (2006) shows that calculated cave temperature based on modern speleothem calcite and its dripwaters underestimate the actual cave temperature for many of the well known paleotemperature equations. The equation by Craig (1965) resulted in more accurate temperatures than most others in this study (McDermott et al., 2006).

$$\mathrm{T} = 16.9 - 4.2 \cdot (\delta^{18}\mathrm{O}_c - \delta^{18}\mathrm{O}_w) + 0.13 \cdot (\delta^{18}\mathrm{O}_c - \delta^{18}\mathrm{O}_w)^2 \tag{8.1}$$

(Craig, 1965)

The temperature equation by Craig (1965) is based on temperature dependent ^{18}O water-calcite fractionation at time of calcite formation. Some fluid inclusion isotope analyses only have δ^2H data. To calculate paleotemperatures using the equation of Craig (1965), δ^2H values are converted to δ^{18}O values assuming that the fossil cave drip water has a meteoric origin and that rainwater composition at that period lay close to the Global Meteoric Water Line (GMWL). The GMWL is defined as:

$$\delta^2\mathrm{H} = 8 \cdot \delta^{18}\mathrm{O} + 10 \tag{8.2}$$

(Craig, 1961)

δ^2H values are converted to δ^{18}O values using equation 8.2, and used to calculate the temperature at time of calcite formation.

8.3 Results

8.3.1 Stable isotope stratigraphy

The age model of stalagmite HUA-8 is based on six uranium series age dates. HUA-8 has grown continuously with a growth rate of 0.066 to 0.10 mm/year for the last ~4500 years (figure 8.5). Calcite samples were drilled at 1 millimetre spatial resolution for stable isotope and trace element analyses (figure 8.6 & 8.7). Stable isotope analyses were performed every millimetre representing a time interval of 10 to 15 years between samples. Trace element analyses were performed at 2 mm spatial resolution, representing a time interval of 20-30 years between samples. The stable isotope records (δ^{18}O, δ^{13}C) together with the trace element records (Mg, Ba, Sr) are presented in figure 8.7. The δ^{18}O profile shows a ~1.5‰ variation over the last 4500 years. The older part of the record shows a trend from relatively high values in δ^{18}O with δ^{18}O values of around -12‰ at 4500 years BP to relatively low values with a minimum δ^{18}O value of -13.5‰ at 2300 yrs BP. From 2300 years BP a trend to higher isotope values is present with a maximum around 1200 years BP. The δ^{18}O values fluctuate around -13.2‰ for the last 1000 years. Particularly in the younger part of the oxygen isotope record cycles can be seen. These cycles are also present, but less well defined, in the older part of the record.

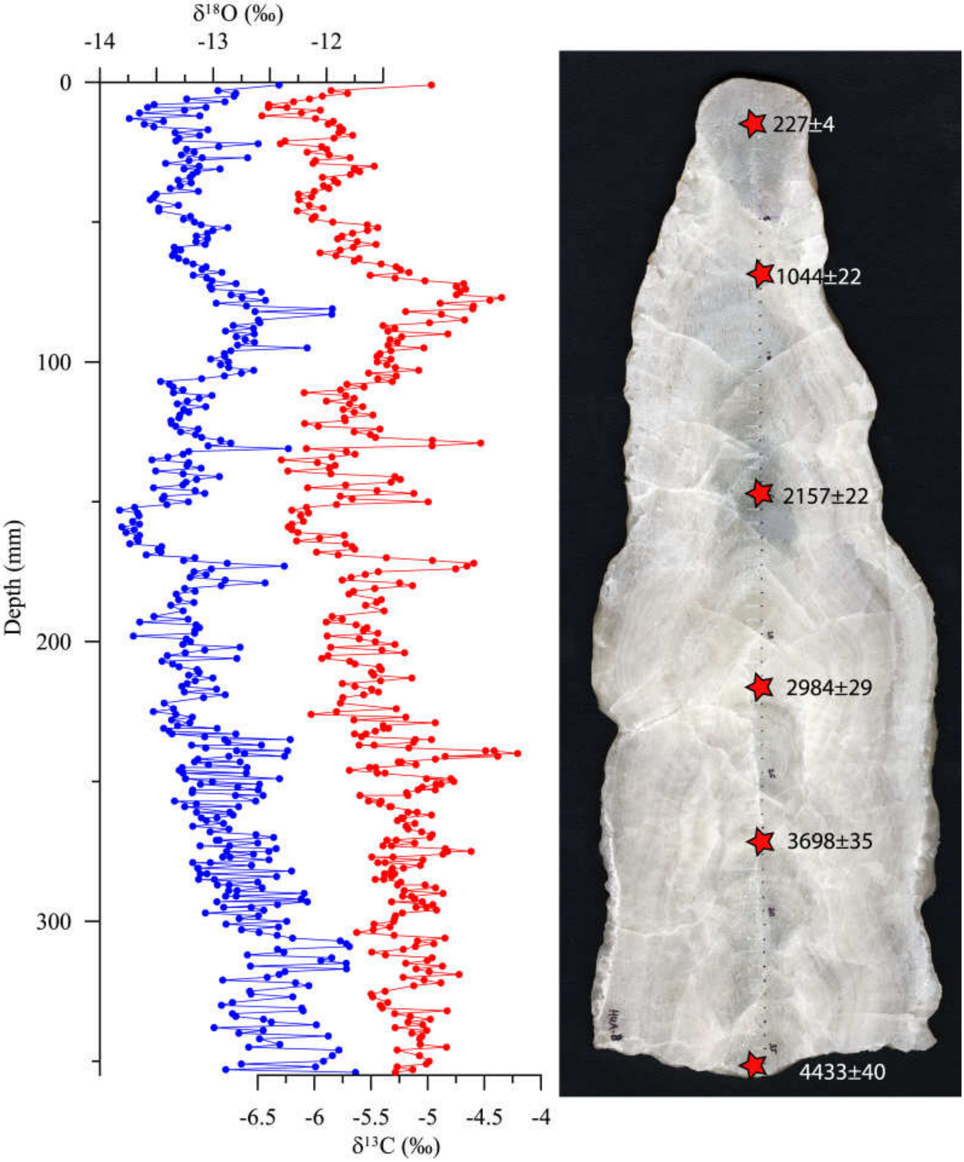

Figure 8.6: The δ^{18}O and δ^{13}C values are plotted stratigraphically. A picture of stalagmite HUA-8 is shown at the right with the Uranium series indicated by stars. The growth layers of HUA-8 are visible in the photo.

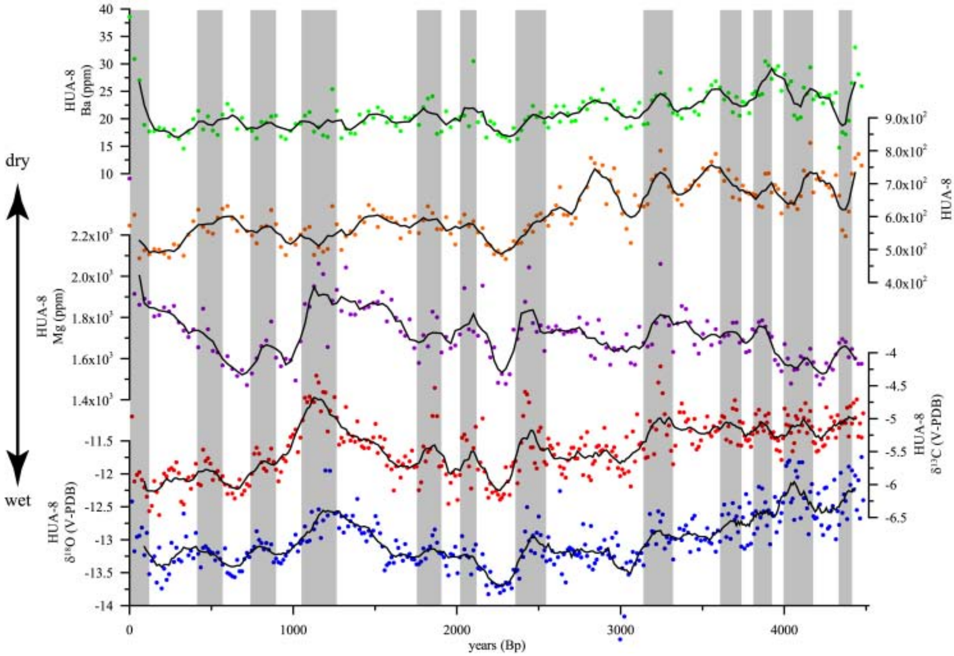

Figure 8.7: This overview plot, shows the variability in δ^{18}O, δ^{13}C and elemental concentrations from the HUA-8 speleothem plotted versus time. The shaded grey areas illustrate the dry periods (low δ^{18}O values). These periods are observed in the δ^{18}O, δ^{13}C and Mg concentration records. However the Ba and Sr elemental concentration shows no correlation to the stable isotope (δ^{13}C, δ^{18}O) and Mg records.

The carbon isotope profile generally varies in phase with the oxygen isotope profile. A correlation exists between δ^{18}O and δ^{13}C values, with an r^2 of 0.44 (figure 8.8).

8.3.2 Fluid inclusions

The stable isotope composition of fluid inclusions is measured throughout the stalagmite and shows a consistent pattern for this late Holocene period (figure 8.9). The δ^2H measurements show relatively stable values for the last ~4500 years, at an average of -104.2 ± 4.3 (1σ) ‰. δ^{18}O shows an average of -13.7 ± 0.66 (1σ) ‰. In the older part of the record, δ^{18}O measurements of fluid inclusion water show a trend towards lower values, which parallels the δ^{18}O profile of speleothem calcite. The δ^2H data of the inclusion water does not seem to show this trend.

Combined δ^{18}O and δ^2H analyses of fluid inclusion water cluster to the right of the Global Meteoric Water Line (figure 8.10). Seepage water samples taken in this cave in September 2003 also plot to the right of the GMWL, but not as far as the fluid inclusion water samples

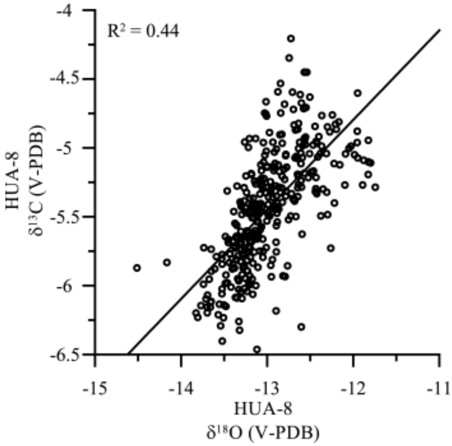

Figure 8.8: δ^{18}O versus δ^{13}C gives a R-square correlation of 0.44.

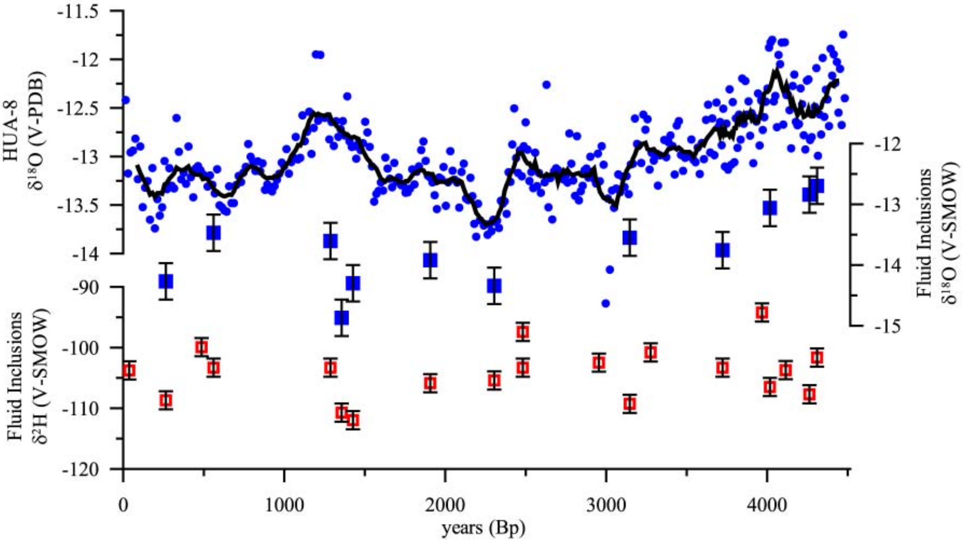

Figure 8.9: Fluid inclusion data of HUA-8, showing the δ^{2}H values as open squarez and δ^{18}O values as solid squarez. Note that the δ^{18}O and δ^{2}H values are measured simultaneously during one analyses of a single crush. More δ^{2}H values are present as for the first series simultaneously measured δ^{2}H and δ^{18}O values were not possible and consequently only δ^{2}H data was collected.

(figure 8.10). This may suggests that some evaporation has influenced the fluid inclusion waters analysed. This could either be a natural process, as suggested by the associated seepage water stable isotope composition, or this could be an analytical artefact due to (undesired) evaporation loss of fluid inclusion water in the 'Amsterdam Device'.

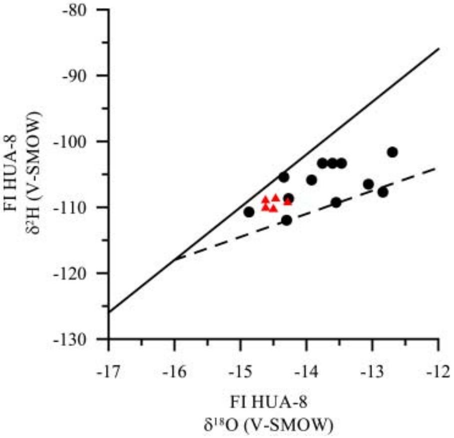

Figure 8.10: Crossplotted δ^2H and δ^{18}O values of fluid inclusion water measured from a single crush. The fluid inclusion data plots right of the Global Meteoric Water Line, suggesting that evaporation has occurred, during transport of the water vapour from the Atlantic Ocean to Gruta de Huagapo, or during percolation of the meteoric water through the soil to the cave interior. Cave seepage water δ^{18}O and δ^2H values are indicated in triangles. The solid line illustrates the GMWL, while the dashed line has a slope of 3.5. Evaporated water bodies have a slope between the dashed line (very dry atmoshpere) and the solid line (close to 100% relative humidity)(Criss, 1999).

8.3.3 Trace elements

The measured trace elements, Mg, Sr and Ba, are plotted in figure 8.7 together with the stable isotope records of speleothem calcite. The Mg concentration record correlates well with the δ^{18}O and δ^{13}C records, showing higher Mg-concentrations to coincide with higher δ^{18}O and δ^{13}C values. Only in the younger part of the record this correlation is relatively poor. For the Sr and Ba records correlations with δ^{18}O and δ^{13}C are poor throughout the entire record. Sr and Ba concentrations do show in-phase cyclicity, but there is a distinct difference in the amplitude of variation, where Sr shows relatively large fluctuations in the concentration (~200 ppm) compared to the ~10 ppm Ba concentration fluctuation.

8.4 Discussion

As Gruta de Huagapo stable isotope records of speleothem calcite and fluid inclusion are constructed, paleo-temperatures calculation can be made for the last ~4500 years. Subsequently, the influence of cave drip water and thus rainfall on the δ^{18}O composition of the speleothem calcite can be reconstructed as the contribution of temperature to the speleothem δ^{18}O record is known.

8.4.1 Stable isotopes and trace element concentrations

Variations in the δ^{18}O record can be influenced by 1) changes in the amount of rainfall or 2) changes in the cave temperature and 3) kinetic fractionation reflecting drip rate and thus rainfall, reinforcing the direct effect of rainfall. δ^{18}O values of cave seepage water are directly influenced by the isotope composition of rainfall above the cave which recharges the hydrological reservoir. δ^{18}O values of the fluid inclusion water of the speleothem will therefore directly represent the isotope composition of the rainfall above our study area. The overall pattern of the δ^{18}O data of the fluid inclusion water follows the δ^{18}O data of the speleothem calcite (figure 8.9). This results in relative stable temperatures for the last ~4500 years. This means that the isotope composition of cave water, and not temperature, is the main controlling factor on δ^{18}O values of speleothem calcite.

Relatively depleted (low) oxygen isotope values of speleothem calcite are therefore interpreted to reflect periods of intensified rainfall above the cave due to increased atmospheric convection. Increased amounts of precipitation will reduce the residence time of percolating water, thus decreasing precipitation of calcite along the flow path, before the seepage water enters the cave. In this way, a reduced seepage water residence time decreases Mg/Ca, Sr/Ca, and Ba/Ca ratios of the seepage water (Fairchild et al., 2000; Verheyden et al., 2000). This mechanism explains the similarity between the Mg record and the δ^{18}O record, but can not explain the different behaviour of Sr and Ba compared to Mg and the stable isotopes records.

Sr and Ba concentrations show an in-phase cyclicity with each other for the late Holocene period. However they show no correlation with the other measured proxies, except that the length of the cycles (200-300 years) is in agreement with the frequency observed in the other records. Ba is often indicative for the amount of organic material from the soil. In this case the Ba concentrations is relative stable showing values between 15-30 ppm.

δ^{13}C values of speleothem calcite are mainly influenced by the soil chemistry. Changes in the vegetation activity will influence the CO_2 concentration and acidity of the percolating water. As the vegetation exists of small bushes and typical alpine vegetation, the response to climate and precipitation changes are relative direct. δ^{13}C values of the seepage water are controlled by a carbon component taken up from the soil and a carbon component from the carbonate host rock. Stalagmite HUA-8 from Gruta de Huagapo shows δ^{13}C values around -5‰. As vegetation has a range in δ^{13}C between approximately -10 to -33‰, it reveals that the host rock carbonate plays a dominant role in the contribution to the δ^{13}C signal in stalagmite HUA-8. The carbonate host rock component will become larger as water becomes more acidified in the soil and consequently dissolves relative more host rock carbonate.

Cyclicity observed in the δ^{18}O, δ^{13}C and Mg records, as illustrated in figure 8.7, show patterns comparable to the record of CLL-1 (chapter 7). The cycles observed in all proxy records show a length between 200-300 years, which is similar to the cycles observed in the Cueva de las Lechuzas stalagmite. Although the Sr and Ba record shows a cyclicity poorly comparable with the δ^{18}O, δ^{13}C and Mg record, they show a similar frequency of 200-300 years. Calculated temperatures, based on fluid inclusion stable isotope data, are relative stable but lack the resolution of speleothem calcite records. The short cycles seen in speleothem calcite records are possibly recording precipitation patterns in the Amazon Basin, comparable to the Cueva de las Lechuzas record. As already suggested in chapter 7 solar insolation cyclicity is the most likely mechanism to cause cyclic rainfall variation in Amazonia at centennial time scales.

8.4.2 Fluid inclusions

Figure 8.10 shows paired δ^{18}O and δ^{2}H analyses of single crushed pieces of stalagmite plotted away from the meteoric water line. This may suggest that the analysed inclusion water is influenced by evaporation. Enriched δ^{18}O values are indicative for water bodies of which water has been evaporated (Mook, 1994). The evaporation line has a lower slope than the GMWL and is plotted for comparison in figure 8.10.

Incomplete recovery of the fluid inclusion water using the extraction technique and protocol as described in Vonhof et al., 2006 and 2007, might cause isotope fractionation of the recovered water. During the pre-heat stage in the crushing device speleothem calcite is heated to ~130°C and fluid inclusion water could already be released and pumped to waste, resulting in an evaporated inclusion water isotope pattern for the measured samples. Furthermore crushed calcite samples might partially open fluid inclusion cavities and small amounts of inclusion water might stay behind in the opened cavities. In both cases this will result in incomplete recovery of inclusion water and possible deviation from their original isotope signal.

An alternative possible explanation for the observed shift of the inclusion water from the GMWL is that evaporation occurred during transport of the water through the soil.

8.4.3 Paleotemperatures

Paleotemperatures are calculated using the paleotemperature equation of Craig (1965). This equation is based on the temperature dependent water-calcite fractionation of oxygen isotopes. However for some measurements of the fluid inclusion record only δ^{2}H data are available. Single δ^{2}H analyses are converted to δ^{18}O along the GMWL, to be used for paleotemperature calculations. Calculated temperatures using δ^{18}O or δ^{2}H values do show a difference, especially when fluid inclusion analyses plot away from the meteoric water line as is observed for this stalagmite. The difference between δ^{18}O and δ^{2}H calculated temperatures is illustrated in figure 8.11. Average calculated temperatures for the last 4500 years are close to 13.7°C using δ^{18}O fluid inclusion values and close to 11.3°C using δ^{2}H fluid inclusion values which are in agreement with the cave temperature of today (12°C). The calculated temperatures using δ^{18}O values of the fluid inclusions are higher than the calculated temperatures using δ^2H. This difference occurs due to the conversion of δ^2H samples to δ^{18}O values using the GMWL, because the measured δ^{18}O values show higher values (right of the GMWL) resulting in higher calculated temperatures. Secondly, the measured δ^{18}O values of fluid inclusion water follow the δ^{18}O record of the speleothem calcite, while the δ^2H values of inclusion water deviate from it for the period 4500-4000 years Bp. Consequently the deviated pattern of fluid inclusion δ^2H values results in a larger variability in calculated temperatures for this particular period. Overall for the last ∼4500 years relative stable cave temperatures are recorded.

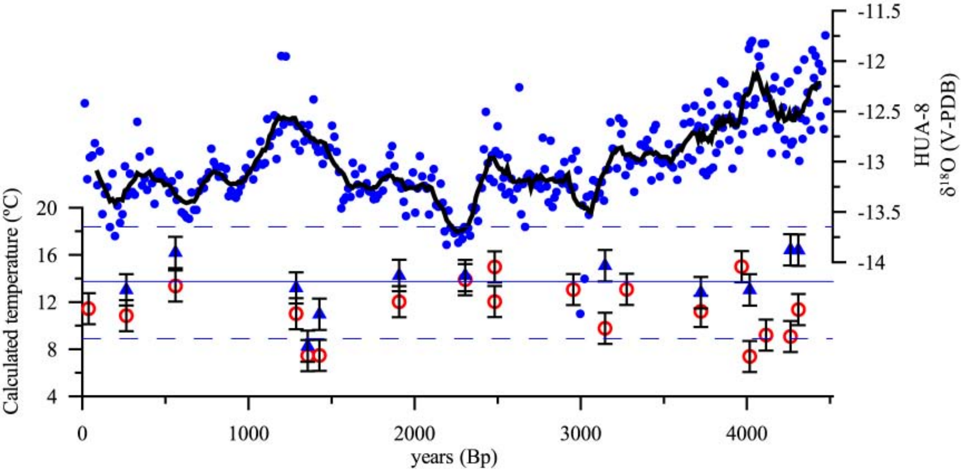

Figure 8.11: δ^{18}O of the speleothem calcite, plotted with the calculated temperatures using δ^{18}O fluid inclusion data (triangles) and δ^2H fluid inclusion data (open dots). The mean paleotemperature of the oxygen isotope period is plotted as a solid line, with the 2 sigma temperature error indicated with dashed lines. δ^2H values are converted using the GMWL, to calculate paleotemperatures using the paleotemperature equation of Craig (1965). It illustrates that some difference in the paleotemperature calculation occurs when seepage water does not plot in the GMWL. We therefore suggest that it is important to use δ^{18}O fluid inclusion to calculate cave temperatures.

8.4.4 Climate interpretation

The Gruta de Huagapo stalagmite has δ^{18}O values fluctuating around -13‰ which is about 5.5‰ lighter than the δ^{18}O values of the Cueva de las Lechuzas stalagmite, with values around -7.5‰. This 5.5‰ shift in oxygen isotope composition is mainly caused by the difference of almost 2900 meters in altitude between the two caves. The stable isotope composition of atmospheric moisture shows a clear trend with altitude which is ultimately recorded in the speleothem calcite. This orographic effect on the stable isotope composition of atmospheric moisture is discussed in detail in Chapter 9.

The speleothem calcite δ^{18}O record of Gruta de Huagapo is indicative for variation in the isotope composition of rainfall above the cave area, as temperature changes are relatively stable, similar to climate interpretation of the speleothem record of Cueva de las Lechuzas. The isotope composition of rainfall is closely related to the amount of convective rainfall in Amazonia, which is mainly controlled by the ITCZ. The ITCZ is a low pressure zone with maximum amounts of convective precipitation. Seasonal north- southward migration of the ITCZ following the caloric equator, results in wet and dry seasons in South America. On interannual timescales the ITCZ is influenced by Sea Surface Temperatures (SST's). Melice and Roucou (1998) show a strong correlation between meridional SST gradients with the isotopic composition of precipitation in South America. This correlation can be explained with the Hadley cell as connecting mechanism. The Hadley cell activity is sensitive for SST resulting in a north-southward migration, causing the ITCZ to move parallel. Solar insolation in turn influences SST and will therefore be the most plausible mechanism to influence the convective rainfall in Amazonia, although solar energy by itself is too small to directly influence the climate in Amazonia. Direct correlation between the Gruta de Huagapo stalagmite records and Cueva de las Lechuzas stalagmite records remains difficult, probably due to local influences of the cave and outside environment.

8.5 Conclusions

The record from Gruta de Huagapo is the first high altitude speleothem record from South America. The Gruta de Huagapo stalagmite record shows cyclicity which is in frequency comparable to the lowland stalagmite record Cueva de las Lechuzas. However interpretation of individual measured proxies remains difficult. δ^{18}O, δ^{13}C and Mg give a consistent pattern but they deviate from the Ba and Sr concentrations. Plausible mechanisms to explain those differences are difficult. Changes in the amount of rainfall seem to be recorded in δ^{18}O, δ^{13}C and Mg concentrations. δ^{18}O values of speleothem calcite are dominantly influenced by the isotope composition of precipitation water when temperatures remain stable for this period. Fluid inclusion data showed relative stable temperatures during the late Holocene period at higher altitude suggesting that the calcite δ^{18}O records the amount of rainfall. Convective rainfall is directly related to the geographical position of the ITCZ system, as the ITCZ is controlling the amount of convective generated rainfall. Change in solar insolation on itself can not influence the climate in Amazonia, however through sensitive reactions of the Hadley cell circulation to SST's, the ITCZ system will ultimately shift in phase with the Hadley cell circulation, changing rainfall patterns over South America (Broccoli et al., 2006; Lohmann et al., 2004). This mechanism would explain the similarity in frequency between Gruta de Huagapo and Cueva de las Lechuzas. The deviating Sr and Ba records of Gruta de Huagapo stalagmite from the δ^{13}C, δ^{18}O and Mg records may be caused by local circumstances as this is not seen in the Cueva de las Lechuzas stalagmite (chapter 7).

9

Late Holocene rainwater stable isotope fractionation patterns as evidenced in fluid inclusions from stalagmites and snow from ice cores in an altitudinal transect over the Andes mountain chain

Abstract

Stalagmite fluid inclusion stable isotope data and ice core stable isotope (δ^2H, δ^{18}O) data reflect changes in the hydrological cycle through time. The combined dataset from both sources is used to reconstruct the stable isotope composition of paleo-rainwater across the Eastern flank of the Andes covering an altitudinal range from 700-∼6000 meter. In two lowland caves (Cueva de las Lechuzas, Cueva de Tigre Perdido) and one highland cave (Gruta de Huagapo) stalagmites were collected along the transect, and existing highland ice cores data of Huascarán and Quelccaya were used to provide snow records in the highest area of the mountain chain transect. The stable isotope data show a significant trend of depletion in ^{2}H and ^{18}O values from low to high altitude. This depletion of stable isotopes is mainly caused by the so called 'orographic effect', a major factor in the hydrological cycle along the Andes. To quantify this orographic effect, a Rayleigh distillation model was used to predict δ^2H and δ^{18}O values of rainwater over the Amazon Basin and the Andes. The predicted rainwater stable isotope values delivered by the model are sufficiently similar to the empirically obtained stable isotope values of the combined stalagmite fluid inclusion and ice core stable isotope dataset to suggest that our stalagmite fluid inclusion stable isotope

values are in good agreement with the predicted rainwater values produced by the Rayleigh fractionation model. This shows that fluid inclusion stable isotope data can indeed be used for investigation of stable isotope paleo-rainwater composition and are complementary to the high altitude ice core data.

9.1 Introduction

In recent years climate change has become a major issue on the global political agenda. To better understand the future evolution of the climate Global Climate Models (GCM) are used. Knowledge of paleo-climates provides crucial information to test outcomes of these GCMs.

Stable isotopes are an outstanding and widely-used land and ocean paleo-climate proxy. For instance temperature dependent calcite-water oxygen isotope fractionation is used for paleo-temperature reconstructions. In paleo-oceanography the oxygen isotope composition of, for example, fossil shells of calcareous foraminifera are used, while land studies often rely on oxygen isotopes in calcareous speleothems and ice cores. The global isotope composition of oceans is well known and more and less predictable for glacial-interglacial intervals.

However, the oxygen isotope composition of atmospheric water over land is variable through recent and past time and it is not well known, and therefore complicating the paleo-climate interpretation. There is direct information on the isotopic composition of meteoric water and the fractionation processes involved in the hydrological cycle today (Gat, 1996; Gat, 2000; Gat and Matsui, 1991; Grootes et al., 1989; Rozanksi and Araguás-Araguás, 1995). Information about the hydrological cycle in the past is mainly indirect. For instance, Cruz et al. (2005a), Seltzer et al. (2000) and Maslin and Burns (2000) have interpreted changes in stable oxygen isotope composition in speleothem carbonates to reflect changes in the meteoric water cycle associated with the South America Inter Tropical Convergence Zone (ITCZ). Their interpretations are ambiguous, because other climatological processes such as temperature might have influenced the oxygen isotope signal recorded in the carbonate.

The hydrological cycle and climate are closely related with each other. Crucial information on the hydrological cycle can be gained when the stable isotope composition of paleo-precipitation can be measured directly, avoiding assumptions and corrections used for reconstructions based on indirect proxies. Fossil rainwater drops included in voids in stalagmites offer such possibility to measure directly stable isotope variations through time. This can be connected to fractionation processes related to amount of rainfall in the past hydrological cycle. It has been established that cave drip water, thus fluid inclusion water, is isotopically identical to local rainwater (Caballero et al., 1996; McDermott et al., 2006; Yonge et al., 1985; chapter 2). Most speleothems contain these so called 'microscopic fluid inclusions' that are formed from cave drip water from the time of formation of the relevant speleothem growth increment (Harmon et al., 1978; Harmon et al., 1979; Schwarcz et al., 1976). Approximately 0.1 wt % of speleothem carbonate contains water (McDermott et al., 2006), which can be liberated by recently developed extraction techniques (Dennis et al., 2001; Verheyden et al., ; Vonhof et al., 2007; Zhang et al., 2006). With their large geographical coverage, speleothems can contribute to in-depth investigation of paleo-meteoric conditions. These paleo-meteoric conditions, including stable isotope fractionation in rainwater, vary dramatically in mountain chains, because of the altitudinal effect of rising air masses, the so called orographic effect (Friedman et al., 1962; Siegenthaler and Oeschger, 1980).

In South America few isotope measurements are available of 'fossil' precipitation water, with exception of ice cores, however these are limited to the high altitude Andes (Thompson et al., 2000).

Here we present fluid inclusion stable isotope data of stalagmites collected from lowland to highland caves located in a transect over the East Andean flank. We have used fluid inclusion data of the lowland caves, 'Cueva de las Lechuzas' (700m a.m.s.l) and 'Cueva del Tigre Perdido' (980m a.m.s.l) and highland cave 'Gruta de Huagapo' (3572m a.m.s.l.) to create this transect of the Andean Mountain Chain (figure 9.1). To extend the transect to the very high altitude, stable isotope data of snow from the Andean Ice cores Quelccaya (5670m a.m.s.l) and Huascarán (6048m a.m.s.l.) are added. Thus the combined fluid inclusion stable isotope data from the caves and the stable isotope data from the snow in ice cores should show the orographic effect on stable isotopic composition of rainwater along the altitudinal range of the Andes through time.

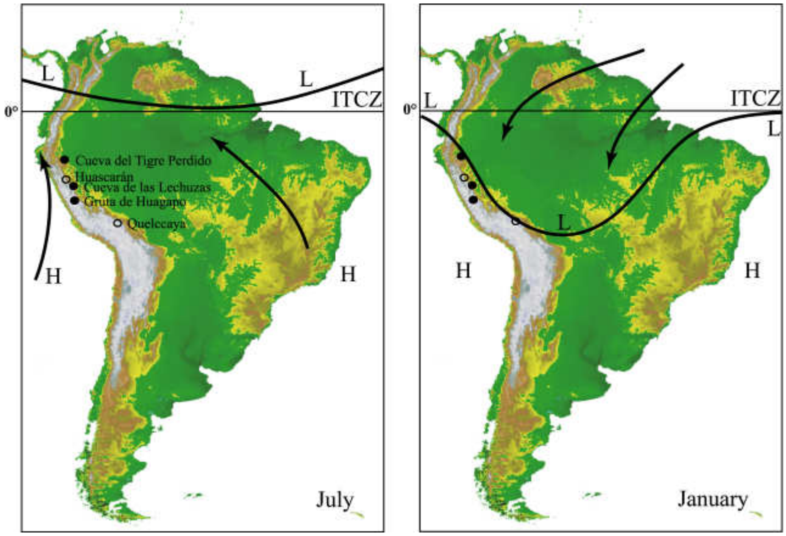

Figure 9.1: Locations of the three caves from where stalagmites were collected (solid dots): Cueva de las Lechuzas; Cueva del Tigre Perdido and Gruta de Huagapo. The ice cores are indicated by open dots: Quelccaya and Huascarán. The black line indicates the position of the ITCZ during July and January. The arrows show the dominant wind directions for the seasons.

A compilation of all fluid inclusion data of the last ∼5000 years from Cueva del Tigre Perdido (chapter 6), Cueva de las Lechuzas (chapter 7), and Gruta de Huagapo (chapter 8) is presented in figure 9.2. The fluid inclusion data from the highland cave Gruta de Huagapo is more depleted in ^{2}H and ^{18}O than the data from two lowland caves, showing the relationship between rainwater stable isotope composition from low to high altitude (figure 9.2). This trend of depletion in ^{2}H and ^{18}O is a result of the orographic effect. To test whether the orographic effect is the main cause of the stable isotope depletion, we use a simple Rayleigh distillation model to quantify potential fractionation of stable isotopes in the various phases of water in the hydrological cycle over the Amazon Basin and the Andean Mountain area with emphasis on the orographic effect.

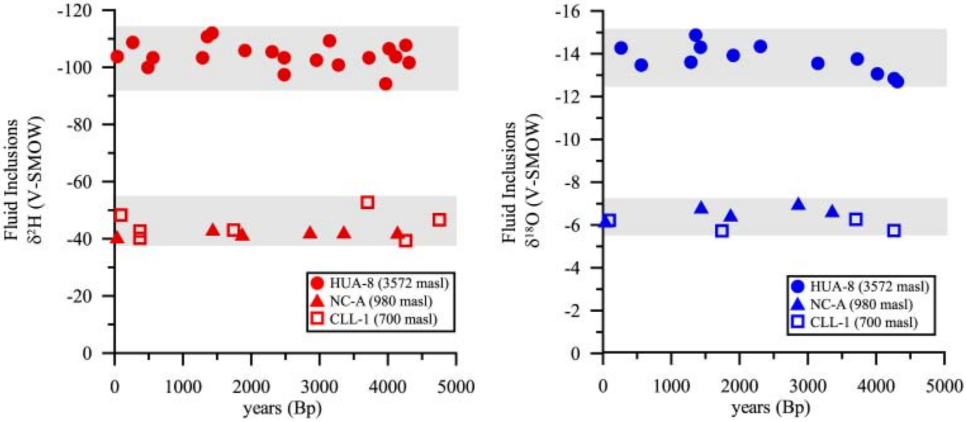

Figure 9.2: Fluid inclusion data of Cueva de las Lechuzas, Cueva del Tigre Perdido and Gruta de Huagapo versus time in years (BP=2000). The solid dots show the isotope values (δ^2H, δ^{18}O) of stalagmite HUA-8 from Gruta de Huagapo located at 3572 meter above sea level (masl). The lowland cave Cueve del Tigre Perdido (stalagmite NC-A) and Cueva de las Lechuzas (stalagmite CLL-1) are illustrated in solid triangles and open squares, repectively. The grey area illustrates the fluid inclusion data from the highland and lowland caves.

9.2 Rayleigh distillation model

9.2.1 Amazon Basin atmospheric circulation

The Amazon Basin contains one of the largest tropical forests in the world. This ecosystem exists due to the enormous amounts of convective rainfall related to the atmospheric circulation of the ITCZ. Evaporated Atlantic Ocean water is transported westward over the Amazon basin by the eastern trade winds. Solar insolation gives rise of the air masses resulting in large amounts of convective generated precipitation. Annual precipitation cycles at the foothills of the Andes (our study area) are associated with a north - southward displacement of the ITCZ, following the caloric equator. During the wet season 80-85% of atmospheric water is lost by runoff, in the dry season almost all precipitation water is recycled by evapo-transpiration (Grootes et al., 1989). Therefore large seasonal variations in the amount of precipitation and in the isotopic composition of the rainfall are present. Figure 9.3 shows schematically the oxygen isotope fractionation over the Amazon Basin and the Andean mountain chain presenting the 'dry' and 'wet' season isotope values of water vapour and rainwater. Figure 9.4 shows the hydrogen isotope fractionation. We used initially a value of 85% atmospheric water vapour loss during the wet season in the Amazon Basin as one of the model parameters, similar to the value of water vapour loss used by Grootes et al. (1989). This estimate of the value of the amount of water vapour loss turns out to be too high to explain the stable isotope data from the stalagmites and snow, see discussion.

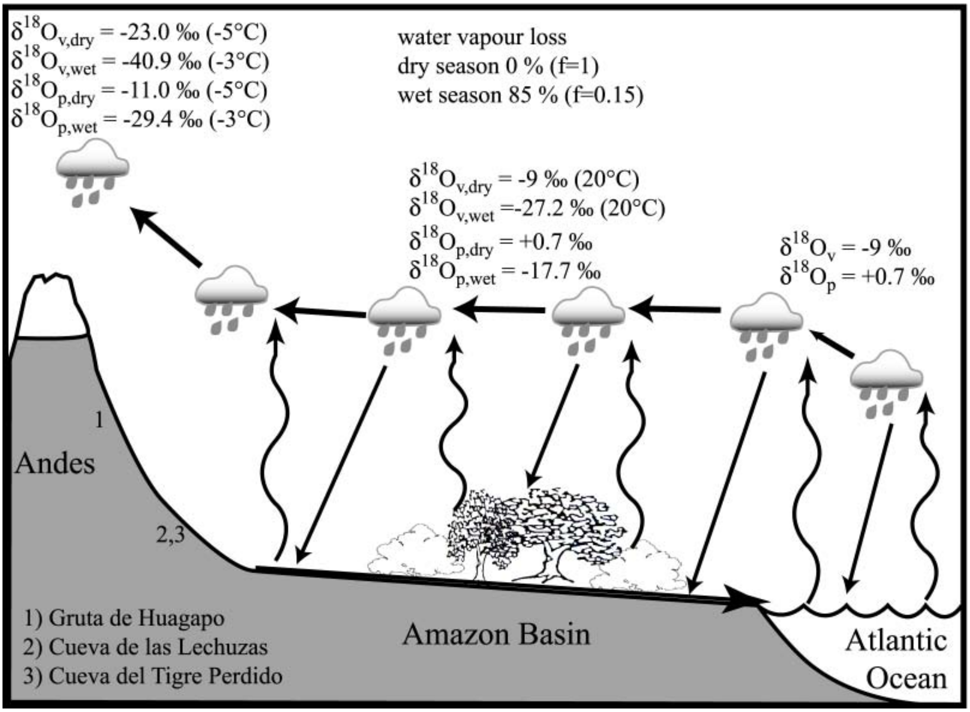

Figure 9.3: Schematic overview of the isotope fractionation of δ^{18}O of atmospheric water over the Amazon Basin. The δ^{18}O values for water vapour ($\delta^{18}O_{v}$) and for precipitation water ($\delta^{18}O_{p}$) during the dry and wet season are shown. The δ^{18}O values are calculated using a Rayleigh distillation model, similar to the approach of Grootes et al. (1989). The location of the caves are indicated by numbers and show schematically the difference in altitude. Figure 9.3 is not in scale and modified from Grootes et al. (1989).

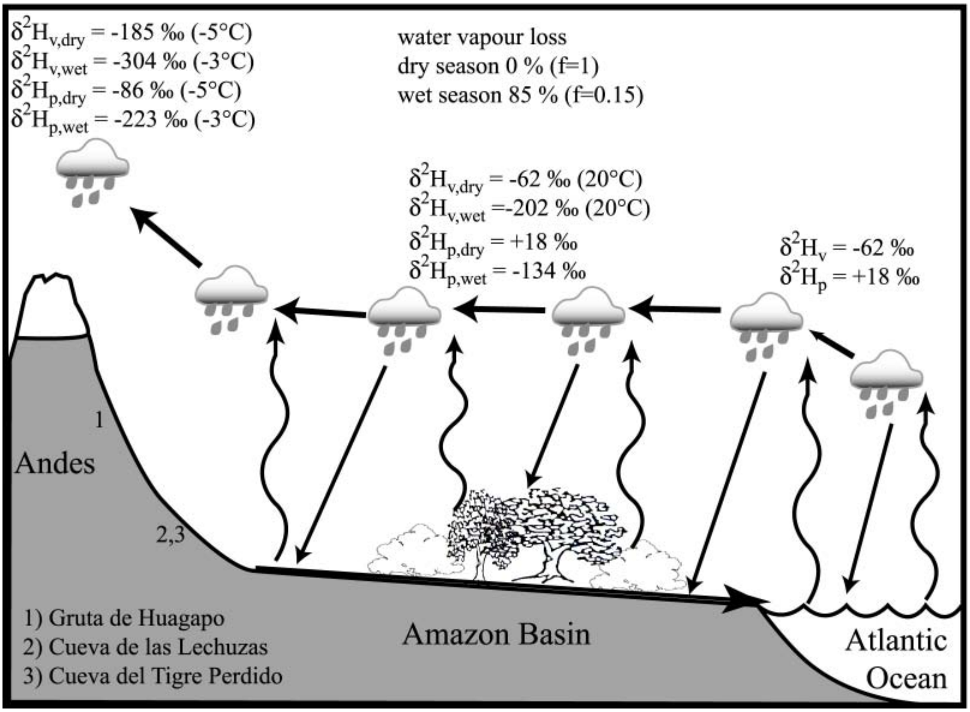

Figure 9.4: Schematic overview of the isotope fractionation of δ^2H of atmospheric water over the Amazon Basin. The δ^2H values for water vapour (δ^2H_v) and for precipitation water (δ^2H_p) during the dry and wet season are shown. The δ^2H values are also calculated using a Rayleigh distillation model.

9.2.2 Rayleigh distillation

The stable isotope variation of water vapour and rainfall over the lowland Amazon Basin is treated as a Rayleigh process (Dansgaard, 1964; Gat, 2000; Gat and Matsui, 1991; Gonfiantini et al., 2001; Grootes et al., 1989). The assumption is made that condensation occurs in equilibrium and that only one state of water can exist so that liquid water is removed from the system. The isotope composition of the remaining fraction is calculated using the Rayleigh equation.

$$\frac{R}{R_0} = \left(\frac{N}{N_0}\right)^{\alpha_{l-v}-1} \tag{9.1}$$

R is the current isotope ratio, while R_0 is the original isotope ratio of $^{18}O/^{16}O$ ($^{2}H/^{1}H$) of the water vapour. α is the water liquid-vapour isotope fractionation factor as defined by Majoube (1971), equation 9.2.

$$10^3 \ln\alpha_{l-v} = 1.137 \cdot 10^6 T^{-2} - 0.4156 \cdot 10^3 T^{-1} - 2.0667 \tag{9.2}$$

(Majoube, 1971)

N_0 is the original amount of water vapour and N is the current amount of water vapour. N/N_0 defines the current fraction (f) of the water vapour.

The δ^{18}O (δ^2H) value is calculated using the δ_v and δ_p for water vapour and precipitation water, respectively.

$$\delta_v = \left(\frac{N}{N_0}\right)^{\alpha_{l-v}-1} \cdot (1 + \delta_{v_0}) - 1 \tag{9.3}$$

$$\delta_p = \alpha_{l-v} \cdot (1 + \delta_v) - 1 \tag{9.4}$$

Oxygen isotope fractionation over the Amazon basin as calculated by Grootes et al. (1989), shows a seasonal variation of +0.07 ‰ (no vapour loss) to -17.7 ‰ (85% water vapour loss). In our experiment we use the same starting conditions as given by Grootes et al. (1989); δ^{18}O water vapour of the Atlantic Ocean has a value of -9‰, condensation temperature has a value of 20°C. Grootes et al. (1989) choose this temperature as it represents the cloud base at ~850 mbar at about ~1500 m altitude.

For hydrogen isotope fractionation we used the same conditions as for oxygen. δ^2H water vapour from the Atlantic Ocean has a value of -62 ‰ converted from the equivalent δ^{18}O water vapour value along the Global Meteoric Water Line (GMWL)

9.2.3 Stable isotope values over the Amazon Basin up to the Andes (model)

Stable isotope fractionation of the atmospheric water fraction during transport over the Amazon basin is illustrated in figures 9.3 & 9.4. Water evaporated ($\delta^{18}O_v$) from the Atlantic Ocean has an oxygen isotope value of about -9‰ (V-SMOW). Condensation of this evaporated water leads to an initial oxygen isotope value of about +0.7‰ in rainfall. During the dry season the oxygen isotope value will remain similar over the entire Amazon Basin, due to evapo-transpiration or simply the fact that no water vapour loss occurs in the system. All the rainwater is evapotranspired back to the atmosphere, mainly through plant leaves of the abundant vegetation. Water evaporated at the leaf surface is not isotopically fractionated (Moreira et al., 1997).

In wet season, however, not all rainwater is completely transpired back to the atmosphere, due to the high amount of rainfall, resulting in a water vapour loss in the atmosphere. Isotopically heavy rainwater is transported back to the ocean resulting in a depletion of heavy isotopes in the atmosphere. The more rainwater is transported back to the ocean and the less is transpired back to the atmosphere, the lower the isotope values of the remaining water vapour will be. In figure 9.3 this is illustrated as the difference in the isotope values of rainfall ($\delta^{18}O_p$) during the dry and wet season. +0.7‰ and -17.7‰, respectively. This process is seasonally dependent.

Our modelling outcome of the hydrogen isotope composition shows a similar pattern as the oxygen isotope values over the Amazon Basin as well as across the Andes (figure 9.4). In the dry season enriched δ^2H of rainwater values occur. During the wet season when 85% water vapour loss occurs, the model outcome results in depleted δ^2H values of rainwater. δ^2H values of rainwater (δ^2H_p) over the Amazon Basin are between +18 and -134‰ for the dry and wet season, respectively.

Figure 9.5 illustrates the $\delta^{18}O$ and δ^2H values of water vapour and precipitation water versus the remaining fraction when the liquid water phase is removed from the system using equation 9.3. A fraction of 0.15 means 85% water vapour loss from the atmosphere and is indicative for the 'wet' season, giving $\delta^{18}O_p$ values of -17.7‰ and δ^2H_p of -134‰.

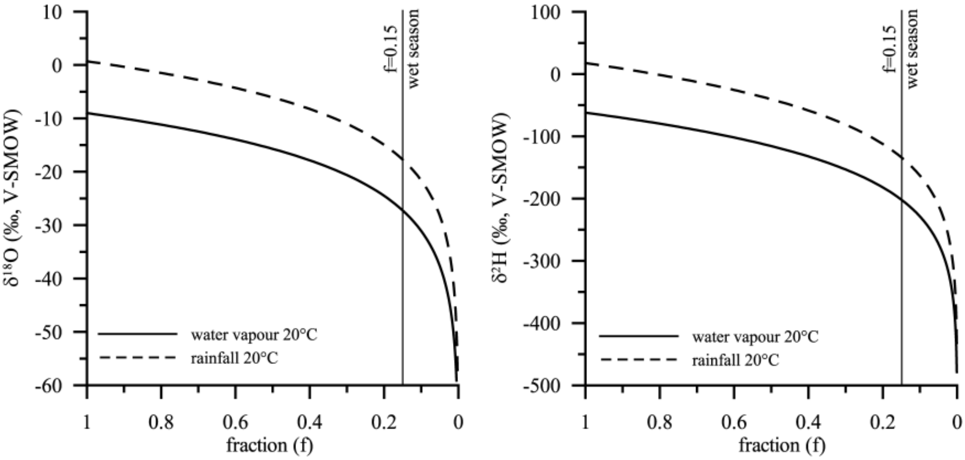

Figure 9.5: The relation between the water vapour fraction and the isotope value of $\delta^{18}O$ (left panel) and δ^2H (right panel) is illustrated. The solid line illustrated the isotope composition at 20°C with a decreasing fraction. Fraction 0.15 is equal to 85% water vapour loss which is chosen as the amount of water vapour loss in the Amazon basin during the wet season.

9.2.4 The altitude effect (model)

To simulate the orographic effect on the isotope fractionation of water vapour due to adiabatically expansion, we use again the Rayleigh isotope fractionation (equation 9.1). The altitude dependent water vapour fraction needed for the Rayleigh equation is calculated based on the approach of Moran et al. (2007). In this approach water vapour content is temperature and pressure dependent. The water vapour content and remaining fraction in the atmosphere are closely related as is illustrated in figure 9.6. The water vapour content (q, g/kg) is atmospheric pressure and temperature dependent according to equation 9.5.

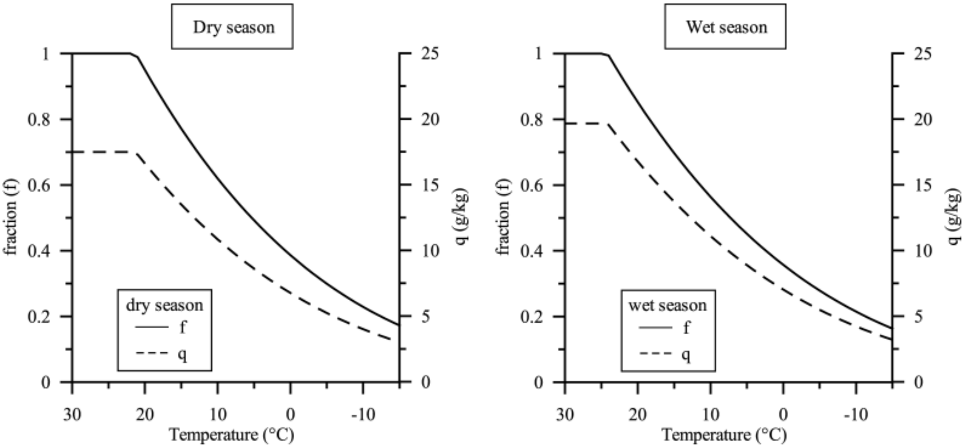

Figure 9.6: The water vapour fraction versus temperature is shown as the solid line. Lower temperatures cause condensation of water vapour resulting in rainfall. The water vapour fraction will decrease when temperature decreases. The water vapour content (q, g/kg; dashed line) changes similarly. The condensation point is reached at 21°C for the dry season and 24°C for the wet season. The figure is modified from Moran et al. (2007).

$$q = \frac{Re_v}{R_v P} \approx 0.622\frac{e_v}{P} \tag{9.5}$$

Where q is the water vapour content of the atmosphere in g/kg. R and R_v are the ideal gas law constants for the bulk air mass and for pure vapour and P is the total pressure; e_v is the vapour pressure.

As the pressure changes with altitude we used equation 9.6 to calculate the pressure with altitude.

$$P = P_0 \cdot \left[\frac{T_0}{T_0 + L \cdot (h - h_0)}\right]^{\frac{g_0 M}{RL}} \tag{9.6}$$

Where P is static pressure in pascals, P_b is the pressure at sealevel. T_0 is temperature in Kelvin (25°C). L is standard temperature lapse rate (Kelvins/m), -0.00536 and -0.00571 for wet and dry season, respectively. g_0 is the gravitational constant. M is molar mass of air.

The vapour pressure for liquid water is calculated from the Clausius-Clapeyron equation.

$$e_v = 6.11\exp\left[6808\left(\frac{1}{T_0} - \frac{1}{T}\right) - 5.09\ln\left(\frac{T}{T_0}\right)\right] \tag{9.7}$$

Where $T_0 = 273.15$ K.

Figure 9.6 shows the water vapour content and water vapour fraction, based on the equations above. To simulate the altitude pressure and temperature changes across the Andean mountain chain equation 9.6 and 9.7 are used, resulting in the water vapour fraction according to equation 9.5. The remaining water vapour fraction is used to calculate the δ^{18}O and δ^{2}H values (equation 9.3)

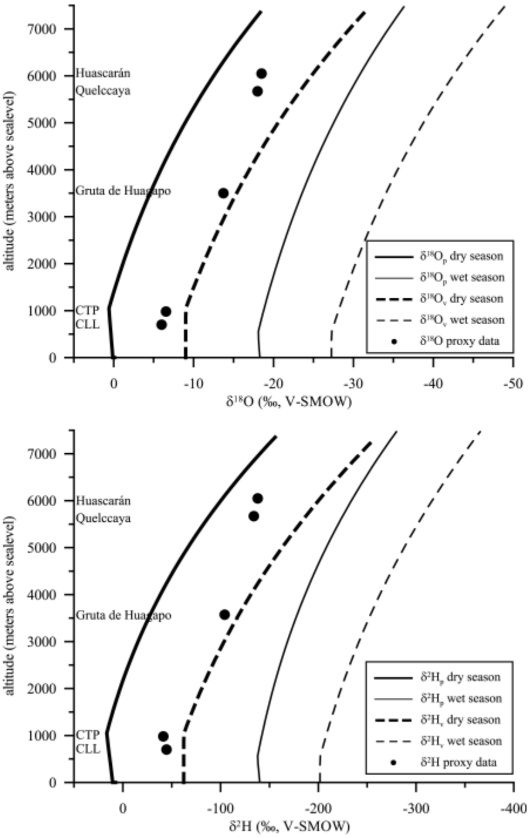

Figure 9.7: Altitude Rayleigh model δ^{18}O values of precipitation water and water vapour with plotted proxy data of three caves and two ice cores. $\delta^{18}O_P$ stands for oxygen isotope composition of precipitation water where $\delta^{18}O_V$ stands for oxygen isotope composition of water vapour. For the dry season the $\delta^{18}O_V$ values = -9‰ for the wet season $\delta^{18}O_V$ = -27.2 ‰ are taken as the δ^{18}O values at the foothills of the Andes, conform Grootes et al. (1989). The hydrogen isotope data of the ice cores are calculated using snow δ^{18}O values converted along the GMWL to δ^{2}H values.

Orographic uplift and adiabatic cooling of air masses lead to saturation, condensation, and rainout, with fractionation during condensation leading to isotopically depleted precipitation of rainwater at higher elevations.

The isotope fractionation due to the altitude effect is almost independent of the seasonal fractionation in the Amazon Basin (Grootes et al. 1989). The model of Grootes et al. (1989) predicts an 11.2 and 11.0 ‰ fractionation for δ^{18}O during the dry and wet season between rainwater in lowland Amazon Basin and the Quelccaya ice cap in the high Andes (figure 9.3). The difference in altitude is 5.6 km and thus an isotope shift of ∼11‰ suggests a ∼2‰ negative shift in the oxygen isotope value per kilometre height. This is in good agreement with the observed range of oxygen isotope data of precipitation water from the Amazon basin (+0.7 to -17.7‰, dry and wet season, respectively,) and the oxygen isotope data from snow in the Quelccaya ice core (-10.5 to -28.7‰; Grootes et al., 1989). The results of our model output shows a difference of 11.7‰ in oxygen isotope values for the altitude effect (figure 9.3), slightly different from the ∼11‰ found by Grootes et al. (1989).

Hydrogen isotope fractionation shows a similar pattern during uplift across the Andean Mountain chain. A relative constant offset is found of 104 and 89‰ for δ^{2}H values during the dry and wet season, respectively (figure 9.4).

9.2.5 Testing the model

For this study a simple Rayleigh distillation model was used to predict stable isotope values of water vapour and rainwater along the altitudinal transect. More advanced models consider different fractionation options, other starting conditions etc. To avoid this complexity and for illustration purposes only we used the fractionation model of Grootes et al. (1989) for the Amazon Basin and an orographic model based on Moran et al. (2007). The model outcome of stable isotope values in water vapour and rainwater along the transect is comparable with the modelled values of of oxygen isotope fractionation by Pierrehumbert (1999) for tropical conditions (Temperature 298 K), although Pierrehumbert (1999) used a more complex thermodynamic model. Pierrehumbert (1999) calculated the expected δ^{18}O values of precipitation water using the Rayleigh distillate, showing that not the temperature in situ is important but the difference between the evaporation temperature and precipitation temperature. Comparison of the output of the two models shows that the overall pattern of the oxygen isotope composition with altitude is comparable. Therefore our simple model fits its purpose of quantification of the altitude effect.

9.3 Results

9.3.1 Stable isotopes of fluid inclusions fromcaves along the transect

Our fluid inclusions dataset is measured from four stalagmites collected from three different caves. Here follows a résumé of the quality of the stable isotope data from the fluid inclusions derived from the stalagmites. Cueva de las Lechuzas, located at approximately 700 meter above sealevel, is one of the lowland caves. The collected stalagmite (CLL-1) shows relative large scatter for the stable isotope data from the fluid inclusions and covers the last ~4500 years.

Another lowland Amazonia cave is Nueva Cajamarca. We collected two speleothems (NC-A & NC-B) from this cave both capturing excellent preserved fluid inclusions. The combined stable isotope record of fluid inclusions of these two stalagmites covers the last 13500 years (chapter 6). For this study we only used fluid inclusion data covering the last 5000 years, the equivalent period covered by the stalagmites from the other caves. This cave is located at 980 meter above sealevel, ~400 km northwards of Cueva de las Lechuzas.

Gruta de Huagapo is a cave located in the Andes at 3572 meters altitude approximately 200km South of Cueva de las Lechuzas. We collected a speleothem (HUA-8) with excellent preserved fluid inclusions covering the last ~5000 years.

The Andean ice cores Huascarán and Quelccaya are used to extend the altitude transect (Thompson et al., 2000).

Table 9.1 gives all the fluid inclusion data for the three caves. Fluid inclusion data of stalagmite CLL-1 show an average value of -44.71 ‰ +/- 4.79 ‰ (1σ) for δ^2H and -6.54 ‰ +/- 0.32 ‰ (1σ) for δ^{18}O over the last ~5000 years. The data for speleothem NC-A and NC-B show an average value of –41.41 ‰ +/- 0.90 ‰ (1σ) for δ^2H and -5.84 ‰ +/- 0.68 ‰ (1σ) for δ^{18}O over the last ~5000 years. The Andean speleothem HUA-8 gives fluid inclusion stable isotope values of -104.17 ‰ +/- 4.35 (1σ) for δ^2H and -13.72 ‰ +/- 0.66 ‰ for δ^{18}O for the last ~4500 years.

Snow from the Quelccaya ice core (5670m a.m.s.l.) has average δ^{18}O values of -18‰ for the last 5000 years. We used the equation of the Global Meteoric WaterLine (GMWL; Craig, 1961) to calculate the equivalent average δ^2H value for Quelccaya which is then close to -126‰, but might deviate from the actual δ^2H value of snow from that area.

Recent seasonal snow δ^{18}O values are available for Quelccaya and show δ^{18}O values of -10.4‰ for the dry season and -33.7‰ during the wet season (Thompson et al., 2000), fitting the modelled range of the dry and wet season oxygen isotope values at 5670 meter altitude.

Huascarán (6048 m a.m.s.l.) shows snow δ^{18}O values of -13.3 and -19.8‰ (average -17.2‰). Modern (0-1ka) snow δ^{18}O values of Huascarán are on average -18.5‰ (Thompson et al., 2000).

The variations in fluid inclusion stable isotope data from stalagmites and snow stable isotope data along the altitude transect reveal clear relationships between altitude and measured oxygen and hydrogen isotope values (figure 9.2). This relationship of depletion in stable isotopes is mainly a result of the orographic effect.

9.3.2 Data-model comparison

To simulate the moisture transport pathway and fractionation of stable isotopes in water vapour and rainwater from the Atlantic Ocean to the high Andes, the model results are presented from two geographical areas: the Amazone Basin and the high Andes. The first part of the model output describes results of the seasonal isotope fractionation of rainfall over the Amazon Basin during the dry and wet season, showing large seasonal variation, as summarised in figures 9.3 & 9.4. These lowland results of the modelled fractionation over the Amazon Basin are important because they are used for starting conditions for the orographic fractionation modelling (second part). The second part of the model, the orographic fractionation, simulates the change in rainwater isotope composition with altitude (figure 9.7). Fractionation of stable isotope values of water vapour and rainwater is also presented for the highland Andes area using the two seasonal isotope fractionation endmembers of lowland Amazonia (figure 9.5). The seasonal endmembers are used to illustrate the total isotope variation over the seasons in lowland Amazonia and in the high Andes. Meteorological studies of modern stable isotope values in water vapour and rainwater for the lowland Amazonia and Andes highland show similar values of seasonal stable isotope composition of water vapour and rainwater as produced by the model (Grootes et al., 1989; Rozanksi and Araguás-Araguás, 1995). Fluid inclusions (cave drip water) usually have an isotope signal which is equal to the weighted annual mean of rainfall above the cave (McDermott et al., 2006; Yonge et al., 1985).

9.4 Discussion

The main objective of this chapter was to quantify the orographic effect on stable isotope values of water vapour and rainwater through time in the Andes area. For this chapter a simple Rayleigh distillation model was used to predict stable isotope values of water vapour and rainwater along the altitudinal transect. These predicted stable isotope values of rainwater are similar to the measured values of stalagmite fluid inclusions and ice core snow along the transect. Thus, similarity of modelling results and empirical findings suggests that the simple model captures in detail the main fractionation processes of the different water phases along the altitudinal transect. The main trends of depletion of the ^{2}H and ^{18}O isotopes in rainwater with altitude can be clearly found in output from the model and in the measured values of the fluid inclusions (figure 9.7). The stable isotope values from the fluid inclusions and snow consistently plot between the modelled stable isotopes of rainwater for the wet and dry seasons. However, the stable isotope values of fluid inclusions and snow are biased towards to the modelled dry season precipitation for δ^{18}O and δ^2H values (figure 9.7). This result is surprising because fluid inclusions (cave drip water) usually have an isotope signal which is equal to the weighted annual mean of rainfall above the cave (McDermott et al., 2006; Yonge et al., 1985). In South America the weighted annual mean of rainfall is mainly dominated by the wet season, and thus cave drip water δ^{18}O values should be closer to the values of stable isotopes of rainwater during the wet season than during the dry season (Rozanksi and Araguás-Araguás, 1995).

The small deviation between predicted and measured stable isotope values is most likely caused by uncertainties in boundary conditions of the initial parameters describing the starting conditions of water vapour and rainwater at the base of the foothills after isotope fractionation in the Amazon Basin. One of the important input parameters is the assumption that 85% water vapour loss occurred along the moisture transport pathway from the Atlantic Ocean towards the foothills of the Andes. To test the validity of this assumption we fed the altitudinal model with four different amounts of moisture loss over the Amazon Basin, ranging from 85% to 70% (figure 9.8). Our findings are that 75% water vapour loss in the Amazon Basin for the model gives better agreement between the modelled stable isotope values and the fluid inclusion and ice core stable isotope data.

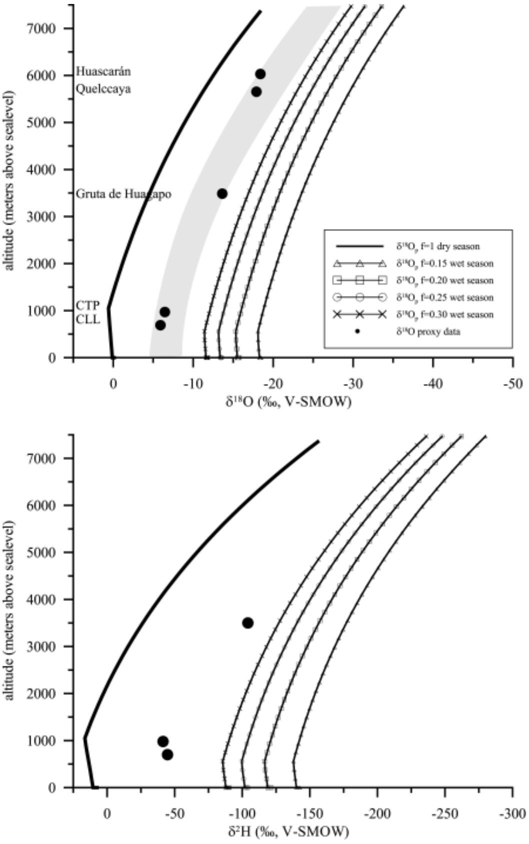

Figure 9.8: The δ^{18}O and δ^{2}H values of versus altitude. The amount of water vapour loss in the Amazon basin is varied between 85% (f=0.15) and 70% (f=0.3). This results in a shift of the starting conditions of the isotope composition of the water vapour. The isotope composition of the rainwater will be relative more positive when the water vapour loss in Amazon Basin is smaller.

9.5 Conclusions

Stalagmite fluid inclusion and snow stable isotope data of meteoric origin can be used to reconstruct atmospheric conditions in the past. The measured fluid inclusion and stable isotope results are in agreement with the predicted isotope range calculated for rainfall at different altitudes across the Andean mountain range using a Rayleigh fractionation model. The measured and predicted stable isotope values of rainwater are primarily influenced by the orographic effect, a major cause of stable isotope fractionation at high altitude. Overall the fluid inclusion and snow stable isotope values are biased to the dry season. We have shown that using a water vapour loss of about 75% in the Amazon Basin would give predicted values by the model in better agreement with our fluid inclusion and snow isotope data than 85% water vapour loss as used by Grootes et al. (1989).

This study shows the clear trend between the stable isotope composition rainfall (preserved as fluid inclusions) and altitude. From a geological perspective, one could use fluid inclusion stable isotope data to study paleo-altitudes at geological timescales (e.g. Gosh et al., 2006; Rowley and Garzione (2007)). Travertine formations deposited during the period of uplift of the Andean mountain chain, could reconstruct tectonic uplift rates. The resolution to quantify the paleo-altitude is potentially a few hundreds of meters as shown by this study.

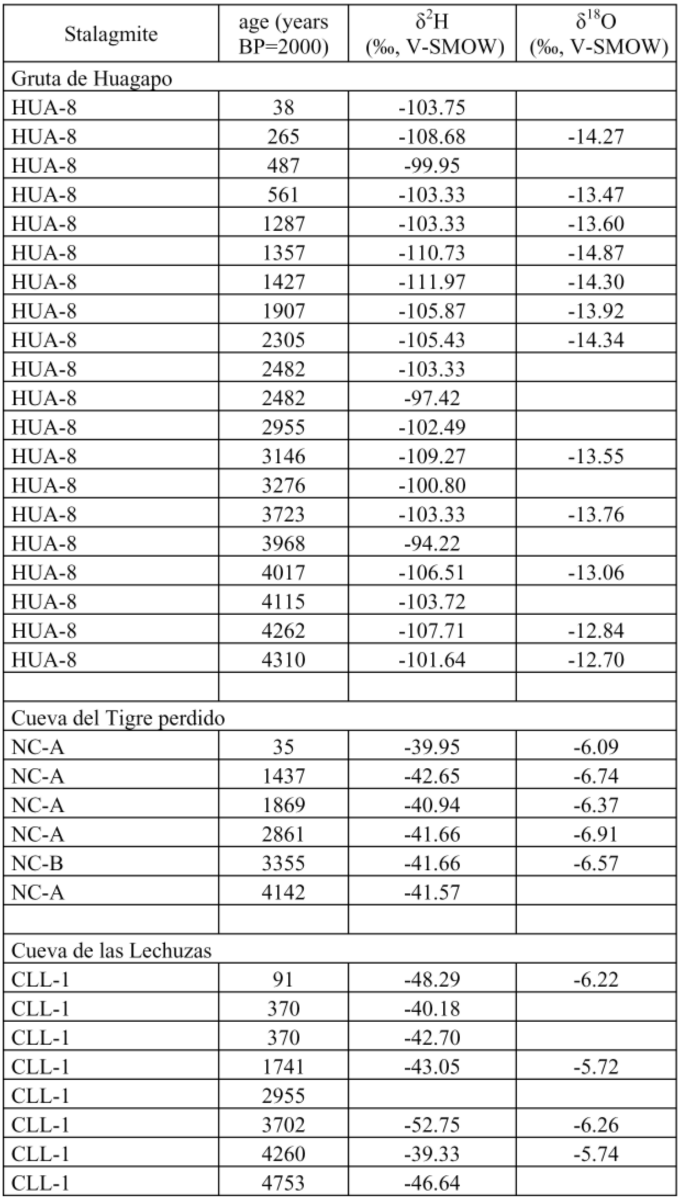

Stalagmite	age (years BP=2000)	δ^2H (‰, V-SMOW)	δ^{18}O (‰, V-SMOW)
Gruta de Huagapo			
HUA-8	38	-103.75	
HUA-8	265	-108.68	-14.27
HUA-8	487	-99.95	
HUA-8	561	-103.33	-13.47
HUA-8	1287	-103.33	-13.60
HUA-8	1357	-110.73	-14.87
HUA-8	1427	-111.97	-14.30
HUA-8	1907	-105.87	-13.92
HUA-8	2305	-105.43	-14.34
HUA-8	2482	-103.33	
HUA-8	2482	-97.42	
HUA-8	2955	-102.49	
HUA-8	3146	-109.27	-13.55
HUA-8	3276	-100.80	
HUA-8	3723	-103.33	-13.76
HUA-8	3968	-94.22	
HUA-8	4017	-106.51	-13.06
HUA-8	4115	-103.72	
HUA-8	4262	-107.71	-12.84
HUA-8	4310	-101.64	-12.70
Cueva del Tigre perdido			
NC-A	35	-39.95	-6.09
NC-A	1437	-42.65	-6.74
NC-A	1869	-40.94	-6.37
NC-A	2861	-41.66	-6.91
NC-B	3355	-41.66	-6.57
NC-A	4142	-41.57	
Cueva de las Lechuzas			
CLL-1	91	-48.29	-6.22
CLL-1	370	-40.18	
CLL-1	370	-42.70	
CLL-1	1741	-43.05	-5.72
CLL-1	2955		
CLL-1	3702	-52.75	-6.26
CLL-1	4260	-39.33	-5.74
CLL-1	4753	-46.64	

Table 9.1: The fluid inclusion data (δ^2H, δ^{18}O) of the three caves. For CLL-1 the age model without hiatus is used (chapter 7). From Cueva del Tigre Perdido the data from stalagmite NC-A and NC-B are used covering the last 5000 years, more fluid inclusion data are available, see chapter 6.

References

Atkinson, T. C. (1977). Carbon dioxide in the atmosphere of the unsaturated zone: An important control of groundwater hardness in limestones. *Journal of Hydrology*, 35(1-2):111–123.

Auler, A. S. & Smart, P. L. (2004). Rates of condensation corrosion in speleothems of semi-arid northeastern Brazil. *Speleogenesis and Evolution of Karst Aquifers*, 2(2):1–2.

Auler, A. S., Wang, X., Edwards, R. L., Cheng, H., Cristalli, P. S., Smart, P. L. & Richards, D. A. (2004). Palaeoenvironments in semi-arid northeastern Brazil inferred from high precision mass spectrometric speleothem and travertine ages and the dynamics of South American rainforests. *Speleogenesis and Evolution of Karst Aquifers*, 2(2):1–4.

Ayalon, A., Bar Matthews, M. & Sass, E. (1998). Rainfall-recharge relationships within a karstic terrain in the Eastern Mediterranean semi-arid region, Israel: δ^{18}O and δ^{2}H characteristics. *Journal of Hydrology*, 207(1-2):18–31.

Baker, A., Barnes, W. L. & Smart, P. L. (1997a). Variations in the discharge and organic matter content of stalagmite drip waters in Lower Cave, Bristol. *Hydrological Processes*, 11(11):1541–1555.

Baker, A. & Brunsdon, C. (2003). Non-linearities in drip water hydrology: an example from Stump Cross Caverns, Yorkshire. *Journal of Hydrology*, 277(3-4):151–163.

Baker, A., Genty, D., Dreybrodt, W., Barnes, W. L., Mockler, N. J. & Grapes, J. (1998). Testing theoretically predicted stalagmite growth rate with Recent annually laminated samples: Implications for past stalagmite deposition. *Geochimica et Cosmochimica Acta*, 62(3):393–404.

Baker, A., Ito, E., Smart, P. L. & McEwan, R. F. (1997b). Elevated and variable values of ^{13}C in speleothems in a British cave system. *Chemical Geology*, 136(3-4):263–270.

Baker, A., Proctor, C. J. & Barnes, W. L. (2002). Stalagmite lamina doublets; a 1000 year proxy record of severe winters in Northwest Scotland? *International Journal of Climatology*, 22(11):1339–1345.

Baker, A., Smart, P. L., Edwards, R. L. & Richards, D. A. (1993). Annual growth banding in a cave stalagmite. *Nature*, 364:518–520.

Baker, P. A., Rigsby, C. A., Seltzer, G. O., Fritz, S. C., Lowenstein, T. K., Bacher, N. P. & Veliz, C. (2001a). Tropical climate changes at millennial and orbital timescales on the Bolivian Altiplano. *Nature*, 409(6821):698–701.

Baker, P. A., Seltzer, G. O., Fritz, S. C., Dunbar, R. B., Grove, M. J., Tapia, P. M., Cross,

S. L., Rowe, H. D. & Broda, J. P. (2001b). The History of South American Tropical Precipitation for the Past 25,000 years. *Science*, 291(5504):640–643.

Baldini, J., McDermott, F. & Fairchild, I. (2006). Spatial variability in cave drip water hydrochemistry: Implications for stalagmite paleoclimate records. *Chemical Geology*, 235(3-4):390–404.

Banner, J. L., Guilfoyle, A., James, E. W., Stern, L. A. & Musgrove, M. (2007). Seasonal variations in modern speleothem calcite growth in Central Texas, U.S.A. *Journal of Sedimentary Research*, 77(8):615–622.

Bar Matthews, M., Ayalon, A. & Kaufman, A. (2000). Timing and hydrological conditions of Sapropel events in the Eastern Mediterranean, as evident from speleothems, Soreq Cave, Israel. *Chemical Geology*, 169(1-2):145–156.

Bar Matthews, M., Ayalon, A., Kaufman, A. & Wasserburg, G. J. (1999). The Eastern Mediterranean paleoclimate as a reflection of regional events; Soreq Cave, Israel. *Earth and Planetary Science Letters*, 166(1-2):85–95.

Bateman, H. (1910). The solution of a system of differential questions occurring in the theory of radioactive transformations. *Proceedings of the Cambridge Philosophical Society*, 15:423–427.

Becquerel, A. H. (1896a). On the invisible rays emitted by phosphorescent bodies. *Comptes Rendus de Séances de l'académie de Sciences*, 122:501–503.

Becquerel, A. H. (1896b). On the rays emitted by phosphorescence. *Comptes Rendus de Séances de l'académie de Sciences*, 122:420–421.

Bertaux, J., Sondag, F., Santos, R., Soubies, F., Causse, C., Plagnes, V., Le Cornec, F. & Seidel, A. (2002). Paleoclimatic record of speleothems in a tropical region: study of laminated sequences from a Holocene stalagmite in Central-West Brazil. *Quaternary International*, 89(1):3–16.

Bourdon, B., Turner, S. P., Henderson, G. M. & Lundstrom, C. C. (2003). Introduction to U-series Geochemistry. In B. Bourdon, G. M. Henderson, C. C. Lundstrom & S. P. Turner, editors, *Uranium-series geochemistry*, volume 52, pp. 1–21.

Broccoli, A., Dahl, K. & Stouffer, R. (2006). Response of the ITCZ to Northern Hemisphere cooling. *Geophysical Research Letters*, 33:L01702 doi:10.1029/2005GL024546.

Broecker, W. S. (1997). Mountain glaciers: Recorders of atmospheric water vapor content? *Global Biogeochemical Cycles*, 11(4):589–597.

Brook, G. A., Rafter, M. A., Railsback, L. B., Sheen, S. W. & Lundberg, J. (1999). A high-resolution proxy record of rainfall and ENSO since AD 1550 from layering in stalagmites from Anjohibe Cave, Madagascar. In S. E. Lauritzen & J. Lundberg, editors, *Speleothems as high-resolution palaeoclimatic archives*, volume 9 of *The Holocene*, pp. 695–705. Edward Arnold, Sevenoaks, United Kingdom.

Caballero, E., Jimenez De Cisneros, C. & Reyes, E. (1996). A stable isotope study of cave seepage waters. *Applied Geochemistry*, 11(4):583–587.

Chen, J. H., Edwards, R. L. & Wasserburg, G. J. (1986). ^{238}U, ^{234}U and ^{232}Th in seawater. *Earth and Planetary Science Letters*, 80(3-4):241–251.

Chen, J. H. & Wasserburg, G. J. (1981). Precise isotopic analysis of uranium in picomole and subpicomole quantities. *Anal. Chem.*, 53(13):2060–2067.

Cheng, H., Edwards, R. L., Hoff, J., Gallup, C. D., Richards, D. A. & Asmerom, Y. (2000). The half-lives of Uranium-234 and Thorium-230. In D. Weis & J. DePaolo Donald, editors, *Isotope tracers in geochemistry and cosmochemistry.* Elsevier. Amsterdam, Netherlands. 2000.

Cherdyntsev, V. V., Kazachevskii, I. V. & Kuz'mina, Y. A. (1965). Age of carbonate determined from the isotopes of thorium and uranium. *Geochemistry International*, 2:749–756.

Cobb, K. M., Charles, C. D., Cheng, H., Kastner, M. & Edwards, R. L. (2003). U/Th-dating living and young fossil corals from the central tropical Pacific. *Earth and Planetary Science Letters*, 210(1-2):91–103.

Coplen, T., Kendall, C. & Hopple, J. (1983). Comparison of stable isotope reference samples. *Nature*, 302(236-239).

Craig, H. (1961). Isotopic Variations in Meteoric Waters. *Science*, 133(346):1702–1703.

Craig, H. (1965). The measurement of oxygen isotope palaeotemperatures. In E. Tongiorgi, editor, *Stable isotopes in oceanographic studies and palaeotemperatures*, pp. 166–182. Pisa, Consiglio Nazionale delle Ricerche Laboratorio di Geologia Nucleare.

Criss, R. (1999). *Principles of Stable Isotope Distribution.* Oxford University Press, New York, Oxford.

Cruz, F. W., Burns, S. J., Karmann, I., Sharp, W. D., Vuille, M., Cardoso, A. O., Ferrari, J. A., Silva Dias, P. L. & Viana, O. (2005a). Insolation-driven changes in atmospheric circulation over the past 116,000 years in subtropical Brazil. *Nature*, 434(7029):63–66.

Cruz, Jr., F. W., Karmann, I., Viana, Jr., O., Burns, S. J., Ferrari, J. A., Vuille, M., Sial, A. N. & Moreira, M. Z. (2005b). Stable isotope study of cave percolation waters in subtropical Brazil: Implications for paleoclimate inferences from speleothems. *Chemical Geology*, 220(3-4):245–262.

Cruz, J. F. W., Burns, S. J., Karmann, I., Sharp, W. D., Vuille, M. & Ferrari, J. A. (2006). A stalagmite record of changes in atmospheric circulation and soil processes in the Brazilian subtropics during the Late Pleistocene. *Quaternary Science Reviews*, 25(21-22):2749–2761.

Dansgaard, W. G. (1964). Stable isotopes in precipitation. *Tellus*, 16:436–468.

Delanghe, D., Bard, E. & Hamelin, B. (2002). New TIMS constraints on the uranium-238 and uranium-234 in seawaters from the main ocean basins and the Mediterranean Sea. *Marine Chemistry*, 80(1):79–93.

Dennis, P., Rowe, P. J. & Atkinson, T. C. (1998). Stable isotope composition of paleoprecipitation and paleogroundwaters from speleothem fluid inclusions. In IAEA, editor, *Isotope techniques in the study of environmental change*, pp. 1–13. IAEA, Vienna.

Dennis, P. F., Rowe, P. J. & Atkinson, T. C. (2001). The recovery and isotopic measurement of water from fluid inclusions in speleothems. *Geochimica et Cosmochimica Acta*, 65(6):871–884.

Dorale, J. A., Edwards, R. L., Alexander, E. C., Shen, C. C., Richards, D. A. & Cheng, H. (2004). Uranium-series dating of speleothems: current techniques, limits and applications. In I. D. Sasowsky & J. E. Mylroie, editors, *Studies of Cave Sediments. Physical and Chemical Records of Palaeoclimate*, pp. 177–197. Kluwer Academic, New York.

Drysdale, R., Zanchetta, G., Hellstrom, J., Fallick, A. & Zhao, J. (2005). Stalagmite evidence for the onset of the Last Interglacial in southern Europe at 129 ± 1 ka. *Geophysical Research Letters*, 32:L24708 doi:10.1029/2005GL024658.

Dulinski, M. & Rozanski, K. (1990). Formation of $^{13}C/^{12}C$ isotope ratios in speleothems: A semi-dynamic model. *Radiocarbon*, 32(1):7–16.

Duplessy, J. C., Labeyrie, J., Lalou, C. & Nguyen, H. V. (1970). Continental Climatic Variations between 130,000 and 90,000 years BP. *Nature*, 226(5246):631–633.

Edwards, R. L., Chen, J. H., Ku, T. L. & Wasserburg, G. J. (1987a). Precise timing of the last interglacial period from mass spectrometric determination of thorium-230 in corals. *Science*, 236(4808):1547–1553.

Edwards, R. L., Chen, J. H. & Wasserburg, G. J. (1987b). ^{238}U- ^{234}U- ^{230}Th- ^{232}Th systematics and the precise measurement of time over the past 500,000 years. *Earth and Planetary Science Letters*, 81(2-3):175–192.

Edwards, R. L., Gallup, C. D. & Cheng, H. (2003). Uranium-series dating of marine and lacustrine carbonates. In B. Bourdon, G. M. Henderson, C. C. Lundstrom & S. P. Turner, editors, *Uranium-series geochemistry*, volume 52, pp. 363–405.

Ehleringer, J. R. & Cerling, T. E. (2002). C3 and C4 Photosynthesis. In H. A. Mooney & J. G. Canadell, editors, *Encyclopedia of Global Environmental Change; Volume 2, The Earth system: biological and ecological dimensions of global environmental change*, volume 2, pp. 186–190. John Wiley Sons, Chichester.

Eiler, J. M. & Kitchen, N. (2001). Hydrogen-isotope analysis of nanomole (picoliter) quantities of H_2O. *Geochimica et Cosmochimica Acta*, 65(24):4467–4479.

Elderfield, H. & Ganssen, G. (2000). Past temperature and $\delta^{18}O$ of surface ocean waters inferred from foraminiferal Mg/Ca ratios. *Nature*, 405(6785):442–445.

Epstein, S., Buchsbaum, R., Lowenstam, H. A. & Urey, H. C. (1951). Carbonate-water isotopic temperature scale. *Geological Society of America Bulletin*, 62(4):417–425.

Epstein, S., Buchsbaum, R., Lowenstam, H. A. & Urey, H. C. (1953). Revised Carbonate-water isotopic temperature scale. *Geological Society of America Bulletin*, 64(11):1315–1326.

Fairchild, I., Frisia, S., Borsato, A. & Tooth, A. (2006a). Speleothems. In D. Nash & S. McLaren, editors, *Geochemical Sediments and Landscapes*, pp. 200–245. Blackwells, Oxford.

Fairchild, I. J., Borsato, A., Tooth, A. F., Frisia, S., Hawkesworth, C. J., Huang, Y., McDermott, F. & Spiro, B. (2000). Controls on trace element (Sr-Mg) compositions of carbonate cave waters: implications for speleothem climatic records. *Chemical Geology*, 166(3-4):255–269.

Fairchild, I. J., Smith, C. L., Baker, A., Fuller, L., Spötl, C., Mattey, D., McDermott, F. & E.I.M.F. (2006b). Modification and preservation of environmental signals in speleothems. *Earth-Science Reviews ISOtopes in PALaeoenvironmental reconstruction (ISOPAL)*, 75(1-4):105–153.

Fajans, K. (1913). Radioactive Transformations and the Periodic System of The Elements. *Berichte der Deutschen Chemischen Gesellschaft*, 46:422–439.

Faure, G. (1986). *Principles of Isotope Geology.* Wiley, New York, 2de edition.

Fernández Cortés, A., Calaforra, J. M., Sánchez Martos, F. & Gisbert, J. (2007). Stalactite drip rate variations controlled by air pressure changes: an example of non-linear infiltration processes in the 'Cueva del Agua' (Spain). *Hydrological Processes*, 21:920–930.

Finkel, R. C. & Nishiizumi, K. (1997). Beryllium 10 concentrations in the Greenland Ice Sheet Project 2 ice core from 3 to 40 ka. *Journal of Geophysical Research*, 102:26,699–26,706.

Fleitmann, D., Burns, S. J., Mudelsee, M., Neff, U., Kramers, J., Mangini, A. & Matter, A. (2003a). Holocene Forcing of the Indian Monsoon Recorded in a Stalagmite from Southern Oman. *Science*, 300(5626):1737–1739.

Fleitmann, D., Burns, S. J., Neff, U., Mangini, A. & Matter, A. (2003b). Changing moisture sources over the last 330,000 years in Northern Oman from fluid-inclusion evidence in speleothems. *Quaternary Research*, 60(2):223–232.

Frappier, A., Sahagian, D., Gonzalez, L. A. & Carpenter, S. J. (2002). El Nino events recorded by stalagmite carbon isotopes. *Science*, 298(5593):565.

Friedman, I., Machta, L. & Soller, R. (1962). Water-Vapor Exchange between a Water Droplet and Its Environment. *Journal of Geophysical Research*, 67(7):2761–2766.

Frisia, S., Borsato, A., Fairchild, I. & McDermott, F. (2000). Calcite fabrics, growth mechanisms, and environments of formation in speleothems from the Italian alps and southwestern Ireland. *Journal of Sedimentary Research, Section A: Sedimentary Petrology and Processes*, 70(5):1183–1196.

Gammage, R. B. & Gregg, S. J. (1972). The sorption of water vapour by ball-milled calcite. *Journal of Colloid and Interface Science*, 38:118–124.

Garreaud, R., Vuille, M. & Clement, A. C. (2003). The climate of the Altiplano; observed current conditions and mechanisms of past changes. In G. O. Seltzer, D. T. Rodbell & H. E. Wright, editors, *Late-Quaternary palaeoclimates of the southern tropical Andes and adjacent regions.* Elsevier. Amsterdam, Netherlands.

Gascoyne, M. (1983). Trace-element partition coefficients in the calcite-water system and their paleoclimatic significance in cave studies. *Journal of Hydrology*, 61(1-3):213–222.

Gat, J. R. (1996). Oxygen and Hydrogen Isotopes in the Hydrological Cycle. *Annual Review of Earth and Planetary Sciences*, 24(1):225–262.

Gat, J. R. (2000). Atmospheric water balance - the isotopic perspective. *Hydrological Processes*, 14(8):1357–1369.

Gat, J. R. & Matsui, E. (1991). Atmospheric water balance in the amazon basin: an isotopic evapotranspiration model. *Journal of Geophysical Research*, 96(D7):13179–13188.

Gehre, M., Geilmann, H., Richter, J., Werner, R. A. & Brand, W. A. (2004). Continuous flow ^{2}H/^{1}H and ^{18}O/^{16}O analysis of water samples with dual inlet precision. *Rapid communications in mass spectrometry*, 18:2650–2660.

Genty, D., Baker, A., Massault, M., Proctor, C., Gilmour, M., Pons, B. E. & Hamelin, B. (2001a). Dead carbon in stalagmites; carbonate bedrock paleodissolution vs. ageing of soil organic matter; implications for ^{13}C variations in speleothems. *Geochimica et Cosmochimica Acta*, 65(20):3443–3457.

Genty, D., Baker, A. & Vokal, B. (2001b). Intra- and inter-annual growth rate of modern stalagmites. *Chemical Geology*, 176(1-4):191–212.

Genty, D., Blamart, D., Ghaleb, B., Plagnes, V., Causse, C., Bakalowicz, M., Zouari, K., Chkir, N., Hellstrom, J., Wainer, K. & Bourges, F. (2006). Timing and dynamics of the last deglaciation from European and North African δ^{13}C stalagmite profiles - comparison with Chinese and South Hemisphere stalagmites. *Quaternary Science Reviews*, 25(17-18):2118–2142.

Genty, D., Blamart, D., Ouahdi, R., Gilmour, M., Baker, A., Jouzal, J. & Van Exter, S. (2003). Precise dating of Dansgaard-Oeschger climate oscillations in western Europe from stalagmite data. *Nature*, 421:833–837.

Genty, D. & Deflandre, G. (1998). Drip flow variations under a stalactite of the Pere Noel cave (Belgium). Evidence of seasonal variations and air pressure constraints. *Journal of Hydrology*, 211(1-4):208–232.

Genty, D. & Massault, M. (1999). Carbon transfer dynamics from bomb-^{14}C and δ^{13}C time series of a laminated stalagmite from SW France - modelling and comparison with other stalagmite records. *Geochimica et Cosmochimica Acta*, 63(10):1537–1548.

Genty, D., Plagnes, V., Causse, C., Cattani, O., Stievenard, M., Falourd, S., Blamart, D., Ouahdi, R. & Van, E. S. (2002). Fossil water in large stalagmite voids as a tool for paleoprecipitation stable isotope composition reconstitution and paleotemperature calculation. *Chemical Geology*, 184(1-2):83–95.

Genty, D. & Quinif, Y. (1996). Annually laminated sequences in the internal structure of some Belgian stalagmites; importance for paleoclimatology. *Journal of Sedimentary Research*, 66(1):275–288.

Ghosh, P., Garzione, C. N. & Eiler, J. M. (2006). Rapid uplift of the Altiplano revealed through ^{13}C-^{18}O bonds in paleosol carbonates. *Science*, 311(5760):511–515.

Gleissberg, W. (1958). The eighty-year sunspot cycle. *Journal British Astronomical Association*, 68(148-152).

Goede, A., Green, D. & Harmon, R. S. (1986). Late Pleistocene paleotemperature record from a Tasmanian speleothem. *Australian Journal of Earth Sciences*, 33:333–342.

Goede, A., Veeh, H. H. & Ayliffe, L. K. (1990). Late Quaternary palaeotemperature records for two Tasmanian speleothems. *Australian Journal of Earth Sciences*, 37:267–278.

Goede, A. & Vogel, J. C. (1991). Trace element variations and dating of a Late Pleistocene Tasmanian speleothem. *Palaeogeography, Palaeoclimatology, Palaeoecology*, 88(1-2):121–131.

Goldstein, S. J. & Stirling, C. H. (2003). Techniques for Measuring Uranium-series Nuclides: 1992-2002. In B. Bourdon, G. M. Henderson, C. C. Lundstrom & S. P. Turner, editors, *Uranium-series geochemistry.* Mineralogical Society of America and Geochemical Society. Washington, DC, United States. 2003.

Gonfiantini, R., Roche, M.-A., Olivry, J.-C., Fontes, J.-C. & Zuppi, G. M. (2001). The altitude effect on the isotopic composition of tropical rains. *Chemical Geology*, 181(1-4):147–167.

Grootes, P. M. & Stuiver, M. (1997). Oxygen 18/16 variability in Greenland snow and ice with 10^3-10^5 year time resolution. *Journal of Geophysical Research*, 102(C12):26,455–26,470.

Grootes, P. M., Stuiver, M., Thompson, L. G. & Mosley Thompson, E. (1989). Oxygen isotope changes in tropical ice, Quelccaya, Peru. *Journal of Geophysical Research, D, Atmospheres*, 94(1):1187–1194.

Grossman, E. L. & Ku, T. L. (1986). Oxygen and carbon isotope fractionation in biogenic aragonite: Temperature effects. *Chemical Geology*, 59(Isotope Geoscience Section):59–74.

Hagemann, R. & Lohez, P. (1978). Deuterium/hydrogen isotope analysis ratio. *Advances in Mass Spectrometry*, 74:85–88.

Harmon, R. S. (1979). An isotopic study of groundwater seepage in the central Kentucky karst. *Water Resources Research*, 15(2):476–480.

Harmon, R. S., Schwarcz, H. P. & Ford, D. C. (1978). Stable isotope geochemistry of speleothems and cave waters from the Flint Ridge-Mammoth Cave system, Kentucky: Implications for terrestrial climate change during the period 230,000 to 100,000 years B.P. *Journal of Geology*, 86:373–384.

Harmon, R. S., Schwarcz, H. P., Gascoyne, M., Hess, M. & Ford, D. C. (2004). Paleoclimate information from speleothems: the present as a guide to the past. In I. D. Sasowsky & J. E. Mylroie, editors, *Studies of Cave Sediments. Physical and Chemical Records of Palaeoclimate.*, pp. 199–226. Kluwer Academic, New York.

Harmon, R. S., Schwarcz, H. P. & O'Neil, J. R. (1979). D/H ratios in speleothem fluid inclusions: A guide to variations in the isotopic composition of meteoric precipitation? *Earth and Planetary Science Letters*, 42(2):254–266.

Haug, G. H., Haughen, K. A., Sigman, D. M., Peterson, L. C. & Roehl, U. (2001). Southward migration of the Intertropical Convergence Zone through the Holocene. *Science*, 293(5533):1304–1308.

Hellstrom, J. (2003). Rapid and accurate U/Th dating using parallel ion-counting multicollector ICP-MS. *Journal of Analytical Atomic Spectrometry*, 18:1346â1351.

Hellstrom, J. (2006). U-Th dating of speleothems with high initial 230Th using stratigraphical constraint. *Quaternary Geochronology*, 1(4):289–295.

Hellstrom, J. C. & McCulloch, M. T. (2000). Multi-proxy constraints on the climatic significance of trace element records from a New Zealand speleothem. *Earth and Planetary Science Letters*, 179(2):287–297.

Henderson, G. M. (2002). Seawater (^{234}U/^{238}U) during the last 800 thousand years. *Earth and Planetary Science Letters*, 199(1-2):97–110.

Henderson, K. A., Thompson, L. G. & Lin, P. N. (1999). Recording of El Niño in ice core δ^{18}O records from Nevado Huascarán, Peru. *Journal of Geophysical Research*, D104:31053–31065.

Hendy, C. H. (1971). The isotopic geochemistry of speleothems; 1, The calculation of the effects of different modes of formation on the isotopic composition of speleothems and their applicability as paleoclimatic indicators. *Geochimica et Cosmochimica Acta*, 35(8):801–824.

Hendy, C. H. & Wilson, A. T. (1968). Palaeoclimatic data from speleothems. *Nature (London)*, 219(5149):48–51.

Hill, C. & Forti, P. (1997). *Cave Minerals of the World (second edition)*. National Speleological Society, Inc., second edition.

Holden, N. E. (1990). Total Half-lives for Selected Nuclides. *Pure and Applied Chemistry*, 62(5):941–958.

Holmgren, K., Karlen, W., Lauritzen, S. E., Lee, T. J. A., Partridge, T. C., Piketh, S., Repinski, P., Stevenson, C., Svanered, O. & Tyson, P. D. (1999). A 3000-year high-resolution stalagmite-based record of palaeoclimate for northeastern South Africa. *The Holocene*, 9(3):295–309.

Hooghiemstra, H. & van der Hammen, T. (1998). Neogene and Quaternary development of the neotropical rain forest: the forest refugia hypothesis, and a literature overview. *Earth-Science Reviews*, 44(3-4):147–183.

Huang, Y. & Fairchild, I. J. (2001). Partitioning of Sr^{2+} and Mg^{2+} into calcite under karst-analogue experimental conditions. *Geochimica et Cosmochimica Acta*, 65(1):47–62.

Imhof, A. (1997). Decomposition of limestone in a solar reactor. *Renewable energy*, 10(2-3):239–246.

Jaffey, A. H., Flynn, K. F., Glendenin, L. E., Bentley, W. C. & Essling, A. M. (1971). Precision measurement of Half-Lives and specific activities of ^{235}U and ^{238}U. *Physical Review C*, 4:1889–1906.

Johnson, K. R., Hu, C., Belshaw, N. S. & Henderson, G. M. (2006). Seasonal trace-element and stable-isotope variations in a Chinese speleothem: The potential for high-resolution paleomonsoon reconstruction. *Earth and Planetary Science Letters*, 244(1-2):394–407.

Keeling, C., Bacastow, R., Bainbridge, A., Ekdahl, C., Guenther, P., Waterman, L. & Chin, J. (1976). Atmospheric carbon dioxide variations at Mauna Loa Observatory, Hawaii. *Tellus*, 28(6):538–551.

Keeling, C., Chin, J. & Whorf, T. (1996). Increased activity of northern vegetation inferred from atmospheric CO_2 measurements. *Nature*, 382(6587):146–149.

Kendall, A. C. & Broughton, P. L. (1978). Origin of Fabrics in Speleothems Composed of Columnar Calcite Crystals. *Journal of Sedimentary Petrology*, 48(2):519–538.

Kim, S. T. & O'Neil, J. R. (1997). Equilibrium and nonequilibrium oxygen isotope effects in synthetic carbonates. *Geochimica et Cosmochimica Acta*, 61(16):3461–3475.

Lachniet, M. S., Burns, S., Piperno, D., Asmerom, Y., Polyak, V., Moy, C. M. & Christenson, K. (2004). A 1500-year El Niño/Southern Oscillation and rainfall history for the Isthmus of Panama from speleothem calcite. *Journal of Geophysical Research*, 109:D20117.

Lally, A. E. (1992). Chemical procedures. In M. Ivanovich & R. Harmon, editors, *Uranium Series Disequilibrium: Applications to Earth, Marine and Environmental Sciences*, p. Chapter 4. Clarendon Press, Oxford.

Laskar, J., Robutel, P., Joutel, F., Gastineau, M., Correia, A. C. M. & Levrard, B. (2004). A long-term numerical solution for the insolation quantities of the Earth. *Astronomy Astrophysics*, 428:261–285.

Leng, M. J. & Marshall, J. D. (2004). Palaeoclimate interpretation of stable isotope data from lake sediment archives. *Quaternary Science Reviews*, 23(7-8):811–831.

Lide, D. R. (2005). *Handbook of Chemistry and Physics*, volume 86th edition. CRC.

Linge, H., Lauritzen, S. E. & Lundberg, J. (2001). Stable Isotope Stratigraphy of a Late Last Interglacial Speleothem from Rana, Northern Norway. *Quaternary Research*, 56:155–164.

Lohmann, G., Rimbu, N. & Dima, M. (2004). Climate signature of solar irradiance variations: analysis of long-term instrumental, historical, and proxy data. *International Journal of Climatology*, 24(8):1045–1056.

Ludwig, K. R. (2003). Mathematical-statistical treatment of data and errors for ^{230}Th/U geochronology. In B. Bourdon, G. M. Henderson, C. C. Lundstrom & S. P. Turner, editors, *Uranium-series geochemistry.* Mineralogical Society of America and Geochemical Society. Washington, DC, United States. 2003.

Majoube, M. (1971). Fractionnement en oxygene 18 et en deuterium entre l'eau et sa vapeur. *Journal de Chimie Physique*, 68:1423–1436.

Marengo, J. A. & Nobre, C. A. (2001). General Characteristics and Variability of Climate in the Amazon Basin and its Links to the Global Climate System. In M. E. McClain, R. L. Victoria & J. E. Richey, editors, *The Biogeochemistry of the Amazon Basin*, pp. 17–41. Oxford University Press.

Maslin, M. & Burns, S. (2000). Reconstruction of the Amazon Basin Effective Moisture Availability over the Past 14,000 years. *Science*, 290:2285–2287.

Matthews, A., Ayalon, A. & Bar Matthews, M. (2000). D/H ratios of fluid inclusions of Soreq Cave (Israel) speleothems as a guide to the Eastern Mediterranean meteoric line relationships in the last 120 ky. *Chemical Geology*, 166(3-4):183–191.

McDermott, F. (2004). Palaeo-climate reconstruction from stable isotope variations in speleothems: a review. *Quaternary Science Reviews*, 23(7-8):901–918.

McDermott, F., Schwarcz, H. P. & Rowe, P. J. (2006). Isotopes in Speleothems. In M. J. Leng, editor, *Isotopes in Palaeoenvironmental Research*, volume 10 of *Developments in Paleoenvironmental Research*, pp. 185–225. Springer, Dordrecht, the Netherlands.

McDonald, J. & Drysdale, R. (2007). Hydrology of cave drip waters at varying bedrock depths from a karst system in southeastern Australia. *Hydrological Processes*, 21(13):1737–1748.

McGarry, S., Bar Matthews, M., Matthews, A., Vaks, A., Schilman, B. & Ayalon, A. (2004). Constraints on hydrological and paleotemperature variations in the Eastern Mediterranean region in the last 140 ka given by the δD values of speleothem fluid inclusions. *Quaternary Science Reviews*, 23(7-8):919–934.

McKinney, C., McCrea, J. M., Epstein, S., Allen, H. A. & Urey, H. C. (1950). Improvements in mass spectrometers for the measurement of small differences in isotope abundance ratios. *Review of Scientific Instruments*, 21(724-730).

Melice, J. L. & Roucou, P. (1998). Decadal time scale variability recorded in the Quelccaya summit ice core δ^{18}O isotopic ratio series and its relation with the sea surface temperature. *Climate Dynamics*, 14(2):117–132.

Mickler, P. J., Banner, J. L., Stern, L., Asmerom, Y., Edwards, R. L. & Ito, E. (2004). Stable isotope variations in modern tropical speleothems: Evaluating equilibrium vs. kinetic isotope effects. *Geochimica et Cosmochimica Acta*, 68(21):4381–4393.

Mickler, P. J., Stern, L. A. & Banner, J. L. (2006). Large kinetic isotope effects in modern speleothems. *Geological Society of America Bulletin*, 118(1-2):65–81.

Miotke, F. D. (1974). Carbon dioxide and the soil atmosphere. *Abhandlungen zur Karst- und Höhlenkunde*, R. A 9:1–49.

Mook, W. G. (1994). Introduction - Theory, Methods, Review. In W. G. Mook, editor, *Environmental Isotopes in the Hydrological Cycle Principles and Applications*, volume I. IAEA, Veinna.

Moran, T. A., Marshall, S. J., Evans, E. C. & Sinclair, K. E. (2007). Altitudinal Gradients of Stable Isotopes in Lee-Slope Precipitation in the Canadian Rocky Mountains. *Arctic, Antarctic and Alpine Research*, 39(3):455–467.

Moreira, M., Sternberg, L., Martinelli, L., Victoria, R., Barbosa, E., Bonates, L. & Nepstad, D. (1997). Contribution of transpiration to forest ambient vapour based on isotopic measurements. *Global Change Biology*, 3(5):439–450.

Mühlinghaus, C., Scholz, D. & Mangini, A. (2007). Modelling stalagmite growth and $\delta^{13}C$ as a function of drip interval and temperature. *Geochimica et Cosmochimica Acta*, 71(11):2780–2790.

Neff, U. (2001). *Massenspektrometische Th/U-Datierung von Höhlensintern aus dem Oman: Klimaarchive des asiatischen Monsuns*. PhD, Heidelberg Academy of Sciences.

Nyberg, J., Kuijpers, A., Malmgren, B. A. & Kunzendorf, H. (2001). Late Holocene Changes in Precipitation and Hydrography Recorded in Marine Sediments from the Northeastern Caribbean Sea. *Quaternary Research*, 56(1):87–102.

Paulsen, D. E., Li, H.-C. & Ku, T.-L. (2003). Climate variability in central China over the last 1270 years revealed by high-resolution stalagmite records. *Quaternary Science Reviews*, 22(5-7):691–701.

Pierrehumbert, R. T. (1999). Huascarán $\delta^{18}O$ as an indicator of tropical climate during the Last Glacial Maximum. *Geophysical Research Letters*, 26(9):1345–1348.

Plagnes, V., Causse, C., Genty, D., Paterne, M. & Blamart, D. (2002). A discontinuous climatic record from 187 to 74 ka from a speleothem of the Clamouse Cave (South of France). *Earth and Planetary Science Letters*, 201(1):87–103.

Preece, R. C., Parfitt, S. A., Bridgland, D. R., Lewis, S. G., Rowe, P. J., Atkinson, T. C., Candy, I., Debenham, N. C., Penkman, K. E. H., Rhodes, E. J., Schwenninger, J. L., Griffiths, H. I., Whittaker, J. E. & Gleed Owen, C. (2007). Terrestrial environments during MIS 11: evidence from the Palaeolithic site at West Stow, Suffolk, UK. *Quaternary Science Reviews*, 26(9-10):1236–1300.

Quinif, Y. & Basin, B. (1986). Le système karstique de Han-sur-Lesse (Belgique). In *Proceedings 9th congresso International Espeleologica*, volume 1, pp. 147–161. Barcelona.

Ramirez, E., Hoffmann, G., Taupin, J. D., Francou, B., Ribstein, P., Caillon, N., Ferron, F. A., Landais, A., Petit, J. R., Pouyaud, B., Schotterer, U., Simoes, J. C. & Stievenard, M. (2003). A new Andean deep ice core from Nevado Illimani (6350 m), Bolivia. *Earth and Planetary Science Letters*, 212(3-4):337–350.

Richards, D. A. & Dorale, J. A. (2003). Uranium-series chronology and environmental applications of speleothems. In B. Bourdon, G. M. Henderson, C. C. Lundstrom & S. P. Turner, editors, *Uranium-series geochemistry*, volume 52, pp. 407–460. Mineralogical Society of America and Geochemical Society, Washington, DC, United States.

Roberts, M. S., Smart, P. L. & Baker, A. (1998). Annual trace element variations in a Holocene speleothem. *Earth and Planetary Science Letters*, 154(1-4):237–246.

Rosholt, J. N. & Antal, P. S. (1962). Evaluation of the Pa231/U - Th230/U method for dating Pleistocene carbonate rocks. *US Geol Surv Pro Paper 450-E*, pp. 108–111.

Roth, S. & Reijmer, J. J. G. (2005). Holocene millennial to centennial carbonate cyclicity recorded in slope sediments of the Great Bahama Bank and its climatic implications. *Sedimentology*, 52(1):161–181.

Rowley, D. B. & Garzione, C. N. (2007). Stable Isotope-Based Paleoaltimetry. *Annual Review of Earth and Planetary Sciences*, 35(1):463–508.

Rozanksi, K. & Araguás Araguás, L. (1995). Spatial and Temporal variability of stable isotope composition of precipitation over the South American Continent. *Bulletin de l'Institut Francais d'Études Andines*, 24(3):379–390.

Rozanksi, K., Araguás Araguás, L. & Gonfiantini, R. (1993). Isotopic Patterns in Modern Global Precipitation. In P. K. Swart, K. C. Lohmann, J. McKenzie & S. Savin, editors, *Climate Change in Continental Isotopic Records*, volume 78 of *Geophysical Monograph 78*, pp. 1–36. 78 edition.

Rozanksi, K. & Dulinski, M. (1987). Deuterium content of European palaeowaters as inferred from isotopic composition of fluid inclusions trapped in carbonate deposits. In IAEA, editor, *Isotope Techniques in Water Resources Development*, pp. 565–578. IAEA, Vienna.

Rutherford, E. (1900). A radioactive substance emitted from thorium compounds. *Philosophical Magazine*, 49:1–14.

Rutherford, E. & Soddy, F. (1902). The Cause and Nature of Radioactivity. *Philosophical Magazine*, 4:370–396.

Scholz, D. (2005). *U-series dating of diagenetically altered fossil reef corals and the application for sea level reconstructions.* PhD, Heidelberg Academy of Sciences.

Schwarcz, H. P. (1986). Geochronology and isotopic geochemistry of speleothems. In Fritz & Peter Fontes, editors, *The terrestrial environment, B.*, pp. 271–303. Elsevier, Amsterdam, Netherlands.

Schwarcz, H. P., Harmon, R. S., Thompson, P. & Ford, D. C. (1976). Stable isotope studies of fluid inclusions in speleothems and their paleoclimatic significance. *Geochimica et Cosmochimica Acta*, 40(6):657–665.

Schwarcz, H. P. & Yonge, C. J. (1983). In Paleoclimates and Paleowaters: A Collection of Environmental Isotope Studies. In *IAEA*, p. 115. Vienna.

Seltzer, G., Rodbell, D. & Burns, S. (2000). Isotopic evidence for late Quaternary climatic change in tropical South America. *Geology*, 28(1):35–38.

Seltzer, G. O., Rodbell, D. T., Baker, P. A., Fritz, S. C., Tapia, P. M., Rowe, H. D. & Dunbar, R. B. (2002). Early warming of tropical South America at the last glacial-interglacial transition. *Science*, 296(5573):1685–1686.

Serefiddin, F., Schwarcz, H. P., Ford, D. C. & Baldwin, S. (2004). Late Pleistocene paleoclimate in the Black Hills of South Dakota from isotope records in speleothems. *Palaeogeography, Palaeoclimatology, Palaeoecology*, 203(1-2):1–17.

Shackleton, N. J. & Opdyke, N. D. (1973). Oxygen isotope and palaeomagnetic stratigraphy of Equatorial Pacific core V28-238: Oxygen isotope temperatures and ice volumes on a 10^5 year and 10^6 year scale. *Quaternary Research*, 3(1):39–55.

Sharp, Z. D., Atudorei, V. & Durakiewicz, T. (2001). A rapid method for determination of hydrogen and oxygen isotope ratios from water and hydrous minerals. *Chemical Geology*, 178(1-4):197–210.

Shi, H., Zhao, Y. & Li, W. (2002). Effects of temperature on the hydration characteristics of free lime. *Cement and Concrete Research*, 32(5):789–793.

Siegenthaler, U. & Oeschger, H. (1980). Correlation of ^{18}O in precipitation with temperature and altitude. *Nature*, 285(5763):314–317.

Siklosy, Z., Demeny, A., Vennemann, T. W., Kramers, J., Lauritzen, S. E. & Leel Ossy, S. (2007). Middle bronze age climate change recorded in a Hungarian stalagmite: triggering by volcanic activity? *Geophysical Research Abstracts*, 9:1607–7962/gra/EGU2007–A–00777.

Simon, K. (2001). Does the δD from fluid inclusion in quartz reflect the original hydrothermal fluid? *Chemical Geology*, 177(3-4):483–495.

Soddy, F. (1913). The Radio-elements and the Periodic Law. *Chemical News*, 107:97–99.

Sondag, F., van Ruymbeke, M., Soubies, F., Santos, R., Somerhausen, A., Seidel, A. & Boggiani, P. (2003). Monitoring present day climatic conditions in tropical caves using an Environmental Data Acquisition System (EDAS). *Journal of Hydrology*, 273(1-4):103–118.

Spötl, C. & Mangini, A. (2002). Stalagmite from the Austrian Alps reveals Dansgaard-Oeschger events during isotope stage 3: Implications for the absolute chronology of Greenland ice cores. *Earth and Planetary Science Letters*, 203(1):507–518.

Spötl, C., Mangini, A., Frank, N., Eichstädter, R. & Burns, S. J. (2002). Start of the last interglacial period at 135 ka: evidence from a high Alpine speleothem. *Geology (Boulder)*, 30(9):815–818.

Stirling, C. H., Esat, T. M., Lambeck, K. & McCulloch, M. T. (1998). Timing and duration of the Last Interglacial: evidence for a restricted interval of widespread coral reef growth. *Earth and Planetary Science Letters*, 160(3-4):745–762.

Stirling, C. H., Lee, D. C., Christensen, J. N. & Halliday, A. N. (2000). High-precision in situ ^{238}U-^{234}U-^{230}Th isotopic analysis using laser ablation multiple-collector ICPMS. *Geochimica et Cosmochimica Acta*, 64(21):3737–3750.

Stuiver, M. & Braziunas, T. F. (1993). Sun, ocean, climate and atmospheric $^{14}CO_2$: an evaluation of causal and spectral relationships. *Holocene*, 3(289-305).

Tardy, Y., Bustillo, V., Roquin, C., Mortatti, J. & Victoria, R. (2005). The Amazon. Biogeochemistry applied to river basin management: Part I. Hydro-climatology, hydrograph separation, mass transfer balances, stable isotopes, and modelling. *Applied Geochemistry*, 20(9):1746–1829.

Thompson, L. G., Davis, M. E., Mosley, T. E., Sowers, T. A., Henderson, K. A., Zagorodnov, V. S., Lin, P. N., Mikhalenko, V. N., Campen, R. K., Bolzan, J. F., Cole, D. J. & Francou, B. (1998). A 25,000-year tropical climate history from Bolivian ice cores. *Science*, 282(5395):1858–1864.

Thompson, L. G., Mosley Thompson, E., Brecher, H., Davis, M. E., León, B., Les, D., Lin, P. N., Mashiotta, T. & Mountain, K. (2006). Abrupt tropical climate change: Past and present. *PNAS*, 103(28):10536–10543.

Thompson, L. G., Mosley Thompson, E., Dansgaard, W. & Grootes, P. M. (1986). The Little Ice Age as recorded in the stratigraphy of the tropical Quelccaya ice cap. *Science*, 234(4774):361–364.

Thompson, L. G., Mosley Thompson, E., Davis, M. E., Lin, P. N., Henderson, K. A., Cole, D. J., Bolzan, J. F. & Liu, K. B. (1995). Late Glacial Stage and Holocene tropical ice core records from Huscarán, Peru. *Science*, 269(5520):46–50.

Thompson, L. G., Mosley Thompson, E. & Henderson, K. A. (2000). Ice-core palaeoclimate records in tropical South America since the Last Glacial Maximum. *Journal of Quaternary Science*, 15(4):377–394.

Thompson, P. (1973). *Speleochronology and late pleistocene climates inferred from O, C, H, U and Th abundances in spelethems.* PhD, Mc Master University.

Thompson, P., Schwarcz, H. P. & Ford, D. C. (1974). Continental Pleistocene climatic variations from speleothem age and isotopic data. *Science*, 184:893–894.

Thompson, P., Schwarcz, H. P. & Ford, D. C. (1976). Stable isotope geochemistry, geothermometry, and geochronology of speleothems from West Virginia. *Geological Society of America Bulletin*, 87(12):1730–1738.

Treble, P., Shelley, J. M. G. & Chappell, J. (2003). Comparison of high resolution subannual records of trace elements in a modern (1911-1992) speleothem with instrumental climate data from southwest Australia. *Earth and Planetary Science Letters*, 216(1-2):141–153.

Urey, H. C. (1947). The thermodynamic properties of isotopic substances. *Journal of Chemical Society*, pp. 562–581.

Vacco, D. A., Clark, P. U., Mix, A. C., Cheng, H. & Edwards, R. L. (2005). A speleothem record of Younger Dryas cooling, Klamath Mountains, Oregon, USA. *Quaternary Research*, 64(2):249–256.

van Beynen, P. & Febbroriello, P. (2006). Seasonal isotopic variability of precipitation and cave drip water at Indian Oven Cave, New York. *Hydrological Processes*, 20(8):1793–1803.

van Calsteren, P. & Thomas, L. (2006). Uranium-series dating applications in natural environmental science. *Earth-Science Reviews ISOtopes in PALaeoenvironmental reconstruction (ISOPAL)*, 75(1-4):155–175.

Vaughn, B. H., White, J. W. C., Delmotte, M., Trolier, M., Cattani, O. & Stievenard, M. (1998). An automated system for hydrogen isotope analysis of water. *Chemical Geology*, 152(3):309–319.

Verheyden, S. (2001). *Speleothem as palaeoclimatic archives. Isotopic and geochemical study of the cave environment and its Late Quaternary records.* PhD, Vrije Universiteit Brussel.

Verheyden, S. (2005). Trace elements in speleothems: a short review of the state of the art. *Speleogenesis and Evolution of Karst Aquifers*, 3(1):1–5.

Verheyden, S., Baele, J. M., Keppens, E., Genty, D., Cattani, O., Cheng, H., Edwards, R. L., Zhang, H., Van Strijdonck, M. & Quinif, Y. (2006). The Proserpine stalagmite

(Han-sur-Lesse Cave, Belgium): Preliminary environmental interpretation of the last 1000 years as recorded in a layered speleothem. *Geologica Belgica*, 9(3-4):245–256.

Verheyden, S., Genty, D., Cattani, O. & van Breukelen, M. (2005). Characterization of fluid inclusions in speleothems: heating experiments and isotopic hydrogen composition of the inclusion water. *Geophysical Research Abstracts*, 7:02772.

Verheyden, S., Genty, D., Cattani, O. & van Breukelen, M. R. (2008). Water release patterns of heated speleothem calcite and hydrogen isotope composition of fluid inclusions. *Chemical Geology*, 247(1-2):266–281.

Verheyden, S., Keppens, E., Fairchild, I. J., McDermott, F. & Weis, D. (2000). Mg, Sr and Sr isotope geochemistry of a Belgian Holocene speleothem: implications for paleoclimate reconstructions. *Chemical Geology*, 169(1-2):131–144.

Vimeux, F., Gallaire, R., Bony, S., Hoffmann, G. & Chiang, J. C. (2005). What are the climate controls on δD in precipitation in the Zongo Valley (Bolivia)? Implications for the Illimani ice core interpretation. *Earth and Planetary Science Letters*, 240(2):205–220.

Vizy, E. K. & Cook, K. H. (2007). Relationship between Amazon and high Andes rainfall. *Journal of Geophysical Research*, 112(D07107):doi:10.1029/2006JD007980.

Vonhof, H., Atkinson, T. C., van Breukelen, M. & Postma, O. (2007). Fluid inclusion hydrogen and oxygen isotope analyses using the ‘Amsterdam Device’: a progress report. *Geophysical Research Abstracts*, 9(SRef-ID: 1607-7962/gra/EGU2007-A-05702):05702.

Vonhof, H. B., van Breukelen, M. R., Postma, O., Rowe, P. J., Atkinson, T. C. & Kroon, D. (2006). A continuous-flow crushing device for on-line δ^2H analysis of fluid inclusion water in speleothems. *Rapid Communications in Mass Spectrometry*, 20(17):2553–2558.

Vuille, M., Bradley, R. S., Werner, M., Healy, R. & Keimig, F. (2003). Modeling δ^{18}O in precipitation over the tropical Americas; 1, Interannual variability and climatic controls. *Journal of Geophysical Research*, 108(D6):4174.

Wang, Y., Cheng, H., Edwards, R. L., He, Y., Kong, X., An, Z., Wu, J., Kelly, M. J., Dykoski, C. A. & Li, X. (2005). The Holocene Asian Monsoon: Links to Solar Changes and North Atlantic Climate. *Science*, 308(5723):854–857.

Wang, Y. J., Cheng, H., Edwards, R. L., An, Z. S., Wu, J. Y., Shen, C. C. & Dorale, J. A. (2001). A high-resolution absolute-dated late Pleistocene monsoon record from Hulu Cave, China. *Science*, 294(5550):2345–2348.

Wedepohl, K. H. (1995). The composition of the continental crust. *Geochimica et Cosmochimica Acta*, 59(7):1217–1232.

White, W. (1988). *Geomorphology and Hydrology of Karst Terrains*. Oxford University Press, New York.

Wigley, T. M. L. & Brown, M. C. (1976). The physics of caves. In T. D. Ford & C. H. D. Cullingford, editors, *The science of speleology.*, pp. 329–358. Academic Press, Inc., London, England, United Kingdom.

Yonge, C. J. (1982). *Stable isotope studies of water extracted from speleothems*. PhD, Mc

Master University.

Yonge, C. J., Ford, D. C., Gray, J. & Schwarcz, H. P. (1985). Stable isotope studies of cave seepage water. *Chemical Geology; Isotope Geoscience Section*, 58(1-2):97–105.

Yuan, D., Cheng, H., Edwards, R. L., Dykoski, C. A., Kelly, M. J., Zhang, M., Qing, J., Lin, Y., Wang, Y., Wu, J., Dorale, J. A., An, Z. & Cai, Y. (2004). Timing, Duration, and Transitions of the Last Interglacial Asian Monsoon. *Science*, 304(5670):575–578.

Zhang, R., Schwarcz, H. P., Ford, D. C., Schroeder, F. S. & Beddows, P. A. (2008). An absolute paleotemperature record from 10 to 6 Ka inferred from fluid inclusion D/H ratios of a stalagmite from Vancouver Island, British Columbia, Canada. *Geochimica et Cosmochimica Acta*, 72(4):1014–1026.

Zhou, J. & Lau, K.-M. (2001). Principal modes of interannual and decadal variability of summer rainfall over South America. *International Journal of Climatology*, 21(13):1623–1644.

Zsako, J. & Hints, M. (1998). Use of thermal analysis in the study of sodium carbonate causticization by means of dolomitic lime. *Journal of Thermal Analysis*, 53(1):323–331.

Data tables

Data table I: stalagmite CLL-1

depth (mm)	age (yr, BP)	age (hiatus)	$\delta^{13}C$	$\delta^{18}O$	Ba (ppm)	Mg (ppm)	Sr (ppm)
0	0	0	-10.79	-8.18	321	6530	40
1	12	12			459	7547	56
2	24	24	-11.14	-7.98	451	6985	67
3	37	37	-11.22	-7.79	348	6149	45
4	49	49	-11.24	-7.97	464	6812	46
5	61	61	-11.69	-7.95	282	5930	40
6	73	73	-11.56	-8.01	325	6555	42
7	85	85	-11.01	-7.61	454	8043	50
8	98	98	-10.92	-7.72	457	7992	48
9	110	110	-10.65	-7.71	462	7277	56
10	122	122	-10.31	-7.59	436	7487	51
11	134	134	-10.34	-7.20	440	7491	54
12	146	146	-10.36	-7.75	504	8636	51
13	159	159	-10.90	-7.75	449	6534	51
14	171	171	-10.84	-8.02	367	6843	45
15	183	183	-10.18	-7.52	380	7043	58
16	195	195	-11.74	-8.21	242	6071	32
17	207	207	-11.06	-7.89	453	7787	55
18	220	220	-11.22	-8.40	428	7457	49
19	232	232	-11.00	-8.09	472	7910	55
20	244	244			442	7028	54
21	262	253	-10.74	-7.88	460	7512	55
22	280	262	-11.33	-8.02	369	6596	45
23	298	271	-11.38	-7.94	182	4840	23
24	316	280	-11.06	-8.00	383	7120	48
25	334	289	-11.14	-7.97	243	5247	30
26	352	298	-11.07	-7.99	344	6838	43
27	370	307	-11.03	-7.85	163	4284	18
28	387	316	-11.07	-8.14	430	7634	48
29	405	325	-11.28	-8.12	306	6643	32
30	423	334	-11.37	-8.17	369	6789	46
31	441	342	-11.05	-7.94	179	5500	20
32	459	351	-10.94	-7.96	381	6873	49
33	477	360	-10.88	-7.69	368	7234	40
34	495	369	-11.03	-7.91	373	6563	45
35	513	378	-10.49	-7.52	297	6526	34
36	531	387	-10.17	-7.71	628	7992	62
37	549	396	-10.03	-7.54	500	6536	54
38	567	405	-10.92	-7.97	525	6892	60
39	585	414	-10.61	-7.57	227	5044	26
40	603	423			427	7066	50
41	621	432	-9.45	-7.38	418	7067	43
42	639	441	-9.68	-7.50	724	8626	74
43	656	450	-10.12	-7.28	450	7140	47
44	674	459	-10.89	-7.95	510	7423	55
45	692	468	-10.25	-7.38	499	7819	56
46	710	477	-10.34	-7.63	491	7718	51
47	728	486	-10.20	-7.43	242	5743	26
48	746	495	-10.77	-7.84	489	6528	52
49	764	504	-10.52	-7.34	442	6761	51
50	782	513	-11.01	-7.84	423	6305	48
51	800	522	-10.34	-7.37	440	6484	54
52	818	530	-11.31	-7.81	415	6139	52
53	836	539	-10.87	-7.62	411	6472	53
54	854	548	-11.27	-7.94	409	6283	45
55	872	557	-10.70	-7.48	292	5761	33
56	890	566	-10.66	-7.59	411	6981	45
57	908	575	-10.65	-7.60	463	6576	55
58	925	584	-10.85	-7.52	404	6201	49
59	943	593	-10.81	-7.67	273	6648	34
60	961	602	-10.81	-8.20	427	7670	43
61	979	611	-10.20	-7.39	419	6982	45
62	997	620	-10.69	-7.92	405	7311	40
63	1015	629	-10.59	-7.49	387	6300	47
64	1033	638	-10.02	-7.87	372	7904	45
65	1051	647	-8.67	-7.22	431	9013	57
66	1069	656	-9.85	-7.62	527	7979	60
67	1087	665	-10.57	-7.42	428	6788	56
68	1105	674	-10.73	-7.60	418	6753	53
69	1123	683	-9.92	-7.21	500	8634	56

depth (cm)	$\delta^{13}C$	$\delta^{18}O$
0	-10.46	-7.81
1	-10.20	-7.63
2	-10.96	-8.21
3	-11.13	-8.16
4	-9.43	-7.57
5	-10.36	-7.69
6		
7	-11.81	-7.86
8	-10.73	-7.68
9	-11.34	-7.92
10	-11.03	-7.84
11	-10.49	-7.75
12	-11.57	-8.22
13	-12.09	-8.25
14	-11.78	-8.25
15	-11.55	-8.09
16	-11.38	-8.14
17	-11.17	-8.04
18	-11.33	-8.22
19	-10.75	-8.08
20	-10.52	-7.99
21	-9.28	-8.04
22	-9.56	-7.51
23	-11.04	-8.03
24	-11.14	-8.01
25	-11.26	-7.86
26	-11.10	-7.89
27	-11.32	-7.96
28	-9.98	-7.59
29	-10.80	-7.92
30	-10.44	-7.67
31	-9.86	-7.60
32		
33	-10.84	-7.86
34	-9.96	-7.36
35	-10.22	-7.64
36	-11.05	-7.81
37	-10.65	-7.56
38	-10.33	-7.49
39	-11.35	-7.94
40	-11.00	-7.76
41	-11.20	-7.69
42	-11.29	-7.53
43	-12.11	-7.76
44	-11.87	-7.69
45	-11.66	-7.48
46	-11.52	-7.49
47	-11.21	-7.41
48	-11.90	-7.64
49	-11.78	-7.68
50	-12.03	-7.76
51	-11.85	-7.71
52	-12.07	-7.50
53		
54	-11.95	-7.70
55	-11.74	-8.08
56	-12.12	-7.52
57	-12.98	-7.83
58	-9.67	-6.12
59	-10.24	-7.30
60	-10.05	-7.46
61		
62	-11.77	-7.34
63	-9.91	-7.25
64	-11.61	-7.45
65	-11.58	-7.52
66	-10.97	-7.27
67		
68		
69	-10.79	-7.43

Data table I: stalagmite CLL-1

depth (mm)	age (yr, BP)	age (hiatus)	$\delta^{13}C$	$\delta^{18}O$	Ba (ppm)	Mg (ppm)	Sr (ppm)
70	1141	692	-10.29	-7.60	555	8523	60
71	1159	701	-10.47	-7.27	499	7442	62
72	1177	710	-11.15	-7.78	452	6617	55
73	1194	718	-11.14	-7.42	427	6315	52
74	1212	727	-10.94	-7.39	458	6388	53
75	1230	736	-10.54	-7.29	534	6736	63
76	1248	745	-10.86	-7.60	446	6562	57
77	1266	754	-10.85	-7.41	443	6324	57
78	1284	763	-10.66	-7.80	484	6557	57
79	1302	772	-11.35	-7.69	443	5836	54
80	1320	781	-11.78	-7.86	353	5911	45
81	1338	790	-11.78	-8.07	322	6374	41
82	1356	799	-11.79	-7.93	305	6060	39
83	1374	808	-11.68	-7.72	361	6186	46
84	1392	817	-11.36	-7.69	384	5944	50
85	1410	826	-11.48	-7.71	370	6310	47
86	1428	835	-11.59	-7.85	265	6383	34
87	1446	844	-10.84	-7.42	401	7104	50
88	1463	853	-10.73	-7.49	445	7113	51
89	1481	862	-11.24	-7.61	389	6112	50
90	1499	871	-11.28	-7.63	372	6098	45
91	1517	880	-11.63	-7.76	378	6426	46
92	1535	889	-10.28	-7.25	404	7438	45
93	1553	897	-10.58	-7.34	478	7431	53
94	1571	906	-10.78	-7.63	451	6096	54
95	1589	915	-11.10	-7.81	412	6631	52
96	1607	924	-10.32	-7.79	457	7067	54
97	1625	933	-10.90	-7.46	469	6162	57
98	1643	942	-10.41	-7.67	523	7113	60
99	1661	951	-10.41	-7.28	483	6924	
100	1679	960	-10.44	-7.90	490	6697	52
101	1697	969	-11.02	-7.61	476	6065	
102	1715	978	-11.22	-7.82	368	6070	47
103	1732	987	-11.42	-7.83	386	6171	
104	1750	996	-11.83	-8.17	379	5649	45
105	1768	1005	-11.91	-8.04	393	5791	
106	1786	1014	-11.74	-8.03	384	5601	49
107	1804	1023	-11.75	-7.99	349	5866	
108	1822	1032	-11.51	-7.86	375	5735	47
109	1840	1041	-11.72	-7.99	366	6042	
110	1858	1050	-11.74	-7.94	359	5782	50
111	1876	1059	-11.60	-7.75	400	6168	
112	1894	1068	-11.11	-7.79	383	6875	44
113	1912	1077	-10.64	-7.56	468	7481	
114	1930	1085	-9.54	-7.20	592	8581	69
115	1948	1094	-10.60	-7.56	519	7445	
116	1966	1103	-10.84	-8.04	497	5882	62
117	1984	1112	-11.51	-8.02	446	5936	
118	2001	1121	-10.26	-7.47	453	7258	57
119	2019	1130	-10.31	-7.81	597	6713	
120	2037	1139	-10.72	-7.86	448	6467	57
121	2055	1148	-10.40	-7.48	506	7158	
122	2073	1157	-9.73	-7.32	619	7727	71
123	2091	1166	-10.29	-7.52	555	7200	
124	2109	1175	-10.62	-7.60	505	6440	59
125	2127	1184	-10.76	-7.93	457	6410	58
126	2145	1193	-10.35	-7.52	448	6910	55
127	2163	1202	-10.38	-7.75	467	7191	58
128	2181	1211	-11.48	-8.22	336	6357	40
129	2199	1220	-11.55	-7.89	388	5752	47
130	2217	1229	-12.02	-8.12	285	5920	36
131	2235	1238	-11.71	-8.00	295	6143	39
132	2253	2324	-11.34	-8.00	405	6684	40
133	2270	2333	-11.14	-7.73	426	6984	45
134	2288	2342	-9.72	-7.66	548	11179	64
135	2306	2351	-10.51	-7.33	524	9089	62
136	2324	2360	-10.16	-7.88	547	11040	65
137	2342	2369	-11.12	-7.96	611	9002	64
138	2360	2378	-11.46	-8.37	581	8390	58
139	2378	2387	-11.88	-8.13	470	8258	52

depth (cm)	$\delta^{13}C$	$\delta^{18}O$
70		
71	-9.98	-7.56
72	-8.02	-7.34
73	-9.66	-7.42
74	-10.80	-7.05
75	-8.57	-6.50
76	-9.66	-7.05
77	-10.48	-7.27
78	-10.74	-7.13
79	-11.48	-7.31
80	-10.87	-7.15
81	-7.65	-6.92
82	-11.84	-7.81
83	-10.24	-7.31
84	-10.68	-7.31
85	-7.36	-6.49
86	-10.95	-7.40
87	-9.95	-7.32
88	-9.82	-7.39
89	-9.59	-7.34
90	-9.70	-7.24
91	-10.34	-7.40
92	-9.39	-7.34
93	-8.65	-6.86
94	-9.64	-7.27
95	-8.95	-7.13
96		
97	-10.91	-7.33
98	-8.31	-7.82
99	-9.76	-6.93
100	-9.82	-6.83
101	-9.99	-7.13
102	-10.56	-7.37
103	-10.44	-7.26
104	-10.77	-7.36
105	-8.31	-7.14
106		
107		
108	-9.57	-7.51
109	-10.18	-7.59
110	-10.07	-7.59
111	-10.19	-7.75
112	-10.69	-7.51
113	-10.32	-7.67
114	-10.47	-7.60
115	-9.92	-7.29
116	-10.73	-7.41
117	-9.18	-7.02
118	-10.84	-7.33
119	-10.59	-7.41
120	-9.98	-7.35
121	-11.08	-7.64
122	-9.65	-7.06
123	-10.14	-7.37
124	-9.88	-7.57
125	-9.17	-6.98
126	-6.36	-6.73
127	-6.45	-7.36
128	-6.46	-7.14
129	-7.52	-7.36
130	-8.53	-7.49
131	-7.56	-7.08

Data table I: stalagmite CLL-1

depth (mm)	age (yr, BP)	age (hiatus)	$\delta^{13}C$	$\delta^{18}O$	Ba (ppm)	Mg (ppm)	Sr (ppm)
140	2396	2396	-11.47	-8.04	593	7720	59
141	2405	2405	-11.63	-8.01	576	8054	57
142	2414	2414	-11.30	-7.98	581	7773	58
143	2423	2423	-10.91	-7.74	485	8174	57
144	2432	2432	-10.64	-7.71	531	8689	58
145	2441	2441	-11.15	-7.67	608	7801	63
146	2450	2450	-11.40	-8.13	599	8170	58
147	2459	2459	-11.14	-7.46	545	7938	60
148	2468	2468	-11.24	-8.19	608	8861	60
149	2477	2477	-11.51	-8.01	594	7724	61
150	2486	2486	-11.40	-8.02	444	7225	50
151	2494	2494	-11.33	-7.85	566	7772	58
152	2503	2503	-11.48	-8.02	547	7437	56
153	2512	2512	-11.00	-7.68	598	8401	63
154	2521	2521	-10.75	-7.56	559	9676	59
155	2530	2530	-10.41	-7.52	621	10496	68
156	2539	2539	-11.11	-7.94	660	8174	67
157	2548	2548	-11.39	-7.95	567	7221	62
158	2557	2557	-11.28	-7.89	497	7662	56
159	2566	2566	-11.31	-7.82	553	7080	59
160	2575	2575	-10.72	-7.62	607	8755	64
161	2584	2584	-10.86	-7.77	529	8388	62
162	2593	2593	-10.68	-7.88	564	8525	65
163	2602	2602	-11.17	-7.84	407	8138	50
164	2611	2611	-11.01	-7.89	512	8003	61
165	2620	2620	-10.81	-7.75	581	8656	64
166	2629	2629	-10.60	-7.66	608	9776	63
167	2638	2638	-10.54	-7.80	571	8777	63
168	2647	2647	-11.29	-8.15	633	7341	61
169	2656	2656	-11.15	-7.88	544	7180	59
170	2665	2665	-10.83	-7.77	574	8383	59
171	2674	2674	-10.74	-7.71	568	7552	62
172	2682	2682	-11.36	-8.00	465	6384	52
173	2691	2691	-11.29	-8.11	581	6593	61
174	2700	2700	-11.75	-8.28	504	6563	52
175	2709	2709			520	6898	57
176	2718	2718	-11.60	-8.18	450	6696	50
177	2727	2727	-11.67	-8.12	334	6754	40
178	2736	2736	-11.00	-8.12	525	7554	53
179	2745	2745	-10.20	-7.54	564	9275	61
180	2754	2754	-11.16	-8.06	492	7251	59
181	2763	2763	-10.98	-7.94	502	7402	59
182	2772	2772	-11.64	-8.25	426	6787	51
183	2781	2781	-11.51	-8.06	399	6464	48
184	2790	2790	-11.12	-7.65	512	7180	58
185	2799	2799	-11.17	-8.14	557	7129	58
186	2808	2808	-11.13	-8.01	574	7521	54
187	2817	2817	-10.77	-8.14	625	7997	68
188	2826	2826	-11.05	-7.83	509	7012	59
189	2835	2835	-11.38	-8.12	393	7115	50
190	2844	2844	-10.71	-7.99	465	8158	55
191	2853	2853	-10.73	-7.88	707	8045	66
192	2862	2862	-10.62	-7.78	699	8146	65
193	2870	2870	-10.34	-7.87	670	8943	67
194	2879	2879	-9.81	-7.51	666	9791	71
195	2888	2888	-9.37	-7.80	711	10054	79
196	2897	2897	-9.21	-7.15	707	10352	76
197	2906	2906	-9.85	-7.45	642	8883	64
198	2915	2915	-9.36	-7.34	566	8709	60
199	2924	2924			467	8001	57
200	2933	2933	-10.28	-7.65	435	7982	57
201	2942	2942	-9.88	-7.67	501	7968	58
202	2951	2951	-9.81	-7.72	464	7925	57
203	2960	2960	-10.18	-7.75	533	8180	60
204	2969	2969	-9.39	-7.56	683	10238	73
205	2978	2978	-9.99	-7.92	622	9677	65
206	2987	2987	-9.44	-7.43	498	8715	57
207	2996	2996	-9.78	-7.88	759	9521	74
208	3005	3005	-9.74	-7.73	545	8780	65
209	3014	3014	-9.52	-7.68	789	9800	75
210	3023	3023	-9.53	-7.58	734	9256	78

Data table I: stalagmite CLL-1

depth (mm)	age (yr, BP)	age (hiatus)	$\delta^{13}C$	$\delta^{18}O$	Ba (ppm)	Mg (ppm)	Sr (ppm)
211	3032	3032	-9.79	-7.69	751	8671	71
212	3041	3041	-9.54	-7.77	763	9972	83
213	3049	3049	-9.31	-7.43	666	10646	69
214	3058	3058	-9.49	-7.67	626	10170	72
215	3067	3067	-7.56	-6.97	626	11769	72
216	3076	3076	-8.32	-7.61	852	11661	95
217	3085	3085	-8.98	-7.54	767	9629	80
218	3094	3094	-10.86	-7.85	612	7418	72
219	3103	3103	-10.87	-7.83	674	7021	65
220	3112	3112	-9.38	-7.70	926	10799	92
221	3121	3121	-9.04	-7.46	737	11177	76
222	3130	3130	-8.87	-7.53	710	12068	82
223	3139	3139	-9.27	-7.50	857	9684	81
224	3148	3148	-9.20	-7.23	854	9665	91
225	3157	3157	-8.75	-7.20	851	10097	85
226	3166	3166	-9.32	-7.38	880	9996	91
227	3175	3175	-10.11	-7.58	903	8010	78
228	3184	3184	-10.90	-8.13	631	6784	68
229	3193	3193	-10.56	-7.89			
230	3202	3202	-10.42	-7.73	750	7441	77
231	3211	3211	-10.03	-7.42			
232	3220	3220	-10.44	-7.72	762	7634	76
233	3229	3229	-10.59	-7.69			
234	3237	3237	-10.38	-7.59	730	8275	72
235	3246	3246	-10.60	-7.85			
236	3255	3255	-10.67	-7.79	619	7249	68
237	3264	3264	-10.58	-7.78			
238	3273	3273	-10.95	-7.90	496	6982	60
239	3282	3282					
240	3291	3291	-11.50	-7.95	292	5404	34
241	3300	3300	-11.39	-8.07			
242	3309	3309	-11.85	-8.12	392	6387	49
243	3318	3318	-10.68	-7.80			
244	3327	3327	-9.66	-7.88	894	9073	85
245	3336	3336	-9.37	-7.32			
246	3345	3345	-9.96	-7.75	649	8240	74
247	3354	3354	-9.68	-7.68			
248	3363	3363	-10.65	-7.74	629	7036	71
249	3372	3372	-10.68	-7.78			
250	3381	3381	-11.07	-7.90	572	6961	65
251	3390	3390	-10.87	-7.64			
252	3399	3399	-11.13	-7.96	719	7110	70
253	3408	3408	-10.88	-7.70			
254	3417	3417	-10.96	-7.78	783	7327	72
255	3425	3425	-9.81	-7.23	661	9620	62
256	3434	3434	-10.42	-7.73	671	8939	67
257	3443	3443	-9.89	-7.71	828	8395	83
258	3452	3452	-11.02	-7.91	379	6019	45
259	3461	3461	-10.01	-7.49	710	8376	73
260	3470	3470	-10.77	-7.87	684	6849	75
261	3479	3479	-10.98	-7.91	513	6833	57
262	3488	3488	-11.23	-7.85	587	6792	66
263	3497	3497	-11.08	-7.80	582	6657	62
264	3506	3506	-11.52	-8.14	471	6403	58
265	3515	3515	-11.27	-7.99	504	6578	56
266	3520	3520	-11.13	-7.69	574	6951	66
267	3525	3525	-10.32	-7.43	661	7194	68
268	3530	3530	-9.74	-7.70	878	8840	93
269	3535	3535	-10.21	-7.39	553	8081	62
270	3540	3540	-11.02	-7.74	488	6880	59
271	3545	3545	-11.39	-8.35	447	6173	50
272	3550	3550	-11.34	-7.85	565	6720	66
273	3555	3555	-10.25	-7.41	736	7723	72
274	3560	3560	-10.73	-7.87	736	8106	80
275	3565	3565	-10.99	-7.90	606	7391	62
276	3570	3570	-10.46	-7.63	641	8804	72
277	3575	3575	-9.89	-7.75	827	9431	80
278	3580	3580	-10.20	-7.84	808	8381	86
279	3585	3585	-10.21	-7.77	655	8369	72
280	3590	3590	-10.04	-7.33	682	9172	70
281	3595	3595	-10.41	-7.53	628	8670	59

Data table I: stalagmite CLL-1

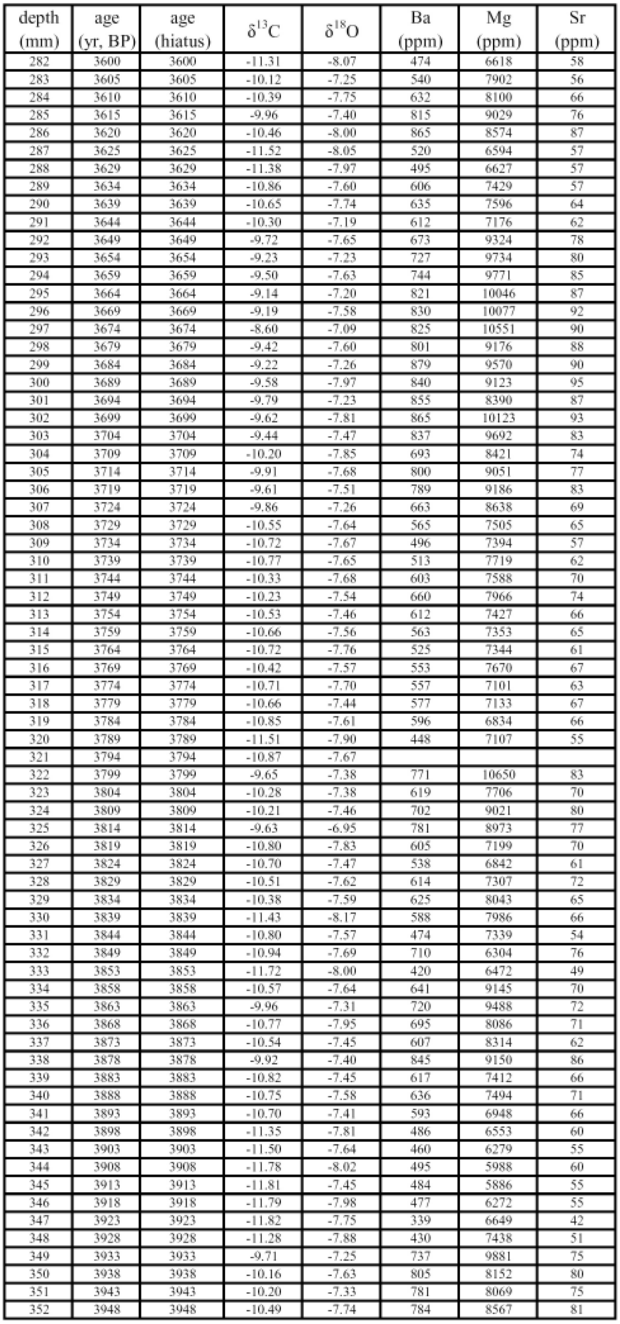

depth (mm)	age (yr, BP)	age (hiatus)	$\delta^{13}C$	$\delta^{18}O$	Ba (ppm)	Mg (ppm)	Sr (ppm)
282	3600	3600	-11.31	-8.07	474	6618	58
283	3605	3605	-10.12	-7.25	540	7902	56
284	3610	3610	-10.39	-7.75	632	8100	66
285	3615	3615	-9.96	-7.40	815	9029	76
286	3620	3620	-10.46	-8.00	865	8574	87
287	3625	3625	-11.52	-8.05	520	6594	57
288	3629	3629	-11.38	-7.97	495	6627	57
289	3634	3634	-10.86	-7.60	606	7429	57
290	3639	3639	-10.65	-7.74	635	7596	64
291	3644	3644	-10.30	-7.19	612	7176	62
292	3649	3649	-9.72	-7.65	673	9324	78
293	3654	3654	-9.23	-7.23	727	9734	80
294	3659	3659	-9.50	-7.63	744	9771	85
295	3664	3664	-9.14	-7.20	821	10046	87
296	3669	3669	-9.19	-7.58	830	10077	92
297	3674	3674	-8.60	-7.09	825	10551	90
298	3679	3679	-9.42	-7.60	801	9176	88
299	3684	3684	-9.22	-7.26	879	9570	90
300	3689	3689	-9.58	-7.97	840	9123	95
301	3694	3694	-9.79	-7.23	855	8390	87
302	3699	3699	-9.62	-7.81	865	10123	93
303	3704	3704	-9.44	-7.47	837	9692	83
304	3709	3709	-10.20	-7.85	693	8421	74
305	3714	3714	-9.91	-7.68	800	9051	77
306	3719	3719	-9.61	-7.51	789	9186	83
307	3724	3724	-9.86	-7.26	663	8638	69
308	3729	3729	-10.55	-7.64	565	7505	65
309	3734	3734	-10.72	-7.67	496	7394	57
310	3739	3739	-10.77	-7.65	513	7719	62
311	3744	3744	-10.33	-7.68	603	7588	70
312	3749	3749	-10.23	-7.54	660	7966	74
313	3754	3754	-10.53	-7.46	612	7427	66
314	3759	3759	-10.66	-7.56	563	7353	65
315	3764	3764	-10.72	-7.76	525	7344	61
316	3769	3769	-10.42	-7.57	553	7670	67
317	3774	3774	-10.71	-7.70	557	7101	63
318	3779	3779	-10.66	-7.44	577	7133	67
319	3784	3784	-10.85	-7.61	596	6834	66
320	3789	3789	-11.51	-7.90	448	7107	55
321	3794	3794	-10.87	-7.67			
322	3799	3799	-9.65	-7.38	771	10650	83
323	3804	3804	-10.28	-7.38	619	7706	70
324	3809	3809	-10.21	-7.46	702	9021	80
325	3814	3814	-9.63	-6.95	781	8973	77
326	3819	3819	-10.80	-7.83	605	7199	70
327	3824	3824	-10.70	-7.47	538	6842	61
328	3829	3829	-10.51	-7.62	614	7307	72
329	3834	3834	-10.38	-7.59	625	8043	65
330	3839	3839	-11.43	-8.17	588	7986	66
331	3844	3844	-10.80	-7.57	474	7339	54
332	3849	3849	-10.94	-7.69	710	6304	76
333	3853	3853	-11.72	-8.00	420	6472	49
334	3858	3858	-10.57	-7.64	641	9145	70
335	3863	3863	-9.96	-7.31	720	9488	72
336	3868	3868	-10.77	-7.95	695	8086	71
337	3873	3873	-10.54	-7.45	607	8314	62
338	3878	3878	-9.92	-7.40	845	9150	86
339	3883	3883	-10.82	-7.45	617	7412	66
340	3888	3888	-10.75	-7.58	636	7494	71
341	3893	3893	-10.70	-7.41	593	6948	66
342	3898	3898	-11.35	-7.81	486	6553	60
343	3903	3903	-11.50	-7.64	460	6279	55
344	3908	3908	-11.78	-8.02	495	5988	60
345	3913	3913	-11.81	-7.45	484	5886	55
346	3918	3918	-11.79	-7.98	477	6272	55
347	3923	3923	-11.82	-7.75	339	6649	42
348	3928	3928	-11.28	-7.88	430	7438	51
349	3933	3933	-9.71	-7.25	737	9881	75
350	3938	3938	-10.16	-7.63	805	8152	80
351	3943	3943	-10.20	-7.33	781	8069	75
352	3948	3948	-10.49	-7.74	784	8567	81

Data table I: stalagmite CLL-1

depth (mm)	age (yr, BP)	age (hiatus)	$\delta^{13}C$	$\delta^{18}O$	Ba (ppm)	Mg (ppm)	Sr (ppm)
353	3953	3953	-10.54	-7.27	721	7639	72
354	3958	3958	-10.51	-7.65	720	8428	76
355	3963	3963	-11.14	-7.61	614	7915	66
356	3969	3969	-11.16	-7.84	631	7199	70
357	3976	3976	-10.58	-7.26	802	7580	81
358	3982	3982	-11.55	-7.98	546	6502	65
359	3988	3988	-11.64	-7.70	521	6406	59
360	3994	3994	-11.29	-7.92	623	6590	67
361	4001	4001	-10.96	-7.44	667	7348	65
362	4007	4007	-10.91	-7.76	646	7705	67
363	4013	4013	-10.75	-7.24	706	7959	68
364	4019	4019	-11.13	-7.76	627	6984	67
365	4026	4026	-11.25	-7.59	609	7776	60
366	4032	4032	-10.97	-7.79	639	7247	67
367	4038	4038	-10.98	-7.42	640	7396	63
368	4044	4044	-11.10	-7.89	628	7152	66
369	4051	4051	-11.05	-7.54	618	6870	63
370	4057	4057	-11.98	-8.02	367	6191	49
371	4063	4063	-10.98	-7.63	544	6941	61
372	4069	4069	-11.46	-7.81	371	6237	50
373	4076	4076	-11.40	-7.48	372	6485	49
374	4082	4082	-10.53	-7.26	521	7288	85
375	4088	4088	-10.92	-7.81	503	7211	62
376	4094	4094	-11.11	-7.79	374	7427	52
377	4101	4101	-10.21	-7.53	431	8812	63
378	4107	4107	-10.85	-7.59	405	7523	60
379	4113	4113	-10.98	-7.81	580	9292	74
380	4119	4119	-10.39	-7.50	631	8721	77
381	4126	4126	-10.69	-7.56	629	8139	69
382	4132	4132	-10.96	-7.70	439	7104	63
383	4138	4138	-11.45	-7.80	414	6938	59
384	4144	4144	-11.17	-7.62	426	6819	60
385	4151	4151	-12.00	-8.19	383	6615	54
386	4157	4157	-11.15	-7.88	650	7422	78
387	4163	4163	-10.98	-7.78	683	7241	77
388	4169	4169	-10.89	-7.70	689	7265	82
389	4176	4176	-11.54	-7.90	346	6583	51
390	4182	4182	-11.20	-8.06	663	7030	79
391	4188	4188	-10.91	-7.49	524	7526	62
392	4194	4194	-10.92	-7.81	589	7508	72
393	4201	4201	-10.57	-7.46	620	8794	70
394	4207	4207	-10.46	-7.56	617	9039	75
395	4213	4213	-10.34	-7.33	589	7783	72
396	4219	4219	-10.01	-7.45	615	8699	82
397	4226	4226	-9.84	-7.24	681	9299	83
398	4232	4232	-10.09	-7.54	715	9452	90
399	4238	4238	-9.88	-7.35	687	9604	86
400	4244	4244	-9.41	-7.25	593	9707	86
401	4251	4251	-11.01	-7.28	360	7503	52
402	4257	4257	-10.43	-7.54	422	8090	64
403	4263	4263	-10.55	-7.28	391	7664	57
404	4269	4269	-10.67	-7.30	397	7786	61
405	4276	4276	-10.01	-7.08		8351	65
406	4282	4282	-10.37	-7.54	454	8052	68
407	4288	4288	-10.44	-7.19		7406	62
408	4294	4294	-10.60	-7.49	501	7339	71
409	4301	4301	-10.53	-7.25		7209	64
410	4307	4307	-11.03	-7.65	389	7163	58
411	4313	4313	-10.90	-7.40	388	7542	54
412	4319	4319	-11.08	-7.68	400	7333	59
413	4326	4326	-10.81	-7.32	440	7134	58
414	4332	4332	-11.25	-7.80	469	6701	65
415	4338	4338	-10.76	-7.43	436	7525	61
416	4344	4344	-11.09	-7.60	402	7376	60
417	4351	4351	-10.00	-6.78	545	9220	68
418	4357	4357	-10.04	-7.18	508	8354	70
419	4363	4363	-9.64	-6.93	576	9159	73
420	4369	4369	-9.94	-7.03	525	8639	71
421	4376	4376	-10.32	-6.92	417	7930	57
422	4382	4382	-10.65	-7.23	391	7766	58
423	4388	4388	-10.99	-7.12	381	7303	54

Data table I: stalagmite CLL-1

depth (mm)	age (yr, BP)	age (hiatus)	$\delta^{13}C$	$\delta^{18}O$	Ba (ppm)	Mg (ppm)	Sr (ppm)
424	4394	4394	-11.19	-7.49	365	7142	54
425	4401	4401	-11.40	-7.41	472	6293	62
426	4407	4407	-11.19	-8.05	440	5776	64
427	4413	4413	-11.49	-7.44	372	6207	51
428	4419	4419	-11.48	-7.72	342	6864	51
429	4426	4426	-11.59	-7.44	372	7978	53
430	4432	4432	-11.43	-7.82	307	6545	48
431	4438	4438	-10.46	-7.24	659	9039	79
432	4444	4444	-10.31	-7.65	675	9493	86
433	4451	4451	-10.57	-7.28	605	9353	74
434	4457	4457	-10.43	-7.30	641	8571	80
435	4463	4463	-11.05	-7.25	548	7318	67
436	4469	4469	-10.80	-7.45	510	7873	66
437	4476	4476	-9.80	-6.80	326	6418	43
438	4482	4482	-10.17	-6.79	512	7526	76
439	4488	4488			197	5234	26
440	4494	4494	-11.15	-7.61	527	6992	66
441	4501	4501	-11.69	-7.46	243	4760	34
442	4507	4507	-12.14	-7.78	331	5959	49
443	4513	4513	-12.11	-7.73	222	5236	32
444	4519	4519	-12.16	-7.88	322	5744	48
445	4526	4526	-12.11	-7.30	225	5185	32
446	4532	4532	-11.65	-7.67	372	6127	53
447	4538	4538	-11.88	-7.46	291	5488	41
448	4544	4544	-11.92	-7.75	357	5828	52
449	4551	4551			321	5657	46
450	4557	4557	-11.77	-7.82	432	6016	58
451	4563	4563	-11.31	-7.07	214	5069	30
452	4569	4569	-10.78	-6.93	403	7027	62
453	4576	4576	-10.83	-6.97	297	6629	42
454	4582	4582	-10.80	-7.46	472	7443	58
455	4588	4588	-10.80	-7.13	303	6914	38
456	4591	4591	-10.50	-7.51	431	7468	55
457	4595	4595	-11.00	-7.12	357	6848	50
458	4598	4598	-11.08	-7.62	369	6844	52
459	4602	4602	-10.51	-6.83	358	7652	49
460	4605	4605	-10.89	-7.50	352	7229	48
461	4609	4609	-11.12	-7.06	316	7088	43
462	4612	4612	-11.18	-7.61	327	6897	47
463	4616	4616	-11.16	-7.35	368	6623	52
464	4619	4619	-11.35	-7.72	350	6459	49
465	4623	4623	-10.80	-6.95	363	7246	50
466	4626	4626	-10.66	-7.29	431	7436	60
467	4630	4630	-11.09	-7.13	347	7172	48
468	4633	4633	-11.09	-7.32	336	6742	49
469	4637	4637	-11.44	-7.35	347	6265	52
470	4640	4640	-11.39	-7.66	433	6748	58
471	4644	4644	-10.79	-6.93	383	7541	50
472	4647	4647	-11.33	-7.68	372	6545	52
473	4651	4651	-11.16	-7.08	413	6794	55
474	4654	4654	-11.31	-7.56	346	6550	50
475	4658	4658	-11.49	-7.32	337	6450	48
476	4661	4661	-11.56	-7.74	363	6233	50
477	4665	4665	-11.72	-7.45	423	6205	52
478	4668	4668	-11.67	-7.65	327	6433	47
479	4672	4672	-11.33	-7.26	391	6969	47
480	4675	4675	-11.33	-7.59	387	6700	51
481	4679	4679	-11.73	-7.67	342	6454	48
482	4682	4682	-11.66	-7.63	381	6587	49
483	4686	4686	-12.10	-7.55	316	5962	45
484	4689	4689	-12.30	-7.94	323	5803	46
485	4693	4693	-12.39	-7.76	292	6185	42
486	4696	4696	-12.21	-8.02	279	6073	40
487	4699	4699	-12.46	-7.81	281	6339	41
488	4703	4703	-12.39	-7.99	297	5093	42
489	4706	4706	-11.96	-7.50	384	6117	49
490	4710	4710	-11.67	-7.63	414	7001	50
491	4713	4713	-11.76	-7.38	401	6433	49
492	4717	4717	-12.01	-8.00	409	6069	51
493	4720	4720	-11.81	-7.50	374	5992	49
494	4724	4724	-12.28	-7.84	308	6011	44

Data table I: stalagmite CLL-1

depth (mm)	age (yr, BP)	age (hiatus)	$\delta^{13}C$	$\delta^{18}O$	Ba (ppm)	Mg (ppm)	Sr (ppm)
495	4727	4727	-12.04	-7.72	392	5956	52
496	4731	4731	-12.08	-7.93	342	6124	48
497	4734	4734	-11.89	-7.60	379	6175	49
498	4738	4738	-11.97	-7.88	416	6220	51
499	4741	4741	-11.63	-7.48	392	6103	52
500	4745	4745	-12.03	-7.94	357	6035	48
501	4748	4748	-12.19	-7.79	313	6031	43
502	4752	4752			266	6101	41
503	4755	4755	-12.02	-7.77	245	6301	38
504	4759	4759			320	5997	46
505	4762	4762	-12.22	-7.75	289	5853	42
506	4766	4766			242	5970	38
507	4769	4769	-12.18	-7.69	261	6205	39
508	4773	4773			253	6080	40
509	4776	4776	-11.50	-7.61	320	6197	43
510	4780	4780			300	6243	43
511	4783	4783	-11.85	-7.29	315	6163	44
512	4787	4787	-11.98	-7.78	292	6042	43
513	4790	4790	-12.22	-7.74	274	6172	40
514	4794	4794	-12.40	-7.85	246	6567	38
515	4797	4797	-12.18	-7.71	239	6409	36
516	4801	4801	-11.94	-7.65	262	6522	40
517	4804	4804	-11.78	-7.56	332	6599	45
518	4808	4808	-12.13	-7.86	277	6682	40
519	4811	4811	-11.77	-7.37	359	6667	48
520	4814	4814	-12.05	-7.81	318	6579	45
521	4818	4818	-11.86	-7.53	368	6498	52
522	4821	4821	-11.67	-7.50	394	6661	55
523	4825	4825	-11.97	-7.38	321	6427	45
524	4828	4828	-11.84	-7.42	311	6282	46
525	4832	4832	-12.15	-7.50	275	6487	40
526	4835	4835	-12.27	-7.86	254	6526	39
527	4839	4839	-12.18	-7.58	275	6489	40
528	4842	4842	-12.18	-7.69	265	6672	39
529	4846	4846	-11.37	-7.49	280	6745	39
530	4849	4849	-11.79	-7.77	253	6342	38
531	4853	4853	-11.98	-7.75	313	6456	44
532	4856	4856	-11.50	-7.31	318	6280	46
533	4860	4860	-11.81	-7.64	325	6283	44
534	4863	4863	-12.25	-8.15	320	6391	44
535	4867	4867			309	6577	40
536	4870	4870	-11.70	-7.47	354	6407	48
537	4874	4874	-12.10	-7.84	304	6344	42
538	4877	4877	-11.92	-7.55	326	6227	44
539	4881	4881	-11.82	-7.71	392	6440	51
540	4884	4884	-11.68	-7.55	289	6527	41
541	4888	4888	-11.95	-7.72	443	6744	55
542	4891	4891	-12.07	-7.73	373	6524	51
543	4895	4895	-12.36	-8.05			
544	4898	4898	-11.88	-7.61	336	6579	48
545	4902	4902	-12.35	-7.86	332	6505	44
546	4905	4905	-12.08	-7.82	318	6425	43
547	4909	4909	-12.37	-7.93	366	6511	47
548	4912	4912	-12.36	-7.85			
549	4916	4916	-12.51	-8.31	304	6476	42
550	4919	4919	-12.56	-7.98	323	6609	45
551	4922	4922	-12.54	-7.75	324	6415	43
552	4926	4926	-12.47	-7.71	353	6544	47
553	4929	4929	-12.38	-8.08	328	6431	43
554	4933	4933	-12.43	-8.04	322	6421	44
555	4936	4936	-12.44	-7.86	310	6475	41
556	4940	4940	-12.60	-8.13	301	6486	41
557	4943	4943	-12.33	-7.84	327	6552	43
558	4947	4947	-12.49	-7.58	338	6561	45
559	4950	4950	-12.25	-7.68	286	6319	39
560	4954	4954	-12.07	-7.28	377	7035	48
561	4957	4957	-11.89	-7.56	419	6953	50
562	4961	4961	-12.37	-7.55	341	6496	46
563	4964	4964	-12.75	-7.95	405	6708	49
564	4968	4968	-12.86	-7.76	367	6579	48
565	4971	4971	-12.38	-7.68	326	6523	42

Data table I: stalagmite CLL-1

depth (mm)	age (yr, BP)	age (hiatus)	$\delta^{13}C$	$\delta^{18}O$	Ba (ppm)	Mg (ppm)	Sr (ppm)
566	4975	4975	-12.02	-7.45	326	6551	43
567	4978	4978	-11.96	-7.76	308	6581	39
568	4982	4982	-11.92	-7.23	314	6781	40
569	4985	4985	-12.46	-7.93	365	7097	43
570	4989	4989	-12.91	-7.46	302	6480	40
571	4992	4992	-12.86	-7.77	322	6930	40
572	4996	4996	-12.52	-7.31	393	6426	50
573	4999	4999	-12.14	-7.68	404	6632	48
574	5003	5003	-11.76	-7.21	484	7521	56
575	5006	5006	-11.24	-7.15	449	7773	50
576	5010	5010	-12.52	-7.44	399	7709	49
577	5013	5013	-13.20	-7.85	406	7458	48
578	5017	5017	-10.14	-6.48	564	10930	68
579	5020	5020	-8.67	-6.36	739	12469	81
580	5024	5024	-10.09	-6.10	839	9513	86
581	5027	5027	-9.01	-5.98	819	10798	82
582	5030	5030	-8.96	-5.91	356	10218	46
583	5034	5034	-11.22	-7.30	344	7802	42
584	5037	5037	-11.07	-6.99	314	7887	42
585	5041	5041	-11.14	-7.25	329	7575	41
586	5044	5044	-11.16	-7.13	363	7173	45
587	5048	5048	-10.85	-7.33	418	7394	48
588	5051	5051	-10.97	-7.08	401	7546	49
589	5055	5055	-10.75	-7.34	470	7345	51
590	5058	5058	-10.70	-7.13	494	7207	56

Data table II: stalagmite CLL-2

depth (cm)	$\delta^{13}C$	$\delta^{18}O$
0	-7.06	-7.19
1	-9.08	-7.77
2	-9.47	-7.89
3		
4	-10.04	-7.64
5	-9.78	-7.69
6	-7.94	-5.92
7	-9.70	-6.28
8	-10.17	-7.33
9	-9.68	-7.17
10	-10.70	-7.59
11	-10.12	-7.43
12	-10.12	-7.28
13	-10.22	-7.38
14	-10.28	-7.38
15	-10.75	-7.74
16		
17	-9.19	-7.14
18	-8.87	-6.92
19	-8.60	-6.92
20	-8.21	-6.57
21	-8.06	-6.56
22	-8.17	-6.56
23	-7.43	-6.51
24	-8.69	-6.93
25	-10.67	-7.80
26	-9.37	-7.66
27	-8.35	-7.89
28	-8.03	-7.96
29	-8.22	-7.12
30	-9.15	-6.85
31		
32	-8.35	-6.98
33	-9.57	-7.04
34	-9.65	-7.31
35	-9.46	-6.82
36	-10.80	-7.44
37	-11.03	-7.47
38		
39	-9.43	-6.89
40		
41	-7.54	-6.84
42	-9.35	-6.96
43	-10.68	-7.39
44	-10.13	-7.19
45	-10.41	-7.71
46	-9.71	-7.00
47	-9.88	-7.17
48	-9.73	-6.90
49	-9.96	-7.81
50	-9.21	-7.37
51	-9.37	-7.63
51	-9.29	-7.50
52	-10.06	-7.70
53	-8.49	-7.49
54	-8.68	-7.37
55	-8.85	-7.25
56	-9.65	-7.43
57	-9.59	-7.42
58	-10.30	-7.91
59	-9.36	-7.58
60	-9.18	-7.34
61	-9.22	-7.42
62	-8.03	-7.27
63	-9.53	-6.94
64	-11.06	-7.35
65	-10.53	-7.20
66	-10.24	-7.16
67	-8.50	-6.71
68	-10.27	-7.51
69	-9.60	-7.00
70	-7.61	-6.77
71	-9.25	-7.28
72		
73	-9.66	-7.15
74	-9.12	-7.14
75	-9.42	-7.46
76		
77	-9.89	-7.35
78	-10.75	-7.52
79	-10.67	-7.71
80	-8.99	-6.87
81	-10.21	-7.39
82	-9.73	-7.16
83	-10.64	-7.67
84	-9.73	-7.19
85	-5.68	-6.38
86	-10.41	-7.64
87	-11.29	-7.90
88	-9.99	-7.34
89	-10.56	-7.50
90	-10.06	-7.56

Data table III: stalagmite CLL-3

depth (cm)	$\delta^{13}C$	$\delta^{18}O$
0	-9.77	-7.55
1	-7.92	-7.16
2	-8.43	-6.08
2	-8.35	-6.00
3	-10.70	-7.45
4	-9.20	-6.75
5	-7.76	-6.77
6	-9.38	-6.88
7	-9.34	-7.22
8	-8.51	-6.76
9	-9.83	-7.35
10	-9.84	-7.32
11	-10.16	-7.50
12	-9.93	-7.28
13	-10.40	-6.72
14	-10.06	-7.18
15	-11.07	-7.73
16	-10.60	-7.49
17	-10.45	-7.42
18	-10.17	-7.38
19	-6.86	-6.49
19	-6.81	-6.51
20	-9.60	-7.49
21	-10.15	-7.41
22	-9.22	-7.49
23	-10.20	-7.85
24	-9.72	-7.55
25	-9.47	-7.09
26	-9.32	-7.04
27	-10.07	-7.59
28	-10.08	-7.59
29	-10.47	-7.60
30	-10.96	-7.79
31	-10.79	-7.54
32	-10.63	-7.49
33	-9.41	-7.30
34	-9.94	-7.42
35	-9.79	-7.33
36	-10.05	-7.66
37	-9.41	-7.72
38	-10.53	-7.86
39	-9.81	-7.77
40	-9.50	-7.62
41	-9.78	-7.72
42		
43	-11.13	-7.66
44	-10.24	-7.54
45	-10.01	-7.39
46	-10.55	-7.58
47	-10.63	-7.81
48	-10.04	-7.59
49	-6.88	-7.07
50	-9.65	-7.16
51	-10.16	-7.40
52	-10.26	-7.15
53	-10.06	-7.42
54	-10.86	-7.59
55	-10.69	-7.67
56	-10.60	-7.46
57	-10.95	-7.82
58	-11.62	-7.79
59	-10.87	-7.79
60	-11.59	-8.05
61	-9.68	-7.38
62	-10.46	-7.60
63	-11.47	-7.97
64	-8.87	-7.10
65	-5.50	-6.37
66	-6.21	-6.85
67	-8.64	-7.65
68	-9.55	-8.03
69	-9.76	-7.99
70	-10.29	-7.92
71		
72	-10.31	-7.87
73	-11.27	-7.92
74	-6.40	-6.99

Data table IV: stalagmite CLL-4

depth (cm)	$\delta^{13}C$	$\delta^{18}O$
0	-11.92	-8.40
1	-11.41	-7.72
2	-12.01	-8.45
3	-11.83	-8.53
4	-11.19	-8.04
5	-11.87	-8.68
6	-10.52	-7.87
7	-8.27	-7.52
8	-9.70	-7.98
9	-10.55	-7.57
10	-11.60	-8.32
11	-11.70	-7.98
12	-11.45	-7.87
13	-10.87	-8.17
14	-11.08	-7.57
15	-11.24	-7.06
16	-11.93	-8.63
17	-11.00	-7.72
18	-11.34	-7.56
19	-11.69	-8.26
20	-10.96	-8.07
21	-11.58	-7.96
22	-11.72	-7.96
23	-9.98	-7.46
24	-11.35	-8.07
25	-11.96	-7.66
26	-10.51	-7.28
27	-10.73	-7.33
28	-11.73	-7.81
29	-11.48	-7.86
30	-11.08	-7.80
31	-11.21	-7.61
32	-11.22	-7.51
33	-11.02	-7.39
34	-10.91	-7.84
35	-11.22	-7.58
36	-11.07	-7.38
37	-8.98	-7.40
38	-10.68	-7.85
39	-11.22	-7.53
40	-12.09	-8.26
41	-9.22	-7.28
42	-9.98	-7.20
43	-7.85	-7.02
44	-10.58	-7.76
45	-11.61	-8.26
46	-11.03	-7.70
47	-9.64	-7.19
48	-11.36	-7.87
49	-11.30	-7.91
50	-12.15	-8.51
51	-9.58	-7.00
52	-11.27	-8.34
53	-11.57	-7.68
54	-11.41	-7.35
55	-10.36	-7.48
56	-11.24	-7.60
57	-11.69	-7.93
57	-11.63	-8.10
58	-11.00	-7.49
58	-10.47	-7.49
59	-9.16	-7.46
60	-11.78	-7.69
61	-10.55	-7.08
62	-11.13	-7.83
63	-10.91	-7.29
64	-11.80	-8.13
65	-10.85	-7.91
66	-11.36	-7.88
67	-10.72	-8.12
68	-11.29	-8.24
69	-11.05	-7.50
70	-10.17	-7.57
71	-10.68	-7.72
72	-11.43	-7.92
73	-12.36	-8.72
74	-12.14	-8.72
75	-11.21	-7.69
76	-11.73	-8.21
77	-11.69	-8.12
78	-11.62	-8.24
79	-11.12	-7.90
80	-10.95	-7.94
81	-10.63	-8.29
82	-10.14	-7.65
83	-11.72	-8.18
84	-11.07	-7.35
85	-10.23	-7.61
86	-11.38	-7.15
87	-12.30	-7.92
88	-11.65	-7.53
89	-10.59	-8.49
90	-12.13	-8.32
91		
92	-11.37	-7.48
93	-11.97	-8.15
94	-12.19	-8.06
95	-11.72	-7.88
96	-10.31	-7.25
97	-10.35	-7.06
98	-11.66	-7.81
99	-10.44	-8.05
100	-11.71	-8.45
101	-9.70	-7.48
102	-10.93	-7.81
103	-11.38	-8.13
104	-11.68	-8.32
105	-12.39	-8.59
106	-11.69	-8.23
107	-10.94	-7.61
108	-12.06	-8.11
109	-10.96	-7.91
110		
111	-11.25	-8.08
112	-10.75	-7.67
113	-11.74	-8.27
114	-9.60	-7.99
115	-10.55	-7.86
116	-11.33	-8.64
117	-10.82	-7.61
118	-10.12	-7.46
119	-12.04	-8.27
120	-10.24	-7.16
121	-10.85	-7.22

Data table V: stalagmite CLL-5

depth (cm)	$\delta^{13}C$	$\delta^{18}O$
0	-10.11	-7.89
1	-6.95	-7.65
2	-8.85	-7.25
3	-10.47	-7.25
4	-10.99	-7.75
5	-9.64	-6.97
6	-11.10	-7.20
7	-10.82	-7.82
8	-9.67	-7.92
9	-9.31	-7.59
10	-10.03	-8.13
11	-9.80	-7.57
12	-9.93	-8.12
13	-8.10	-6.76
14	-8.99	-7.47
15	-10.06	-7.43
16	-10.22	-7.53
17	-10.14	-7.28
18	-10.84	-7.16
19	-10.88	-7.44
20	-9.63	-7.21
21	-9.17	-6.64
22		
23	-8.88	-5.61
24	-10.55	-6.33
25	-10.55	-5.79
26		
27	-10.73	-6.21
28	-8.09	-5.48
29	-9.26	-5.65
30	-10.91	-6.56
31	-12.67	-6.16
32	-11.40	-7.19
33	-11.09	-6.75
34	-11.89	-7.13
35	-11.41	-7.52
36	-11.11	-7.03
37	-10.38	-6.28
38	-9.88	-6.67
39	-9.19	-6.98
40	-9.13	-7.03
41	-8.59	-6.41
42	-10.23	-7.54
43	-8.70	-5.59
44	-11.24	-7.49
45	-10.03	-6.61
46	-9.54	-7.92
47	-9.38	-7.14
48	-10.04	-6.17
49		
50	-9.60	-7.38
51	-9.14	-7.55
52	-7.67	-7.92
53	-9.40	-8.23
54	-9.69	-8.71
55	-11.03	-9.00
56		
57	-9.64	-9.04
58	-8.28	-8.05
59	-9.26	-9.23
60	-8.06	-7.53
61	-9.02	-8.72
62	-8.76	-7.66
63	-8.87	-8.33
64	-9.03	-8.42
65	-8.70	-8.60
66	-9.27	-8.54
67	-9.25	-8.48
68	-9.34	-9.50
69	-9.07	-8.67
70	-9.53	-8.70
71	-9.55	-8.50
72		
73	-9.60	-8.29
74		
75	-9.04	-8.70
76	-9.66	-9.06
77	-8.95	-7.74
78	-9.35	-8.24
79	-9.75	-9.02
80	-9.41	-9.01
81	-9.23	-9.16
82	-9.13	-8.53
83	-8.98	-9.27
84	-10.07	-8.93
85		
86	-7.93	-7.93
87		
88	-9.84	-8.25
89	-8.96	-9.20
90	-8.93	-8.96
91	-8.84	-8.32
92	-9.10	-8.85
93	-8.61	-8.49
94	-8.55	-8.27
95		
96		
97		
98	-8.47	-7.91
99	-8.67	-10.45
100	-8.33	-8.17
101	-8.28	-8.33
102	-8.53	-8.47
103	-8.61	-8.23
104	-8.95	-7.99
105	-9.32	-8.78
106	-9.16	-8.63
107	-8.50	-8.38
108	-8.89	-9.25
109	-8.06	-9.07
110	-8.28	-8.08
111		
112	-9.62	-8.42
113		
114	-9.12	-7.64
115		
116	-9.25	-8.25
117		
118		
119	-9.12	-8.34
120	-9.40	-8.47
121	-8.42	-7.94
122	-8.83	-7.95
123	-8.66	-8.64
124	-9.03	-8.65
125		
126	-8.81	-8.96
127	-9.11	-8.70
128	-8.27	-8.24
129	-8.46	-8.80
130	-8.57	-8.55

Data table VI: stalagmite HUA-6

depth (cm)	$\delta^{13}C$	$\delta^{18}O$
0	-2.09	-14.99
1	-3.17	-14.95
2	-3.09	-16.04
3		
4	-3.83	-17.61
5	-3.14	-16.57
6	-3.42	-15.19
7	-3.65	-16.46
8	-5.27	-14.38
9	-6.61	-14.81
10	-6.56	-14.28
11	-6.87	-14.02
12	-6.81	-15.65
13	-5.38	-15.10
14		
15	-7.08	-13.99
16	-6.86	-13.09
17	-7.50	-14.94
18	-6.16	-16.01
19	-7.38	-15.90
20	-6.96	-16.30
21	-8.10	-16.27
22	-7.06	-16.35
23	-6.20	-16.48
24	-5.70	-15.66
25		
26	-5.13	-14.49
27	-6.29	-15.48
28	-6.41	-14.94
29	-7.17	-14.90
30	-6.96	-14.63
31		
32	-7.48	-14.82
33	-7.44	-14.57
34	-7.11	-14.27
35	-7.01	-13.88
36	-7.58	-14.15
37	-6.89	-13.56
38	-7.35	-14.23
39	-7.46	-13.86
40	-6.85	-13.43
41	-6.36	-13.05
42	-6.57	-12.92
43	-6.68	-12.81
44	-7.08	-13.04
45	-7.27	-13.17
46	-6.98	-13.19
47	-6.15	-13.03
48	-6.53	-13.21
49	-6.54	-13.01
50	-6.27	-12.95
51	-6.43	-13.40
52	-6.28	-12.85
53	-7.11	-13.21
54	-6.36	-13.29
55	-5.83	-13.26
56	-7.10	-13.08
57	-6.85	-13.37
58	-7.37	-13.70
59	-7.20	-13.50
60	-6.94	-13.81
61	-5.84	-13.29
62	-5.88	-13.42
63	-5.97	-13.74
64	-5.75	-13.40
65	-6.57	-13.95
66	-6.04	-14.25
67	-6.21	-14.04
68	-5.66	-13.86
69	-6.74	-13.70
70	-6.96	-14.47
71	-7.41	-14.00
72	-7.87	-14.48
73	-6.48	-13.87
74	-6.66	-13.76
75	-7.18	-13.37
76	-6.71	-13.54
77	-7.52	-13.13
78	-7.31	-13.13
79	-7.96	-13.67
80	-7.30	-13.18
81	-5.63	-12.99

Data table VII: stalagmite HUA-7

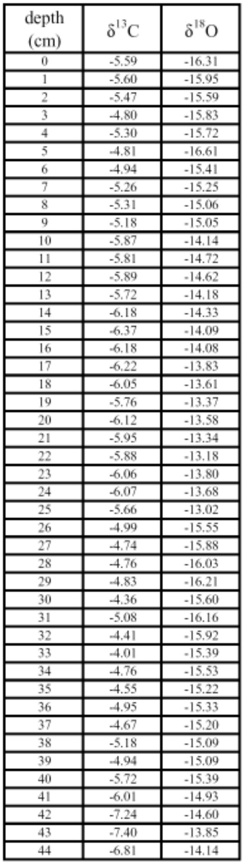

depth (cm)	$\delta^{13}C$	$\delta^{18}O$
0	-5.59	-16.31
1	-5.60	-15.95
2	-5.47	-15.59
3	-4.80	-15.83
4	-5.30	-15.72
5	-4.81	-16.61
6	-4.94	-15.41
7	-5.26	-15.25
8	-5.31	-15.06
9	-5.18	-15.05
10	-5.87	-14.14
11	-5.81	-14.72
12	-5.89	-14.62
13	-5.72	-14.18
14	-6.18	-14.33
15	-6.37	-14.09
16	-6.18	-14.08
17	-6.22	-13.83
18	-6.05	-13.61
19	-5.76	-13.37
20	-6.12	-13.58
21	-5.95	-13.34
22	-5.88	-13.18
23	-6.06	-13.80
24	-6.07	-13.68
25	-5.66	-13.02
26	-4.99	-15.55
27	-4.74	-15.88
28	-4.76	-16.03
29	-4.83	-16.21
30	-4.36	-15.60
31	-5.08	-16.16
32	-4.41	-15.92
33	-4.01	-15.39
34	-4.76	-15.53
35	-4.55	-15.22
36	-4.95	-15.33
37	-4.67	-15.20
38	-5.18	-15.09
39	-4.94	-15.09
40	-5.72	-15.39
41	-6.01	-14.93
42	-7.24	-14.60
43	-7.40	-13.85
44	-6.81	-14.14

Data table VIII: stalagmite HUA-8

depth (mm)	age (yr, BP)	$\delta^{13}C$	$\delta^{18}O$	Ba (ppm)	Mg (ppm)	Sr (ppm)
0	0			39	2475	573
1	15	-4.97	-12.42			
2	30	-5.95	-13.17	31	1914	605
3	45	-5.85	-12.96			
4	61	-5.81	-12.94	27	1861	473
5	76	-5.93	-12.82			
6	91	-6.04	-13.23	19	1891	498
7	106	-6.18	-12.90			
8	121	-6.40	-13.52	18	1871	486
9	136	-6.32	-13.32			
10	151	-5.95	-13.25	18	1805	501
11	166	-6.11	-13.65			
12	182	-6.46	-13.12	18	1811	500
13	197	-5.99	-13.74			
14	212	-5.83	-13.44	18	1849	488
15	227	-5.88	-13.61			
16	242	-5.77	-13.52	17	1829	476
17	257	-5.75	-13.05			
18	272	-5.78	-13.34	18	1856	516
19	286	-5.66	-13.12			
20	301	-5.83	-13.30	16	1776	511
21	316	-6.26	-13.33			
22	331	-6.30	-12.60	15	1735	481
23	346	-5.94	-12.95			
24	361	-5.89	-13.24	17	1704	545
25	376	-6.06	-13.17			
26	390	-5.87	-13.28	20	1741	586
27	405	-5.68	-12.90			
28	420	-5.99	-13.21	21	1655	621
29	435	-6.01	-13.42			
30	450	-5.47	-13.12	18	1842	569
31	465	-5.64	-13.10			
32	480	-5.60	-13.14	20	1742	554
33	494	-5.68	-13.18			
34	509	-5.93	-13.20	18	1637	548
35	524	-5.82	-13.31			
36	539	-5.79	-13.19	17	1630	597
37	554	-5.92	-13.29			
38	569	-5.87	-13.38	21	1567	624
39	584	-6.00	-13.13			
40	598	-6.14	-13.50	23	1611	632
41	613	-6.02	-13.52			
42	628	-6.14	-13.56	22	1550	594
43	643	-6.21	-13.57			
44	658	-6.05	-13.31	18	1515	556
45	673	-5.92	-13.48			
46	687	-6.15	-13.48	20	1545	599
47	702	-6.09	-13.29			
48	717	-5.99	-13.20	18	1471	556
49	732	-6.02	-13.26			
50	747	-5.84	-13.17	18	1528	543
51	762	-5.53	-13.11			
52	777	-5.44	-12.87	16	1601	519
53	791	-5.53	-13.00			
54	806	-5.66	-13.05	19	1660	569
55	821	-5.76	-13.15			
56	836	-5.79	-13.05	19	1688	571
57	851	-5.62	-13.15			
58	866	-5.46	-13.07	20	1780	620
59	881	-5.66	-13.34			
60	895	-5.77	-13.29	21	1604	577
61	910	-5.95	-13.34			
62	925	-5.81	-13.36	17	1563	508
63	940	-5.61	-13.31			
64	955	-5.65	-13.24	16	1599	483
65	970	-5.41	-13.18			
66	985	-5.28	-13.06	18	1593	532
67	999	-5.24	-13.10			
68	1014	-5.16	-12.92	19	1493	515
69	1029	-5.51	-13.18			

depth (cm)	$\delta^{13}C$	$\delta^{18}O$
0	-4.68	-12.58
1	-6.29	-13.44
2	-5.77	-13.35
3	-5.58	-13.33
4	-6.22	-13.64
5	-5.97	-13.31
6	-5.34	-13.15
7	-5.40	-13.23
8	-4.72	-12.79
9	-4.67	-12.73
10	-5.43	-13.01
11	-5.73	-13.23
12	-5.69	-13.39
13	-5.41	-13.17
14	-5.85	-13.29
15	-4.90	-13.14
16	-6.26	-13.77
17	-5.24	-13.25
18	-5.15	-13.06
19	-5.84	-13.43
20	-5.38	-13.16
21	-5.36	-13.35
22	-5.72	-13.32
23	-5.29	-13.11
24	-4.22	-12.70
25	-4.89	-13.07
26	-4.99	-13.03
27	-5.36	-13.18
28	-5.23	-13.07
29	-5.11	-12.68
30	-5.30	-12.85
31	-5.40	-12.81
32	-5.44	-12.84
33	-5.54	-13.15
34	-4.98	-12.66
35	-5.04	-12.72

Data table VIII: stalagmite HUA-8

depth (mm)	age (yr, BP)	$\delta^{13}C$	$\delta^{18}O$	Ba (ppm)	Mg (ppm)	Sr (ppm)
70	1044	-5.29	-13.06	19	1683	546
71	1058	-5.02	-13.01			
72	1072	-4.68	-12.80	21	1865	561
73	1086	-4.75	-13.03			
74	1100	-4.66	-13.01	21	1852	569
75	1114	-4.72	-12.58			
76	1127	-4.75	-12.84	18	1950	484
77	1141	-4.35	-12.75			
78	1155	-4.45	-12.54	19	2061	507
79	1169	-4.89	-12.97			
80	1183	-4.60	-12.71	17	2011	493
81	1197	-4.60	-11.95			
82	1211	-5.19	-12.63	17	1656	502
83	1225	-4.88	-11.95			
84	1239			25	1881	632
85	1253	-4.67	-12.60			
86	1267	-4.98	-12.59	21	1934	577
87	1281	-5.39	-12.82			
88	1294	-5.29	-12.64	16	1832	499
89	1308	-5.35	-12.89			
90	1322	-4.82	-12.64	18	2043	540
91	1336	-5.23	-12.80			
92	1350	-5.33	-12.72	17	1815	555
93	1364	-5.27	-12.64			
94	1378	-5.35	-12.78	17	1813	545
95	1392	-5.04	-12.38			
96	1406	-5.32	-12.85	21	1876	599
97	1420	-5.42	-12.90			
98	1434	-5.45	-12.90	19	1844	583
99	1447	-5.32	-13.02			
100	1461	-5.44	-12.87	21	1851	635
101	1475	-5.36	-12.94			
102	1489	-5.29	-12.86	20	1870	621
103	1503	-5.08	-12.64			
104	1517	-5.52	-12.75	22	1876	569
105	1531	-5.28	-12.90			
106	1545	-5.44	-13.10	21	1923	602
107	1559	-5.31	-13.46			
108	1573	-5.71	-13.39	19	1781	596
109	1587	-5.56	-13.35			
110	1601	-5.77	-13.27	20	1886	596
111	1614	-6.09	-13.35			
112	1628	-5.72	-13.01	19	1798	583
113	1642	-5.65	-13.12			
114	1656	-5.89	-13.23	18	1731	534
115	1670	-5.69	-13.32			
116	1684	-5.57	-13.07	20	1710	592
117	1698	-5.75	-13.26			
118	1712	-5.65	-13.22	20	1790	553
119	1726	-5.48	-13.29			
120	1740	-5.74	-13.30	21	1651	601
121	1754	-5.73	-13.37			
122	1767	-6.09	-13.37	19	1579	550
123	1781	-5.97	-13.33			
124	1795	-5.42	-13.13	22	1714	589
125	1809	-5.65	-13.29			
126	1823	-5.51	-13.16	24	1659	631
127	1837	-5.46	-13.10			
128	1851	-4.96	-12.93	24	1828	611
129	1865	-4.53	-12.85			
130	1879	-4.96	-13.04	17	1801	562
131	1893	-5.73	-13.20			
132	1907	-5.72	-13.22	18	1629	561
133	1920	-5.64	-13.27			
134	1934	-5.85	-13.40	21	1705	598
135	1948	-6.29	-13.54			
136	1962	-5.97	-13.22	18	1650	548
137	1976	-5.82	-13.23			
138	1990	-5.87	-13.11	20	1664	515
139	2004	-6.23	-13.51			

Data table VIII: stalagmite HUA-8

depth (mm)	age (yr, BP)	$\delta^{13}C$	$\delta^{18}O$	Ba (ppm)	Mg (ppm)	Sr (ppm)
140	2018	-5.85	-13.27	20	1717	583
141	2032	-5.29	-12.95			
142	2046	-5.24	-13.15	21	1942	606
143	2060	-5.32	-13.24			
144	2074	-5.72	-13.27	19	1742	571
145	2087	-6.06	-13.53			
146	2101	-5.45	-13.16	30	1731	586
147	2115	-5.12	-13.07			
148	2129	-5.77	-13.43	19	1711	552
149	2143	-5.67	-13.45			
150	2157	-5.00	-13.22	21	1954	565
151	2169	-5.80	-13.41			
152	2181	-6.07	-13.69	17	1681	514
153	2192	-6.20	-13.83			
154	2204	-5.98	-13.49	20	1606	512
155	2216	-6.12	-13.66			
156	2228			19	1654	486
157	2240	-6.10	-13.71			
158	2252	-6.16	-13.70	17	1483	496
159	2263	-6.23	-13.81			
160	2275	-6.20	-13.70	17	1526	483
161	2287	-6.14	-13.77			
162	2299	-5.74	-13.65	17	1477	471
163	2311	-5.95	-13.67			
164	2322	-6.16	-13.66	16	1524	502
165	2334	-5.73	-13.74			
166	2346	-5.67	-13.46	18	1740	525
167	2358	-5.64	-13.49			
168	2370	-5.98	-13.46	16	1696	519
169	2381	-5.79	-13.59			
170	2393	-5.36	-13.16	18	1743	521
171	2405	-4.96	-13.26			
172	2417	-4.59	-12.88	20	1876	557
173	2429	-4.63	-12.50			
174	2441	-4.75	-13.02	20	2043	574
175	2452	-5.44	-13.17			
176	2464	-5.44	-12.94	22	1772	554
177	2476	-5.68	-13.20			
178	2488	-5.76	-12.89	20	1730	602
179	2500	-5.19	-12.65			
180	2511	-5.13	-12.93	21	1761	609
181	2523	-5.47	-13.25			
182	2535	-5.66	-13.16	19	1637	590
183	2547	-5.69	-13.33			
184	2559	-5.30	-12.96	18	1752	572
185	2571	-5.41	-13.30			
186	2582	-5.45	-13.17	21	1735	608
187	2594	-5.55	-13.37			
188	2606			22	1757	634
189	2618	-5.38	-13.27			
190	2630	-5.73	-12.26	19	1739	690
191	2641	-5.84	-13.52			
192	2653	-5.75	-13.22	22	1719	606
193	2665	-5.90	-13.65			
194	2677	-5.63	-13.15	21	1731	604
195	2689	-5.54	-13.12			
196	2700	-5.44	-13.14	20	1729	578
197	2712	-5.44	-13.16			
198	2724	-5.60	-13.23	20	1734	596
199	2736	-5.60	-13.24			
200	2748	-5.46	-13.20	22	1800	651
201	2760	-5.29	-13.27			
202	2771	-5.86	-12.76	23	1725	
203	2783	-5.40	-13.07			
204	2795	-5.20	-13.25	22	1770	689
205	2807	-5.88	-13.40			
206	2819	-5.93	-12.79	24	1614	778
207	2830	-5.69	-13.45			
208	2842	-5.64	-13.36	23	1600	762
209	2854	-5.43	-13.30			
210	2866	-5.41	-13.14	23	1788	737

Data table VIII: stalagmite HUA-8

depth (mm)	age (yr, BP)	$\delta^{13}C$	$\delta^{18}O$	Ba (ppm)	Mg (ppm)	Sr (ppm)
211	2878	-5.50	-13.12			
212	2889	-5.48	-13.22	25	1724	756
213	2901	-5.14	-13.00			
214	2913	-5.42	-13.16	20	1653	638
215	2925	-5.75	-13.23			
216	2937	-5.64	-13.28	23	1570	711
217	2949	-5.50	-12.97			
218	2960	-5.43	-13.25	23	1650	747
219	2972	-5.57	-12.89			
220	2984	-5.75	-13.09	22	1642	675
221	2997	-5.87	-14.51			
222	3010	-5.77	-13.43	21	1655	609
223	3023	-5.83	-14.17			
224	3036	-5.28	-13.35	18	1718	563
225	3049	-5.80	-13.53			
226	3062	-6.03	-13.33	19	1578	520
227	3075	-5.19	-13.18			
228	3088	-5.65	-13.37	22	1570	665
229	3101	-4.93	-13.21			
230	3114	-5.39	-13.31	23	1755	633
231	3127	-5.37	-13.20			
232	3140	-5.46	-13.39	19	1676	631
233	3153	-5.60	-13.08			
234	3166	-5.58	-13.08	19	1658	637
235	3179	-5.04	-12.61			
236	3192	-5.12	-12.87	23	1669	712
237	3205	-5.54	-12.88			
238	3218	-5.17	-13.07	24	1772	725
239	3231	-4.45	-12.57			
240	3244	-4.21	-12.72	28	2060	800
241	3257	-4.61	-12.62			
242	3270	-4.93	-13.13	24	1803	743
243	3283	-5.25	-12.96			
244	3296	-5.10	-13.04	23	1762	691
245	3309	-5.49	-12.99			
246	3322	-5.69	-13.30	21	1632	674
247	3335	-5.41	-12.99			
248	3347			21	1771	652
249	3360	-4.90	-12.83			
250	3373	-4.77	-13.01	20	1855	636
251	3386	-4.90	-12.85			
252	3399	-5.05	-12.78	22	1841	682
253	3412	-5.01	-12.89			
254	3425	-5.19	-13.19	25	1776	694
255	3438	-5.39	-12.68			
256	3451	-5.00	-12.64	21	1667	708
257	3464	-5.47	-12.98			
258	3477	-5.42	-13.15	21	1625	695
259	3490	-5.33	-13.01			
260	3503			23	1720	746
261	3516	-5.13	-13.00			
262	3529	-4.97	-12.83	25	1782	743
263	3542	-5.22	-13.04			
264	3555	-5.27	-13.06	26	1665	767
265	3568	-5.11	-12.91			
266	3581	-5.19	-13.18	27	1743	790
267	3594	-5.17	-12.86			
268	3607	-5.05	-13.03	26	1679	737
269	3620	-4.96	-12.62			
270	3633	-4.98	-12.47	24	1708	708
271	3646	-5.32	-12.96			
272	3659	-5.12	-12.61	25	1714	742
273	3672	-5.36	-12.99			
274	3685	-4.84	-12.44	21	1774	659
275	3698	-4.72	-12.70			
276	3708	-4.86	-12.64	24	1775	714
277	3718	-5.40	-12.88			
278	3727	-5.04	-12.51	21	1677	652
279	3737	-5.41	-13.10			
280	3747	-5.06	-12.66	23	1689	694
281	3757	-5.26	-13.13			

Data table VIII: stalagmite HUA-8

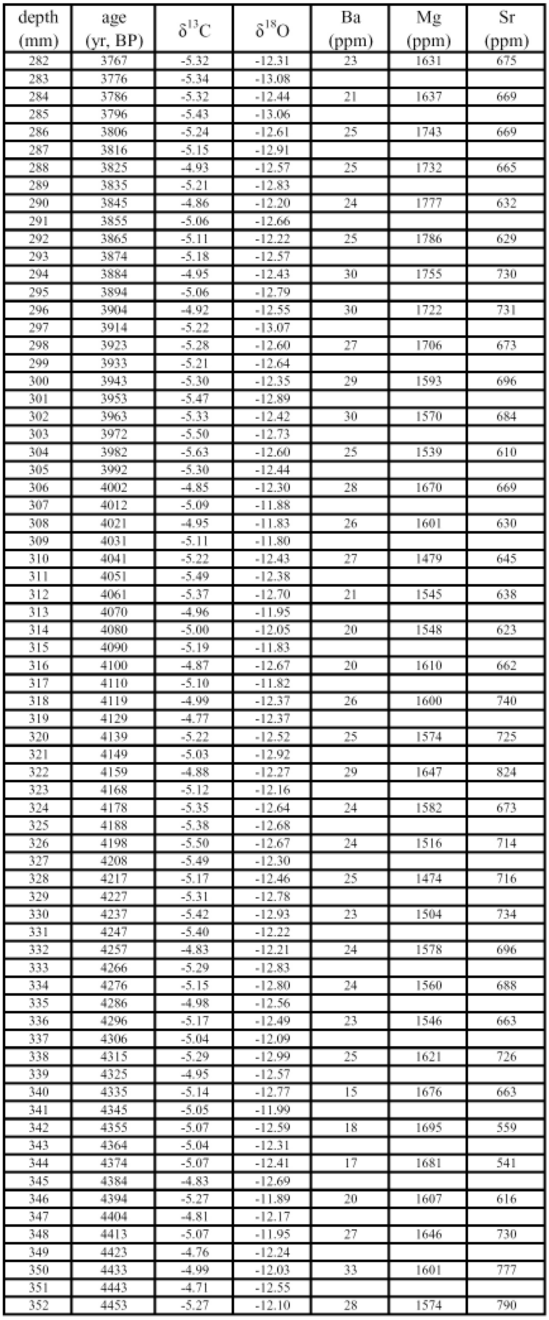

depth (mm)	age (yr, BP)	$\delta^{13}C$	$\delta^{18}O$	Ba (ppm)	Mg (ppm)	Sr (ppm)
282	3767	-5.32	-12.31	23	1631	675
283	3776	-5.34	-13.08			
284	3786	-5.32	-12.44	21	1637	669
285	3796	-5.43	-13.06			
286	3806	-5.24	-12.61	25	1743	669
287	3816	-5.15	-12.91			
288	3825	-4.93	-12.57	25	1732	665
289	3835	-5.21	-12.83			
290	3845	-4.86	-12.20	24	1777	632
291	3855	-5.06	-12.66			
292	3865	-5.11	-12.22	25	1786	629
293	3874	-5.18	-12.57			
294	3884	-4.95	-12.43	30	1755	730
295	3894	-5.06	-12.79			
296	3904	-4.92	-12.55	30	1722	731
297	3914	-5.22	-13.07			
298	3923	-5.28	-12.60	27	1706	673
299	3933	-5.21	-12.64			
300	3943	-5.30	-12.35	29	1593	696
301	3953	-5.47	-12.89			
302	3963	-5.33	-12.42	30	1570	684
303	3972	-5.50	-12.73			
304	3982	-5.63	-12.60	25	1539	610
305	3992	-5.30	-12.44			
306	4002	-4.85	-12.30	28	1670	669
307	4012	-5.09	-11.88			
308	4021	-4.95	-11.83	26	1601	630
309	4031	-5.11	-11.80			
310	4041	-5.22	-12.43	27	1479	645
311	4051	-5.49	-12.38			
312	4061	-5.37	-12.70	21	1545	638
313	4070	-4.96	-11.95			
314	4080	-5.00	-12.05	20	1548	623
315	4090	-5.19	-11.83			
316	4100	-4.87	-12.67	20	1610	662
317	4110	-5.10	-11.82			
318	4119	-4.99	-12.37	26	1600	740
319	4129	-4.77	-12.37			
320	4139	-5.22	-12.52	25	1574	725
321	4149	-5.03	-12.92			
322	4159	-4.88	-12.27	29	1647	824
323	4168	-5.12	-12.16			
324	4178	-5.35	-12.64	24	1582	673
325	4188	-5.38	-12.68			
326	4198	-5.50	-12.67	24	1516	714
327	4208	-5.49	-12.30			
328	4217	-5.17	-12.46	25	1474	716
329	4227	-5.31	-12.78			
330	4237	-5.42	-12.93	23	1504	734
331	4247	-5.40	-12.22			
332	4257	-4.83	-12.21	24	1578	696
333	4266	-5.29	-12.83			
334	4276	-5.15	-12.80	24	1560	688
335	4286	-4.98	-12.56			
336	4296	-5.17	-12.49	23	1546	663
337	4306	-5.04	-12.09			
338	4315	-5.29	-12.99	25	1621	726
339	4325	-4.95	-12.57			
340	4335	-5.14	-12.77	15	1676	663
341	4345	-5.05	-11.99			
342	4355	-5.07	-12.59	18	1695	559
343	4364	-5.04	-12.31			
344	4374	-5.07	-12.41	17	1681	541
345	4384	-4.83	-12.69			
346	4394	-5.27	-11.89	20	1607	616
347	4404	-4.81	-12.17			
348	4413	-5.07	-11.95	27	1646	730
349	4423	-4.76	-12.24			
350	4433	-4.99	-12.03	33	1601	777
351	4443	-4.71	-12.55			
352	4453	-5.27	-12.10	28	1574	790

Data table VIII: stalagmite HUA-8

depth (mm)	age (yr, BP)	$\delta^{13}C$	$\delta^{18}O$	Ba (ppm)	Mg (ppm)	Sr (ppm)
353	4462	-5.07	-12.68			
354	4472	-5.29	-11.74	26	1575	755
355	4482	-4.92	-12.40			

Data table IX: stalagmite NC-A

depth (mm)	age (yr, BP)	$\delta^{13}C$	$\delta^{18}O$	Ba (ppm)	Mg (ppm)	Sr (ppm)
1	12			0.4	555	54
2	24	-12.52	-7.19			
3	35				505	55
4	47					
5	59				472	57
6	71	-12.30	-7.39			
7	83				532	47
8	94	-12.21	-6.87			
9	106			0.5	522	41
10	118	-12.22	-6.74			
11	130			1.9	453	75
12	142	-11.86	-6.62			
13	153				509	66
14	165	-12.02	-7.27			
15	177				557	63
16	189	-12.07	-6.74			
17	200				522	61
18	212	-12.20	-7.06			
19	224				548	60
20	236	-11.89	-6.66			
21	248				560	64
22	259	-11.57	-7.08			
23	265				606	49
24	272	-11.78	-6.91			
25	277				618	56
26	282	-11.49	-6.26			
27	288	-10.82	-7.72	0.9	632	71
28	292	-10.94	-7.02			
29	296	-11.13	-6.86	0.8	626	73
30	300	-11.27	-7.22			
31	304	-11.17	-7.45	0.4	594	64
32	309	-11.19	-7.13			
33	314	-10.83	-7.51	1.0	666	63
34	321	-11.32	-7.66			
35	336				609	65
36	364	-10.84	-7.50			
37	411	-10.83	-7.28		648	69
38	452	-10.81	-6.98			
39	494	-9.77	-6.39		727	62
40	547	-10.66	-7.00			
41	588				831	46
42	627	-10.41	-6.81			
43	673	-10.62	-7.25	9.9	1012	83
44	711	-10.09	-6.72			
45	755	-10.58	-6.98	7.9	1118	81
46	792	-10.56	-7.13			
47	828	-10.71	-7.09	11.4	920	103
48	870	-10.77	-7.55			
49	907	-9.36	-7.68	14.4	1122	70
50	951	-10.15	-7.51			
51	988	-9.09	-7.01	7.6	820	45
52	1026	-9.75	-7.04			
53	1075	-9.39	-7.24	7.3	868	73
54	1116	-9.72	-6.78			
55	1159	-10.28	-7.20	6.0	784	90
56	1210	-10.05	-7.23			
57	1251	-10.68	-6.73	8.4	910	87
58	1293	-10.42	-7.05			
59	1316	-10.10	-7.01	5.9	915	80
60	1332	-10.58	-6.95			
61	1349	-9.43	-7.32	7.9	887	56
62	1362	-9.69	-7.02			
63	1376	-10.15	-7.14	6.8	786	85
64	1388	-9.68	-6.62			
65	1400	-11.10	-8.03	8.8	764	86
66	1414	-11.06	-7.60			
67	1425	-11.61	-7.74	9.1	877	79
68	1437	-11.05	-7.50			
69	1453	-11.00	-7.53	5.9	986	87
70	1465	-11.38	-7.84			

depth (cm)	$\delta^{13}C$	$\delta^{18}O$
0	-12.55	-6.88
0.5	-12.47	-6.75
1	-11.93	-6.52
1.5	-12.06	-7.19
2	-11.70	-7.08
2.5	-11.65	-6.67
3	-11.16	-7.15
3.5	-10.84	-7.66
4	-10.45	-6.87
4.5	-10.81	-6.92
5	-9.71	-7.31
5.5	-9.81	-7.49
6	-10.84	-7.04
6.5	-10.17	-6.88
7	-11.19	-7.90
7.5	-10.60	-6.83
8	-11.27	-6.99
8.5	-11.14	-7.13
9	-10.97	-6.85
9.5	-10.90	-6.97
10	-10.35	-7.53
10.5	-11.04	-7.58
11	-11.22	-7.42
11.5	-11.06	-7.43
12	-10.90	-7.29
12.5	-11.53	-6.84
13	-11.33	-7.66
13.5	-11.40	-6.76
14	-11.49	-6.95
14.5	-11.44	-7.68
15	-11.39	-7.81
15.5	-10.98	-7.49
16	-11.38	-6.72
16.5	-9.82	-8.27
17	-9.50	-6.22
17.5	-11.35	-7.18
18	-10.85	-7.44
18.5	-10.81	-7.21
19	-11.03	-7.28
19.5	-10.92	-7.94
20	-11.18	-7.54
20.5	-11.14	-7.18
21	-10.95	-7.04
21.5	-11.11	-8.62
22	-11.35	-7.55
22.5	-11.08	-7.70
23	-11.04	-7.16
23.5	-10.88	-7.14
24	-11.03	-7.69
24.5	-10.64	-6.84
25	-10.69	-7.05
25.5	-10.48	-8.07
26	-10.66	-7.22
26.5	-10.68	-7.09
27	-10.42	-7.26
27.5	-11.08	-7.25
28	-10.52	-6.95
28.5	-9.98	-6.56
29	-10.86	-7.01
29.5	-11.15	-6.84
30	-11.39	-6.93
30.5	-10.31	-7.13
31	-11.41	-7.26

Data table IX: stalagmite NC-A

depth (mm)	age (yr, BP)	$\delta^{13}C$	$\delta^{18}O$	Ba (ppm)	Mg (ppm)	Sr (ppm)
71	1481	-10.79	-6.94	3.8	1026	51
72	1495	-11.75	-7.58			
73	1509	-10.66	-7.48	5.0	980	62
74	1525	-10.08	-6.40			
75	1539	-10.68	-7.05	4.7	1016	69
76	1554	-10.81	-6.71			
77	1567	-11.07	-7.18	5.5	796	84
78	1579	-11.22	-6.77			
79	1593			5.2	746	77
80	1605	-11.27	-6.84			
81	1615	-11.05	-6.94	1.5	1034	75
82	1629	-10.86	-6.89			
83	1640			2.1	910	76
84	1653	-11.76	-7.09			
85	1664	-10.96	-6.90	2.3	878	85
86	1674	-11.94	-6.51			
87	1687	-11.40	-8.46	1.0	897	77
88	1697	-11.52	-7.24			
89	1710	-11.09	-6.97	1.3	984	72
90	1720	-10.84	-6.63			
91	1731	-10.73	-6.89	1.2	982	82
92	1743	-11.21	-6.94			
93	1753	-10.79	-7.03	2.1	961	87
94	1763	-10.96	-6.89			
95	1775	-10.24	-7.52	1.9	1002	82
96	1785	-10.36	-6.58			
97	1798	-10.55	-6.66	1.5	1044	80
98	1809	-10.75	-6.49			
99	1820	-10.69	-6.94	2.5	1055	89
100	1833	-10.55	-7.23			
101	1844	-10.63	-6.92	1.6	1047	86
102	1858	-10.73	-6.85			
103	1869	-10.80	-6.66	4.9	1064	82
104	1880	-10.80	-6.70			
105	1895	-10.35	-7.19	2.7	885	94
106	1908	-11.21	-7.67			
107	1921	-10.55	-7.02	1.5	1071	83
108	1939	-11.28	-6.97			
109	1955			2.2	946	85
110	1974	-11.06	-7.23			
111	1990	-10.88	-7.28	1.5	910	89
112	2005	-10.96	-7.04			
113	2021	-10.58	-7.32	2.4	905	91
114	2034	-10.88	-7.36			
115	2050	-11.25	-7.30	3.8	688	97
116	2061	-10.94	-7.44			
117	2072	-10.50	-7.34	2.3	819	93
118	2086	-11.03	-7.12			
119	2096	-10.80	-7.29	2.2	841	86
120	2106	-11.05	-7.24			
121	2119	-11.17	-7.24	2.3	637	79
122	2129	-11.10	-7.57			
123	2141	-10.73	-7.44	3.5	809	95
124	2151	-10.79	-6.92			
125	2161	-11.09	-6.67	2.1	747	81
126	2173	-11.15	-7.00			
127	2183	-11.04	-7.12	2.3	762	81
128	2195	-10.94	-7.11			
129	2204	-11.13	-7.39	2.3	752	81
130	2213	-11.21	-7.78			
131	2225	-10.65	-6.98	2.9	852	88
132	2234	-10.93	-6.95			
133	2243	-10.67	-6.75	1.6	778	85
134	2255	-11.12	-6.76			
135	2264	-10.65	-6.50	2.8	723	91
136	2275	-10.98	-6.86			
137	2285	-10.83	-6.84	2.4	683	86
138	2295	-11.01	-7.00			
139	2307	-10.94	-6.77	2.7	698	86
140	2317	-11.43	-7.32			

Data table IX: stalagmite NC-A

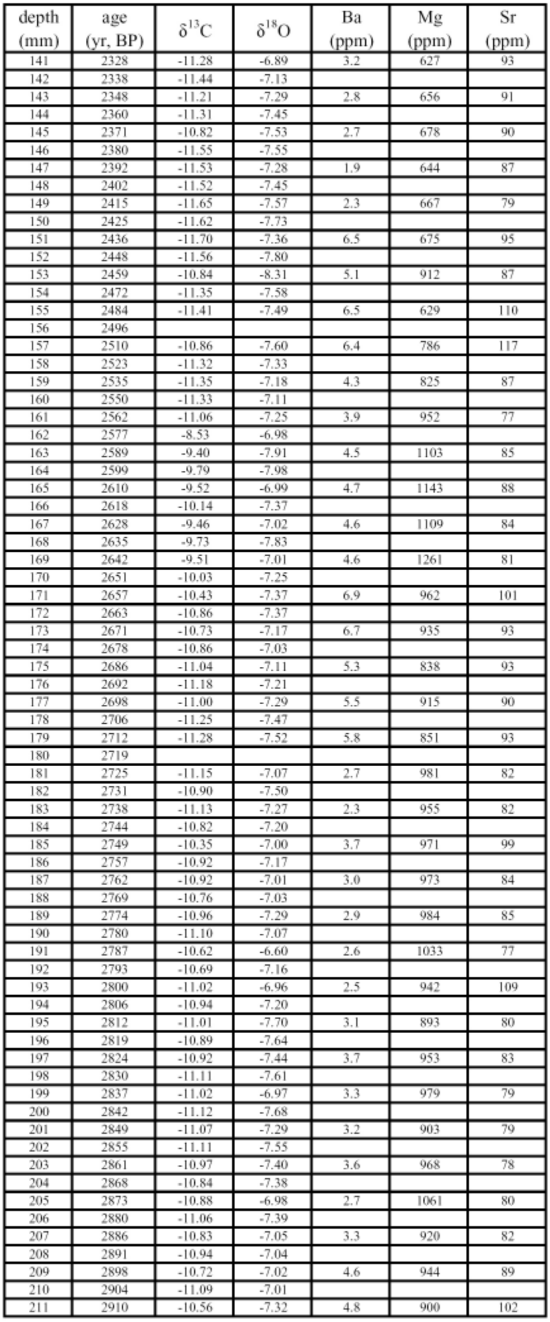

depth (mm)	age (yr, BP)	$\delta^{13}C$	$\delta^{18}O$	Ba (ppm)	Mg (ppm)	Sr (ppm)
141	2328	-11.28	-6.89	3.2	627	93
142	2338	-11.44	-7.13			
143	2348	-11.21	-7.29	2.8	656	91
144	2360	-11.31	-7.45			
145	2371	-10.82	-7.53	2.7	678	90
146	2380	-11.55	-7.55			
147	2392	-11.53	-7.28	1.9	644	87
148	2402	-11.52	-7.45			
149	2415	-11.65	-7.57	2.3	667	79
150	2425	-11.62	-7.73			
151	2436	-11.70	-7.36	6.5	675	95
152	2448	-11.56	-7.80			
153	2459	-10.84	-8.31	5.1	912	87
154	2472	-11.35	-7.58			
155	2484	-11.41	-7.49	6.5	629	110
156	2496					
157	2510	-10.86	-7.60	6.4	786	117
158	2523	-11.32	-7.33			
159	2535	-11.35	-7.18	4.3	825	87
160	2550	-11.33	-7.11			
161	2562	-11.06	-7.25	3.9	952	77
162	2577	-8.53	-6.98			
163	2589	-9.40	-7.91	4.5	1103	85
164	2599	-9.79	-7.98			
165	2610	-9.52	-6.99	4.7	1143	88
166	2618	-10.14	-7.37			
167	2628	-9.46	-7.02	4.6	1109	84
168	2635	-9.73	-7.83			
169	2642	-9.51	-7.01	4.6	1261	81
170	2651	-10.03	-7.25			
171	2657	-10.43	-7.37	6.9	962	101
172	2663	-10.86	-7.37			
173	2671	-10.73	-7.17	6.7	935	93
174	2678	-10.86	-7.03			
175	2686	-11.04	-7.11	5.3	838	93
176	2692	-11.18	-7.21			
177	2698	-11.00	-7.29	5.5	915	90
178	2706	-11.25	-7.47			
179	2712	-11.28	-7.52	5.8	851	93
180	2719					
181	2725	-11.15	-7.07	2.7	981	82
182	2731	-10.90	-7.50			
183	2738	-11.13	-7.27	2.3	955	82
184	2744	-10.82	-7.20			
185	2749	-10.35	-7.00	3.7	971	99
186	2757	-10.92	-7.17			
187	2762	-10.92	-7.01	3.0	973	84
188	2769	-10.76	-7.03			
189	2774	-10.96	-7.29	2.9	984	85
190	2780	-11.10	-7.07			
191	2787	-10.62	-6.60	2.6	1033	77
192	2793	-10.69	-7.16			
193	2800	-11.02	-6.96	2.5	942	109
194	2806	-10.94	-7.20			
195	2812	-11.01	-7.70	3.1	893	80
196	2819	-10.89	-7.64			
197	2824	-10.92	-7.44	3.7	953	83
198	2830	-11.11	-7.61			
199	2837	-11.02	-6.97	3.3	979	79
200	2842	-11.12	-7.68			
201	2849	-11.07	-7.29	3.2	903	79
202	2855	-11.11	-7.55			
203	2861	-10.97	-7.40	3.6	968	78
204	2868	-10.84	-7.38			
205	2873	-10.88	-6.98	2.7	1061	80
206	2880	-11.06	-7.39			
207	2886	-10.83	-7.05	3.3	920	82
208	2891	-10.94	-7.04			
209	2898	-10.72	-7.02	4.6	944	89
210	2904	-11.09	-7.01			
211	2910	-10.56	-7.32	4.8	900	102

Data table IX: stalagmite NC-A

depth (mm)	age (yr, BP)	$\delta^{13}C$	$\delta^{18}O$	Ba (ppm)	Mg (ppm)	Sr (ppm)
212	2917	-11.06	-7.56			
213	2923	-10.74	-7.62	6.3	985	95
214	2930	-10.75	-7.74			
215	2936	-10.89	-8.27	4.2	1052	94
216	2942	-10.83	-7.91			
217	2950	-10.48	-7.39	4.9	978	108
218	2956	-10.77	-7.62			
219	2964	-10.84	-7.58	3.5	890	98
220	2970	-11.49	-7.50			
221	2977	-11.18	-7.52	2.6	1076	96
222	2985	-10.96	-7.41			
223	2992	-10.79	-7.51	3.5	1110	98
224	2999	-10.81	-7.40			
225	3007	-10.64	-7.88	11.7	1141	106
226	3015	-11.03	-7.26			
227	3025	-10.66	-7.37			
228	3033	-11.00	-6.84			
229	3041	-10.64	-6.92	14.4	1178	98
230	3052	-10.94	-7.30			
231	3061	-10.67	-7.18	11.4	1045	94
232	3073	-10.91	-7.11			
233	3086	-10.67	-7.19	17.0	1232	96
234	3110	-10.68	-7.06			
235	3143	-10.58	-7.01	12.4	1122	101
236	3172	-11.18	-7.16			
237	3200	-10.84	-7.56	13.1	1033	118
238	3233	-10.98	-7.47			
239	3260	-10.58	-7.23	10.5	1032	86
240	3293	-11.03	-7.82			
241	3320	-10.27	-7.63	11.8	1107	94
242	3346	-10.97	-7.12			
243	3376	-9.85	-7.12	10.3	1076	89
244	3403	-10.33	-7.08			
245	3435	-10.23	-7.07	8.0	1015	80
246	3462	-10.24	-7.21			
247	3492	-10.22	-6.61	12.7	1193	89
248	3529	-10.84	-7.37			
249	3562	-10.53	-7.36	8.9	1061	85
250	3594	-11.04	-6.79			
251	3628	-10.88	-6.87	12.7	1096	89
252	3649	-10.66	-7.21			
253	3671	-10.56	-7.32	9.7	962	97
254	3685	-10.80	-7.24			
255	3701	-10.25	-7.82	8.2	953	94
256	3716	-10.49	-7.44			
257	3728	-10.72	-7.45	7.3	819	84
258	3742	-10.93	-6.77			
259	3754	-10.73	-7.09	7.3	963	94
260	3764	-10.79	-7.17			
261	3776	-10.82	-6.64	9.4	1068	88
262	3786	-10.66	-7.25			
263	3797	-10.45	-7.31	6.6	973	87
264	3809	-10.68	-6.92			
265	3818	-10.52	-6.55	6.8	896	91
266	3830	-10.94	-6.81			
267	3839	-10.45	-7.00	7.1	975	93
268	3849	-10.57	-7.27			
269	3860	-10.78	-7.51	8.2	929	97
270	3868	-10.43	-7.00			
271	3880	-10.56	-7.20	7.9	878	91
272	3889	-10.65	-7.42			
273	3899	-10.38	-8.11	7.0	860	100
274	3911	-10.71	-7.62			
275	3920	-10.21	-7.37	7.9	869	104
276	3929	-10.87	-7.33			
277	3941	-10.36	-6.95	7.2	882	99
278	3950	-10.79	-7.17			
279	3960	-10.48	-6.93	6.3	898	94
280	3968	-10.47	-7.20			
281	3976	-10.37	-7.25	15.0	934	101
282	3986	-10.45	-6.75			

Data table IX: stalagmite NC-A

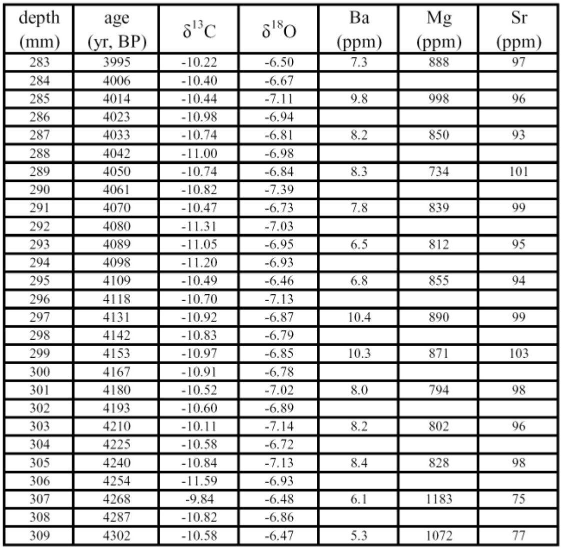

depth (mm)	age (yr, BP)	$\delta^{13}C$	$\delta^{18}O$	Ba (ppm)	Mg (ppm)	Sr (ppm)
283	3995	-10.22	-6.50	7.3	888	97
284	4006	-10.40	-6.67			
285	4014	-10.44	-7.11	9.8	998	96
286	4023	-10.98	-6.94			
287	4033	-10.74	-6.81	8.2	850	93
288	4042	-11.00	-6.98			
289	4050	-10.74	-6.84	8.3	734	101
290	4061	-10.82	-7.39			
291	4070	-10.47	-6.73	7.8	839	99
292	4080	-11.31	-7.03			
293	4089	-11.05	-6.95	6.5	812	95
294	4098	-11.20	-6.93			
295	4109	-10.49	-6.46	6.8	855	94
296	4118	-10.70	-7.13			
297	4131	-10.92	-6.87	10.4	890	99
298	4142	-10.83	-6.79			
299	4153	-10.97	-6.85	10.3	871	103
300	4167	-10.91	-6.78			
301	4180	-10.52	-7.02	8.0	794	98
302	4193	-10.60	-6.89			
303	4210	-10.11	-7.14	8.2	802	96
304	4225	-10.58	-6.72			
305	4240	-10.84	-7.13	8.4	828	98
306	4254	-11.59	-6.93			
307	4268	-9.84	-6.48	6.1	1183	75
308	4287	-10.82	-6.86			
309	4302	-10.58	-6.47	5.3	1072	77

Data table X: stalagmite NC-B

depth (mm)	age (yr, BP)	$\delta^{13}C$	$\delta^{18}O$	Ba (ppm)	Mg (ppm)	Sr (ppm)
0	3236	-7.29	-6.29	3.7	1398	31
1	3276	-10.51	-7.28			
2	3315	-9.82	-6.88	7.4	1661	59
3	3355	-9.17	-6.10			
4	3395	-9.60	-7.15	10.1	1473	74
5	3435	-9.71	-6.82			
6	3475	-8.09	-6.52	5.9	1633	54
7	3515	-10.01	-7.41			
8	3554	-10.27	-7.81	22.8	1070	106
9	3594	-10.84	-7.28			
10	3634	-10.09	-6.98	17.6	1078	100
11	3674	-10.09	-7.02			
12	3714	-10.08	-6.70	17.6	1222	97
13	3753	-9.83	-6.64			
14	3798	-10.23	-7.03	14.8	1327	91
15	3837	-10.45	-6.84			
16	3876	-9.91	-6.78	11.1	1321	76
17	3922	-9.31	-6.59			
18	3959	-10.67	-6.93	7.6	1398	62
19	3994	-11.39	-6.78			
20	4035	-11.06	-7.00	12.0	1209	77
21	4067	-11.05	-6.80			
22	4105	-10.72	-6.78	6.8	1340	58
23	4138	-11.17	-6.99			
24	4170	-11.01	-6.57	7.5	1308	59
25	4209	-10.39	-6.45			
26	4241	-10.87	-6.39	8.7	1239	59
27	4273	-11.17	-6.91			
28	4311	-11.14	-6.82	9.9	1250	69
29	4345	-11.10	-7.17			
30	4381	-11.22	-6.96	8.4	1203	68
31	4428	-11.33	-7.12			
32	4469	-11.40	-7.19	9.8	1237	69
33	4519	-11.07	-7.12			
34	4564	-11.03	-6.96	7.9	1396	62
35	4612	-11.02	-6.92			
36	4667	-11.18	-6.93	8.8	1437	68
37	4710	-10.82	-6.64			
38	4752	-11.05	-6.75	11.9	1649	84
39	4803	-11.22	-6.75			
40	4844	-11.38	-7.06	9.7	1342	74
41	4886	-11.23	-6.74			
42	4937	-11.21	-6.55	8.0	1516	69
43	4980	-10.81	-6.46			
44	5034	-10.66	-6.64	9.6	1626	71
45	5081	-10.96	-6.61			
46	5125	-10.87	-6.42	10.0	1576	73
47	5173	-10.61	-6.38			
48	5212	-11.13	-6.91	12.8	1376	82
49	5253	-11.13	-6.97			
50	5302	-11.06	-6.88	10.2	1439	72
51	5342	-10.81	-6.44			
52	5380	-10.92	-6.80	8.3	1389	64
53	5427	-11.08	-6.64			
54	5464	-10.38	-5.98	6.6	1554	45
55	5499	-11.08	-6.71			
56	5541	-11.13	-6.86	9.4	1608	70
57	5574	-11.19	-6.62			
58	5617	-11.23	-6.97	10.0	1456	72
59	5650	-10.99	-6.89			
60	5684	-11.13	-6.92	10.7	1528	74
61	5724	-10.97	-7.12			
62	5758	-10.92	-6.99	11.2	1585	76
63	5792	-10.78	-6.85			
64	5832	-11.25	-6.91	10.8	1513	73
65	5866	-10.92	-6.64			
66	5900	-11.30	-7.26	12.2	1468	74
67	5942	-11.18	-6.72			
68	5979	-10.97	-6.68	12.3	1492	76
69	6023	-10.81	-6.21			

depth (cm)	$\delta^{13}C$	$\delta^{18}O$
0	-9.80	-7.18
1	-10.01	-7.14
2	-10.89	-6.65
3	-11.51	-6.99
4	-11.21	-6.70
5	-11.39	-6.85
6	-11.10	-6.69
7	-10.95	-6.48
8	-10.14	-6.46
9	-10.95	-6.32
10	-10.64	-6.18
11	-8.59	-5.65
12	-10.56	-5.89
13	-11.23	-6.04
14	-10.95	-6.12
15	-11.02	-5.95
16	-11.34	-6.12
17	-11.07	-5.86
18	-11.20	-5.78
19	-10.75	-5.58
20	-10.36	-5.39
21	-10.20	-5.77
22	-10.37	-5.64
23	-10.69	-6.21
24	-10.96	-5.53
25	-10.87	-5.93
26	-10.07	-5.98
27	-10.94	-5.97

Data table X: stalagmite NC-B

depth (mm)	age (yr, BP)	$\delta^{13}C$	$\delta^{18}O$	Ba (ppm)	Mg (ppm)	Sr (ppm)
70	6059	-10.54	-6.64	9.6	1759	64
71	6097	-10.69	-6.59			
72	6141	-10.48	-6.59	9.4	1560	67
73	6177	-10.45	-6.42			
74	6216	-10.23	-6.36	9.5	1802	71
75	6266	-10.59	-6.56			
76	6310	-10.05	-6.41	9.7	1684	73
77	6352	-9.48	-6.47			
78	6400	-9.85	-6.61	9.1	1665	69
79	6438	-9.78	-6.40			
80	6476	-9.82	-6.49	5.8	1589	66
81	6505	-10.11	-6.62			
82	6534	-10.90	-6.33	38.2	2077	145
83	6566	-10.91	-6.17			
84	6593	-11.32	-6.55	9.1	1241	68
85	6618	-11.18	-6.01			
86	6649	-10.70	-5.87	7.5	1226	63
87	6674	-10.81	-6.13			
88	6699	-11.12	-6.50	9.7	1380	80
89	6728	-10.78	-6.47			
90	6753	-10.43	-6.09	9.6	1357	70
91	6781	-11.09	-6.02			
92	6804	-10.89	-6.07	7.8	1340	63
93	6828	-10.98	-5.96			
94	6857	-10.53	-6.23	7.9	1331	65
95	6879	-10.53	-6.49			
96	6902	-10.62	-6.05	7.9	1329	69
97	6929	-10.41	-6.36			
98	6951	-10.49	-6.17	7.5	1470	62
99	6974	-10.54	-6.27			
100	7001	-10.82	-6.49	8.5	1246	69
101	7023	-10.68	-6.19			
102	7043	-10.72	-6.35	9.1	1240	70
103	7069	-10.70	-6.34			
104	7091	-10.55	-6.34	7.4	1318	59
105	7116	-10.70	-6.38			
106	7137	-10.91	-6.30	8.7	1164	70
107	7159	-10.64	-6.18			
108	7185	-9.59	-5.86	4.6	1492	50
109	7205	-10.58	-6.38			
110	7226	-10.58	-5.89	10.5	1399	73
111	7255	-10.88	-6.26			
112	7277	-10.23	-5.78	7.6	1414	63
113	7298	-10.38	-5.99			
114	7324	-10.64	-6.23	9.6	1403	74
115	7344	-10.30	-6.19			
116	7369	-10.21	-5.91	8.1	1405	66
117	7392	-10.09	-6.01			
118	7414	-10.49	-6.24	6.4	1297	68
119	7442	-10.41	-5.94			
120	7463	-10.24	-5.80	7.2	1436	67
121	7485	-10.29	-6.10			
122	7510	-10.60	-5.74	8.5	1247	77
123	7531	-11.24	-6.05			
124	7552	-10.56	-6.23	15.5	1309	86
125	7576	-10.73	-6.06			
126	7597	-10.31	-5.73	4.4	1173	57
127	7622	-11.20	-6.30			
128	7643	-11.16	-5.73	7.0	1500	65
129	7666	-10.74	-6.13			
130	7692	-11.46	-6.09	10.4	1120	72
131	7714	-11.07	-6.06			
132	7736	-11.62	-6.35	10.8	911	74
133	7763	-12.27	-6.41			
134	7785	-12.20	-6.04	9.9	1147	62
135	7808	-11.53	-5.86			
136	7837	-10.81	-6.09	7.9	1271	61
137	7862	-10.56	-6.16			
138	7891	-10.92	-6.02	6.4	1222	65
139	7914	-10.62	-6.21			

Data table X: stalagmite NC-B

depth (mm)	age (yr, BP)	$\delta^{13}C$	$\delta^{18}O$	Ba (ppm)	Mg (ppm)	Sr (ppm)
140	7938	-10.89	-5.16	340.4	1112	74
141	7969	-11.63	-6.98			
142	7994	-10.95	-6.47	6.5	1328	65
143	8019	-10.79	-6.07			
144	8050	-11.07	-6.17	7.9	1285	63
145	8076	-10.42	-6.36			
146	8103	-11.40	-6.44	9.2	1164	64
147	8135	-10.76	-6.91			
148	8161	-10.71	-6.15	1.4	1428	55
149	8188	-10.37	-5.69			
150	8221	-11.18	-5.98	82.4	1361	438
151	8248	-11.40	-6.19			
152	8283	-11.35	-5.90	30.7	1528	125
153	8310	-11.06	-6.07			
154	8338	-11.10	-6.23	8.5	1240	65
155	8375	-11.00	-5.93			
156	8404	-11.20	-5.89	11.2	1271	79
157	8433	-11.11	-5.74			
158	8470	-11.84	-6.34	13.9	1125	87
159	8500	-11.28	-6.06			
160	8532	-11.42	-5.81	9.7	1241	71
161	8568	-11.57	-5.77			
162	8596	error	error	13.5	1261	86
163	8628	-10.62	-6.21			
164	8655	error	error	8.2	1136	65
165	8680	-10.88	-5.76			
166	8712	-11.12	-6.15	6.0	1235	71
167	8737	-10.80	-5.90			
168	8763	-11.09	-6.24	7.1	1112	66
169	8795	-10.91	-6.01			
170	8819	-11.18	-5.50	6.1	1064	71
171	8844	-11.18	-5.62			
172	8873	-11.26	-5.72	6.6	983	66
173	8898	-11.24	-6.07			
174	8927	-10.84	-6.15	8.8	1384	76
175	8952	-11.08	-5.95			
176	8977	-11.26	-6.08	5.2	1210	67
177	9009	-10.72	-5.71			
178	9034	-10.83	-5.77	6.7	1295	62
179	9059	-10.77	-5.78			
180	9091	-10.67	-5.39	4.2	1496	68
181	9118	-10.32	-5.49			
182	9146	-10.62	-5.71	7.6	1417	78
183	9180	-10.07	-5.37			
184	9209	-10.91	-5.49	8.5	1241	78
185	9244	-10.95	-5.52			
186	9276	-10.91	-5.74	12.5	1269	83
187	9308	-10.49	-5.61			
188	9345	-9.85	-4.27	3.5	1619	61
189	9376	-10.51	-5.73			
190	9404	-10.26	-5.40	5.7	1458	70
191	9434	-10.41	-5.49			
192	9457	-10.69	-5.53	6.7	1372	71
193	9480	-10.61	-5.46			
194	9506	-10.86	-5.89	4.7	1315	68
195	9527	-10.24	-5.31			
196	9550	-10.30	-5.52	5.4	1592	67
197	9577	-10.30	-5.46			
198	9599	-10.29	-5.58	5.7	1768	71
199	9625	-10.41	-5.59			
200	9645	-10.65	-5.63	10.5	1434	81
201	9665	-10.52	-5.53			
202	9689	-10.55	-5.50	7.7	1551	77
203	9710	-10.45	-5.62			
204	9731	-10.53	-5.56	7.8	1625	80
205	9756	-10.32	-5.44			
206	9775	-10.29	-5.63	6.9	1751	74
207	9795	-10.68	-5.76			
208	9818	-10.73	-5.86	13.7	1445	84
209	9838	-10.51	-5.69			
210	9860	-10.65	-5.93	11.4	1510	80

Data table X: stalagmite NC-B

depth (mm)	age (yr, BP)	$\delta^{13}C$	$\delta^{18}O$	Ba (ppm)	Mg (ppm)	Sr (ppm)
211	9879	-10.43	-5.61			
212	9899	-10.36	-5.66	8.1	1600	71
213	9922	-10.41	-5.62			
214	9940	-10.69	-5.61	10.0	1517	80
215	9960	-10.62	-5.96			
216	9983	-10.74	-5.81	7.9	1258	74
217	10002	-11.03	-5.76			
218	10021	-11.09	-5.89	4.4	1292	75
219	10044	-10.52	-5.61			
220	10063	-10.56	-5.55	16.0	1470	84
221	10086	-10.83	-5.93			
222	10105	-11.00	-5.85	12.4	1205	82
223	10125	-10.97	-5.89			
224	10150	-10.95	-5.88	12.4	1343	84
225	10170	-10.94	-5.92			
226	10189	-10.83	-5.10	10.7	1440	79
227	10215	-10.59	-5.61			
228	10237	-10.57	-5.46	4.8	1331	67
229	10259	-10.73	-5.87			
230	10286	-10.99	-5.90	4.7	1475	72
231	10310	-11.10	-6.10			
232	10340	-11.05	-5.95	9.0	1229	72
233	10371	-10.96	-5.97			
234	10411	-10.86	-5.75	6.9	1359	72
235	10491	-11.01	-5.81			
236	10636	-11.07	-5.61	5.5	1280	64
237	10791	-10.92	-5.52			
238	10928	-11.03	-5.69	5.2	1315	66
239	10981	-11.23	-5.76			
240	11027	-11.13	-5.68	9.4	1228	66
241	11081	-11.17	-6.19			
242	11126	-11.02	-5.81	7.3	1360	63
243	11170	-10.61	-5.53			
244	11224	-10.78	-5.24	5.0	1316	58
245	11269	-10.72	-5.44			
246	11322	-10.76	-5.91	8.1	1381	70
247	11366	-11.05	-5.93			
248	11407	-11.08	-5.95	8.6	1325	70
249	11459	-10.77	-5.88			
250	11500	-10.71	-5.75	7.1	1281	66
251	11539	-11.21	-5.83			
252	11586	-11.00	-5.87	4.8	1211	65
253	11625	-10.78	-5.83			
254	11661	-10.96	-5.94	5.2	1278	59
255	11706	-11.12	-5.82			
256	11742	-11.29	-5.84	5.0	1094	63
257	11787	-11.13	-5.86			
258	11824	-10.82	-6.00	3.3	1097	60
259	11860	-10.65	-5.92			
260	11909	-11.08	-6.16	8.2	1046	67
261	11945	-10.37	-5.86			
262	11981	-11.17	-5.76	5.6	1123	58
263	12025	-11.36	-5.89			
264	12060	-11.22	-5.79	4.9	1090	56
265	12096	-11.70	-6.61			
266	12143	-11.57	-6.01	4.5	892	61
267	12182	-11.49	-5.98			
268	12228	-11.45	-6.16	6.9	932	70
269	12262	-11.44	-6.03			
270	12299	-8.85	-6.44		1019	48
271	12346	-11.17	-5.71			
272	12386	-11.08	-5.76	6.8	1010	48
273	12423	-11.01	-5.85			
274	12468	-10.75	-6.00		1218	41
275	12506	-11.10	-6.32			
276	12542	-10.99	-5.98			
277	12588	-10.83	-6.72			
278	12628	-10.98	-6.53			
279	12676	-11.13	-6.05			
280	12713	-10.97	-6.24			
281	12755	-10.93	-6.20			

Data table X: stalagmite NC-B

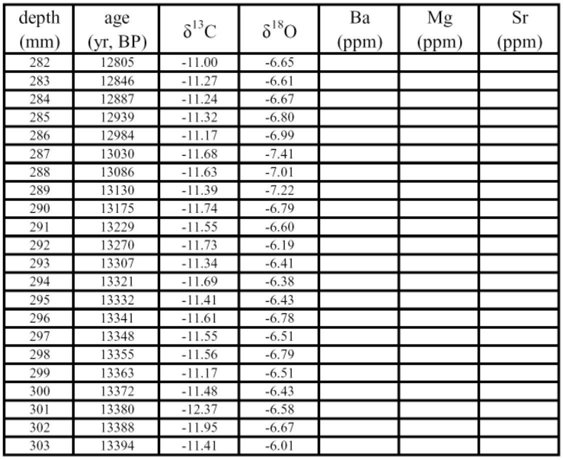

depth (mm)	age (yr, BP)	$\delta^{13}C$	$\delta^{18}O$	Ba (ppm)	Mg (ppm)	Sr (ppm)
282	12805	-11.00	-6.65			
283	12846	-11.27	-6.61			
284	12887	-11.24	-6.67			
285	12939	-11.32	-6.80			
286	12984	-11.17	-6.99			
287	13030	-11.68	-7.41			
288	13086	-11.63	-7.01			
289	13130	-11.39	-7.22			
290	13175	-11.74	-6.79			
291	13229	-11.55	-6.60			
292	13270	-11.73	-6.19			
293	13307	-11.34	-6.41			
294	13321	-11.69	-6.38			
295	13332	-11.41	-6.43			
296	13341	-11.61	-6.78			
297	13348	-11.55	-6.51			
298	13355	-11.56	-6.79			
299	13363	-11.17	-6.51			
300	13372	-11.48	-6.43			
301	13380	-12.37	-6.58			
302	13388	-11.95	-6.67			
303	13394	-11.41	-6.01			